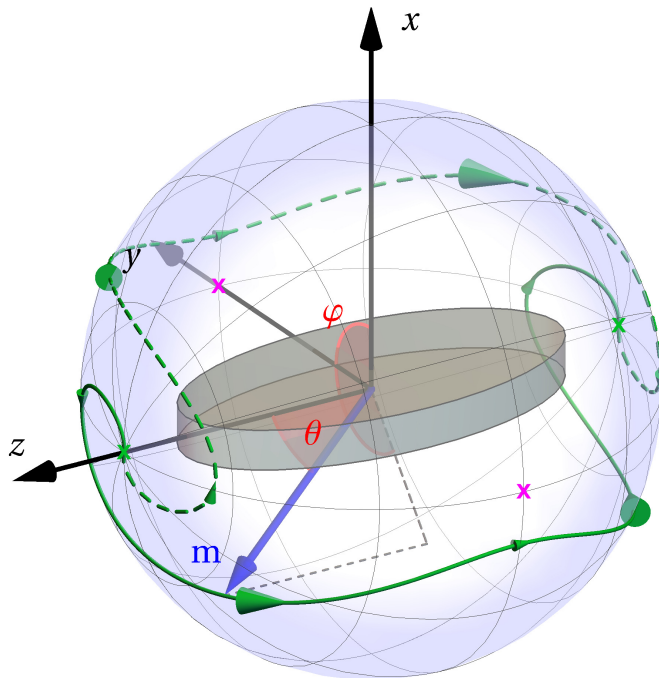




Energy-efficient control of magnetic states



Mohammad H. Badarneh



Faculty of Physical Sciences
University of Iceland
2024

ENERGY-EFFICIENT CONTROL OF MAGNETIC STATES

Mohammad H. Badarneh

Dissertation submitted in partial fulfillment of a
Philosophiae Doctor degree in Physics

Advisor

Dr. Pavel F. Bessarab

PhD committee

Dr. Pavel F. Bessarab (supervisor)

Prof. Hannes Jónsson

Prof. Unnar B. Arnalds

Dr. Cecilia Holmqvist

Opponents

Prof. Vitaliy Lomakin

Prof. Elton Santos

Faculty of Physical Sciences
School of Engineering and Natural Sciences
University of Iceland
Reykjavik, February 2024

Energy-efficient control of magnetic states

Dissertation submitted in partial fulfillment of a *Philosophiae Doctor* degree in Physics

Copyright © 2024 Mohammad H. Badarneh
All rights reserved

Faculty of Physical Sciences
School of Engineering and Natural Sciences
University of Iceland
Dunhagi 3
IS-107, Reykjavik, Reykjavik
Iceland

Telephone: 525 4000

Bibliographic information:

Mohammad H. Badarneh, 2024, *Energy-efficient control of magnetic states*, PhD dissertation, Faculty of Physical Sciences, University of Iceland, 172 pp.

ISBN 978-9935-9742-9-7

Printing: Háskólaprent, Fálkagata 2, 107 Reykjavík
Reykjavik, Iceland, February 2024

*This thesis is dedicated to my parents, Monerah and Hussein, for their endless love
and support*

Abstract

Encoding data with magnetic states is currently used in various devices for data transmission, storage, and processing. The operating principle in these devices is often based on controlled switching, e.g., using a pulse of an external magnetic field, between stable magnetic states characterized by a certain direction of magnetization. However, for each act of magnetization change, a certain amount of energy is used. The challenge is to ensure that this operation is energy-efficient. In this thesis, we present the development and implementation of a theoretical framework for energy-efficient control of magnetization using an external magnetic field. The theory makes it possible to identify optimal control paths (OCPs) – dynamical transition trajectories in the configuration space connecting the target states in the magnetic system and minimizing the energy cost – from which all properties of optimal control pulses, including spatial and temporal distribution are systematically obtained without the need for an exhaustive scan over a range of amplitudes, frequencies or shapes. Therefore, the theory provides fundamental knowledge about the optimal manipulation of magnetization and solutions for low-power digital technologies based on magnetic materials. The theory is applied to the problem of energy-efficient control of magnetization switching in uniaxial and biaxial nanoparticles, as well as nanowires. For these systems, we show that following an OCP involves the rotation of magnetic moments in a manner that minimizes the impact of external stimuli while effectively harnessing the system's internal dynamics to facilitate the desired change in magnetization. Additionally, we show that the derived optimal switching protocols are robust with respect to thermal fluctuations in the technologically relevant regime and when the perturbation in the material parameters is not too large. Finally, we develop a method for enhancing the thermal stability of energy-efficient magnetization switching by applying an additional longitudinal magnetic field. The time-dependence of the stabilizing field can be obtained in a definite way by demanding bound dynamics of local perturbations induced by the thermal bath. The work presented in this thesis facilitates the development of energy-efficient information technology based on magnetic materials.

Útdráttur

Skráning gagna með segulástöndum er nú notuð í ýmiskonar tækni fyrir gagnaflytning, geymslu og úrvinnslu. Þessi tækni byggist á því að geta stjórnað breytingum á seguástöndum, t.d. með púls af ytra segulsviði sem breytir stefnu seglunar. Hver segulbreyting krefst orku og það er mikilvægt að minnka þessa orkunotkun eins mikið og mögulegt er. Þessi ritgerð lýsir þróun og innleiðingu á kennilegri umgjörð fyrir stjórn segulástanda með segulsviði þar sem orkunotkunin er lágörkuð. Með þessari aðferð er hægt að finna bestu stjórn ferla (BSF), þ.e. ferla fyrir breytingu í segulstefnu milli gefinna segulástanda þannig að lágmarksorku er krafist, og leiða út bestu stjórnpúlsa, bæði í tíma og rúmi, á kerfisbundinn hátt, án þess að skanna útslag, tíðni og lögun púlssanna. Þessi aðferðafræði veitir því grundvallarþekkingu fyrir bestu stjórn á seglun og lausnum fyrir lág-orku stafræna tækni sem byggist á seglandi efnum. Aðferðafræðinni er beitt á stjórn segulbreytinga í nanóögnum með einum og tveimur segulásum, sem og nanóvírum. Fyrir þessi kerfi er sýnt fram á að BSF fela í sér snúnig segulvígna á þann hátt sem krefst lágmarksáhrifa af ytra sviðinu á meðan eiginleg tímaframvinda kerfanna nýtist sem best til að fá fram breytingarnar úr einu segulástandi í annað. Þar að auki er sýnt fram á að lausnirnar sem fást fyrir bestu aðferðirnar fyrir seglunarbreytingar eru ekki næmar fyrir áhrifum hitastigs innan þeirra marka sem eru eðlileg fyrir notkun í tækni eða fyrir frávikum í efnaeiginleikum svo lengi sem þau eru ekki of stór. Að lokum, er þróuð aðferð til að auka enn frekar stöðulgeika bestu ferlanna með því að bæta við segulsviði langsum. Tímaframvindu stöðgunarsviðsins er hægt að ákvarða með því að stja mörk á staðbundnar truflanir frá varmabaðinu. Aðferðafræðin sem lýst er í ritgerðinni auðveldar þróun á upplýsingatækni byggða á segulástöndum þar sem orkunotkunin er lágörkuð.

Table of Contents

Abstract	i
Útdráttur	iii
Table of Contents	v
List of Figures	vii
List of Original Articles	xix
Acknowledgements	xxii
1 Introduction	1
1.1 Motivation and state-of-the-art	1
1.2 Significance, scientific novelty, and general outline of the thesis	4
1.3 Description of magnetic states	5
1.3.1 The classical atomistic Hamiltonian	6
1.3.2 Macrospin model	7
1.4 Landau-Lifshitz-Gilbert equation	8
2 Optimal control theory for magnetic systems	11
2.1 Energy cost of magnetization transition	12
2.2 Unconstrained optimization of the energy cost functional	16
2.3 Constrained optimization of the energy cost functional	20
3 Thermal effects	27
3.1 Local dynamics of perturbation	29
3.2 Derivation of a time-dependent longitudinal magnetic field	33
4 Applications	39
4.1 Unconstrained optimization	39
4.1.1 Optimal control of magnetization reversal in a uniaxial nanoparticle	39
4.1.2 Optimal control of magnetization reversal in a biaxial nanoparticle	50
4.1.3 Optimal control of magnetization reversal in a bistable nanowire	59
4.2 Constrained optimization	64
4.2.1 Domain wall movement using an optimized uniform time-dependent magnetic field	64

Table of Contents

4.3	Enhancing thermal stability of optimal magnetization switching in a uniaxial nanoparticle	69
4.3.1	Effects of time-independent longitudinal magnetic field on the magnetization switching probability	72
4.3.2	Effects of time-dependent longitudinal magnetic field on the magnetization switching probability	76
5	Conclusions and outlook	85
6	Appendices	89
	Appendix A: Velocity and force calculations	98
	Appendix B: Testing FORTRAN implementation and the reproducibility of the calculated OCPs by directly solving LLG equation	100
	Appendix C: The stochastic Landau-Lifshitz-Gilbert equation	109
	Appendix D: Magnetization dynamics under constant magnetic field vs time-dependent magnetic field	112
	Appendix E: Testing robustness of the derived optimal protocols against thermal fluctuations and material parameters perturbation	116
7	Original articles	119
	Article I: Optimal Control of Magnetization Reversal in a Monodomain Particle by Means of Applied Magnetic Field	137
	Article II: Reduction of energy cost of magnetization switching in a biaxial nanoparticle by use of internal dynamics	150
	Article III: Enhancing thermal stability of optimal magnetization reversal in nanoparticles	157
	Article IV: Mechanisms of energy-efficient magnetization switching in a bistable nanowire	165
	Bibliography	165

List of Figures

1.1	Damped precessional magnetization switching of a magnetic moment	9
2.1	(a) Schematic representation of the current-carrying \mathbf{I} wire part of an electric circuit generating an external magnetic field \mathbf{B} and the associated energy lost due to the resistance of the electric circuit. The energy used is defined by Joule heating, while radiation is neglected. The magnetic field is shown with the blue circular lines, while the arrows on the lines signify the direction of \mathbf{B} . (b) Magnetization reversal of a macrospin pointing along the unit vector \mathbf{m} , where the reversal is induced by the magnetic field \mathbf{B} . The reversal trajectory connecting the initial and the final stable states is shown with the green line.	13
2.2	(a) Illustration of a trajectory, indicated by the green line, connecting the initial and final stable states of a macrospin pointing along the unit vector \mathbf{m} . The initial and final stable states are marked with blue points. Along this trajectory, each discrete point, represented by a red point, corresponds to a state of the system in the configuration space and is referred to as an image denoted by $\mathbf{m}_p = \mathbf{m}(t_p)$. These red points signify movable images that can be repositioned in the configuration space during the optimization process. (b) Illustration of the midpoint scheme used in the numerical method for finding OCPs. Two images \mathbf{m}_p and \mathbf{m}_{p+1} are connected by a geodesic path in the configuration space. The position $\mathbf{m}_{p+\frac{1}{2}}$ and the velocity $\dot{\mathbf{m}}_{p+\frac{1}{2}}$ at the midpoint of the path are defined by \mathbf{m}_p and \mathbf{m}_{p+1} , and the angle δ_p between them.	16

LIST OF FIGURES

3.1 Calculated dynamics of the magnetic moment for a uniaxial nanoparticle induced by the optimal switching magnetic field. The black line shows the zero-temperature trajectory of the magnetic moment which corresponds to the optimal control path $\mathbf{m}_0(t)$ for the magnetization switching. The green (red) line shows the trajectory for successful (unsuccessful) switching at finite temperature corresponding to the thermal stability factor $\Delta = 20$. The light red (blue) shaded area for $\pi/4 \leq \theta \leq 3\pi/4$ ($\theta < \pi/4$ and $\theta > 3\pi/4$) marks the domain where the perturbation dynamics is unstable (stable). The damping factor α is 0.2, the switching time T is $5\tau_0$ 28

3.2 Velocity diagrams showing the dynamics of the perturbation in the tangent space depending on the eigenvalues of the Hessian for $\alpha = 0$ and $B_r = 0$. (a) $w_1 = 1, w_2 = -1$, (b) $w_1 = 1, w_2 = 0$, (c) $w_1 = 1, w_2 = 1$. The black arrows in (a)-(c) show the distribution of the dynamics with the size of the arrows being proportional to the magnitude of the perturbation, and the colors in the background indicate if the amplitude of the perturbation is increasing (red), decreasing (blue), or constant (gray) in amplitude. 31

3.3 Velocity diagrams showing the dynamics of the perturbation in the tangent space depending on the eigenvalues of the Hessian for $\alpha = 0$ and $B_r = 1.0$. a) $w_1 = 1, w_2 = -1$, b) $w_1 = 1, w_2 = 0$, c) $w_1 = 1, w_2 = 1$. Notations and colors are the same as in Figure. (3.2) 31

3.4 Stability diagram for classifying the trajectories of the perturbation as stable or unstable depending on the sign of w_1/μ and w_2/μ . The condition $w_1 + w_2 > 0$ ($w_1 + w_2 < 0$) is fulfilled in the area above (below) the dashed gray line. Green points signify selected eigenvalues calculated along the zero temperature reversal trajectory, see the black line in Fig. (3.1). The unstable eigenvalues are displaced using two schemes as described in the legend. Blue circles and red points define the newly shifted eigenvalues, while the angle η defines their location in the plane. The letters (A-D) label the velocity diagrams showing the dynamics of the perturbation in the tangent space. The black arrows in Figs. (A)-(D) show the distribution of the dynamics with the size of the arrows being proportional to the magnitude of the perturbation, and the colors in the background indicate if the amplitude of the perturbation is increasing (blue), decreasing (red), or constant (gray). The notations Q_1 - Q_4 signify the quarter numbers. 35

4.1 Calculated optimal control paths (OCPs) for the reversal of a macrospin pointing along the unit vector \mathbf{m} . The initial and the final states are at the north and the south poles of the unit sphere, respectively. The damping factor α is 0.1. The switching time T is $10\tau_0$ and $100\tau_0$ for the paths shown with thick and thin green lines, respectively. The optimal external magnetic field \mathbf{B}_m at $t = T/4$, $t = T/2$ and $t = 3T/4$ is shown for the shorter path with the brown arrows. Figure adapted from Ref. [45]. 40

4.2 The optimal control path represented by the polar angle θ (a) and the azimuthal angle φ (b) as a function of time for $T = 100\tau_0$ and several values of the damping parameter α . Figure adapted from Ref. [45] . . . 43

4.3 Amplitude of the switching field as a function of time for $T = 100\tau_0$ and several values of α (solid lines). Dashed lines show αb_i^\perp which is proportional to the polar component of the torque generated by the internal field. Figure adapted from Ref. [45]. 44

4.4 The θ -projection of the internal and external torques along the optimal control path for damping value $\alpha = 0.2$ (a), $\alpha = 0.4$ (b), and $\alpha = 0.8$ (c). The magnitude of the switching time is $T = 10\tau_0$ 46

4.5 The θ -projection of the internal and external torques along the optimal control path for damping value $\alpha = 0.2$ (a), $\alpha = 0.4$ (b), and $\alpha = 0.8$ (c). The magnitude of the switching time is $T = 100\tau_0$ 46

4.6 Minimum energy cost of magnetization switching as a function of the inverse of the switching time. Dashed (dotted) lines show long (infinite) switching time asymptotics. Thin vertical lines indicate switching time T_ε , for which the minimum energy cost is $\varepsilon = 10\%$ larger than the infinite switching time limit Φ_∞ . Figure adapted from Ref. [45] 47

4.7 (a) Transverse Mercator projection [71] of the energy surface of a uniaxial macrospin. The meridians and the parallels are shown with thin white lines. The blue arrows show the distribution of the internal torque, with the size of the arrows being proportional to the magnitude of the torque. The calculated OCPs between the energy minima at $+Z$ and $-Z$ are shown with the green, pink, and orange lines for $T = 2\tau_0$, $T = 4\tau_0$, and $T = 14\tau_0$, respectively. The arrows along each OCP show the velocity at $t = T/6$, $t = T/3$, $t = T/2$, $t = 2T/3$, and $t = 5T/6$, where the arrow size codes the magnitude of the velocity. The damping factor α is 0.1. (b) The calculated optimal pulse as a function of the time for $T = 4\tau_0$ and $\alpha = 0.1$ 48

LIST OF FIGURES

- 4.8 Optimal switching of a flat elongated nanomagnet representing a biaxial anisotropy system. The direction of the normalized magnetic moment \mathbf{m} is shown with the blue arrow. Orientations of \mathbf{m} that correspond to the minima and the saddle points on the energy surface are marked with the green and magenta crosses, respectively. The calculated optimal control paths between the energy minima are shown with the solid and the dashed green lines. The damping factor α is 0.1, the switching time T is $8\tau_0$, and the hard-axis anisotropy constant is twice as large as the easy-axis anisotropy constant. The green arrows along the reversal paths show the velocity of the system at $t = T/6$, $t = T/3$, $t = T/2$, $t = 2T/3$, and $t = 5T/6$, with the size of the arrowheads being proportional to the magnitude of the velocity. The contours of constant azimuthal angle φ (meridians) and polar angle θ (parallels) are shown with thin black lines. Figure adapted from Ref. [47]. 51
- 4.9 Transverse Mercator projection [71] of the energy surface of a macrospin with (a) uniaxial anisotropy and biaxial anisotropy with (b) $\xi = 1$ and (c) $\xi = 2$. The meridians and the parallels (see Fig. 4.8) are shown with thin white lines. The blue arrows show the distribution of the internal torque, with the size of the arrows being proportional to the magnitude of the torque. The calculated OCPs between the energy minima at $+Z$ and $-Z$ are shown with the green, pink, and orange lines for $T = 2\tau_0$, $T = 4\tau_0$, and $T = 14\tau_0$, respectively. The arrows along each OCP show the velocity at $t = T/6$, $t = T/3$, $t = T/2$, $t = 2T/3$, and $t = 5T/6$, where the arrow size codes the magnitude of the velocity. The damping factor α is 0.1. The solid and the dashed lines of the same color show equivalent OCPs. They differ by an arbitrary rotation around the easy axis for the uniaxial case; For finite ξ , the degeneracy is lifted and there are two OCPs, symmetrical with respect to a π -angle rotation around the easy axis, for a given T . Note that the OCPs do not pass through saddle points (SP) on the energy surface. The θ -projection of the internal torque along the OCPs from (a)-(c) are shown in (d)-(f), respectively. Figure adapted from Ref. [47]. 52
- 4.10 Calculated optimal switching pulse of external magnetic field for a macrospin with (a) uniaxial anisotropy and biaxial anisotropy with (b) $\xi = 1$ and (c) $\xi = 2$. The switching time T is $14\tau_0$ and the damping parameter α is 0.1. The pulses are derived from the OCPs shown in Fig. 4.9(a)-(c). Figure adapted from Ref. [47]. 53
- 4.11 The θ -projection of the internal, external, and the total torques along the optimal control path for damping value $\alpha = 0$ (a), $\alpha = 0.1$ (b). The magnitude of the switching time is $T = 2\tau_0$, while the dimensionless parameter ξ determining the strength of the hard axis is 5. 54

- 4.12 The θ -projection of the internal, external, and the total torques along the optimal control path for damping value $\alpha = 0$ (a), $\alpha = 0.1$ (b). The magnitude of the switching time is $T = 2\tau_0$, while the dimensionless parameter ξ determining the strength of the hard axis is 10. 54
- 4.13 Minimum energy cost of magnetization reversal as a function of (a) inverse of the switching time for $\alpha = 0.2$, (b) damping parameter for $T = 20\tau_0$, for various ξ values. Green dashed line corresponds to the solution of the reversal of a free macrospin, while the black dashed line shows the infinite switching time asymptotic $\Phi_\infty \equiv 4\alpha K/(\gamma\mu)$. Figure adapted from Ref. [47]. 55
- 4.14 Minimum energy cost of magnetization reversal as a function of ξ for various T values (solid lines). The dashed color lines show the switching cost for a free macrospin. The magnitude of the damping factor α is 0.2. Black dashed line shows the infinite switching time asymptotic. Figure adapted from Ref. [47]. 56
- 4.15 Approximation for the minimum energy cost of magnetization reversal for a macrospin within the zero- (Φ_f), first- ($\Phi^{(1)}$), and second-order ($\Phi^{(2)}$) perturbation theory [see Eq. (4.32)], as indicated in the legend, vs the inverse of the switching time. The strength of the hard-axis anisotropy ξ is (a) 0 and (b) 1. Red solid line shows the numerically exact solution. Black dashed line shows the infinite switching time asymptotic. The intersection of the short and the long switching time asymptotes provides the optimal switching time T^* [see Eq. (4.26)]. The magnitude of α is 0.2. Figure adapted from Ref. [47]. 59
- 4.16 Stable orientations of the magnetization in a nanowire. The nanowire is represented by a chain of $N = 30$ magnetic moments. Arrows indicate orientation of the moments. Direction of the anisotropy axis is shown with the double-headed arrow. Transition between the states is schematically shown with the black arrow. In the OCP, the initial state is realized at $t = 0$, while the final state is realized at $t = T$. Figure adapted from Ref. [46]. 60
- 4.17 Magnetic configurations realized along OCPs (a)-(c) and MEP (d) for magnetization switching in the nanowire of length $N = 30$. For the OCPs, configurations at $t = T/2$ are shown where $T = 1$ ns. For the MEP, the saddle point configuration is presented. OCP corresponds to a coherent rotation of magnetic moments for $\alpha = 0.1$ (a) and to spin wave assisted switching with 1.5 wave periods for $\alpha = 0.5$ (b) and with 1 wave period for $\alpha = 0.6$ (c). MEP corresponds to a transient domain wall nucleation and propagation (d). Figure adapted from Ref. [46]. 61

LIST OF FIGURES

4.18 Minimum energy cost of magnetization switching as a function of the nanowire length N for $\alpha = 0.4$ and $T = 1$ ns (a) and damping parameter α for $N = 50$ and $T = 1$ ns (b). Uniform rotation and spin wave solutions are shown with blue and red circles, respectively. Red labels indicate the number of wavelengths in the spin-wave solutions. Solution for the macrospin approximation is shown with a gray line. Figure adapted from Ref. [46]. 62

4.19 Variation of the energy of the nanowire with $N = 50$ along the MEP (black line) and the OCP for $T = 1$ ns, $\alpha = 0.1$ (blue line) and $\alpha = 0.6$ (red line). Reaction coordinate is defined as a normalized displacement along the path. Figure adapted from Ref. [46]. 63

4.20 Stable 2π domain wall in a nanowire. The nanowire is represented by a chain of $N = 32$ magnetic moments. Arrows indicate orientation of the moments. Periodic boundary conditions are applied along x direction. 65

4.21 Stable 2π domain wall in a nanowire. The nanowire is represented by a chain of $N = 32$ magnetic moments. Arrows indicate orientation of the moments. Direction of the anisotropy axis is shown with the double-headed arrow. Transition between the states is schematically shown with the black arrow. In the constrained OCP calculations, the initial stable state is realized at $t = 0$, while the final stable state is realized at $t = T$ 65

4.22 Penalty term, see Eq. 2.28, as a function of time. 66

4.23 Initial guess of \mathbf{B}^* (a) and after convergence (b) as a function of time. 66

4.24 space- time-dependent magnetic field \mathbf{B} (a) and the site-dependent parameter (b) as a function of time. 67

4.25 (a) and (c) Stable 2π domain wall, while (b) magnetic configurations realized along OCP at $t = T/2$. The switching time $T = 1$ ns and damping $\alpha = 0.1$ 68

4.26 Average magnetization realized along OCP (solid line) and obtained by direct LLG simulations (points) as a function of time. The switching time $T = 1$ ns and damping $\alpha = 0.1$ 68

4.27 Calculated dynamics of the magnetic moment for a uniaxial nanoparticle induced by the optimal switching magnetic field. The black line shows the zero-temperature trajectory of the magnetic moment which corresponds to the optimal control path $\mathbf{m}_0(t)$ for the magnetization switching. The green (red) line shows the trajectory for successful (unsuccessful) switching at finite temperature corresponding to the thermal stability factor $\Delta = 20$. Labels A and B show positions of the magnetic moment for which the dynamics of local perturbations in the magnetization is illustrated in the corresponding insets of Fig. 4.28. The light red (blue) shaded area marks the domain for $\pi/4 \leq \theta \leq 3\pi/4$ ($\theta < \pi/4$ and $\theta > 3\pi/4$) where the perturbation dynamics is unstable (stable). The damping factor α is 0.2, and the switching time T is $5\tau_0$ 70

4.28 Diagram classifying dynamics of perturbations in the magnetization. The green, blue, and red lines show how the Hessian's eigenvalues w_1 and w_2 change along the zero temperature reversal trajectory (see the black line in Fig. 4.27) for three values of the longitudinal magnetic field as indicated in the legend. The right end of the lines correspond to the initial and the final states at the energy minima, while the left end of the lines corresponds to the top of the energy barrier. The gray shaded area marks the domain of possible w_1, w_2 . Labels A-D indicate pairs of the eigenvalues for which the velocity diagrams illustrating the perturbation dynamics are shown in the insets. The background color in the insets signify whether the amplitude of the perturbation is increasing (blue), decreasing (red), or constant (gray). The damping factor α is 0.2. 73

4.29 Calculated success rate of magnetization reversal as a function of the longitudinal magnetic field B_r for various values of the switching time T (a) and the damping parameter α (b). In (a), $\alpha = 0.1$; In (b), $T = 10\tau_0$. The thermal stability factor $\Delta = 20$. The shaded areas around the curves indicate the statistical error. 74

4.30 Calculated distribution of the copies of the system in the statistical ensemble at $t = T/2$ and various values of the longitudinal magnetic field, superimposed on the Lambert azimuthal projection [99] of the energy surface of the system. The green dots correspond to the copies that will eventually reach the final state at $-Z$ (successful switching), while the red dots mark the copies that will end up at the initial state at $+Z$ (unsuccessful switching). The black line shows the calculated OCP for the reversal. The damping factor α is 0.1, the thermal stability factor Δ is 20, and the switching time T is $10\tau_0$ 74

LIST OF FIGURES

4.31 (a) Calculated success rate of magnetization reversal as a function of damping parameter α for switching time $T = 10\tau_0$. (b)-(c) Calculated success rate as a function of T for $\alpha = 0.1$ and $\alpha = 0.2$. The red, blue, and black lines correspond to the three values of the longitudinal magnetic field B_r as indicated in the legend. The thermal stability factor $\Delta = 20$. The shaded areas around the curves indicate the statistical error. 75

4.32 (a) Velocity diagram showing the dynamics of the perturbation in the tangent space obtained for $w_1 > 0$ and $w_2 > 0$ and zero B_r . Values of w_1 and w_2 are taken from (b) at which the dashed vertical green line intersects the solid and dashed black lines. Figure (b) shows the calculated eigenvalues of the projected Hessian along the zero-temperature reversal trajectory, see the black line in Figure. 4.27, as a function of the switching time. (c) The calculated radial field obtained using the scheme I defined in Chapter 3, see Eq. 3.10, as a function of the switching time. The green point shows the value of B_r used for shifting the eigenvalues. (d) Velocity diagram showing the effect of B_r on the dynamics of the perturbation in the tangent space after shifting the eigenvalues, compared to (a). The magnitude of the switching time T is $5\tau_0$, while the damping factor $\alpha = 0.2$ and $\lambda = 0.5$. The black arrows in Figures (a) and (d) show the distribution of the dynamics with the size of the arrows being proportional to the magnitude of the perturbation, and the colors in the background indicate that the amplitude of the perturbation is decreasing (red), or constant (gray). 76

4.33 Similar to Figure 4.32, but for $w_1 > 0$ and $w_2 < 0$ and different value of B_r as shown in (c). The black arrows in Figures (a) and (d) show the distribution of the dynamics with the size of the arrows being proportional to the magnitude of the perturbation, and the colors in the background indicate if the amplitude of the perturbation is increasing (blue), decreasing (red), or constant (gray). 77

4.34 Similar to Figure 4.32, but for $w_1 = 0$ and $w_2 < 0$ and different value of B_r as shown in (c). The black arrows in Figures (a) and (d) show the distribution of the dynamics with the size of the arrows being proportional to the magnitude of the perturbation, and the colors in the background indicate if the amplitude of the perturbation is increasing (blue), decreasing (red), or constant (gray). 77

- 4.35 Calculated distribution of the copies of the system in the statistical ensemble at $t = T/2$ and various values of the longitudinal magnetic field, superimposed on the Lambert azimuthal projection [99] of the energy surface of the system. White points signify the energy minima at $\pm Z$. The black line shows the calculated reversal trajectory at zero temperature. The arrows along the black line demonstrate the velocity at different partitions of T , while the size of the arrows code the magnitude of the velocity. The copies of the ensemble that will eventually succeed and not succeed in the magnetization switching are marked with green and red points, respectively, and shown at $t = T/2$ without applying B_r (a) and with B_r for $\lambda = 1/\sqrt{2}$ (b), $\lambda = 0.85$ (c), and $\lambda = 0.95$ (d). The damping factor α is 0.2, the thermal stability factor Δ is 20, while the switching time T is $10\tau_0$ 78
- 4.36 (a) Magnetization reversal success rate as a function of λ for damping $\alpha = 0.2$ and different values of the switching time T , as depicted in the legend. The solid and dashed lines are obtained with the corresponding B_r defined in scheme *I* and *II*, respectively. The gray shading area signifies the range of λ values at which B_r is zero for scheme *I*, while $B_r = 0$ for $\lambda \in (-1, 0]$ in scheme *II*. The vertical gray dashed lines mark the critical values of λ at $\lambda = 0$ and $\lambda = \pm 1/\sqrt{2}$. (b) Success rate as a function of damping α for $T = 10\tau_0$, where the black solid line shows the results for zero B_r , and the blue solid (dashed) line is obtained by applying B_r defined in scheme *I* (*II*) for $\lambda = 0.8$. (c) Success rate as a function of T for $\alpha = 0.2$ where the black, solid and dashed blue lines are the same as in (b). The thermal stability factor Δ is 20. 79
- 4.37 Lambert azimuthal equal-area projection of the energy surface of a macrospin with uniaxial anisotropy. The energy minima at $\pm Z$ are marked with the white points. Black line shows the calculated zero temperature reversal trajectory. The arrows along the black line show the velocity at $t = T/6$, $t = T/3$, $t = T/2$, $t = 2T/3$, and $t = 5T/6$, where the arrow size codes the magnitude of the velocity. The green cloud and red points show the distribution of the copies of the ensemble realized at a partition of the switching time T along OCP. The green cloud and red points signify the successful and unsuccessful copies, respectively. The radial component of the pulse B_r is included in the calculations with $\lambda = 0.88$. The damping factor α is 0.2, the thermal stability factor Δ is 20, while the switching time T is $13\tau_0$ 81

LIST OF FIGURES

4.38 Magnetization reversal success rate as a function of λ for damping factor $\alpha = 0.2$ and different values of the switching time T , as depicted in the legend. The vertical gray dashed lines mark the critical values of λ at $\lambda = 0$ and $\lambda = \pm 1/\sqrt{2}$. The gray shading area signifies the range of λ values at which B_r is zero. The thermal stability factor Δ is 20. 82

4.39 (a) Energy cost of magnetization switching as a function of the inverse of the switching time T for various values of the thermal stability factor Δ , as depicted in the legend. The gray solid line shows the minimum switching cost Φ_m [Eq. (4.22)], while the black dashed line is the infinite switching time asymptotic, $\Phi_\infty \equiv 2\alpha K/(\gamma\mu)$. The solid points deviating from Φ_m at specific T show the switching cost Φ at fixed success rate, 99.2%, as shown in (b). For instance, $\Phi|_{\Delta=50}$ coincides with (deviates from) Φ_m for $T \ll (\alpha + 1/\alpha)\tau_0$ ($T \gg (\alpha + 1/\alpha)\tau_0$) located to the right (left) of the black dotted line, where the success rate in this timescale is larger than 99.2% (fixed at 99.2%) without (with) applying B_r . The magnitude of the damping factor α is 0.2 83

6.1 Evolution of the magnetic moment \mathbf{m} along the OCP for switching time $T = 10\tau_0$ and damping parameter $\alpha = 0$, and the corresponding optimal pulse \mathbf{B} derived from the calculated OCP. Analytical solution is given by solid lines, position of images included in the numerical calculations is shown with points. $Q = 50$ number of movable images were used in the numerical OCP calculations. 101

6.2 Similar to Figure 6.1 but for switching time $T = 100\tau_0$ and $Q = 500$ movable images. 101

6.3 Similar to Figure 6.1 but for switching time $T = 10\tau_0$, damping parameter $\alpha = 2.0$ and $Q = 50$ movable images. 101

6.4 Similar to Figure 6.1 but for switching time $T = 100\tau_0$, damping parameter $\alpha = 2.0$ and $Q = 100$ movable images. 102

6.5 Log-log plot of the error as a function of the step size Δt . The magnitude of the damping parameter $\alpha = 0$ (a) $\alpha = 0.2$ (b). The switching time T is $10\tau_0$. The gray line on the graph represents a fitted line with a slope as shown in the legend. 102

6.6 Evolution of the magnetic moment \mathbf{m} along the OCP (trajectory obtained by directly solving LLG) is shown with data points (solid lines). The optimal pulse \mathbf{B} is derived from the calculated OCP. The switching time $T = 10\tau_0$ and damping parameter $\alpha = 0.0$. The dimensionless parameter ξ determining the magnitude of the hard axis anisotropy is 30. 102

6.7	Similar to Figure 6.6 but for damping $\alpha = 0.01$ and $\xi = 10$	103
6.8	Similar to Figure 6.6 but for damping $\alpha = 0.1$ and $\xi = 10$	103
6.9	Dynamics of a magnetic moment \mathbf{m} induced by an effective magnetic field \mathbf{B}^{eff} under the effects of thermal fluctuations. The green line shows the calculated trajectory described by the stochastic Landau-Lifshitz-Gilbert equation, see Eq. (6.35). The black arrows in the tangent space show the precessional torque $-\mathbf{m} \times \mathbf{B}^{\text{eff}}$ and the damping torque $-\mathbf{m} \times (\mathbf{m} \times \mathbf{B}^{\text{eff}})$. The orientation of the magnetic moment is described by the polar angle θ and an azimuthal angle φ . The effective field \mathbf{B}^{eff} is pointing along z direction.	106
6.10	Average energy of a uniaxial nanoparticle, see Eq. 4.1, as a function of the equilibration time for damping $\alpha = 0.01$ (a) $\alpha = 0.2$ (b) for different timesteps dt as depicted in the legend. The magnitude of the thermal stability factor $\Delta = K/(k_B T)$ is 40. Dashed green line shows the thermal energy level due to the equipartition theorem.	114
6.11	Effect of thermal fluctuations on the magnetization reversal induced by the optimal switching pulse. Dashed lines mark the beginning and the end of the applied pulse. Blue (red) line shows evolution of the z -component of the normalized magnetic moment during successful (unsuccessful) reversal at finite temperature. Black line corresponds to the zero-temperature reversal. The magnitude of the damping factor is	115
6.12	Effect of perturbations in the material parameters τ_0 (a) and α (b) on the magnetization reversal induced by the optimal switching pulse. Magnitude of the perturbations $\Delta\tau_0$ and $\Delta\alpha$ is shown in the legend. Blue (red) lines show evolution of the z -component of the normalized magnetic moment during successful (unsuccessful) reversal. Black line corresponds to the reversal in a particle characterized by unperturbed material parameters.	116
6.13	Effect of perturbations in the material parameters α (a), τ_0 (b), and ξ (c) on the magnetization reversal induced by the optimal switching pulse. Magnitude of the perturbations $\Delta\tau_0$, $\Delta\alpha$, and $\Delta\xi$ is shown in the legend. Blue (red) lines show evolution of the z -component of the normalized magnetic moment during successful (unsuccessful) reversal. Black line corresponds to the reversal in a particle characterized by unperturbed material parameters: $\alpha = 0.1$, $\xi = 5$. The switching time $T = 2\tau_0$	116

List of Original Articles

- I. Kwiatkowski, G. J., **Badarneh, M. H.**, Berkov, D. V., & Bessarab, P. F. *Optimal control of magnetization reversal in a monodomain particle by means of applied magnetic field*. Physical Review Letters, **126**, 177206 (2021).
- II. **Badarneh, M. H.**, Kwiatkowski, G. J., & Bessarab, P. F. *Reduction of energy cost of magnetization switching in a biaxial nanoparticle by use of internal dynamics*. Physical Review B, **107**, 214448. (2023).
- III. **Badarneh, M. H.**, Kwiatkowski, G. J., & Bessarab, P. F. *Enhancing thermal stability of optimal magnetization reversal in nanoparticles* (2023), arXiv: 2312.11293 (Submitted for publication in Physical Review B).
- IV. **Badarneh, M. H.**, Kwiatkowski, G. J., & Bessarab, P. F. *Mechanisms of energy-efficient magnetization switching in a bistable nanowire*. Nanosystems: Physics, Chemistry, Mathematics **11**, 294 (2020).

Acknowledgements

I would like to extend my sincere appreciation to my supervisor, Dr. Pavel F. Bessarab, whose guidance, patience, and unwavering support have been instrumental throughout this research journey. I am also grateful for the opportunities he provided to visit fellow research groups in Russia and Germany. His expertise, insightful feedback, and constructive criticism have shaped this work and enriched my understanding in the field of modern magnetism. I feel incredibly fortunate to have had the opportunity to work with him, and his trust and advice have contributed greatly to my development as a scientist. I have gained a wealth of knowledge, and I truly appreciate the time spent working with him.

I am very grateful to Dr. Grzegorz Kwiatkowski for his valuable input and expertise. Working with him was truly enjoyable, and his thoughtful comments and suggestions have immensely contributed to the refinement of this thesis. Infinite scientific discussions spanning various physics subjects and his immense support in my endeavors have proven to be highly fruitful, reshaping my perspective on modern magnetism. I have gained a wealth of knowledge. Additionally, I would like to express my gratitude to Dr. Grzegorz Kwiatkowski for proofreading my thesis.

I would like to thank my PhD committee, Prof. Hannes Jónsson, Prof. Unnar B. Arnalds, and Dr. Cecilia Holmqvist for support and guidance. I also thank my opponents Prof. Elton Santos and Prof. Vitaly Lomakin for the thorough evaluation of my thesis. Special thanks to Prof. Dmitry Berkov (General Numerics Research Lab, Germany), Prof. Stefan Heinze (University of Kiel, Germany), Prof. Stefan Blügel (Jülich Research Centre, Germany), and Prof. Valery Uzdin (ITMO University, St. Petersburg, Russia) for welcoming me into their groups. To my friends and colleagues that I have met from all over the world, thank you for the collaborative spirit and the good times we shared. I also thank the administrative staff at Tæknigarður, in particular, Þuríður, Iris, Sandra, Anna Kristín, and Harpa for always being helpful.

Special thanks to my brothers, Obada Badarneh & Dr. Khalid Badarneh, and Prof. Abdalla Obeidat for their friendship and support. Finally, I sincerely thank my parents, sisters, and brothers for their endless love and support. Special thanks to my dear wife, *Ola*, for her help, patience, and love.

This thesis was funded by the Icelandic Research Fund (IRF), grant number 217813, for which I am very grateful.

1 Introduction

1.1 Motivation and state-of-the-art

The ever-increasing flow of data inherent in the processes of modern society establishes a vast demand for the development of information and communication technologies. The purpose of science is to make sure that these advancements are energy-efficient and sustainable. Encoding data with magnetic degrees of freedom has proved successful and is currently used in various devices for data transmission, storage, and processing. In particular, writing data is achieved by a controlled magnetization switching between stable magnetic states, where for each act of magnetization reversal — a physical implementation of a bit operation — a certain amount of energy is used. The challenge is to minimize the energy cost.

One approach to solving the problem of minimizing the energy cost is to optimize the characteristics of the magnetic information bits. Instead of single-phase grains, heterostructures combining large magnetization of the soft magnetic layer and the high coercitivity of the hard magnetic layer have been introduced [1]. These systems, also known as exchange spring magnets, provide enhanced thermal stability and improved writability.

Magnetic textures with topological charges hold great promise as a basis for future technologies. In particular, information can be carried by topological magnetic textures such as domain walls [2] and skyrmions [3]. These objects are characterized by properties making them ideal information bits: they can be very small in size, which is beneficial for the realization of high data density, and relatively stable due to non-trivial topology, which is crucial for reliable information storage. Additionally, the sensitivity of the topological spin textures to stimuli of various kinds, e.g., external magnetic and electric fields [5, 105] and electric current [6], opens up a wide range of possibilities for manipulation, which is beneficial for information processing.

Improvement of the performance of digital devices can be achieved not only by the adjustment of the characteristics of the information carriers but also by optimization of the switching stimuli involved in bit operations. The possibility to optimize was demonstrated, e.g., in the experiments on the magnetic vortex core reversal [106]. A straightforward way to switch the magnetization of the core is to apply a large

1 Introduction

static magnetic field of the order of 0.5 Tesla opposite to the vortex core polarization. Alternatively, the core reversal can be achieved by applying short bursts of the sinusoidal magnetic field needed to excite selected modes in the system. Interestingly, the amplitude of the pulse turned out to be more than three hundred times smaller than that of the stationary switching field. The more efficient field protocol triggers a highly nontrivial switching mechanism involving vortex-antivortex pair formation and subsequent annihilation.

The possibility to achieve the same changes in the magnetic structure by different techniques, which are not equivalent in terms of energy cost, appears to be a general property as it has been demonstrated, theoretically and experimentally, for various magnetization switching phenomena [8–18]. The multiplicity of transition paths between stable magnetic states leads to an idea about an existence of an optimal switching mechanism that is defined solely by the intrinsic parameters of the magnetic system. The question arises as to whether it is possible to identify such an optimal mechanism in a definite way and, based on this knowledge, predict the properties of an optimal switching pulse, including shape, duration, and amplitude. A traditional approach to solving this problem involves the excitation of the lowest-energy modes of the system and the search for the dynamical instabilities, which are precursors of the magnetic transition [19–21]. In practice, analysis based on this method requires an assumption of some ansatz for the switching pulse, e.g., monochromatic wave, then scanning over various parameters of the pulse, such as frequency and amplitude, and finally verifying the desired switching event *a posteriori*. Unfortunately, this approach does not guarantee that the resulting mechanism is optimal in a certain sense due to constraints initially imposed on the control stimulus. Moreover, if the shape of the pulse is not optimized, additional, uncontrolled modes could be excited, slowing down the transition, as has been demonstrated, e.g., in Ref. [22].

Optimal control theory (OCT) [23] represents a conceptually different approach to pulse optimization. In contrast to the traditional methods based on exhaustive scanning over possible control protocols followed by inspection of the system’s response, the OCT provides a more systematic approach as it focuses on a definite identification of the optimal switching trajectory that makes the energy of the control pulse minimum. This powerful approach finds widespread application across various scientific disciplines due to its versatility in addressing complex systems and dynamic processes. Its applications span diverse fields, including engineering, economics, biology, and physics. Interestingly, although OCT has gained prominence in various fields, its application in magnetism remains relatively unexplored. Based on optimization principles, this theory is employed to determine the most effective control inputs that steer a system toward a desired state while considering possible constraints and minimizing a defined cost function. Barros *et al.* [24, 25] have applied OCT to the reversal of a single magnetic moment. Within the approach, the optimal switching pulse is found as a result of a minimization of the switching cost functional under the constraint defined by a system-specific magnetization dynamics. In this thesis, we revisited the OCT due to Barros *et al.* [24, 25] and developed a more efficient approach based on unconstrained

minimization. In particular, we solve the equation of motion as an inverse problem for the pulse of the external magnetic field thereby enabling us to express the pulse in terms of the dynamical trajectory of the magnetic transition. This formalism has led to a notion of optimal control path (OCP) — a dynamical trajectory connecting the target magnetic states and minimizing the energy cost. All properties of the optimal protocols can be found from OCP in a straightforward way.

It is noteworthy that Vlasov *et al.* [26] has recently applied OCT to the problem of energy-efficient control of magnetization reversal of a perpendicular macrospin by means of spin-orbit torque. Moreover, the principle of Ohmic loss minimization was applied by Tretiakov *et al.* [27] to predict the optimal pulse of electric current for efficient control of the domain wall motion described by two collective coordinates.

1.2 Significance, scientific novelty, and general outline of the thesis

This thesis bridges the domains of optimal control theory and magnetic dynamics, introducing novelty through a robust and elegant formulation for achieving energy-efficient control of magnetic states using the pulse of the external magnetic field. This formulation treats the control pulse as a dependent variable of the system's dynamical trajectory, leading to a simple, unconstrained optimization problem. Additionally, the thesis provides fundamental knowledge about the energy-efficient manipulation of magnetic states and the link between optimal control of magnetic states and material fundamentals. The processes investigated in this thesis are physical realizations of bit operations in digital devices. Therefore, the reported optimal mechanisms can facilitate the development of energy-efficient information and communication technologies based on magnetic states. The optimal switching stimuli derived in this thesis can also motivate the development of experimental techniques for shaping pulses of external magnetic field. Although the external stimulus considered in this thesis is an external magnetic field, the methodology employed here is quite general thereby, can be extended to various techniques used to manipulate magnetic states. These methods include optical switching and the utilization of electric currents for magnetization switching [26].

The scientific novelty of the thesis lies in utilizing the optimal control theory to the manipulation of magnetic states. The presented method relies on systematic determination of the optimal control paths (OCPs), i.e., dynamical transition trajectories in the configuration space connecting the target states in the magnetic system and minimizing the energy cost functional. All properties of the optimal switching pulses, including spatial and temporal distribution, are systematically derived from the OCPs without the need to exhaustively scan over a range of amplitudes, frequencies, or shapes, as has been done in previous studies. We show that the derived optimal switching protocols in a nanoparticle are robust with respect to thermal fluctuations in the technologically relevant regime of low temperatures, as well as when the perturbation in the material parameters is not too large.

Moreover, the thesis presents a method for enhancing the thermal stability of optimal magnetization reversal in nanoparticles. We demonstrate that magnetization reversal is mostly disturbed by unstable perturbations arising in a certain domain of the configuration space of a nanomagnet. These instabilities can be suppressed, and the probability of magnetization switching enhanced by applying an additional stimulus, such as a weak longitudinal magnetic field. The time dependence of the stabilizing longitudinal field for magnetization switching in a uniaxial nanomagnet is derived from the requirement of maintaining bounded dynamics of the perturbations.

The thesis is organized as follows:

- In Chapter 2, a new theoretical framework for energy-efficient control of magnetization by means of external magnetic field is presented: In Sec. 2.1 the OCT for magnetic systems is developed, and a connection between the pulse of the external magnetic field and both the dynamical trajectory of the magnetic system and its internal magnetic field is shown. In Sec. 2.2 the numerical method for finding OCPs and corresponding energy-efficient control pulses via direct unconstrained minimization of the cost functional is presented. In Sec. 2.3 a method for constrained optimization of the energy cost functional is developed.
- In Chapter 3, we propose a method for enhancing thermal stability of optimal magnetization switching by means of additional longitudinal magnetic field. In Sec. 3.1, an equation of the first-order perturbation term in the eigenvector coordinates of the projected Hessian is derived, the effects of the longitudinal field on the dynamics of the perturbation is shown. In Sec. 3.2, an equation for the radial field that depends on time and the material properties is derived.
- In Chapter 4, the methods presented in chapters 2-3 are applied to various systems including the energy-efficient manipulation of magnetization in uniaxial and bistable nanoparticles as well as biaxial nanowire.

1.3 Description of magnetic states

The study of magnetic phenomena in solids encompasses a wide range of intriguing phenomena [28]. These phenomena can be effectively described across various energy and length scales. Atomistic and micromagnetic models [28, 29] enable description of magnetic materials at scales ranging from atomic lattices and beyond. While these models are adept at capturing macroscopic behaviors, it is essential to acknowledge the quantum nature of magnetic phenomena. However, the complexity of quantum-mechanical models poses challenges when attempting to describe magnetic phases and magnetization processes in realistic systems comprising billions of atoms, with typical dimensions ranging from a few nanometers to a few micrometers. In navigating these complexities, the atomistic Heisenberg model emerges as a valuable tool. Serving as the classical limit of its quantum-mechanical counterpart, the Heisenberg model assumes the localization of magnetic moments on a given lattice, treating them as conventional classical vectors.

The aim of the following subsection is to introduce the atomistic model which is used throughout this thesis for describing magnetic states.

1.3.1 The classical atomistic Hamiltonian

Consider a magnetic system consisting of N localized atoms, where the i th atom carries a net magnetic moment $\mathbf{m}_i = \mathbf{M}_i/\mu_i$ with $i = 1, \dots, N$. Here, \mathbf{m}_i is a unit vector describing the orientation of the i th total magnetic moment \mathbf{M}_i , while the magnitude of the moment is denoted as $\mu_i = |\mathbf{M}_i|$ in units of the Bohr magneton μ_B . In principle, the total energy E of a magnetic system consisting of different terms capturing the interactions between magnetic moments and external factors is defined as

$$E = E_{ex} + E_{SO} + E_{dip} + E_{Zee}, \quad (1.1)$$

where E_{ex} is the short-range exchange interactions, E_{SO} signifies the interactions arising due to the spin-orbit coupling, E_{dip} is the long-range magnetostatic interaction, and E_{Zee} is the interaction between the magnetic moments with an external magnetic field. Such interactions contribute to the overall magnetic behavior of the system, and will be briefly discussed in the following.

Short-range exchange interactions

The exchange interaction of N magnetic moments is given by,

$$E_{ex} = -\frac{1}{2} \sum_{\langle i,j \rangle} J_{ij} \mathbf{m}_i \cdot \mathbf{m}_j, \quad (1.2)$$

where the summation is done over pairs of neighboring magnetic moments $\langle i, j \rangle$ with $i, j = 1, \dots, N$. The exchange constant J_{ij} accounts for the strength of the interaction between the i th magnetic moment \mathbf{m}_i and the j th magnetic moment \mathbf{m}_j . A positive sign of J_{ij} leads to a parallel alignment of \mathbf{m}_i with \mathbf{m}_j , while a negative sign favors an antiparallel alignment.

Interactions arising due to spin-orbit coupling

The contribution from the spin-orbit coupling is defined as

$$E_{SO} = -\sum_q K_q \sum_i (\hat{\mathbf{e}}_q \cdot \mathbf{m}_i)^2 - \frac{1}{2} \sum_{\langle i,j \rangle} \mathbf{D}_{ij} \cdot (\mathbf{m}_i \times \mathbf{m}_j), \quad (1.3)$$

where the first term signifies the magnetocrystalline anisotropy (MCA) with K_q being the anisotropy constant along direction \mathbf{e}_q . Note that MCA describes the tendency of a material to have different magnetic properties along different crystallographic axes. Thus, the energy associated with the alignment of the magnetic moments varies depending on their orientation relative to the crystal lattice. In particular, the energy is lowest (highest) when the magnetic moments are aligned along easy axes (hard axes), e.g., Iron has a bcc structure, where its easy and hard axes lie along [100] and

[111] direction, respectively [30]. An easy axis (easy plane) can be realized in the system if $K_q > 0$ ($K_q < 0$).

The second term in Eq. (1.3) signifies the antisymmetric exchange Dzyaloshinskii-Moriya interaction (DMI) [31, 32] with \mathbf{D}_{ij} being the DMI vector. The orientation of \mathbf{D}_{ij} is dependent on the symmetries of the crystal lattice — note that \mathbf{D}_{ij} vanishes if a center of inversion is present between the sites i and j . An important aspect of the DMI is its ability to break degeneracy in the energy by favoring a specific chirality within existing spin textures. One can easily notice that the energy contribution linked to DMI is minimized when neighboring spins are perpendicular to each other, with the sense of rotation determined by the orientation of \mathbf{D}_{ij} . This tendency leads to a competition between the DMI and other interactions, resulting in diverse non-collinear magnetic configurations [33–37].

Long-range classic dipole-dipole interaction

The energy of the dipole-dipole interaction has the form:

$$E_{dip} = \frac{\mu_0 M_s^2}{4\pi} \sum_{i \neq j} \left[\frac{\mathbf{m}_i \cdot \mathbf{m}_j}{r_{i,j}^3} - \frac{3(\mathbf{m}_i \cdot \mathbf{r}_{i,j})(\mathbf{m}_j \cdot \mathbf{r}_{i,j})}{r_{i,j}^5} \right] \quad (1.4)$$

where $\mathbf{r}_{i,j}$ connects sites i and j , and μ_0 being the the vacuum magnetic permeability.

Zeeman interaction

The Zeeman energy arises due to the interaction between a magnetic system and an external magnetic field can be expressed as follows:

$$E_{Zee} = - \sum_i^N \mu \mathbf{B} \cdot \mathbf{m}_i. \quad (1.5)$$

1.3.2 Macrospin model

The transition from bulk size to nanoparticle size in magnetic materials occurs when the volume of the particle decreases below a critical value, typically in the range of a few nanometers [38, 39]. Below this critical volume, magnetic moments within the nanoparticle align uniformly, forming a single magnetic domain. Assuming a monodomain particle with uniaxial crystalline anisotropy and subjected to an external magnetic field, the nanomagnet experiences two competing alignment forces: one from the anisotropy favoring a particular direction and the other from the external magnetic field. In this context, we assume that exchange interactions strongly couple all magnetic moments parallel to each other, resulting in a uniform magnetization inside the nanoparticle, with no significant role in energy minimization.

1 Introduction

The magnetization behavior of such a monodomain particle under the influence of an external magnetic field can be described using the Stoner and Wohlfarth (SW) model [40]. It is worth noting that Wernsdorfer *et al* [41–43] conducted the first experimental validation of the SW model in monodomain particles and nanowires at low temperatures.

Let the uniaxial anisotropy be along the z-axis, then orientation-dependent part of the energy \mathcal{E} of the nanoparticle is given by

$$\begin{aligned}\mathcal{E} &= -KV \cos^2 \theta - M_s V \mathbf{B} \cdot \mathbf{m}, \\ &= -KV \cos^2 \theta - M_s V B \cos(\psi - \theta),\end{aligned}\tag{1.6}$$

where K is the anisotropy constant, V is the volume of the particle, M_s is the saturation magnetization, and θ is the angle between the anisotropy axis and the magnetic moment vector. Here, \mathbf{B} is making an angle ψ with the anisotropy axis. The first term in the right-hand side of Eq. (1.6) signifies the anisotropy energy, while the second term in Eq. (1.6) is the interaction of the magnetic moment with the applied external magnetic field \mathbf{B} .

1.4 Landau-Lifshitz-Gilbert equation

An equation of motion describing the magnetization dynamics of a ferromagnet is given by the Landau-Lifshitz-Gilbert (LLG) equation [44]

$$(1 + \alpha^2) \frac{d\mathbf{m}_i}{dt} = \underbrace{-\gamma \mathbf{m}_i \times \mathbf{B}_i^{\text{eff}}}_{\text{precession}} - \underbrace{\alpha \gamma \mathbf{m}_i \times (\mathbf{m}_i \times \mathbf{B}_i^{\text{eff}})}_{\text{damping}}\tag{1.7}$$

where γ is the gyromagnetic ratio, α is the damping parameter, and $\mathbf{B}_i^{\text{eff}} = -\mu^{-1} \frac{\partial E}{\partial \mathbf{m}_i}$ is the effective magnetic field defined by the magnetic configuration, with μ and E being the magnetic moment length and the energy of the system, respectively [see Eq. 1.1]. The first term in Eq. (1.7) describes the precessional motion of the magnetization around an effective magnetic field. The second term in Eq. (1.7) accounts for the dissipation of the energy by pushing \mathbf{m}_i towards $\mathbf{B}_i^{\text{eff}}$. Note that in the overdamped regime, the LLG equation predicts that the speed of the precessional motion of the magnetic moment slows down as α increases, that is

$$\left| \frac{d\mathbf{m}_i}{dt} \right| = \frac{\gamma |\mathbf{m}_i \times \mathbf{B}_i^{\text{eff}}|}{\sqrt{1 + \alpha^2}},\tag{1.8}$$

where $d\mathbf{m}_i/dt \rightarrow 0$ as $\alpha \rightarrow \infty$.

Figure (1.1) illustrates the damped precessional motion of a single magnetic moment \mathbf{m} under the effect of an effective magnetic field, \mathbf{B}^{eff} , where the damping motion is perpendicular to the precessional one. The magnetic moment \mathbf{m} eventually aligns with \mathbf{B}^{eff} due to damping torque.

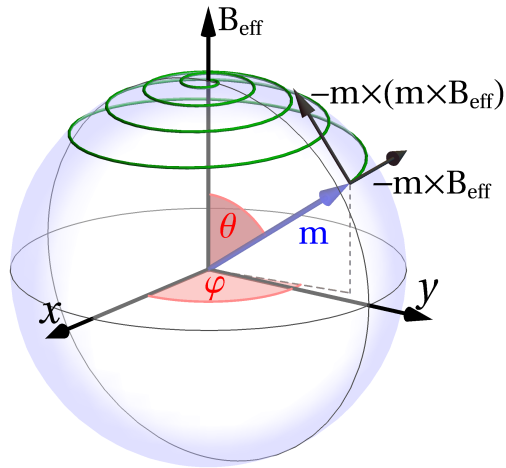


Figure 1.1: Dynamics of a magnetic moment \mathbf{m} induced by effective magnetic field \mathbf{B}_{eff} . The green line shows the calculated trajectory described by the Landau-Lifshitz-Gilbert equation, see Eq. (1.7). The black arrows in the tangent space show the precessional torque $-\mathbf{m} \times \mathbf{B}_{\text{eff}}$ and the damping torque $-\mathbf{m} \times (\mathbf{m} \times \mathbf{B}_{\text{eff}})$. The orientation of the magnetic moment is described by the polar angle θ and an azimuthal angle φ . The effective field \mathbf{B}_{eff} is pointing along z direction.

2 Optimal control theory for magnetic systems

The optimal control theory (OCT) [23] is a powerful theoretical approach used to determine control stimulus that will cause a dynamical system to satisfy physical constraints such that an objective function is optimized. The methodology presented in this chapter is based on the OCT and applied to the energy-efficient control of magnetic states. Here, the stimulus is considered to be a pulse of the external magnetic field, and the objective function — defining the cost of the magnetization switching — is defined as the amount of energy used to generate the control pulse that produces the desired change in the magnetic structure of the system. This energy cost functional is directly proportional to the amplitude squared of the pulse integrated over time and space [45–47]. Therefore, the cost functional is minimized subject to boundary conditions defined by the system at hand and a constraint imposed by the LLG equation of motion (see Eq. 1.7). Since the boundary conditions are set on the dynamical trajectory connecting the desired magnetic states, this poses a significant challenge in optimizing the cost functional [24, 25]. Here, we have develop the OCT using unconstrained optimization by solving the dynamical equations inversely with respect to the applied external magnetic field, given the total time of the switching and the Hamiltonian of the system.

Consequently, the presented theory rests on the postulate that the energy cost of a given magnetization change is a functional of the transition trajectory in the configuration space. Thus, the optimal control paths (OCPs) — dynamical transition trajectories in the configuration space connecting the target states in the magnetic system and minimizing the energy cost — can be found directly by minimizing the cost functional. Such formulation is ideally suited for highly predictive calculations that are free from subjective assumptions. After finding the OCPs for a given transition, reconstruction of the desired optimal pulse becomes a straightforward task. In particular, the reconstruction procedure is based on the requirement that the superposition of the sought-for pulse and internal magnetic field defined by the Hamiltonian of the system makes the system advance precisely along the optimal switching path, and this advancement also satisfies the equations of motion and terminates at a predefined switching time.

2.1 Energy cost of magnetization transition

In an electrical circuit, the dissipation of power through Joule heating and radiation can be described by the Poynting theorem [48]

$$\dot{u} = -\frac{1}{\mu_0} \nabla \cdot (\mathcal{E} \times \mathbf{B}) - \mathbf{j} \cdot \mathcal{E}, \quad (2.1)$$

where u is the energy density, μ_0 is magnetic permeability of vacuum, \mathcal{E} is the electric field, \mathbf{B} is the magnetic field, and \mathbf{j} is the current density. In an integral form one can write

$$P = IU + \frac{1}{\mu_0} \oint_S (\mathcal{E} \times \mathbf{B}) \cdot d\mathbf{S}, \quad (2.2)$$

where P is the power loss, I is the total current flow through the system—neglecting changes in charge, U is the potential difference between influx and outflow of current, and S is an arbitrary surface encompassing the system.

In this thesis, we define the cost of the magnetization switching as the amount of energy used to generate the control pulse that produces the desired change in the magnetic structure of the system. Consequently, the cost associated with magnetization switching Φ is defined as

$$\Phi = \int_0^T P dt = \int_0^T \left(IU + \frac{1}{\mu_0} \oint_S (\mathcal{E} \times \mathbf{B}) \cdot d\mathbf{S} \right) dt, \quad (2.3)$$

where first term reduces to the Joule heating, i.e., $I^2 R$ with R being the resistance of the electric circuit, yielding a non-zero result. The second term, as indicated in Eq. 2.3 (radiation), is heavily dependent on the system's geometry and the pulse of the external magnetic field. Assuming the enclosing surface is in a vacuum, we can derive, from Maxwell's equations, $|\mathcal{E} \times \mathbf{B}| = cB^2$, with c being the phase speed of the electromagnetic waves in vacuum. Notably, the radiation term is proportional to $|\mathbf{B}|^2$, bearing a strong dependence on the specific construction of the system and the degree of confinement of the switching field. The connection between the switching pulse and the cost functional in Eq. (2.3) is dependent on the particular experimental setup used and the method for generating the pulse.

Assuming the control stimulus to be an external magnetic field generated by an electric circuit, the energy cost is mainly defined by Joule heating due to the resistance of the electric circuit. This is proportional to the square of the electric current integrated over the switching time. Assuming a linear relationship between the current magnitude and the strength of the generated field, the cost functional can be written as [24, 45, 46]

$$\Phi = \int_0^T \int_V |\mathbf{B}(\mathbf{r}, t)|^2 dt d\mathbf{r}, \quad (2.4)$$

where V is the volume of the magnetic sample. In the framework of the discrete model, the spatial integration for a continuous system in Eq. (2.4) is replaced by

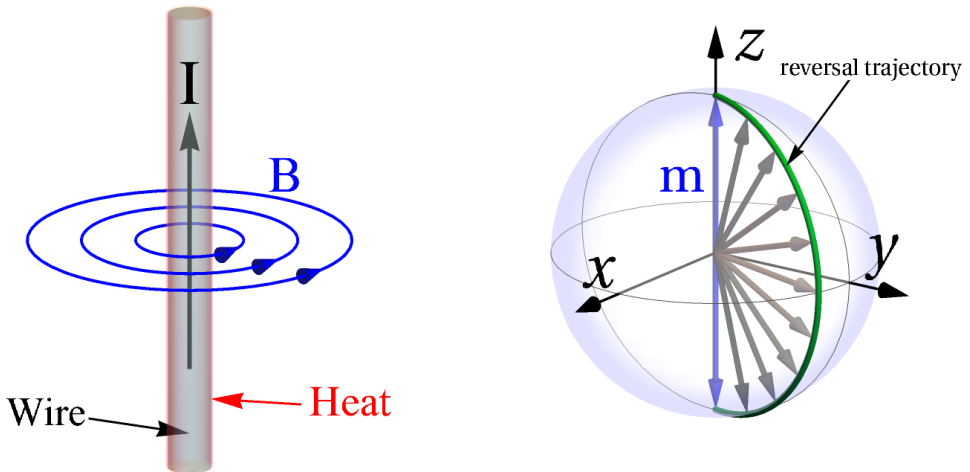


Figure 2.1: (a) Schematic representation of the current-carrying \mathbf{I} wire part of an electric circuit generating an external magnetic field \mathbf{B} and the associated energy lost due to the resistance of the electric circuit. The energy used is defined by Joule heating, while radiation is neglected. The magnetic field is shown with the blue circular lines, while the arrows on the lines signify the direction of \mathbf{B} . (b) Magnetization reversal of a macrospin pointing along the unit vector \mathbf{m} , where the reversal is induced by the magnetic field \mathbf{B} . The reversal trajectory connecting the initial and the final stable states is shown with the green line.

a summation over the sites where magnetic moments are localized, resulting in the following equation for the cost functional:

$$\Phi = C \int_0^T \sum_{i=1}^N |\mathbf{B}_i(t)|^2 dt, \quad (2.5)$$

where the factor C is proportional to the volume of the unit cell. In the entire thesis, we consider $C = 1$. It is noteworthy that Φ characterizes the energy spent by the external field source and not the energy dissipated in the magnetic system, see Figure. (2.1).

The optimal control theory aims to identify the optimal pulse $\mathbf{B}_i^m(t)$ that brings the system to the desired final state such that Φ is minimized. Whenever thermal fluctuations are negligible, the dynamics of the system can be described by the Landau-Lifshitz-Gilbert (LLG) equation. To make the following discussion clear, we recall the LLG equation (see Eq. (1.7)):

$$(1 + \alpha^2) \frac{d\mathbf{m}_i}{dt} = -\gamma \mathbf{m}_i \times (\mathbf{b}_i^{\text{eff}} + \mathbf{B}_i) - \alpha \gamma \mathbf{m}_i \times [\mathbf{m}_i \times (\mathbf{b}_i^{\text{eff}} + \mathbf{B}_i)], \quad (2.6)$$

where \mathbf{B}_i is the external magnetic field, and $\mathbf{b}_i^{\text{eff}}$ is the internal magnetic field defined

by the magnetic configuration through the following equation:

$$\mathbf{b}_i^{\text{eff}} = \mathbf{b}_i^{\text{eff}}(\mathcal{M}) = -\frac{1}{\mu_i} \frac{\partial E}{\partial \mathbf{m}_i}, \quad (2.7)$$

where $\mathcal{M} := (\mathbf{m}_1, \dots, \mathbf{m}_N)$ is a $3N$ dimensional vector, μ_i is the i th magnetic moment length, and E the internal energy of the system excluding the Zeeman term. It is noteworthy that due to the structure of the LLG equation, only the perpendicular part of the magnetic field (whether internal or applied) is affecting the zero-temperature spin dynamics as both \mathbf{B}_i and $\mathbf{b}_i^{\text{eff}}$ enter the equation explicitly through a cross product with the spin vector \mathbf{m}_i . Therefore, we can without losing generality disregard parallel components of the applied and internal fields, i.e.,

$$\mathbf{m}_i \times (\mathbf{b}_i^{\text{eff}} + \mathbf{B}_i) = \mathbf{m}_i \times (\mathbf{b}_i^{\perp, \text{eff}} + \mathbf{B}_i^{\perp}), \quad (2.8)$$

with $\mathbf{b}_i^{\perp, \text{eff}} = \mathbf{b}_i^{\text{eff}} - \mathbf{m}_i(\mathbf{b}_i^{\text{eff}} \cdot \mathbf{m}_i)$ being the transverse component of the internal field, and similarly for \mathbf{B}_i^{\perp} .

Nevertheless, both $\mathbf{B}_i(t)$ and $\mathbf{m}_i(t)$ can be treated as independent variables, and Φ minimized subject to the constraint defined by Eq. (2.6) [24, 25]. Alternatively, the optimal pulse $\mathbf{B}_i^m(t)$ can be calculated via unconstrained minimization of Φ . For this, Eq. (2.6) is used to express the external magnetic field in terms of the dynamical trajectory and the internal magnetic field [45, 46]:

$$\mathbf{B}_i(\mathbf{m}_i, \dot{\mathbf{m}}_i) = \frac{\alpha}{\gamma} \dot{\mathbf{m}}_i + \frac{1}{\gamma} [\mathbf{m}_i \times \dot{\mathbf{m}}_i] - \mathbf{b}_i^{\perp, \text{eff}}, \quad (2.9)$$

and the result substituted into Eq. (2.5). Subsequently, the energy cost Φ becomes a functional of the switching trajectory \mathcal{M} :

$$\Phi = \Phi[\mathcal{M}] = \int_0^T \sum_{i=1}^N A(\mathbf{m}_i, \dot{\mathbf{m}}_i) dt, \quad (2.10)$$

where $A(\mathbf{m}_i, \dot{\mathbf{m}}_i)$ is given by

$$A(\mathbf{m}_i, \dot{\mathbf{m}}_i) = \frac{\alpha^2 + 1}{\gamma^2} |\dot{\mathbf{m}}_i|^2 - \frac{2\alpha}{\gamma} \dot{\mathbf{m}}_i \cdot \mathbf{b}_i^{\perp, \text{eff}} - \frac{2}{\gamma} (\mathbf{m}_i \times \dot{\mathbf{m}}_i) \cdot \mathbf{b}_i^{\perp, \text{eff}} + |\mathbf{b}_i^{\perp, \text{eff}}|^2. \quad (2.11)$$

We find the optimal mechanism by minimizing Φ with respect to the path connecting the initial and the final state in the configuration space. The minimization process can be done in two ways, either analytically or numerically, depending on the complexity of the problem. Analytical minimization entails solving the Euler-Lagrange equations, while numerical minimization involves utilizing gradient-based numerical techniques to nullify the force, which is the first-order variation of Φ with respect to the spin orientation. The dynamical reversal trajectory in the configuration space minimizing Φ is denoted as the optimal control path (OCP) to distinguish it from other switching

trajectories and highlight its physical meaning. The optimal switching pulse is found upon substituting the OCP into Eq. (2.6), thereby derived from the system's intrinsic magnetic properties, which are available via well-established techniques [49].

In the following, Sec. 2.2 will be devoted to the unconstrained minimization of the energy cost functional Φ . This involves optimizing Φ while adhering to boundary conditions specific to the magnetic system and incorporating the dynamics of magnetic moments through the zero-temperature Landau-Lifshitz-Gilbert equation, with no restrictions on the pulse of the external magnetic field. Subsequently, Sec. 2.3 expands upon this by introducing an additional constraint in the optimal control problem. This constraint ensures that the pulse remains uniform and time-dependent, which enhances the practicality of implementing the optimal pulse in experimental settings.

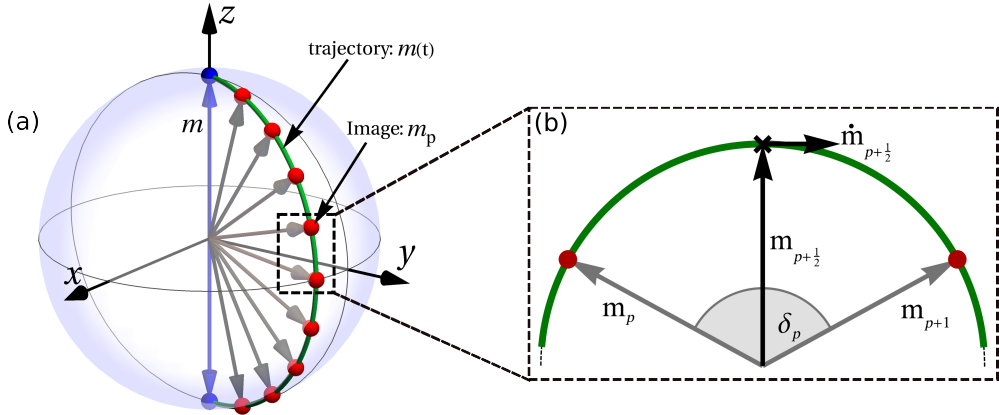


Figure 2.2: (a) Illustration of a trajectory, indicated by the green line, connecting the initial and final stable states of a macrospin pointing along the unit vector \mathbf{m} . The initial and final stable states are marked with blue points. Along this trajectory, each discrete point, represented by a red point, corresponds to a state of the system in the configuration space and is referred to as an image denoted by $\mathbf{m}_p = \mathbf{m}(t_p)$. These red points signify movable images that can be repositioned in the configuration space during the optimization process. (b) Illustration of the midpoint scheme used in the numerical method for finding OCPs. Two images \mathbf{m}_p and \mathbf{m}_{p+1} are connected by a geodesic path in the configuration space. The position $\mathbf{m}_{p+\frac{1}{2}}$ and the velocity $\dot{\mathbf{m}}_{p+\frac{1}{2}}$ at the midpoint of the path are defined by \mathbf{m}_p and \mathbf{m}_{p+1} , and the angle δ_p between them.

2.2 Unconstrained optimization of the energy cost functional

We find OCPs numerically via the direct minimization of the cost functional. For this, we discretize Φ using the midpoint rule

$$\Phi[\mathcal{M}(t)] \approx \Phi[\mathbf{S}(t)] = \sum_{p=0}^Q \sum_{i=1}^N |\mathbf{B}_{p+\frac{1}{2},i}|^2 (t_{p+1} - t_p), \quad (2.12)$$

where $\{t_p\}$ is a partition of the time interval $[0, T]$ such that $0 = t_0 < t_1 < \dots < t_{Q+1} = T$. Here, the partition has a regular spacing, i.e. $t_{p+1} - t_p = \Delta t = T/(Q+1)$, $p = 0, \dots, Q$. A switching trajectory $\mathcal{M}(t)$ is represented by a polygeodesic line connecting $Q+2$ points, referred to as ‘images’: $\mathcal{M}(t) \rightarrow \{\mathcal{M}_0, \mathcal{M}_1, \dots, \mathcal{M}_{Q+1}\}$, with $\mathcal{M}_p := \{\mathbf{m}_{p,1}, \dots, \mathbf{m}_{p,N}\}$ and $\mathbf{m}_{p,i} = \mathbf{m}_i(t_p)$. The first image \mathcal{M}_0 and the last image \mathcal{M}_{Q+1} correspond to the initial and the final orientation of the magnetic moments, respectively; They are fixed, but Q intermediate images can be moved, see Figure 2.2(a). The external field $\mathbf{B}_{p+\frac{1}{2},i} \equiv \mathbf{B}(\mathbf{m}_{p+\frac{1}{2},i}, \dot{\mathbf{m}}_{p+\frac{1}{2},i})$ is defined by the position and the velocity of the magnetic moments at the midpoint of discretization intervals via Eq. (2.9). On the other hand, both $\mathbf{m}_{p+\frac{1}{2},i}$ and $\dot{\mathbf{m}}_{p+\frac{1}{2},i}$ can be expressed

in terms of the position of the images:

$$\mathbf{m}_{p+\frac{1}{2},i} = \frac{\mathbf{m}_{p+1,i} + \mathbf{m}_{p,i}}{|\mathbf{m}_{p+1,i} + \mathbf{m}_{p,i}|}, \quad (2.13)$$

$$\dot{\mathbf{m}}_{p+\frac{1}{2},i} = \frac{\delta_{p,i}}{\Delta t} \frac{\mathbf{m}_{p+1,i} - \mathbf{m}_{p,i}}{|\mathbf{m}_{p+1,i} - \mathbf{m}_{p,i}|}, \quad (2.14)$$

where $\delta_{p,i}$ is the angle between $\mathbf{m}_{p,i}$ and $\mathbf{m}_{p+1,i}$, see Figure. 2.2(b). Note that the magnitude of $\dot{\mathbf{m}}_{p+\frac{1}{2},i}$ is defined by the finite-difference approximation for the angular velocity, and its direction is along the unit vector $(\mathbf{m}_{p+1,i} - \mathbf{m}_{p,i})/|\mathbf{m}_{p+1,i} - \mathbf{m}_{p,i}|$ ensuring orthogonality to $\mathbf{m}_{p+\frac{1}{2},i}$, see Appendix A for more details about the derivation of the velocity. Upon substituting Eqs. (2.29), (2.30), and (2.9) into Eq. (2.12), the functional Φ becomes a function of a $3QN$ -dimensional vector \mathbf{S} defining the position of the movable images, $\mathbf{S} = (\mathcal{M}_1, \dots, \mathcal{M}_Q)$.

Possible OCPs of the magnetization switching can be identified by locating minima of $\Phi(\mathbf{S})$. This is done using the velocity projection optimization (VPO) method [50] and/or the limited-memory Broyden-Fletcher-Goldfarb-Shanno (LBFGS) algorithm [51, 52] equipped with the force acting on the movable images:

$$\mathbf{F} = -\nabla^\perp \Phi[\mathbf{S}], \quad (2.15)$$

where ∇^\perp denotes the gradient projected on the tangent space of the configuration space, which is a curved manifold due to the constraint $|\mathbf{m}_{p,i}| = 1$, $p = 1, \dots, Q$ and $i = 1, \dots, N$. Explicitly:

$$\nabla^\perp = \left(\vec{\nabla}_{1,1}^\perp, \vec{\nabla}_{1,2}^\perp, \dots, \vec{\nabla}_{1,N}^\perp, \vec{\nabla}_{2,1}^\perp, \dots, \vec{\nabla}_{Q,N}^\perp \right), \quad (2.16)$$

where $\vec{\nabla}_{p,i}^\perp \equiv \partial/\partial \mathbf{m}_{p,i} - \mathbf{m}_{p,i} (\mathbf{m}_{p,i} \cdot \partial/\partial \mathbf{m}_{p,i})$, see Appendix A for more details about the derivation of the force.

For a given number of images involved in the local minimization of $\Phi(\mathbf{S})$, the calculation is considered converged when the magnitude of the force, $|\mathbf{F}|$, has dropped below the set tolerance. However, even convergence with a tight force tolerance may be insufficient for a satisfactory resolution of the OCP if Q is not large enough. On the other hand, including too many images in the calculation would result in an unnecessarily high computational effort. Therefore, the following strategy is applied: The OCP search is started with a moderate number of images, and the switching path is first converged only to a rather high tolerance to bring the images relatively close to the OCP with a reduced computational effort; after that, images are progressively added to the path and minimization of the energy cost is reiterated with a low force tolerance until $\Phi(\mathbf{S})$ stops changing. In this thesis, up to $Q = 1500$ movable images were used depending on the system at hand as well as the parameters of the system and the switching time, with the lowest force tolerance corresponding to the drop of the force by ten orders of magnitude with respect to the initial force calculated from the initial path.

Some initial arrangement of the images is needed to start an OCP calculation. On one hand, this can be generated, for example, by placing the images uniformly along the shortest-distance path between the initial state \mathcal{M}_0 and the final state \mathcal{M}_{Q+1} of the transition. In particular, generating an intermediate movable images Q along the short geodesic path can be achieved by rotating the magnetic moments from \mathcal{M}_0 to \mathcal{M}_{Q+1} using Rodrigues' formula [50, 53] as follows:

$$\mathbf{m}_{q,i} = \mathbf{m}_{0,i} \cos \theta_{q,i} + (\mathbf{k}_i \times \mathbf{m}_{0,i}) \sin \theta_{q,i}, \quad (2.17)$$

with $q = (1, 2, \dots, Q)$. Here, $\mathbf{m}_{0,i}$ is the i th magnetic unit vector in the zeroth image, while $\mathbf{m}_{q,i}$ is the i th magnetic unit vector in the q th image. $\theta_{q,i} = (q - 1)\theta_i/Q$ is an angle of rotation with θ_i being an angle between the vectors $\mathbf{m}_{0,i}$ and $\mathbf{m}_{Q+1,i}$ belonging to the initial and final fixed images, respectively. The unit vector \mathbf{k}_i describing an axis of rotation is defined as

$$\mathbf{k}_i = \frac{(\mathbf{m}_{0,i} \times \mathbf{m}_{Q+1,i})}{|(\mathbf{m}_{0,i} \times \mathbf{m}_{Q+1,i})|}. \quad (2.18)$$

On the other hand, the initial arrangement of the images can be generated using some previously found OCP. It is also recommended to add small random noise to the initial path to avoid convergence on maxima or saddle points of $\Phi(\mathbf{s})$ due to possible symmetries in the system. A local minimization of $\Phi(\mathbf{s})$ will most likely converge to the OCP closest to the initially generated path. If multiple OCPs are present between the initial and the final state, several initial estimates need to be produced to enable convergence on the various solutions. A brief description of an algorithm for the minimization of the energy cost functional is described in the following.

Algorithm

Let $\mathcal{M}_p := \{\mathbf{m}_{p,1}, \dots, \mathbf{m}_{p,N}\}$ be a $3N$ dimensional vector with $\mathbf{m}_{p,i} = \mathbf{m}_i(t_p)$. The steps of the algorithm go as follows

1. Set up values for the the switching time T , magnetic damping parameter α , the total number of movable images Q , and the Hamiltonian parameters. Choose the fixed initial and final stable states \mathcal{M}_0 and \mathcal{M}_{Q+1} , respectively. Construct an initial switching trajectory $\mathcal{M}(t) \rightarrow \{\mathcal{M}_0, \mathcal{M}_1, \dots, \mathcal{M}_{Q+1}\}$. Set the counter $l = 0$ and value for the convergence tolerance ϵ (e.g., $\epsilon = 10^{-14}$ sT²).
2. Set the initial step length $\eta^{(0)}$, e.g., $\eta^{(0)} = 1$.
3. Calculate the initial magnitude of the projected forces Γ^1 .
4. Do while $\Gamma > \epsilon$:
 - a) Determine the step length $\eta^{(l)}$ using inexact line search method [54].
 - b) Calculate the search direction $\mathcal{R}_{p,i}^{(l)}$ using VPO [50] or LBFGS [51, 52].
 - c) For a given image p , rotate the magnetic moments $\mathbf{m}_{p,i}^{(l+1)} = e^{-\eta^{(l)} \mathcal{R}_{p,i}^{(l)}} \mathbf{m}_{p,i}^{(l)}$.
 - d) Update the search direction $\mathcal{R}_{p,i}^{(l+1)}$.
 - e) Calculate the maximum magnitude of the projected forces defined by Eq. 2.34, that is $\Gamma = \max(|\mathbf{F}^{(l+1)}|)$.
5. Update the value of the index l and go to step 4.

mohammad badarneh

Note that one can employ the inexact line search method for determining a suitable value for the step size η . The inexact line search typically involves satisfying two conditions: (i) the sufficient decrease condition and (ii) the curvature condition. The curvature condition is a supplementary criterion used with the sufficient decrease condition to prevent choosing excessively small step sizes. These conditions ensure that the step size guarantees a decrease in the value of the energy cost functional while avoiding very small step sizes. In practice, the inexact line search often involves an initial guess for η and then iteratively adjusts its value until the desired conditions (i)-(ii) are satisfied [54].

¹Instead of setting an arbitrary value for the magnitude of the initial force, it is recommended to calculate it from the initial path.

2.3 Constrained optimization of the energy cost functional

The energy cost functional shown in Sec. 2.2 is minimized subject to boundary conditions determined by the system at hand and a constraint imposed by the equation of motion of magnetic moments, i.e., the zero-temperature Landau-Lifshitz-Gilbert equation, but without constraint on the magnetic field. As a result, when finding an optimal mechanism describing a non-uniform rotation of magnetization, e.g., excitation of a spin wave, the corresponding optimal pulse of the external magnetic field inherently manifests non-uniform spatial distributions. Achieving such a complex pulse profile in experimental settings could present significant challenges. This motivates us to extend the optimal control problem by imposing a constraint that ensures the pulse remains uniform and time-dependent, thereby enhancing the feasibility of realizing the optimal pulse experimentally.

In this section, we briefly present the mathematical formulation of the constrained optimization problem and discuss possible techniques for solving such problems. Subsequently, we apply these concepts to address the constrained optimization of the energy cost functional.

Definition of the constrained optimization

The primary aim of the constrained theory revolves around the maximization or minimization of an objective function while adhering to a specified array of constraints. The objective function represents the quantity to be optimized, which can be a measure of performance, cost, or any other relevant metric. The constraints, however, signify the conditions that must be satisfied.

Mathematically, constrained optimization problems can be formulated as follows: minimize the objective function $f : \mathbb{R}^N \rightarrow \mathbb{R}$ where f is real-valued and twice continuously differentiable on \mathbb{R}^N [54]:

$$\text{minimize } f(\mathbf{x}), \quad \mathbf{x} \in \mathbb{R}^N, \quad \mathbf{x} = \{x_1, x_2, \dots, x_N\} \quad (2.19)$$

subject to

$$\begin{aligned} h_i(\mathbf{x}) &= 0, \forall i \in \mathcal{I} := \{1, 2, \dots, n_{eq}\} \\ g_j(\mathbf{x}) &\geq 0, \forall j \in \mathcal{J} := \{1, 2, \dots, n_{ineq}\} \end{aligned} \quad (2.20)$$

where $h_i(\mathbf{x}) : \mathbb{R}^N \rightarrow \mathbb{R}^{n_{eq}}$ and $g_j(\mathbf{x}) : \mathbb{R}^N \rightarrow \mathbb{R}^{n_{ineq}}$ are the equality and inequality constraints, respectively, and n_{eq} , n_{ineq} are the number of constraints. Here, $f(\mathbf{x})$, $h_i(\mathbf{x})$, $g_j(\mathbf{x})$ are sufficiently smooth real-valued functions. Smoothness guarantees a reasonably predictable behavior for both the objective function and the constraints, enabling the gradient-based numerical methods to effectively select search directions.

In a more compact form, the constrained optimization problem can be formulated as:

$$\underset{\mathbf{x} \in \Omega}{\text{minimize}} \quad f(\mathbf{x}), \quad (2.21)$$

such that the set of feasible solutions, where we confine the objective function f , is defined as

$$\Omega := \{\mathbf{x} \in \mathbb{R}^N \mid h_i(\mathbf{x}) = 0 \ (i \in \mathcal{I}), \ g_j(\mathbf{x}) \geq 0 \ (j \in \mathcal{J})\}. \quad (2.22)$$

Note that if we take $f(\mathbf{x}) \equiv 0$, then the constrained optimization becomes root-finding on the function $h_i(\mathbf{x})$, while if we take $h_i(\mathbf{x}) = g_j(\mathbf{x}) \equiv 0$, then the problem becomes unconstrained optimization on the objective function f .

One of the techniques for solving constrained optimization problems is the augmented Lagrangian methods [55]. The basic idea behind these methods is to convert a constrained optimization problem into a series of unconstrained optimization subproblems by adding penalty terms to the objective function that measures the violation of the constraints. The penalty terms are weighted by Lagrange multipliers, which are updated iteratively during the optimization process. Another method for solving the constrained optimization problems is the quadratic penalty method [54]. We have utilized the quadratic penalty method as discussed in the following.

Quadratic penalty method

The basic idea behind the quadratic penalty method is to modify the original objective function f by adding a penalty term for each constraint. The penalty term is constructed as the squared norm of the constraint violation, weighted by a penalty parameter λ . This penalty parameter controls the trade-off between satisfying the constraints and optimizing the objective function. Note that by converting constrained optimization problems into unconstrained ones, one can employ unconstrained optimization techniques to resolve them effectively.

Mathematically, the objective function in the quadratic penalty method, consider only equality constraints, is given by:

$$\mathcal{Q}(\mathbf{x}, \lambda) := f(\mathbf{x}) + \lambda \sum_{i \in \mathcal{I}} h_i^2(\mathbf{x}), \quad (2.23)$$

where $\mathcal{Q}(\mathbf{x}, \lambda)$ is the quadratic penalty function and $\lambda > 0$ is the penalty parameter. Note that, during the optimization process, the constraints are enforced more strictly as λ increases, enabling the gradient-based numerical methods to approach a feasible solution. One has to be careful when working with such a method since very large λ can lead to numerical instabilities or convergence issues. The quadratic penalty method is typically solved iteratively. In each iteration, the penalty function is added to the objective function, then gradient-based algorithms can be used to find a solution. The

penalty parameter λ is increased gradually in each iteration until the solution satisfies the constraints to a desired degree.

In the following, we apply the concept of penalty method to the problem of optimizing the energy cost functional under the constraint that the external magnetic field is uniform.

Constrained optimization of the energy cost functional

To simplify the following discussion, we recall the energy cost functional Φ (see Eq. 2.5)

$$\Phi = \int_0^T \sum_{i=1}^N |\mathbf{B}_i(t)|^2 dt, \quad (2.24)$$

then, by employing the LLG equation, the external magnetic field \mathbf{B}_i can be expressed in terms of the dynamical trajectory and the internal magnetic field as follows:

$$\mathbf{B}_i(\mathbf{m}_i, \dot{\mathbf{m}}_i) = \left(\frac{\alpha}{\gamma} \dot{\mathbf{m}}_i + \frac{1}{\gamma} [\mathbf{m}_i \times \dot{\mathbf{m}}_i] - \mathbf{b}_i^{\perp, \text{eff}} \right) + c_i(t) \mathbf{m}_i, \quad (2.25)$$

where the terms in the parenthesis represent the transverse component of the pulse, while the term $c_i(t) \mathbf{m}_i$ signifies the parallel component of the pulse with $c_i(t)$ being a site-dependent parameter. Upon substituting Eq. (2.25) into Eq. (2.24), the energy cost Φ becomes a functional of the switching trajectory $\mathcal{M}(t) := \{\mathbf{m}_1(t), \dots, \mathbf{m}_N(t)\}$. The aim of the OCT is to identify an optimal path $\mathcal{M}_m(t)$ by minimizing $\Phi[\mathcal{M}(t)]$ with respect to path connecting the initial and the final stable state in the configuration space, and subject to the constraint that $\mathbf{B}_i(\mathbf{m}_i, \dot{\mathbf{m}}_i)$ is uniform. Such constrained optimization problem can be formulated as

$$\underset{\mathcal{M} \in \Omega}{\text{minimize}} \Phi[\mathcal{M}(t)], \quad (2.26)$$

where $\Omega := \{\mathcal{M} \in \mathbb{R}^{3N} | \mathbf{B}_i(\mathbf{m}_i, \dot{\mathbf{m}}_i) = \mathbf{B}^*(t)\}$ is a set of feasible solutions that satisfy the equality constraints, i.e., $\mathbf{B}_i(\mathbf{m}_i, \dot{\mathbf{m}}_i) - \mathbf{B}^*(t) = 0$ with $\mathbf{B}^*(t)$ being a time-dependent uniform field.

Nevertheless, solving constrained optimization problems directly can be computationally challenging and may require specialized algorithms. To simplify the problem and leverage existing optimization techniques, the constrained optimization problem, see Eq. (2.26), is reformulated as unconstrained one by means of the quadratic penalty function approach. In particular, we modify the original objective function $\Phi[\mathcal{M}(t)]$ by adding a penalty term for each constraint. Thus, the objective function in the quadratic penalty method $\Phi^*[\mathcal{M}(t)]$ is given by

$$\Phi^*[\mathcal{M}(t)] = \int_0^T \left(|\mathbf{B}^*(t)|^2 + \lambda \sum_{i=1}^N [\mathbf{B}^*(t) - \mathbf{B}_i(\mathbf{m}_i, \dot{\mathbf{m}}_i)]^2 \right) dt, \quad (2.27)$$

2.3 Constrained optimization of the energy cost functional

where the penalty term is defined as the sum of squares which penalizes the violation of the equality constraints, and weighted by a penalty parameter $\lambda > 0$ controlling the trade-off between satisfying the constraints and optimizing the objective function. The larger the value of λ , the more significant the penalty for constraint violations. Finding an optimal mechanism $\mathcal{M}_m(t)$ minimizing the cost functional $\Phi^*[\mathcal{M}(t)]$ can be achieved numerically as follows.

We start by discretizing $\Phi^*[\mathcal{M}(t)] \approx \Phi^*[\mathbf{S}]$ using the midpoint rule

$$\Phi^*[\mathbf{S}] = \sum_{p=0}^Q \left(|\mathbf{B}_{p+\frac{1}{2}}^*|^2 + \lambda \sum_{i=1}^N [\mathbf{B}_{p+\frac{1}{2}}^* - \mathbf{B}_{p+\frac{1}{2},i}]^2 \right) \Delta t, \quad (2.28)$$

where $\Delta t = t_{p+1} - t_p = T/(Q+1)$, $p = 0, \dots, Q$. Here, a regular spacing is considered for the partition $\{t_p\}$ of the time interval $[0, T]$ such that $0 = t_0 < t_1 < \dots < t_{Q+1} = T$. A switching trajectory $\mathcal{M}(t)$ is represented by a polygeodesic line connecting $Q+2$ points, referred to as ‘images’: $\mathcal{M}(t) \rightarrow \{\mathcal{M}_0, \mathcal{M}_1, \dots, \mathcal{M}_{Q+1}\}$, with $\mathcal{M}_p := \{\mathbf{m}_{p,1}, \dots, \mathbf{m}_{p,N}\}$ and $\mathbf{m}_{p,i} = \mathbf{m}_i(t_p)$. The first image \mathcal{M}_0 and the last image \mathcal{M}_{Q+1} correspond to the initial and the final orientation of the magnetic moment, respectively; They are fixed, but Q intermediate images can be moved. The external field $\mathbf{B}_{p+\frac{1}{2},i} \equiv \mathbf{B}(\mathbf{m}_{p+\frac{1}{2},i}, \dot{\mathbf{m}}_{p+\frac{1}{2},i})$ is defined by the position and the velocity of the magnetic moment at the midpoint of discretization intervals via Eq. (2.25). On the other hand, both $\mathbf{m}_{p+\frac{1}{2},i}$ and $\dot{\mathbf{m}}_{p+\frac{1}{2},i}$ as well as $\mathbf{B}_{p+\frac{1}{2}}^*$ and $c_{p+\frac{1}{2},i}$ can be expressed in terms of the position of the images:

$$\mathbf{m}_{p+\frac{1}{2},i} = \frac{\mathbf{m}_{p+1,i} + \mathbf{m}_{p,i}}{|\mathbf{m}_{p+1,i} + \mathbf{m}_{p,i}|}, \quad (2.29)$$

$$\dot{\mathbf{m}}_{p+\frac{1}{2},i} = \frac{\delta_{p,i} \mathbf{m}_{p+1,i} - \mathbf{m}_{p,i}}{\Delta t |\mathbf{m}_{p+1,i} - \mathbf{m}_{p,i}|}, \quad (2.30)$$

$$\mathbf{B}_{p+\frac{1}{2}}^* = \frac{(\mathbf{B}_{p+1}^* + \mathbf{B}_p^*)}{2}, \quad (2.31)$$

$$c_{p+\frac{1}{2},i} = \frac{(c_{p+1,i} + c_{p,i})}{2}, \quad (2.32)$$

where $\delta_{p,i}$ is the angle between $\mathbf{m}_{p,i}$ and $\mathbf{m}_{p+1,i}$, $\mathbf{B}_p^* = \mathbf{B}^*(t_p)$, and $c_{p,i} = c_i(t_p)$. Note that the magnitude of $\dot{\mathbf{m}}_{p+\frac{1}{2},i}$ is defined by the finite-difference approximation for the angular velocity, and its direction is along the unit vector $(\mathbf{m}_{p+1,i} - \mathbf{m}_{p,i})/|\mathbf{m}_{p+1,i} - \mathbf{m}_{p,i}|$ ensuring orthogonality to $\mathbf{m}_{p+\frac{1}{2},i}$. Upon substituting Eqs. (2.29-2.32), and (2.25) into Eq. (2.28), the functional Φ^* becomes a function of a $3NQ$ -dimensional vector \mathbf{S} defining the position of the movable images, $\mathbf{S} = (\mathcal{M}_1, \dots, \mathcal{M}_Q)$.

Possible OCPs of the magnetization switching can be identified by locating minima of $\Phi^*(\mathbf{S})$. Note that $\Phi^*(\mathbf{S})$ depends on fast and slow variables. The slow variables are the direction of the magnetic moments $\mathbf{m}_{p,i}$, while the fast variables are denoted as

\mathbf{B}_p^* , and $c_{p,i}$ and found using self-consistency calculations for given directions of the magnetic moments. Therefore, the minimization process of Φ^* is done in two stages as follows:

Stage I—For a given orientation of the slow degrees of freedom, the fast degrees of freedom are adjusted according to the self-consistency equations

$$\frac{\partial \Phi^*}{\partial c_{p,i}} = 0, \text{ and } \frac{\partial \Phi^*}{\partial \mathbf{B}_p^*} = 0, \quad (2.33)$$

which are used to calculate the self-consistent values of \mathbf{B}_p^* and $c_{p,i}$.

Stage II—After calculating the self-consistent values of \mathbf{B}_p^* and $c_{p,i}$, the slow degrees of freedom are updated by performing rotation of the magnetic moments using the velocity projection optimization (VPO) method [50] and/or the limited-memory Broyden-Fletcher-Goldfarb-Shanno (LBFGS) algorithm [51, 52] equipped with the force acting on the movable images:

$$\mathbf{F} = -\nabla^\perp \Phi^* [\mathbf{S}], \quad (2.34)$$

where ∇^\perp is defined by Eq. (2.16).

The variation of Φ^* with respect to the independent variables \mathbf{B}_q^* , $c_{q,j}$, and $\mathbf{m}_{q,j}$ is given by

$$\frac{\partial \Phi^*}{\partial \mathbf{B}_q^*} = \begin{cases} \left[\mathbf{B}_{\frac{1}{2}}^* + \lambda \sum_{i=1}^N (\mathbf{B}_{\frac{1}{2}}^* - \mathbf{B}_{\frac{1}{2},i}) \right] \Delta t, & q = 0 \\ \sum_{p=0}^Q \left[\mathbf{B}_{p+\frac{1}{2}}^* + \lambda \sum_{i=1}^N (\mathbf{B}_{p+\frac{1}{2}}^* - \mathbf{B}_{p+\frac{1}{2},i}) \right] (\delta_{qp} + \delta_{qp+1}) \Delta t, & 0 < q < Q \\ \left[\mathbf{B}_{Q-\frac{1}{2}}^* + \lambda \sum_{i=1}^N (\mathbf{B}_{Q-\frac{1}{2}}^* - \mathbf{B}_{Q-\frac{1}{2},i}) \right] \Delta t, & q = Q \end{cases} \quad (2.35)$$

$$\frac{\partial \Phi^*}{\partial c_{q,j}} = \begin{cases} \lambda [c_{\frac{1}{2},j} - \mathbf{B}_{\frac{1}{2}}^* \cdot \mathbf{m}_{\frac{1}{2},j}] \Delta t, & q = 0 \\ \lambda \sum_{p=0}^Q [c_{p+\frac{1}{2},j} - \mathbf{B}_{p+\frac{1}{2}}^* \cdot \mathbf{m}_{p+\frac{1}{2},j}] (\delta_{qp} + \delta_{qp+1}) \Delta t, & 0 < q < Q \\ \lambda [c_{Q-\frac{1}{2},j} - \mathbf{B}_{Q-\frac{1}{2}}^* \cdot \mathbf{m}_{Q-\frac{1}{2},j}] \Delta t, & q = Q \end{cases} \quad (2.36)$$

$$\frac{\partial \Phi^*}{\partial \mathbf{m}_{q,j}} = -2\lambda \left[\sum_{p=0}^Q \sum_{i=1}^N (\mathbf{B}_{p+\frac{1}{2}}^* - \mathbf{B}_{p+\frac{1}{2},i}) \cdot \nabla_{q,j} \otimes \mathbf{B}_{p+\frac{1}{2},i} \right] \Delta t \quad (2.37)$$

2.3 Constrained optimization of the energy cost functional

where

$$\begin{aligned} \nabla_{q,j} \otimes \mathbf{B}_{p+\frac{1}{2},i} &= \frac{\alpha}{\gamma} \left(\nabla_{q,j} \otimes \dot{\mathbf{m}}_{p+\frac{1}{2},i} \right) + \frac{1}{\gamma} \nabla_{q,j} \otimes \left(\mathbf{m}_{p+\frac{1}{2},i} \times \dot{\mathbf{m}}_{p+\frac{1}{2},i} \right) \\ &\quad - \nabla_{q,j} \otimes \mathbf{b}_{p+\frac{1}{2},i}^{\perp,\text{eff}} + c_{p+\frac{1}{2}} \nabla_{q,j} \otimes \mathbf{m}_{p+\frac{1}{2},i}. \end{aligned}$$

The \otimes notation represents the outer product, which can be defined by index notation as follows: $(\mathbf{U} \otimes \mathbf{V})_{\alpha\beta} = u_\alpha v_\beta$ with $(\alpha, \beta) \in \{x, y, z\}$, where \mathbf{U} and \mathbf{V} are arbitrary vectors. Thus, the matrices $\nabla_{q,j} \otimes \mathbf{m}_{p+\frac{1}{2},i}$, $\nabla_{q,j} \otimes \dot{\mathbf{m}}_{p+\frac{1}{2},i}$, and $\nabla_{q,j} \otimes \mathbf{b}_{p+\frac{1}{2},i}^{\perp,\text{eff}}$ are defined as follows:

$$\begin{aligned} \nabla_{q,j} \otimes \mathbf{m}_{p+\frac{1}{2},i} &= \frac{\partial m_{p+\frac{1}{2},i,\beta}}{\partial m_{q,j,\alpha}}, \\ \nabla_{q,j} \otimes \dot{\mathbf{m}}_{p+\frac{1}{2},i} &= \frac{\partial \dot{m}_{p+\frac{1}{2},i,\beta}}{\partial m_{q,j,\alpha}}, \\ \nabla_{q,j} \otimes \mathbf{b}_{p+\frac{1}{2},i}^{\perp,\text{eff}} &= \frac{\partial b_{p+\frac{1}{2},i,\beta}^{\perp,\text{eff}}}{\partial m_{q,j,\alpha}}. \end{aligned} \tag{2.38}$$

3 Thermal effects

Identification of energy-efficient methods for controlling magnetization is both fundamentally interesting and technologically relevant, e.g., in the development of magnetic memory devices. While magnetization switching in magnetic recording is conventionally achieved by applying a static external magnetic field opposite to the initial magnetization direction, previous studies have demonstrated that the energy cost of this process can be reduced by applying time-varying stimuli, such as a microwave magnetic field [56–60]. For a uniaxial monodomain particle, the optimal magnetization reversal is achieved by a rotating magnetic field synchronized with the precessional dynamics of the magnetic moment [24, 25, 45, 61].

The assessment of the stability of energy-efficient switching protocols with respect to ever-present thermal fluctuations is an important problem. The thermal fluctuations perturb the phase locking between the magnetization and the external stimulus. As a result, the magnetization switching can be compromised unless the energy barrier between the initial and final states is much larger than the thermal energy, and the switching time does not exceed a few periods of Larmor precession [45]. This poses a challenge for the realization of energy-efficient switching protocols at elevated temperatures, such as a combination of a microwave and heat-assisted technique. Even at low temperatures, the perturbations in the dynamics can accumulate in time potentially leading to decoherence between the magnetization and the microwave pulse for relatively slow switching which is required for the autoresonance-based protocols [62]. In general, the assessment and control of dynamical stability of magnetic systems is a crucial problem [63, 64].

Energy-efficient switching of nanoscale magnets requires application of time-varying magnetic field characterized by microwave frequency [45]. At finite temperatures, even weak thermal fluctuations create perturbations in the magnetization that can accumulate in time, break the phase locking between the magnetization and the applied field, and eventually compromise magnetization switching. In this chapter, we present a theory for stabilizing the magnetization switching in a nanoparticle with respect to thermal fluctuations. We demonstrate that the magnetization reversal is mostly disturbed by unstable perturbations arising in a certain domain of the configuration space of a nanomagnet. The instabilities can be suppressed and probability of magnetization switching enhanced by applying an additional stimulus such as a weak longitudinal magnetic field. The time dependence of the stabilizing longitudinal field for the magnetization switching in a uniaxial nanomagnet is derived from the requirement of having

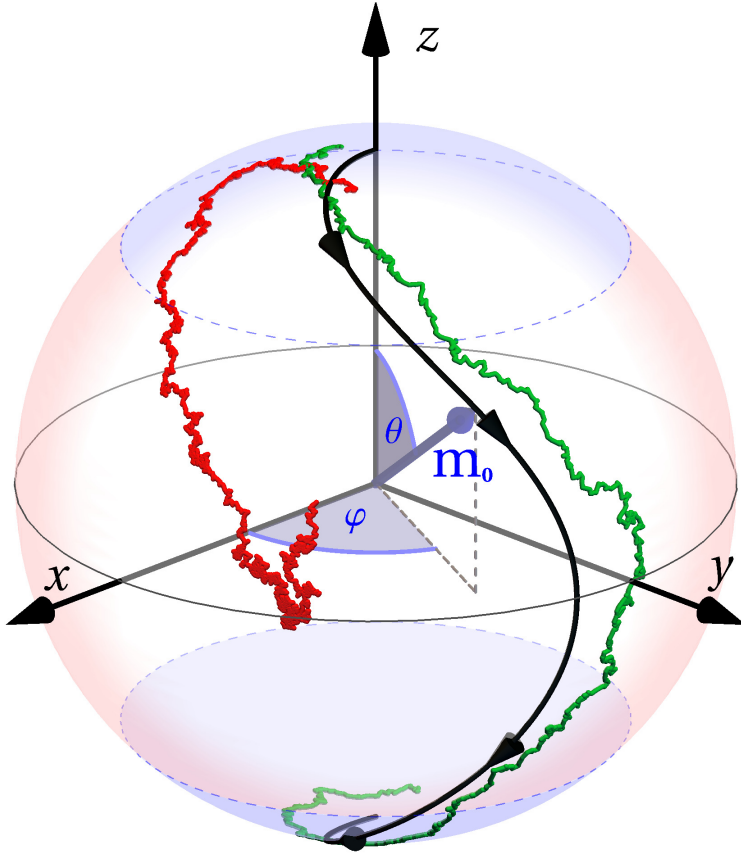


Figure 3.1: Calculated dynamics of the magnetic moment for a uniaxial nanoparticle induced by the optimal switching magnetic field. The black line shows the zero-temperature trajectory of the magnetic moment which corresponds to the optimal control path $\mathbf{m}_0(t)$ for the magnetization switching. The green (red) line shows the trajectory for successful (unsuccessful) switching at finite temperature corresponding to the thermal stability factor $\Delta = 20$. The light red (blue) shaded area for $\pi/4 \leq \theta \leq 3\pi/4$ ($\theta < \pi/4$ and $\theta > 3\pi/4$) marks the domain where the perturbation dynamics is unstable (stable). The damping factor α is 0.2, the switching time T is $5\tau_0$

bound dynamics of the perturbations.

3.1 Local dynamics of perturbation

The magnetization dynamics of the nanoparticle can be described by the Landau-Lifshitz-Gilbert (LLG) equation (see Eq. 1.7)

$$\dot{\mathbf{m}} = -\gamma^\dagger \mathbf{m} \times (\mathbf{B}^{\text{eff}} + \mathbf{B} + \boldsymbol{\xi}) - \alpha \gamma^\dagger \mathbf{m} \times [\mathbf{m} \times (\mathbf{B}^{\text{eff}} + \mathbf{B} + \boldsymbol{\xi})], \quad (3.1)$$

where \mathbf{m} is the normalized magnetic moment vector, α is the damping factor, $\gamma^\dagger = \gamma / (1 + \alpha^2)$ with γ being the gyromagnetic ratio, \mathbf{B} is the external magnetic field, $\mathbf{B}^{\text{eff}} = -\mu^{-1} \partial E / \partial \mathbf{m}$ is the internal magnetic field defined by the magnetic configuration, with μ and E being the magnetic moment length and the internal energy of the system, respectively, and the stochastic term $\boldsymbol{\xi}$ mimicking interaction of the system with the heat bath [65]. Here, the transverse component of the external field \mathbf{B} induces the magnetization switching as shown in Fig. 3.1. The calculated reversal trajectory at zero-temperature connecting the stable states is denoted as $\mathbf{m}_0(t)$, see the black line in Fig. 3.1.

The interaction of the nanoparticle with the heat bath results in the perturbed trajectory:

$$\mathbf{m}(t) = \mathbf{m}_0(t) + \delta \mathbf{m}(t), \quad (3.2)$$

where the condition $\delta \mathbf{m}(t) \cdot \mathbf{m}_0(t) = 0$ must be satisfied at all times due to the constraint on the length of the spin vector. If the perturbation becomes too large, the coherence between the switching pulse and the magnetic moment will be lost resulting in a failed switching attempt (see red trajectory in Fig. 3.1). Therefore, the dynamical stability of the system can be investigated by analyzing the time evolution of the perturbation $\delta \mathbf{m}(t)$. A basis for the representation of $\delta \mathbf{m}(t)$ in the tangent space to $\mathbf{m}_0(t)$ is given by the unit vectors \hat{v}_1 and \hat{v}_2 :

$$\delta \mathbf{m}(t) = \epsilon_1(t) \hat{v}_1 + \epsilon_2(t) \hat{v}_2, \quad (3.3)$$

where $\epsilon_1(t)$ and $\epsilon_2(t)$ are coefficients of $\delta \mathbf{m}(t)$ in the basis $\{\hat{v}_1, \hat{v}_2\}$. Therefore, the dynamical stability of the system can be investigated by analyzing the time behavior of the perturbation. An equation governing the evolution of the first-order perturbation term can be obtained by substituting Eq. (3.3) into Eq. (3.1) and linearization with respect to $\delta \mathbf{m}(t)$

$$\frac{1 + \alpha^2}{\gamma} \delta \dot{\mathbf{m}}(t) = \begin{bmatrix} -\alpha & -1 \\ 1 & -\alpha \end{bmatrix} \left(B_r \mathbf{I}_2 + \frac{1}{\mu} \mathcal{H} \right) \delta \mathbf{m}(t), \quad (3.4)$$

where B_r is the longitudinal component of the external pulse (parallel to the spin vector \mathbf{m}), \mathbf{I}_2 is a two-dimensional identity matrix, and \mathcal{H} is the projected Hessian to the tangent space obtained using a projection operator approach [66]. Interestingly, local dynamics of the perturbations does not depend on the optimal switching pulse, for which $B_r = 0$. Since the tangent space coordinates, \hat{v}_1 and \hat{v}_2 , can have an

3 Thermal effects

arbitrary orientation, we can choose them to align with the eigenvectors of \mathcal{H} . In particular, $\mathcal{H}\hat{v}_1^* = w_1\hat{v}_1^*$ and $\mathcal{H}\hat{v}_2^* = w_2\hat{v}_2^*$, where w_1 and w_2 are the eigenvalues of \mathcal{H} with the corresponding eigenvectors \hat{v}_1^* and \hat{v}_2^* , respectively. Hence, the equation of the first-order perturbation term in the eigenvector coordinates of \mathcal{H} becomes

$$\frac{1 + \alpha^2}{\gamma} \dot{\boldsymbol{\epsilon}}(t) = \begin{bmatrix} -\alpha & -1 \\ 1 & -\alpha \end{bmatrix} \cdot D \cdot \boldsymbol{\epsilon}(t), \quad (3.5)$$

where $\boldsymbol{\epsilon}(t) = (\epsilon_1(t), \epsilon_2(t))^T$ and D is a matrix given by

$$D = \begin{bmatrix} B_r + \frac{w_1}{\mu} & 0 \\ 0 & B_r + \frac{w_2}{\mu} \end{bmatrix}, \quad (3.6)$$

where values of $w_1(t)/\mu$ and $w_2(t)/\mu$ can be derived from the reversal trajectory at zero temperature, $\mathbf{m}_0(t)$.

For zero damping, Eq. (3.5) predicts two types of dynamical trajectories for the perturbation depending on the sign of w_1w_2 . The trajectories are elliptic, bound for $w_1w_2 > 0$. For the optimal switching pulse with $B_r = 0$, this regime is realized in the vicinity of the energy minima for $\theta < \pi/4$ and $\theta > 3\pi/4$ (see the blue regions in Fig. 3.1). However, the perturbation trajectories become hyperbolic, divergent for $\pi/4 \leq \theta \leq 3\pi/4$ where $w_1w_2 \leq 0$ (see the red region in Fig. 3.1). It is important to realize that for $\alpha = 0$ the trajectories are equally stable regardless of whether both w_1 and w_2 are positive or negative. Situation changes with non-zero damping: for positive w_1, w_2 , the perturbations tend to relax toward $\mathbf{m}_0(t)$, while for negative w_1, w_2 , the relaxation amplifies the perturbations. In principle, the latter case is unstable. However, this instability is expected not to significantly affect the magnetization switching if the switching time is short on the time scale of relaxation dynamics which is defined by the damping parameter α . We conclude that the hyperbolic instabilities in the perturbation dynamics are the primary reason for the decoherence between the magnetization and the switching pulse. These instabilities ultimately define thermal stability of magnetization dynamics.

Effects of the longitudinal magnetic field on the dynamics of the perturbation

The stability of the dynamical system defined by Eq. (3.5) is controlled by the eigenvalues of the matrix D , which can be shown by investigating the possible solutions of Eq. (3.5). For instance, the solution of Eq. (3.5) for the case $B_r = 0$ and $\alpha = 0$ results in three types of trajectories in the tangent space depending on the sign of w_1w_2 , see Figures 3.2(a)-3.2(c). The trajectories are elliptic for $w_1w_2 > 0$, straight for $w_1w_2 = 0$, and hyperbolic for $w_1w_2 < 0$. Note that the solution is stable only for $w_1w_2 > 0$, and diverges to infinity under small perturbation for $w_1w_2 \leq 0$, where increasing the ratio w_1/w_2 results in increasing the amplitude of the perturbation. On the other hand, for nonzero α and $B_r = 0$ the trajectories of the perturbation become more tilted towards (away from) \mathbf{m}_0 for $w_1 + w_2 > 0$ ($w_1 + w_2 \leq 0$), where for a fixed value of α the amplitude of the perturbation increases depending on the ratio w_1/w_2 .

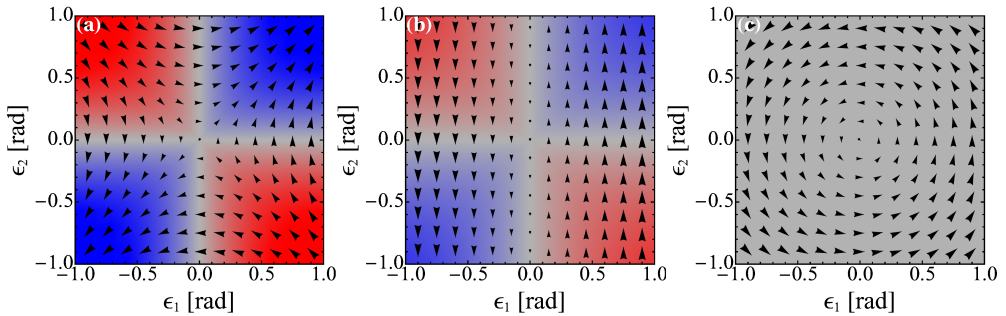


Figure 3.2: Velocity diagrams showing the dynamics of the perturbation in the tangent space depending on the eigenvalues of the Hessian for $\alpha = 0$ and $B_r = 0$. (a) $w_1 = 1$, $w_2 = -1$, (b) $w_1 = 1$, $w_2 = 0$, (c) $w_1 = 1$, $w_2 = 1$. The black arrows in (a)-(c) show the distribution of the dynamics with the size of the arrows being proportional to the magnitude of the perturbation, and the colors in the background indicate if the amplitude of the perturbation is increasing (red), decreasing (blue), or constant (gray) in amplitude.

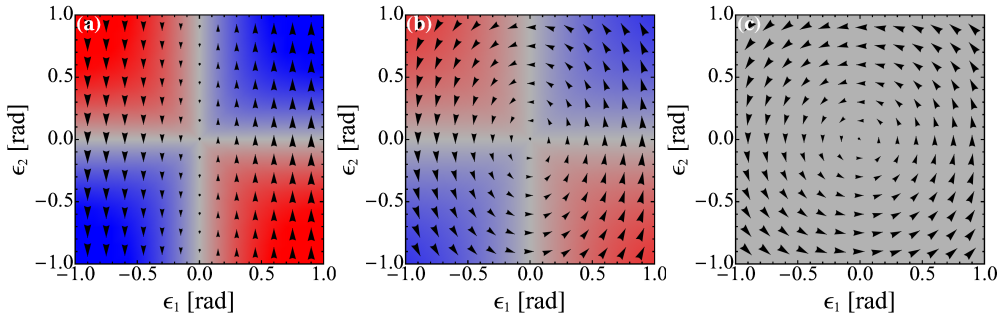


Figure 3.3: Velocity diagrams showing the dynamics of the perturbation in the tangent space depending on the eigenvalues of the Hessian for $\alpha = 0$ and $B_r = 1.0$. a) $w_1 = 1$, $w_2 = -1$, b) $w_1 = 1$, $w_2 = 0$, c) $w_1 = 1$, $w_2 = 1$. Notations and colors are the same as in Figure. (3.2)

Nevertheless, according to Eq. (3.5), the longitudinal field B_r shifts both eigenvalues w_1/μ and w_2/μ equally, hence, suggesting that B_r can be utilized as a parameter to control the dynamics of the perturbation from being divergent into confined ones. Figures. 3.3(a)-3.3(c) illustrate the effects of $B_r = 1.0$ on the dynamics of the perturbation in the tangent space for $\alpha = 0$ and various values of the eigenvalues w_1 and w_2 . By comparing Fig. 3.2(a) and Fig. 3.3(a), we can see that by adding $B_r = 1.0$ to Eq. (3.5) the dynamics of the perturbation is changed from being hyperbolic into straight one due to a shift in the eigenvalues, i.e., $(w_1/\mu, w_2/\mu) \rightarrow (B_r + w_1/\mu, B_r + w_2/\mu)$. Similarly, the straight trajectory in Fig. 3.2(b) is changed into an elliptic one as shown in Fig. 3.2(b).

3 Thermal effects

So far, we have shown that a constant B_r can indeed change the dynamics of the perturbation in the tangent space by shifting the eigenvalues calculated along the zero-temperature reversal trajectory. However, some of these eigenvalues are stable, and some of them are not, e.g., eigenvalues near the minima result in a stable trajectory as shown in Figure. 3.1(A), while eigenvalues near the equator result in unstable trajectories as shown in Figures. 3.1(B)-(C), suggesting that we only need to shift the unstable eigenvalues towards the region in the $(w_1/\mu, w_2/\mu)$ plane where the dynamics are stable. In particular,

$$(w_1/\mu, w_2/\mu) = \begin{cases} (w_1^*/\mu, w_2^*/\mu), & \text{if the eigenvalues are unstable} \\ (w_1/\mu, w_2/\mu), & \text{if the eigenvalues are stable} \end{cases} \quad (3.7)$$

where $(w_1^*/\mu, w_2^*/\mu) = (B_r(t) + w_1/\mu, B_r(t) + w_2/\mu)$ are the newly shifted eigenvalues. The motivation behind the formalism that appears in Eq. (3.7) is that we want to enhance the stability against thermal fluctuations and simultaneously reduce the magnetization switching cost. In particular, the cost functional $\Phi \sim T|\mathbf{B}(t)|^2$ where T is the switching time and $\mathbf{B}(t) = \mathbf{B}^\perp(t) + B_r(t)\hat{r}$. Thus, one needs to find the optimal $\mathbf{B}^\perp(t)$ that induces the magnetization switching and an efficient $B_r(t)$ that enhances the stability against thermal fluctuations. The time dependence of the longitudinal field can be obtained from the requirement of having bound dynamics of the perturbations. An equation for $B_r(t)$ that depends on the eigenvalues $(w_1/\mu, w_2/\mu)$ is derived in the following.

3.2 Derivation of a time-dependent longitudinal magnetic field

Dynamical stability is controlled by the determinant, \det and the trace, tr , of the matrix D (see Eq. (3.6)), where

$$\begin{aligned} \det D &= (\mu B_r + w_1)(\mu B_r + w_2), \\ tr D &= 2\mu B_r + w_1 + w_2. \end{aligned} \quad (3.8)$$

To gain insight into the stability conditions, we refer to the stability diagram depicted in Figure (3.4). This diagram categorizes perturbation trajectories as either stable or unstable, based on the sign of w_1/μ and w_2/μ . For instance, consider the dynamics of perturbations illustrated in Figure 3.4(A). These correspond to eigenvalues situated in the Q_1 quadrant of the $(w_1/\mu, w_2/\mu)$ -plane (as shown in Figure 3.4) and exhibit stability. Such eigenvalues satisfy the conditions $\det D > 0$ and $tr D > 0$. However, the trajectories of perturbations associated with eigenvalues in the Q_2 quadrant are unstable (refer to Figure 3.4(B)). They meet the conditions $\det D < 0$ and $tr D > 0$ for eigenvalues positioned above the dashed gray line, $tr D = 0$ for eigenvalues along the dashed gray line, and $tr D < 0$ for eigenvalues below the dashed gray line.

Since B_r equally shifts both eigenvalues w_1/μ and w_2/μ , see Eq. (3.6), this suggests that B_r can be employed to enhance stability by controlling the dynamics of the perturbation and ensuring bounded behavior. Consequently, the location of the eigenvalues in the $(w_1/\mu, w_2/\mu)$ plane, as shown in Fig. (3.4), can be systematically controlled using B_r . In the following, we present two schemes for shifting the eigenvalues using a time-dependent B_r derived from the necessity for the bounded dynamics of perturbations and defined in terms of the angle η shown in Fig. (3.4).

Scheme I.—Here, the eigenvalues of \mathcal{H} are always shifted towards the $(1, 1)$ direction using B_r , see the blue circles in Fig. (3.4). The connection of B_r with η is described as follows: Let \mathbf{a}_1 be a unit vector in the $(1, 1)$ direction and $\mathbf{a}_2 = (w_1/\mu, w_2/\mu)$ be a vector defining the eigenvalues and making an angle η with \mathbf{a}_1 . Smooth shifting of \mathbf{a}_2 towards the reference vector \mathbf{a}_1 can be done by reducing the value of the angle η to zero, where the vectors \mathbf{a}_1 and \mathbf{a}_2 become aligned at zero η . The cosine of the angle η is defined as $\cos \eta = (w_1 + w_2) / \left(\sqrt{2} \sqrt{w_1^2 + w_2^2} \right)$. Thus, if $\cos \eta \geq \lambda$ is fulfilled, then it guarantees that both conditions $w_1 w_2 > 0$ and $w_1 + w_2 < 0$ are fulfilled for $\eta > 3\pi/4$ ($\lambda < -1/\sqrt{2}$), see Fig. (3.4). Therefore, for $\lambda \in (-1, -1/\sqrt{2}]$ one should substitute $B_r = 0$ in Eq. (3.6), otherwise, B_r will shift the eigenvalues towards the quarter Q_3 , see Fig. (3.4), which is unstable with respect to relaxation. Nevertheless, if $\cos \eta < \lambda$ is fulfilled then one needs to add B_r to Eq. (3.6) to shift the eigenvalues in the direction of \mathbf{a}_1 . In particular, we can add B_r^* to the vector \mathbf{a}_2 resulting in $\mathbf{a}_2^* = (B_r^* + w_1/\mu, B_r^* + w_2/\mu)$. Hence, a formula for B_r^* can be obtained by projecting

\mathbf{a}_2^* onto \mathbf{a}_1 , normalizing with respect to \mathbf{a}_2^* , and equating that to λ resulting in

$$B_r^*(t) = -\frac{w_1(t) + w_2(t) - \frac{\lambda|w_1(t) - w_2(t)|}{\sqrt{1-\lambda^2}}}{2\mu}, \quad (3.9)$$

where λ is a control parameter describing the strength of $B_r^*(t)$. Since we have two conditions on $\cos \eta$, i.e., ($\cos \eta \geq \lambda$ and $\cos \eta < \lambda$), then the final formula for $B_r(t)$ is given by

$$B_r(t) = \begin{cases} 0, & \frac{w_1(t) + w_2(t)}{\sqrt{2}\sqrt{(w_1^2(t) + w_2^2(t))}} \geq \lambda \\ B_r^*(t), & \text{otherwise} \end{cases} \quad (3.10)$$

Note that scheme *I* guarantees the fulfillment of the stability conditions for $\lambda > 1/\sqrt{2}$.

Scheme II.—Here, the eigenvalues are shifted either towards the (1, 1) or (−1, −1) directions using $B_r(t)$ depending on their location in the $(w_1/\mu, w_2/\mu)$ plane, see red points in Fig. (3.4). In particular, shifting the eigenvalues towards the (1, 1) direction can be achieved using Eq. (3.9), while shifting them towards the (−1, −1) direction can be achieved using

$$B_r^\dagger(t) = -\frac{w_1(t) + w_2(t) + \frac{\lambda|w_1(t) - w_2(t)|}{\sqrt{1-\lambda^2}}}{2\mu}, \quad (3.11)$$

where Eq. (3.11) is obtained by projecting $\mathbf{a}_2^* = (B_r^\dagger(t) + w_1(t)/\mu, B_r^\dagger(t) + w_2(t)/\mu)$ towards the (−1, −1) direction, normalizing with respect to \mathbf{a}_2^* and equating that to λ . One can define the final formula for $B_r(t)$ as follows

$$B_r(t) = \begin{cases} 0, & \lambda \leq \left| \frac{w_1(t) + w_2(t)}{\sqrt{2}\sqrt{(w_1^2(t) + w_2^2(t))}} \right| \\ B_r^*(t), & |B_r^*(t)| \leq |B_r^\dagger(t)| \\ B_r^\dagger(t), & |B_r^\dagger(t)| < |B_r^*(t)| \end{cases} \quad (3.12)$$

where $B_r^*(t)$ and $B_r^\dagger(t)$ are given by Eq. (3.9) and Eq. (3.11), respectively, and an absolute value in the condition $\lambda \leq |(w_1(t) + w_2(t))/(\sqrt{2}\sqrt{(w_1^2(t) + w_2^2(t))})|$ is introduced to guarantee that both eigenvalues can get closer to either (1, 1) or (−1, −1) directions. Notably, Eq. (3.12) picks the lowest amplitude of B_r needed for shifting the eigenvalues towards the gray regions in Fig. (3.4). For instance, if the eigenvalues are close to the quarter Q_1 (Q_3) shown in Fig. (3.4), then B_r reduces to B_r^* (B_r^\dagger) in order to shift the eigenvalues towards (1, 1) or (−1, −1) direction, respectively. It is noteworthy that $B_r^* = B_r^\dagger$ is fulfilled for the eigenvalues located at the dashed gray line in Fig. (3.4), signifying that it is energetically equivalent to shift them towards either of the gray regions, see Fig. 3.4. Scheme *II* is unstable to relaxation, i.e., for $w_1 + w_2 < 0$ and high values of α the trajectories of the perturbation become unstable. Thus, one would expect that scheme *II* will break down for large values of α .

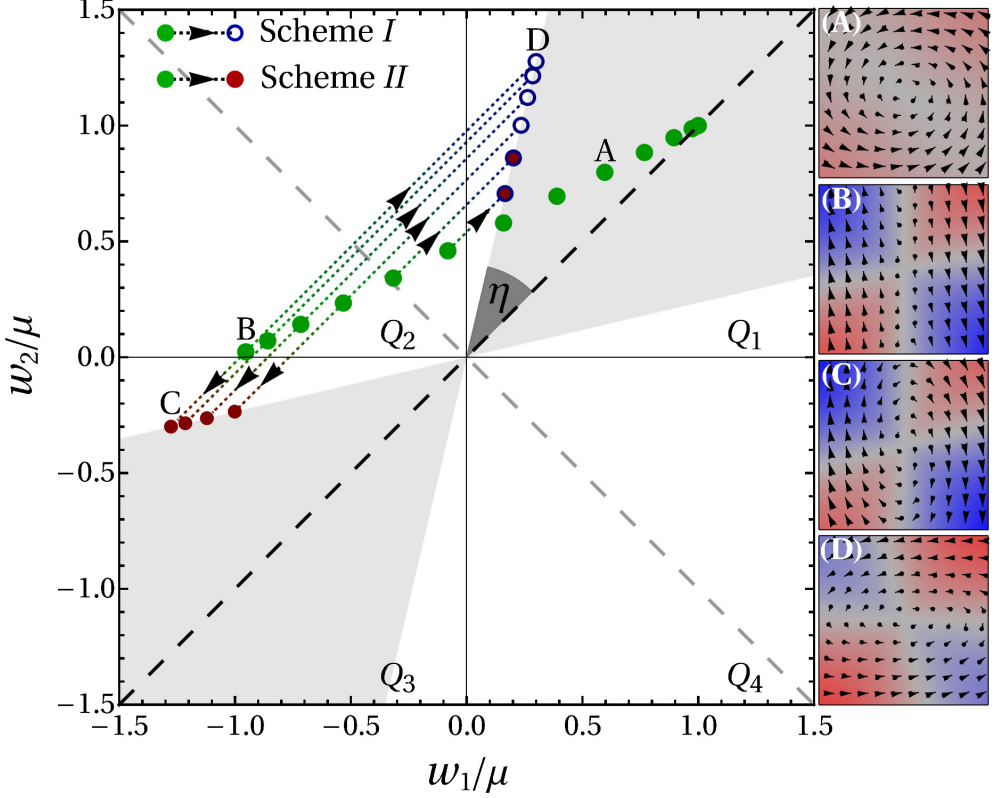


Figure 3.4: Stability diagram for classifying the trajectories of the perturbation as stable or unstable depending on the sign of w_1/μ and w_2/μ . The condition $w_1+w_2 > 0$ ($w_1+w_2 < 0$) is fulfilled in the area above (below) the dashed gray line. Green points signify selected eigenvalues calculated along the zero temperature reversal trajectory, see the black line in Fig. (3.1). The unstable eigenvalues are displaced using two schemes as described in the legend. Blue circles and red points define the newly shifted eigenvalues, while the angle η defines their location in the plane. The letters (A-D) label the velocity diagrams showing the dynamics of the perturbation in the tangent space. The black arrows in Figs. (A)-(D) show the distribution of the dynamics with the size of the arrows being proportional to the magnitude of the perturbation, and the colors in the background indicate if the amplitude of the perturbation is increasing (blue), decreasing (red), or constant (gray). The notations Q_1 - Q_4 signify the quarter numbers.

Derivation of the projected Hessian matrix

For magnetic system consisting of N magnetic moments, the configuration space is a $2N$ -dimensional Riemannian manifold, \mathcal{R} , corresponding to the direct product of N two-dimensional unit spheres i.e., $\mathcal{R} = \prod_{i=1}^N S_i^2$, where S_i^2 is a two-dimensional unit sphere associated with the i th magnetic moment vector. Defining the Hessian in such

3 Thermal effects

curved configuration space can be achieved by applying a projection operator approach [66]. This approach is based on calculating the constrained Hessian by introducing the Lagrange multipliers and then projecting on the tangent space of the \mathcal{R}

$$\tilde{E}(\mathcal{M}) = E(\mathcal{M}) + \sum_{i=1}^N \mathcal{L}_i (m_i^\alpha m_i^\alpha - 1), \quad (3.13)$$

where \tilde{E} is the new magnetic Hamiltonian, $\mathcal{M} = \{\mathbf{m}_1, \mathbf{m}_2, \dots, \mathbf{m}_N\}$, $\alpha = \{x, y, z\}$, and \mathcal{L}_i are the Lagrange multipliers introduced due to the constraint on the length of the magnetic moments, i.e., $|\mathbf{m}_i| = 1$. At the extremum, the derivative of \tilde{E} with respect to m_i^α vanishes. Thus,

$$\frac{\partial \tilde{E}}{\partial m_j^\beta} = \frac{\partial E}{\partial m_j^\beta} + 2\mathcal{L}_j m_j^\beta = 0, \quad (3.14)$$

by taking the dot product with respect to m_j^β , one obtain the following expression for the Lagrange multiplier for the j th magnetic moment

$$\mathcal{L}_j = -\frac{1}{2} \left(\frac{\partial E}{\partial m_j^\beta} \cdot m_j^\beta \right) \mathcal{I}, \quad (3.15)$$

where \mathcal{I} is a 3×3 identity matrix. The Hessian \mathcal{H} in the Riemannian manifold can be calculated by taking the second-order partial derivative of Eq. (3.13) with respect to the Cartesian components of the magnetic moments

$$\mathcal{H} \equiv \frac{\partial^2 \tilde{E}}{\partial m_i^\alpha \partial m_j^\beta} = \frac{\partial^2 E}{\partial m_i^\alpha \partial m_j^\beta} + 2\mathcal{L}_i \delta_{\alpha\beta}, \quad (3.16)$$

The Lagrange multipliers of the whole system is a direct sum of \mathcal{L}_i

$$\mathcal{L} = \bigoplus_{i=1}^N \mathcal{L}_i \equiv \begin{bmatrix} \mathcal{L}_1 & 0 & \dots & 0 \\ 0 & \mathcal{L}_2 & \dots & 0 \\ \vdots & \vdots & \ddots & \vdots \\ 0 & 0 & \dots & \mathcal{L}_N \end{bmatrix}, \quad (3.17)$$

then,

$$\mathcal{H} = H + 2\mathcal{L}, \quad (3.18)$$

where H is defined by

$$H \equiv H_{p,q}^{\beta,\alpha} = \frac{\partial^2 E}{\partial m_{p,\beta} \partial m_{q,\alpha}}, \quad (3.19)$$

where the indices p and q are the p th and q th magnetic moments, and both α, β signify the $\{x, y, z\}$ components of the magnetic moment. One can notice that \mathcal{H} is a $(3N \times 3N)$ matrix whose basis are $3N$ Euclidean basis. Our next step is to transform the $3N$ Euclidean basis into a $2N$ tangent space basis. This can be done by

3.2 Derivation of a time-dependent longitudinal magnetic field

introducing a $(3N, 2N)$ projecting matrix $U = \bigoplus_{i=1}^N \mathcal{U}_i$, whose columns are a pair of arbitrary orthonormal vectors, $\boldsymbol{\xi}_i$ and $\boldsymbol{\eta}_i$, representing the basis of the tangent of \mathcal{R} for the i th magnetic moment. One can obtain $\boldsymbol{\eta}$ by orthonormalization of a random vector with respect to \mathbf{m}_i , i.e., $\boldsymbol{\eta}_i = [\boldsymbol{\eta}_i - \mathbf{m}_i (\boldsymbol{\eta}_i \cdot \mathbf{m}_i)] / |\boldsymbol{\eta}_i|$ and then $\boldsymbol{\xi}_i$ can be generated as $\boldsymbol{\xi}_i = [\boldsymbol{\eta}_i \times \mathbf{m}_i]$

$$U = \bigoplus_{i=1}^N \mathcal{U}_i \equiv \begin{bmatrix} \mathcal{U}_1 & 0 & \dots & 0 \\ 0 & \mathcal{U}_2 & \dots & 0 \\ \vdots & \vdots & \ddots & \vdots \\ 0 & 0 & \dots & \mathcal{U}_N \end{bmatrix}, \quad (3.20)$$

where

$$\mathcal{U}_i = \begin{bmatrix} \xi_i^x & \eta_i^x \\ \xi_i^y & \eta_i^y \\ \xi_i^z & \eta_i^z \end{bmatrix}. \quad (3.21)$$

Thus, the constrained Hessian in the $2N$ tangent space basis can be obtained by

$$\mathcal{H} = U^T (H + 2\mathcal{L}) U. \quad (3.22)$$

4 Applications

In this chapter, we apply the optimal control theory to the energy-efficient manipulation of magnetization in uniaxial and biaxial nanoparticles and nanowires. The identification of optimal control for all switching processes considered in this chapter will be carried out using a general approach consisting of the following steps: (i) *Selection of a magnetic Hamiltonian and identification of target magnetic states*. The magnetic system will be characterized within an atomistic approach using classical Heisenberg-type Hamiltonians or a macrospin models. Parameters of the Hamiltonians, such as strengths of the magnetic exchange, Dzyaloshinskii-Moriya interaction, and magnetic anisotropy, will be treated as phenomenological constants. Target magnetic states will be defined by locating minima on the energy surface of the system as a function of the orientation of the moments. (ii) *Calculation of optimal control paths*. For relatively simple systems such as magnetic nanoparticles, the search for optimal control paths will be pursued using analytical methods based on the calculus of variations. But for nanowire systems, the trajectories will be calculated numerically using our in-house FORTRAN code. (iii) *Calculation of optimal control pulses*. The recovery of the optimal control pulses will be carried out based on the calculated optimal control paths, specific dynamical equations, and switching time. Landau-Lifshitz-Gilbert equation of motion will be used for the identification of the external magnetic field pulses.

4.1 Unconstrained optimization

In this section, we apply the unconstrained optimization to the problem of energy-efficient magnetization switching in a uniaxial nanoparticle, biaxial nanoparticle, as well as a bistable nanowire.

4.1.1 Optimal control of magnetization reversal in a uniaxial nanoparticle

Exact results concerning energy-efficient manipulation of magnetic structure are highly important for fundamental science and technological applications, as they could help improve the performance of computing and memory devices based on magnetic ele-

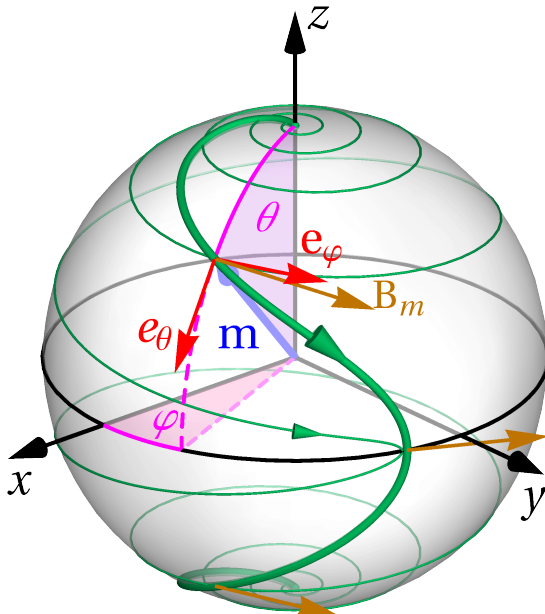


Figure 4.1: Calculated optimal control paths (OCPs) for the reversal of a macrospin pointing along the unit vector \mathbf{m} . The initial and the final states are at the north and the south poles of the unit sphere, respectively. The damping factor α is 0.1. The switching time T is $10\tau_0$ and $100\tau_0$ for the paths shown with thick and thin green lines, respectively. The optimal external magnetic field \mathbf{B}_m at $t = T/4$, $t = T/2$ and $t = 3T/4$ is shown for the shorter path with the brown arrows. Figure adapted from Ref. [45].

ments. Optimization of magnetization switching in bistable nanomagnets by tuning the external magnetic field has come under special focus. Here, we apply OCT to a uniaxial nanoparticle whose magnetic moment is reversed from one stable orientation to the other (see Figure (4.1)). The energy barrier between the stable states is assumed to be much larger than the thermal energy. This model mimics, e.g., a bit operation in a nanoscale magnetic memory element, where strong magnetic anisotropy ensures the stability of the element against thermal fluctuations [67]. So far, theoretical studies of optimal magnetization switching have been based on particular ansatzes for the switching field or involved numerical simulations, but a general analytical solution providing a transparent physical picture *is still missing*.

Here we present a complete analytical solution to the problem of energy-efficient switching of a nanomagnet with easy-axis anisotropy. In contrast to previous studies, our solution does not involve any assumptions about the shape of the optimal switching pulse, therefore providing a true theoretical limit to the energy cost of the switching as a function of the switching time and establishing a link between the optimal pulse and material properties. Our results reveal new fundamental properties of the reversal, including two asymptotic regimes of the energy cost and the optimal

switching time.

The internal energy E of the uniaxial nanoparticle is defined by the anisotropy along z axis,

$$E = -Km_z^2, \quad (4.1)$$

where $K > 0$ is the anisotropy constant. Such system has two distinct stable states at $\theta = 0$ and $\theta = \pi$, see Figure (4.1). Finding an energy-efficient protocols for the magnetization reversal for such system requires minimizing the magnetization switching cost functional Φ . This will be discussed in the following.

Optimal protocols for magnetization reversal

Due to the inherent symmetry of the uniaxial nanoparticle, the functional Φ , see Eq. (2.10), will be written in spherical coordinates as follows:

$$\begin{aligned} \Phi = \int_0^T & \left[\frac{\alpha^2 + 1}{\gamma^2} \left(\frac{\partial \theta}{\partial t} \right)^2 + \frac{(\alpha^2 + 1) \sin^2 \theta}{\gamma^2} \left(\frac{\partial \varphi}{\partial t} \right)^2 + \frac{2K\alpha}{\mu\gamma} \sin 2\theta \frac{\partial \theta}{\partial t} \right. \\ & \left. - \frac{4K}{\mu\gamma} \cos \theta \sin^2 \theta \frac{\partial \varphi}{\partial t} + \frac{K^2}{\mu^2} \sin^2 2\theta \right] dt, \end{aligned} \quad (4.2)$$

for which we have well defined boundary condition

$$\theta(0) = 0 \quad (4.3)$$

$$\theta(T) = \pi, \quad (4.4)$$

corresponding to the transition between the energy minima within the switching time T . We also have a degree of freedom in φ , which is the result of the singularity of spherical coordinate system. Note that due to rotational symmetry of the uniaxial nanoparticle we do not lose generality by assuming

$$\varphi(0) = 0. \quad (4.5)$$

Nevertheless, the optimal control paths minimizing Φ can be found by solving the Euler-Lagrange (EL) equations. The EL equations can be derived by varying Φ with respect to θ and φ (see Figure. (4.1) for the definition of θ and φ), which results in the following equations

$$\tau_0^2 \ddot{\theta} = \frac{\alpha^2}{4(1 + \alpha^2)^2} \sin 4\theta, \quad \tau_0 \dot{\phi} = \frac{\cos \theta}{1 + \alpha^2}, \quad (4.6)$$

where the period of Larmor precession $\tau_0 = \mu(2\gamma K)^{-1}$ defines the timescale. Equation (4.6) for θ is the well known Sine-Gordon equation [68, 69], whose solutions are expressed by Jacobi elliptic functions [70]. In particular, the solution is given by

$$\theta(t) = \frac{1}{2} \text{am}(\mathcal{A}|\mathcal{B}) \quad (4.7)$$

4 Applications

where $\text{am}(\cdot)$ is the Jacobi amplitude and the parameters \mathcal{A} and \mathcal{B} are given by

$$\begin{aligned}\mathcal{A} &= \frac{\sqrt{2}\sqrt{2\mu^2c_1\alpha^4 + 4\mu^2c_1\alpha^2 - \alpha^2\gamma^2K^2 + 2\mu^2c_1}(t + c_2)}{\mu\sqrt{\alpha^4 + 2\alpha^2 + 1}}, \\ \mathcal{B} &= -\frac{2\alpha^2\gamma^2K^2}{2\mu^2c_1\alpha^4 + (4\mu^2c_1 - \gamma^2K^2)\alpha^2 + 2\mu^2c_1},\end{aligned}\quad (4.8)$$

with c_1 and c_2 being the constants of integration and will be calculated by applying the boundary conditions. The first boundary condition is $\theta(0) = 0$ resulting in the following equation

$$\frac{1}{2}\text{am}(\mathcal{A}|\mathcal{B}) = 0 \quad (4.9)$$

which is satisfied when the first argument of the Jacobi amplitude is zero, i.e., $\mathcal{A} = 0$ [70]. Thus, the constant of integration $c_2 = 0$. In order to find the constant of integration c_1 we apply the second boundary condition, that is $\theta(T) = \pi$ resulting in

$$\text{am}\left(\frac{T}{\tau_0p(1 + \alpha^2)} \middle| -\alpha^2P^2\right) = 2\pi \quad (4.10)$$

where $p = \sqrt{2}\gamma K / \left(\sqrt{2\mu^2c_1\alpha^4 + 4\mu^2c_1\alpha^2 - \alpha^2\gamma^2K^2 + 2\mu^2c_1}\right)$, see Eq. (4.8). However, by using the fact that $\text{am}(4\mathcal{K}(x), x) = 4\pi$, then according to Eq. (4.10) one can connect the parameter p with the switching time T as follows

$$T = 4\tau_0p(1 + \alpha^2)\mathcal{K}(-\alpha^2p^2), \quad (4.11)$$

with $\mathcal{K}(\cdot)$ being the complete elliptic integral of the first kind [70]. Thus, the solutions of the EL equations, see Eq. (4.6), defining OCP in spherical coordinates read

$$\theta(t) = \frac{1}{2}\text{am}\left(\frac{t}{p\tau_0(1 + \alpha^2)} \middle| -\alpha^2p^2\right), \quad (4.12)$$

$$\varphi(t) = \frac{1}{\tau_0}\int_0^t \frac{\cos(\theta(\tau))}{1 + \alpha^2} d\tau + \varphi_0, \quad (4.13)$$

with φ_0 is an arbitrary phase at $t = 0$ arises due to the axial symmetry of the system. The OCP described by Eqs. (4.12)-(4.13) reveals the mechanism for the magnetic moment reversal. The moment moves steadily from the initial state upward the energy surface while precessing counter-clockwise around the anisotropy axis until it reaches the top of the energy barrier at $t = T/2$. At this point, the precession reverses its direction and the system slides down to the target state minimum, see Figure (4.1). The exact analytical solution given by Eqs. (4.12)-(4.13) makes it possible to derive general properties of the OCP. Specifically, the solution is symmetric with respect to $t = T/2$, i.e., the top of the energy barrier at $\theta = \pi/2$ is reached exactly at half of the switching time, that is $\theta(T/2) = \pi/2$, and the following equations hold:

$$\theta(t + T/2) = \pi/2 + \theta(t), \quad (4.14)$$

$$\varphi(T/2 + t) = \varphi(T/2 - t), \quad (4.15)$$

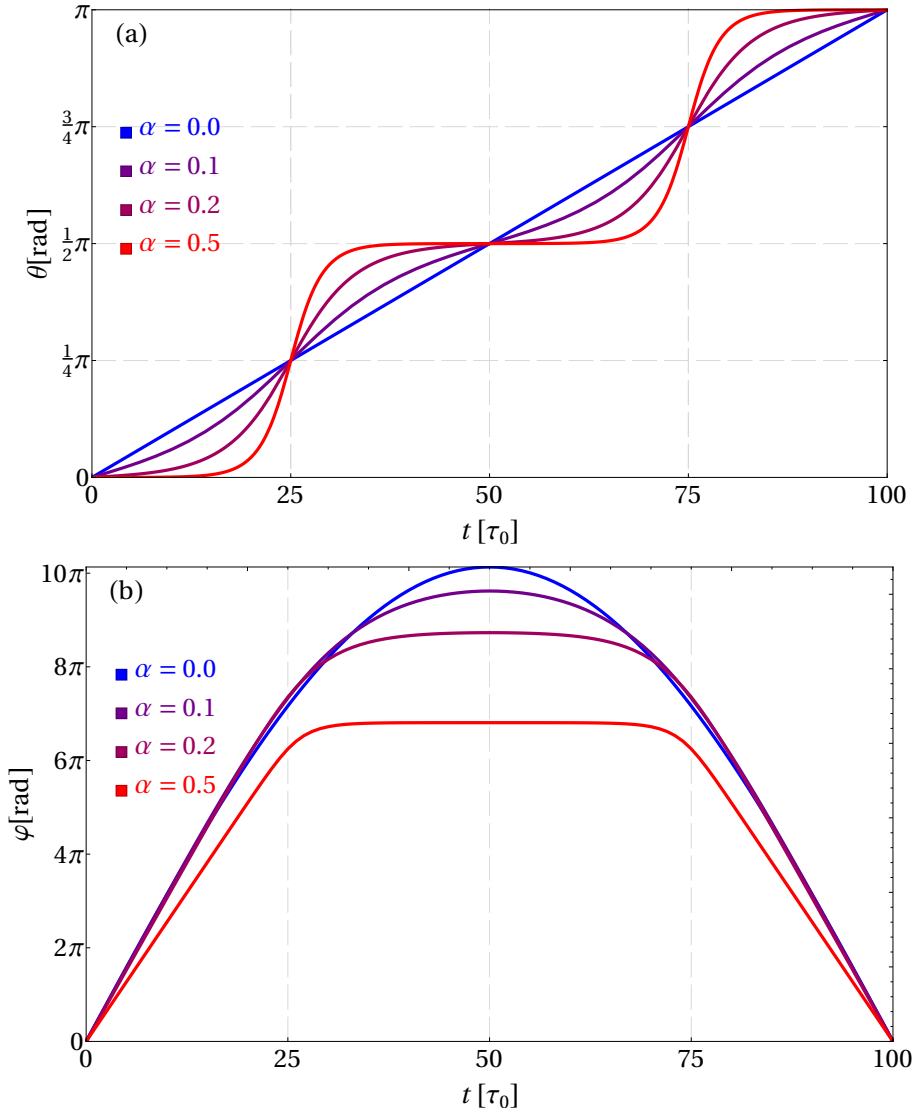


Figure 4.2: The optimal control path represented by the polar angle θ (a) and the azimuthal angle φ (b) as a function of time for $T = 100\tau_0$ and several values of the damping parameter α . Figure adapted from Ref. [45]

The symmetries particularly imply that the following equations hold:

$$\theta\left(\frac{T}{4}\right) = \frac{\pi}{4}, \quad (4.16)$$

$$\theta\left(\frac{T}{2}\right) = \frac{\pi}{2}, \quad (4.17)$$

$$\theta\left(\frac{3T}{4}\right) = \frac{3\pi}{4}, \quad (4.18)$$

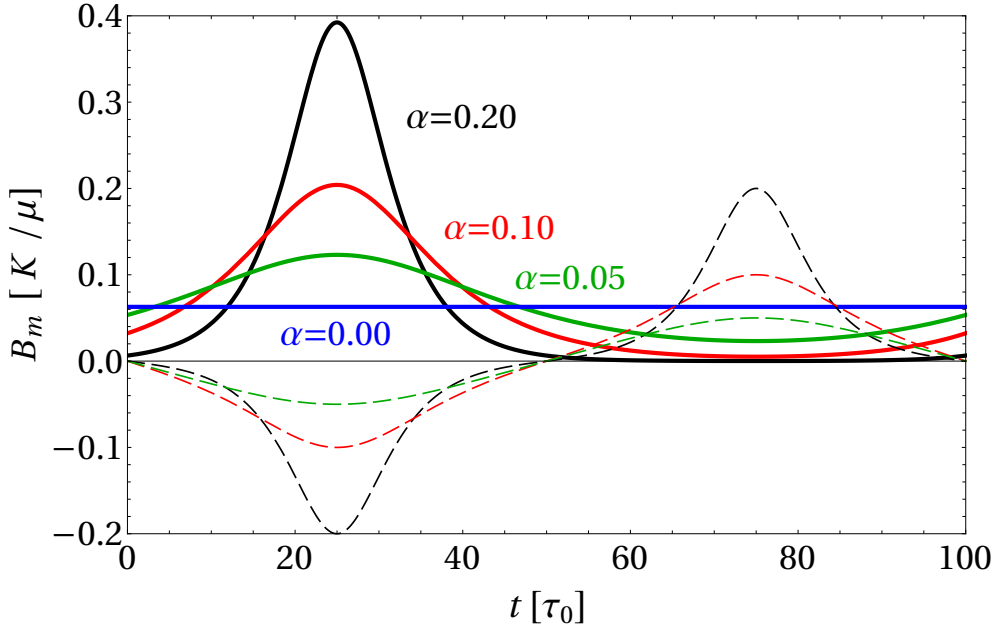


Figure 4.3: Amplitude of the switching field as a function of time for $T = 100\tau_0$ and several values of α (solid lines). Dashed lines show αb_i^+ which is proportional to the polar component of the torque generated by the internal field. Figure adapted from Ref. [45].

regardless of the value of the switching time T and damping parameter α , see Figure 4.2(a). It is noteworthy that the symmetries come from the symmetries of internal field amplitude.

Optimal switching pulses of the external magnetic field

The optimal switching pulse of the external magnetic field \mathbf{B}_m can be found upon substituting OCP given by Eqs. (4.12)-(4.13) into Eq. (2.9), resulting in the following equation

$$\mathbf{B}_m = \frac{B_m}{\sqrt{1+\alpha^2}}(\alpha\mathbf{e}_\theta + \mathbf{e}_\phi), \quad (4.19)$$

$$B_m = \frac{K}{\mu p \sqrt{1+\alpha^2}} \left[\operatorname{dn} \left(\frac{t}{p\tau_0(1+\alpha^2)} \middle| -\alpha^2 p^2 \right) + \alpha p \operatorname{sn} \left(\frac{t}{p\tau_0(1+\alpha^2)} \middle| -\alpha^2 p^2 \right) \right], \quad (4.20)$$

where \mathbf{e}_θ , \mathbf{e}_ϕ are local orthogonal unit vectors in the directions of increasing θ , and ϕ , respectively (see Fig. 4.1), while $\operatorname{dn}(\cdot)$ and $\operatorname{sn}(\cdot)$ are Jacobi elliptic functions [70]. The orientation of \mathbf{B}_m is such that its contribution to the precession around

the anisotropy axis is exactly zero. In particular, we prove that the external torque generated by \mathbf{B}_m has exactly zero component in the φ direction, but with a component in the θ direction, i.e., $\Gamma_\theta = \gamma B_m / (\sqrt{1 + \alpha^2})$. Therefore, the external pulse contributes only to the part of motion which is relevant for switching, i.e. progressive increase in θ .

The calculated amplitude of the optimal pulse $B_m(t)$ is illustrated in Figure. 4.3. Interestingly, when $\alpha = 0$, the amplitude is time independent: $B_m(t)|_{\alpha=0} = \pi/(\gamma T)$. For $\alpha > 0$, $B_m(t)$ has a more complex structure, but the symmetry $B_m(0) = B_m(T/2) = B_m(T)$ holds. Moreover, damping gives rise to the internal torque — produced by the anisotropy field — in the polar direction. This torque counteracts the switching motion before crossing the energy barrier at $\theta = \pi/2$, see Figure. 4.7(a). Thus, a maximum in $B_m(t)$ forms at $t = T/4$ so as to neutralize this unfavorable effect of the torque (see Fig. 4.3). After crossing the equator at $t = T/2$, the internal torque aids the switching, causing $B_m(t)$ to reach a minimum at $t = 3T/4$. Also, $B_m(t)$ is reduced but still needed for timely reversal. However, for long enough switching time, $T \gg (\alpha + 1/\alpha)\tau_0$, damping alone is sufficient to complete the switching, and virtually no field needs to be applied after crossing the energy barrier (see black curve in Fig. 4.3). Note that the position of the maximum and the minimum of $B_m(t)$ align with polar torque extrema.

Internal and external torques

The components of the internal torque produced by the internal field of the uniaxial nanoparticle can be written as follows:

$$\begin{aligned}\Gamma_\theta^{int} &= -\alpha \frac{\sin 2\theta}{2\tau_0(1 + \alpha^2)} \hat{\theta}, \\ \Gamma_\varphi^{int} &= \frac{\sin 2\theta}{2\tau_0(1 + \alpha^2)} \hat{\varphi},\end{aligned}\tag{4.21}$$

where $\theta(t)$ is calculated along the OCP, see Eq. (4.12). As expected, for zero damping the θ -projection of the internal torque Γ_θ^{int} is exactly zero thereby does not counteracts the reversal motion.

The θ -projection of the internal torque as well as the external torque Γ_θ^{ext} , generated by the optimal pulse, as a function of the switching time for various value of damping is illustrated in Figures 4.4-4.5. Note that positive (negative) Γ_θ^{int} signifies the positive (negative) contribution of the internal torque to the reversal. Thus, the position of the maximum and the minimum of Γ_θ^{ext} coincides with that of Γ_θ^{int} .

4 Applications

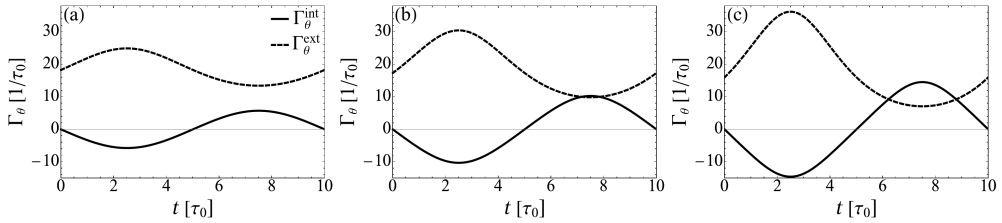


Figure 4.4: The θ -projection of the internal and external torques along the optimal control path for damping value $\alpha = 0.2$ (a), $\alpha = 0.4$ (b), and $\alpha = 0.8$ (c). The magnitude of the switching time is $T = 10\tau_0$.

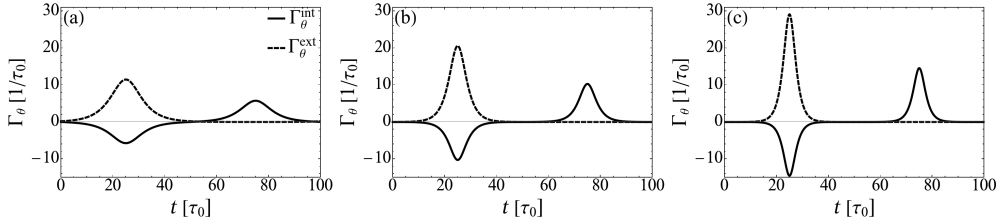


Figure 4.5: The θ -projection of the internal and external torques along the optimal control path for damping value $\alpha = 0.2$ (a), $\alpha = 0.4$ (b), and $\alpha = 0.8$ (c). The magnitude of the switching time is $T = 100\tau_0$.

Minimum energy cost of magnetization switching

After we have obtained a closed form for the optimal pulse, its substitution into Eq. (4.2) leads to the following formula for the minimum energy cost Φ_m :

$$\Phi_m = \frac{2K [2\mathcal{E}(-\alpha^2 p^2) - \mathcal{K}(-\alpha^2 p^2)]}{\gamma\mu p}, \quad (4.22)$$

where $\mathcal{E}(\cdot)$ is the complete elliptic integral of the second kind [70]. According to (4.22), Φ_m is a monotonically decreasing (increasing) function of the switching time T (damping parameter α), as illustrated in Fig. 4.6. The minimum energy cost of the reversal scales inversely with the switching time for fast switching, follows exponential asymptotics for slow switching, and reaches the lower limit proportional to the energy barrier between the target states and to the damping parameter at infinitely long switching time. In particular, the lower limit of the energy cost $\Phi_\infty \equiv 4\alpha K/(\gamma\mu)$ is reached at infinitely long switching time, see dotted lines in Fig. 4.6.

For long switching time $T \gg (\alpha + 1/\alpha)\tau_0$, the minimum switching cost Φ_m is reduced to

$$\Phi_m \approx \Phi_\infty \left(1 + 4 \exp \left[-\frac{\alpha T}{2\tau_0(1 + \alpha^2)} \right] \right), \quad T \gg (\alpha + 1/\alpha)\tau_0, \quad (4.23)$$

which makes it possible to analyze to what extent the limit Φ_∞ can be approached within finite T . In particular, termination of the reversal within time $T_\varepsilon = 2 \ln(4/\varepsilon)[\alpha +$

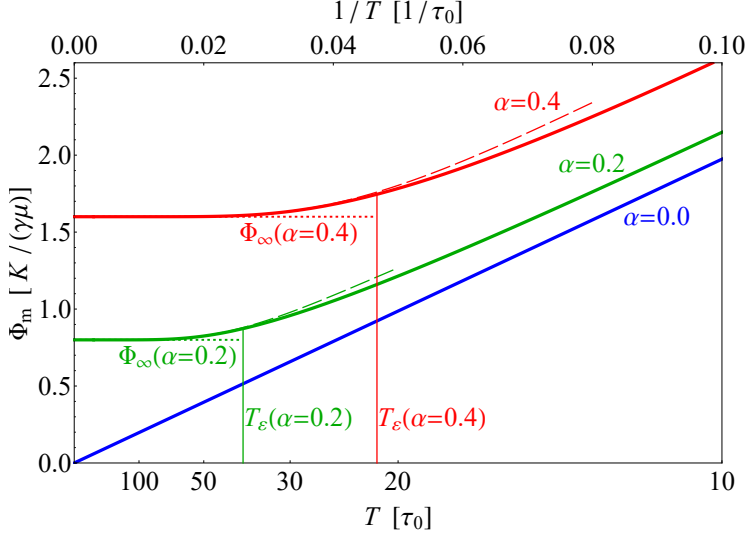


Figure 4.6: Minimum energy cost of magnetization switching as a function of the inverse of the switching time. Dashed (dotted) lines show long (infinite) switching time asymptotics. Thin vertical lines indicate switching time T_ε , for which the minimum energy cost is $\varepsilon = 10\%$ larger than the infinite switching time limit Φ_∞ . Figure adapted from Ref. [45]

$1/\alpha]\tau_0$ corresponds to the energy cost which is only by a fraction of $\varepsilon < 1$ larger than Φ_∞ : $\Phi_m(T_\varepsilon)/\Phi_\infty = 1 + \varepsilon$. Therefore, T_ε has a meaning of optimal switching time in a sense that an increase in T beyond T_ε does not lead to a significant gain in energy efficiency (see Fig. 4.6). Nevertheless, analysis of Eq. (4.22) shows that for a given switching time T , the energy cost is never smaller than that in a zero-potential case: $\Phi_m(T) \geq \Phi_0(T) \equiv \pi^2(1 + \alpha^2)/(\gamma^2 T)$, where the equality is reached for $\alpha = 0$. In other words, the internal energy of the system can only obstruct the reversal in a system with uniaxial anisotropy, and the purpose of the switching pulse optimization is just to minimize the unfavorable effect caused by the magnetic potential in this case. This limitation can be bypassed by adding a hard anisotropy axis anisotropy to the system that activates the internal torque in the desired switching direction, as discussed in the following subsection.

As a final note, we performed additional spin dynamics simulation to test the robustness of the optimal switching protocol for the uniaxial monodomain particle against thermal fluctuations and perturbations in the material parameters. The simulations were carried out by integrating the stochastic Landau-Lifshitz-Gilbert (LLG) equation equipped with the optimal switching pulse, see Appendix E, as an external field. We have found that the optimal pulse is robust with respect to thermal fluctuations in the technologically relevant regime, and even with an imperfect implementation of our optimal pulse, it can bring the magnetic moment vector close to the final stable state if the perturbation in the material parameters is not too large. Moreover, experimen-

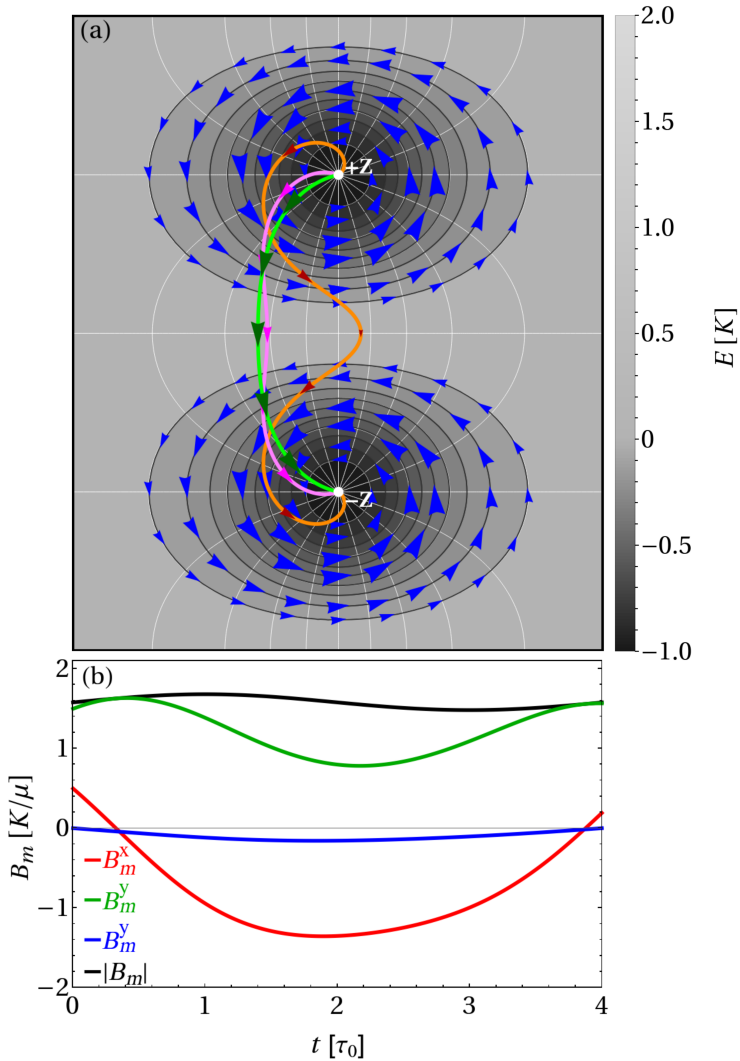


Figure 4.7: (a) Transverse Mercator projection [71] of the energy surface of a uniaxial macrospin. The meridians and the parallels are shown with thin white lines. The blue arrows show the distribution of the internal torque, with the size of the arrows being proportional to the magnitude of the torque. The calculated OCPs between the energy minima at $+Z$ and $-Z$ are shown with the green, pink, and orange lines for $T = 2\tau_0$, $T = 4\tau_0$, and $T = 14\tau_0$, respectively. The arrows along each OCP show the velocity at $t = T/6$, $t = T/3$, $t = T/2$, $t = 2T/3$, and $t = 5T/6$, where the arrow size codes the magnitude of the velocity. The damping factor α is 0.1. (b) The calculated optimal pulse as a function of the time for $T = 4\tau_0$ and $\alpha = 0.1$.

tal realization of optimal control pulses is challenging but still feasible within current technology for pulse shaping [72–76].

4.1.2 Optimal control of magnetization reversal in a biaxial nanoparticle

In the previous subsection, we have presented an exact analytical solution to the problem of optimal switching of a uniaxial nanoparticle via the coherent rotation mode used in most modern magnetic memories. However, the easy-axis anisotropy alone can only increase the energy cost of the switching compared to the free-nanoparticle case, but this effect is minimized by following the optimal control path.

Nevertheless, to be able to use the internal energy landscape to aid the switching process, additional terms in the magnetic potential are necessary. Note that the phenomenon of internal torque assisting the magnetization switching was previously recognized experimentally for several systems, e.g., for Co films [77] and Co nanoclusters [78], but a complete physical picture describing this effect is still missing. Here, we investigate utilizing the optimal control theory to what extent the energy cost of magnetization switching can be minimized by pulse shaping and how this depends on the parameters of the biaxial system and the switching time. We focus on nanomagnets with biaxial anisotropy, which can arise due to the demagnetizing field [79]. This scenario is realized in flat elongated nanoelements; see Fig. 4.8. Such systems are used, e.g., as single bits in in-plane memory [67], or as elements of artificial spin ice arrays [80, 81].

The internal energy of the biaxial nanoparticle is given by the following equation

$$E = \xi K m_x^2 - K m_z^2, \quad (4.24)$$

where the easy axis and the hard axis are along the z and x directions, respectively, $K > 0$ is the anisotropy constant, and ξ is a dimensionless parameter defining the relative strength of the hard-axis anisotropy. The energy surface of the system has two minima at $\mathbf{m} = (0, 0, 1)$ and $\mathbf{m} = (0, 0, -1)$, and two saddle points at $\mathbf{m} = (0, 1, 0)$ and $\mathbf{m} = (0, -1, 0)$ (see Fig. 4.8).

Optimal protocols for magnetization reversal

Finding optimal protocols for the magnetization reversal of biaxial nanoparticles requires minimizing the magnetization switching cost functional Φ . However, for such a system, the corresponding Euler-Lagrange (EL) equations cannot be solved fully analytically, which is in contrast to the uniaxial case. To address this, we numerically obtain the optimal control paths that minimize Φ , as explained in Sec.2.2. Additionally, we derive analytical estimates of the energy cost reduction based on perturbation theory [47].

A typical outcome of the OCP calculations is shown in Figures 4.9(a)-(c), illustrating the calculated OCPs for the magnetization reversal at $\alpha = 0.1$ and various switching times and strengths of the hard-axis anisotropy. These OCPs are superimposed on

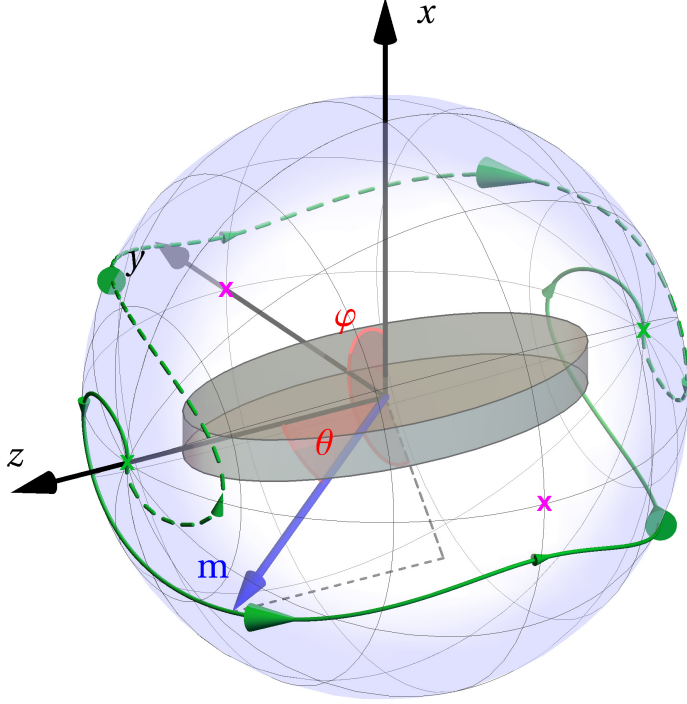


Figure 4.8: Optimal switching of a flat elongated nanomagnet representing a biaxial anisotropy system. The direction of the normalized magnetic moment \mathbf{m} is shown with the blue arrow. Orientations of \mathbf{m} that correspond to the minima and the saddle points on the energy surface are marked with the green and magenta crosses, respectively. The calculated optimal control paths between the energy minima are shown with the solid and the dashed green lines. The damping factor α is 0.1, the switching time T is $8\tau_0$, and the hard-axis anisotropy constant is twice as large as the easy-axis anisotropy constant. The green arrows along the reversal paths show the velocity of the system at $t = T/6$, $t = T/3$, $t = T/2$, $t = 2T/3$, and $t = 5T/6$, with the size of the arrowheads being proportional to the magnitude of the velocity. The contours of constant azimuthal angle φ (meridians) and polar angle θ (parallels) are shown with thin black lines. Figure adapted from Ref. [47].

the energy surface of the system. In the uniaxial case ($\xi = 0$), the OCPs exhibit degeneracy due to the axial symmetry, as seen in the solid and dashed pink lines. However, in the biaxial system ($\xi \neq 0$), the axial symmetry is broken due to the addition of the hard axis, resulting in well-separated OCPs between energy minima. In most cases, there are two equivalent mirror-symmetric OCPs with a π -angle rotation around the easy axis. We have found that more co-existing OCPs can be present for $\xi \gtrsim 4$, where the paths differ in the amount of precession around the initial and final states. Interestingly, in the biaxial nanoparticle, OCPs can break the XY -plane mirror symmetry. For certain parameter values, such asymmetric OCPs minimize the functional Φ . Nevertheless, the OCPs never pass through saddle points (SPs) on the

4 Applications

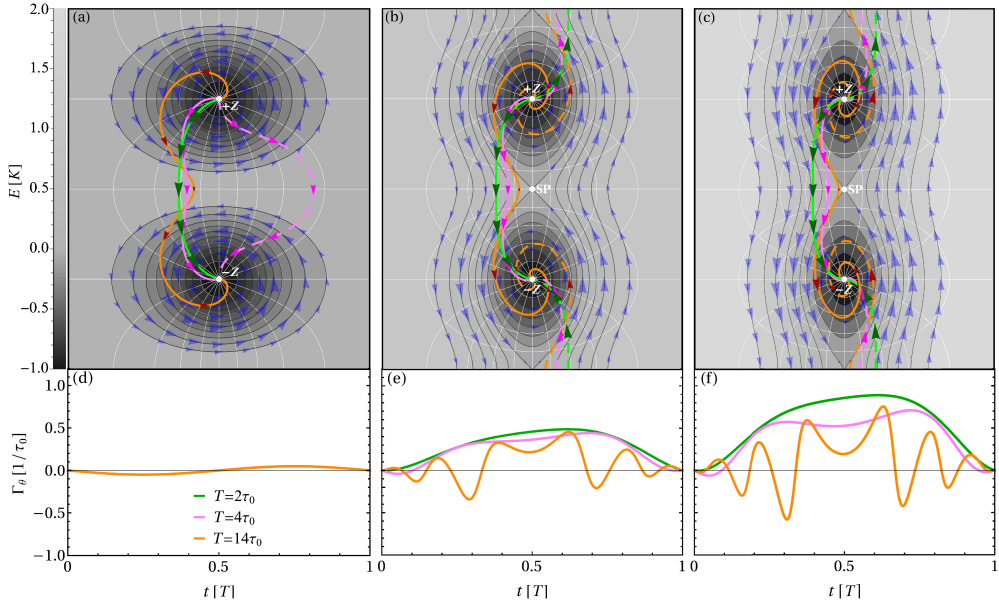


Figure 4.9: Transverse Mercator projection [71] of the energy surface of a macrospin with (a) uniaxial anisotropy and biaxial anisotropy with (b) $\xi = 1$ and (c) $\xi = 2$. The meridians and the parallels (see Fig. 4.8) are shown with thin white lines. The blue arrows show the distribution of the internal torque, with the size of the arrows being proportional to the magnitude of the torque. The calculated OCPs between the energy minima at $+Z$ and $-Z$ are shown with the green, pink, and orange lines for $T = 2\tau_0$, $T = 4\tau_0$, and $T = 14\tau_0$, respectively. The arrows along each OCP show the velocity at $t = T/6$, $t = T/3$, $t = T/2$, $t = 2T/3$, and $t = 5T/6$, where the arrow size codes the magnitude of the velocity. The damping factor α is 0.1. The solid and the dashed lines of the same color show equivalent OCPs. They differ by an arbitrary rotation around the easy axis for the uniaxial case; For finite ξ , the degeneracy is lifted and there are two OCPs, symmetrical with respect to a π -angle rotation around the easy axis, for a given T . Note that the OCPs do not pass through saddle points (SP) on the energy surface. The θ -projection of the internal torque along the OCPs from (a)-(c) are shown in (d)-(f), respectively. Figure adapted from Ref. [47].

energy surface, preventing the system from crossing the lowest energy barrier during the switching process.

To understand the mechanism of energy-efficient magnetization switching in biaxial systems and explain the position and shape of calculated OCPs, we show the distribution of the internal torque, see the blue arrows in Figs. 4.9(a)-(c). The component of the internal torque in the direction of increasing θ , relevant for the reversal process, I_θ is shown in Fig. 4.9(d)-(f). Positive (negative) I_θ signifies the positive (negative) contribution of the internal torque to the reversal. When $\xi = 0$, the torque only generates precession around the easy axis, and in the case of nonzero damping, relax-

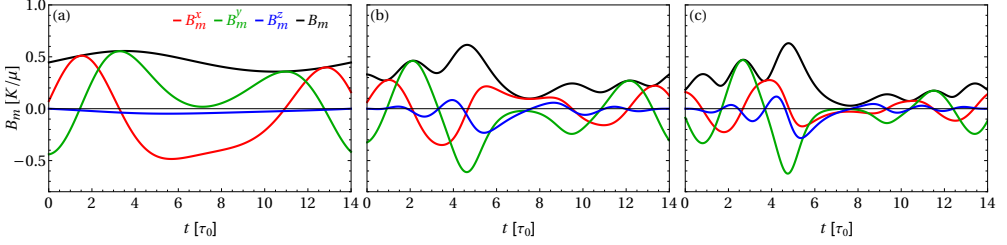


Figure 4.10: Calculated optimal switching pulse of external magnetic field for a macrospin with (a) uniaxial anisotropy and biaxial anisotropy with (b) $\xi = 1$ and (c) $\xi = 2$. The switching time T is $14\tau_0$ and the damping parameter α is 0.1. The pulses are derived from the OCPs shown in Fig. 4.9(a)-(c). Figure adapted from Ref. [47].

ation to the energy minima. In this case, the internal torque does not assist switching since it does not point in the direction of the final state anywhere in the region of the initial state ($m_z > 0$), see Fig. 4.9(d). The addition of hard-axis anisotropy ($\xi > 0$) contributes to the internal torque in a specific region of the configuration space, see Fig. 4.9(b)-(c). The location of the calculated OCPs within this region highlights the energy-efficient control principle, which lies in the effective use of the system's internal dynamics. The OCPs avoid passing through SP, where internal torque is zero, which becomes clear: ascending the energy surface is advantageous, enhancing the torque's contribution and aiding the switching process. Particularly, T_θ reaches its maximum at the equator ($\theta = \pi/2$) for $\varphi = \pi/4$ and $\varphi = 5\pi/4$. We have discovered that an optimal protocol strikes a balance between the effort to climb the energy surface and the strength of the internal torque. Consequently, the OCPs cross the equator at optimal points $\pi/4 < \varphi_m < \pi/2$ or $5\pi/4 < \varphi_m < 3\pi/2$ (Fig. 4.9(b)-(c)). It is noteworthy that increased damping makes the internal torque deviate stronger from the energy contours toward the energy minima, leading to an increase in the energy cost of switching.

Optimal switching pulses of the external magnetic field

In Fig. 4.10, we present the optimal pulses of the external magnetic field for $T = 14\tau_0$, $\alpha = 0.1$, and $\xi = 0, 1, 2$. The pulses are derived from the OCPs presented in Fig. 4.9 using Eq. (2.9). We have found that stronger hard-axis anisotropy reduces field amplitude, although its peak values can exceed the maximum field value in the $\xi = 0$ case. Pulse strength differs between reversal halves due to relaxation. Interestingly, the broken axial symmetry in the biaxial system introduces amplitude oscillation, persisting at zero damping, in contrast to the uniaxial case. It is noteworthy that the switching field is always perpendicular to the magnetic moment; amplitude symmetry holds for $\xi > 0$ ($B_m(0) = B_m(T)$). For $\xi = 0$, extra symmetry is observed ($B_m(0) = B_m(T/2) = B_m(T)$) [45].

4 Applications

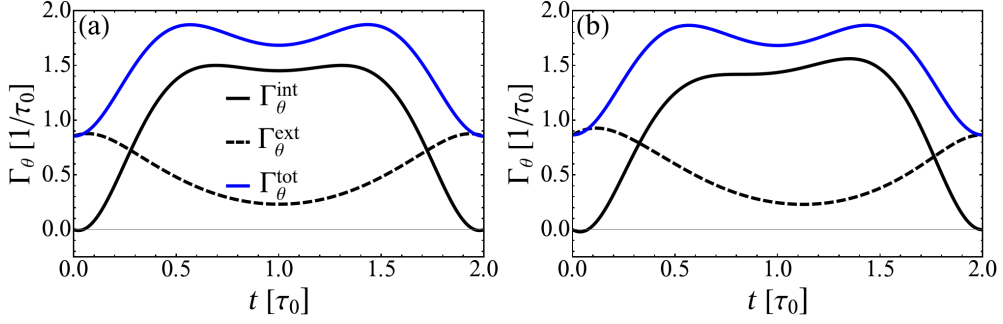


Figure 4.11: The θ -projection of the internal, external, and the total torques along the optimal control path for damping value $\alpha = 0$ (a), $\alpha = 0.1$ (b). The magnitude of the switching time is $T = 2\tau_0$, while the dimensionless parameter ξ determining the strength of the hard axis is 5.

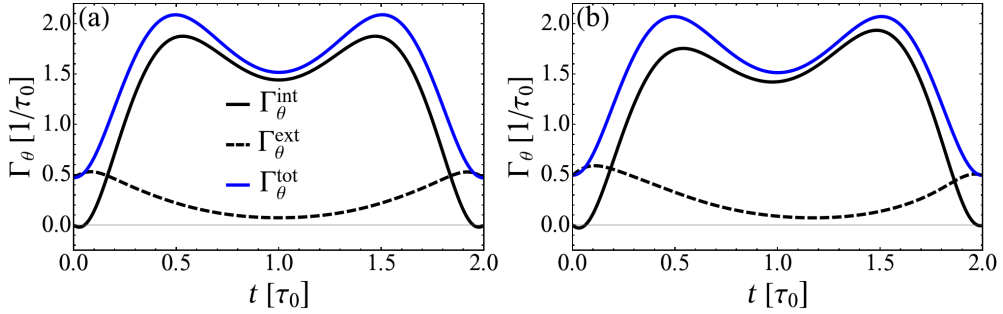


Figure 4.12: The θ -projection of the internal, external, and the total torques along the optimal control path for damping value $\alpha = 0$ (a), $\alpha = 0.1$ (b). The magnitude of the switching time is $T = 2\tau_0$, while the dimensionless parameter ξ determining the strength of the hard axis is 10.

Internal and external torques

The components of the internal torque produced by the internal field of the biaxial nanoparticle can be written as follows:

$$\begin{aligned} \Gamma_{\theta}^{int} &= \Gamma_0 \sin \theta [\xi \sin(2\varphi) - 2\alpha \cos \theta (1 + \xi \cos^2 \varphi)] \hat{\theta}, \\ \Gamma_{\varphi}^{int} &= \Gamma_0 \sin \theta [\alpha \xi \sin(2\varphi) + 2 \cos \theta (1 + \xi \cos^2 \varphi)] \hat{\varphi}, \end{aligned} \quad (4.25)$$

where $\Gamma_0 = 2\tau_0(1 + \alpha^2)$, $\theta(t)$ and $\varphi(t)$ are calculated along the OCP. Here, we are interested in the θ -projection of the internal torque relevant to the reversal process. Note that for $\xi = 0$, Eq. 4.25 reduces to Eq. 4.21 as expected. The θ -projection of the internal torque as well as the external torque Γ_{θ}^{ext} , generated by the optimal pulse, as a function of the switching time for various values of damping is illustrated in Figures 4.11-4.12. Interestingly, for zero damping and $\xi > 0$, the θ -projection of the

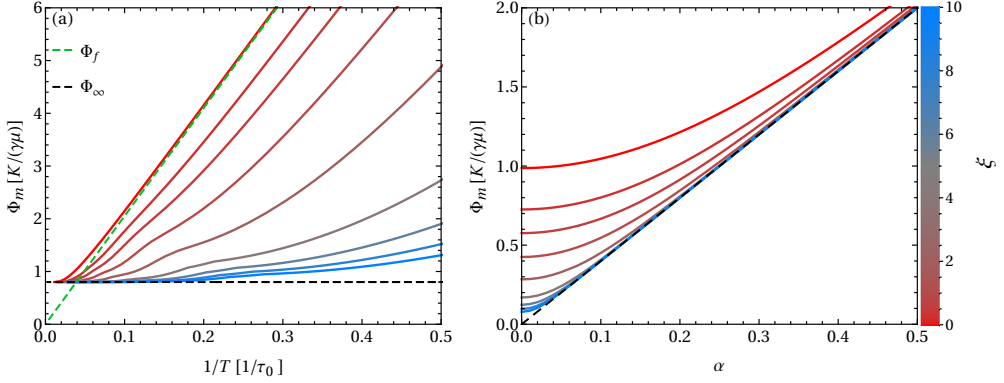


Figure 4.13: Minimum energy cost of magnetization reversal as a function of (a) inverse of the switching time for $\alpha = 0.2$, (b) damping parameter for $T = 20\tau_0$, for various ξ values. Green dashed line corresponds to the solution of the reversal of a free macrospin, while the black dashed line shows the infinite switching time asymptotic $\Phi_\infty \equiv 4\alpha K/(\gamma\mu)$. Figure adapted from Ref. [47].

internal torque Γ_θ^{int} does not reduce to zero as in the uniaxial case, suggesting that the addition of the hard-axis anisotropy has a favorable effect on the switching. In particular, the positive Γ_θ^{int} signifies the positive contribution of the internal torque to the reversal, see the solid black line in Figures 4.11(a) and 4.12(a).

It is worth mentioning that the asymmetric shape of Γ_θ^{int} about $T/2$ shown in Figures 4.11(b) and 4.12(b) – the result of the damping contribution to the torque – does not contradict to the mirror-symmetry of the OCPs. For symmetric OCPs, the total torque stays symmetric, see the blue line in Figures 4.11-4.12.

Minimum energy cost of magnetization switching

The calculated optimal reversal protocols can now be used to calculate the minimum energy cost of switching Φ_m . Figure 4.13(a) illustrates how Φ_m changes with the inverse of switching time for different hard-axis anisotropy strengths. Irrespective of the ξ value, Φ_m decreases monotonically with T and approaches the universal lower limit Φ_∞ at infinitely long switching time [25]. Larger ξ values lead to a faster approach of Φ_m to the lower limit Φ_∞ . Overall, there is a decrease in Φ_m with ξ , as expected from the distribution of the torque in biaxial systems, see Figures. 4.9(a)-(c). The switching cost for a free macrospin $\Phi_f(T)$ (see the green dashed line in Fig. 4.13(a)) provides a useful benchmark for evaluating the favorable effect of the torque produced by the hard axis. Notably, the switching cost can be significantly lower than $\Phi_f(T)$ in a certain range of T for finite strengths of the hard-axis anisotropy. For example, $\Phi_m(T)$ becomes almost an order of magnitude smaller than $\Phi_f(T)$ for $\xi = 10$ and $T \approx 2\tau_0$. This is in contrast to the uniaxial-anisotropy case ($\xi = 0$), where $\Phi_m(T) \geq \Phi_f(T)$ (the equality is reached for $\alpha = 0$) for any given T .

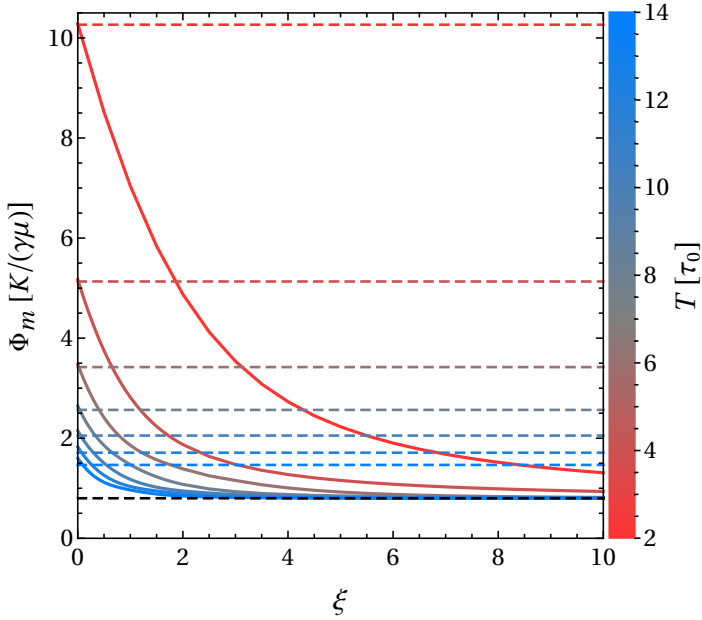


Figure 4.14: Minimum energy cost of magnetization reversal as a function of ξ for various T values (solid lines). The dashed color lines show the switching cost for a free macrospin. The magnitude of the damping factor α is 0.2. Black dashed line shows the infinite switching time asymptotic. Figure adapted from Ref. [47].

The α -dependencies of the minimum switching cost for $T = 20\tau_0$ and several values of ξ are shown in Fig. 4.13(b). Irrespective of the strength of the hard-axis anisotropy, Φ_m is a monotonically increasing function of the damping parameter, approaching the Φ_∞ asymptote when $\alpha \rightarrow \infty$. It is noteworthy that the reduction in the switching cost with ξ becomes more pronounced as α decreases.

It is noteworthy that reducing switching costs in biaxial magnets can be achieved without sacrificing their thermal stability. Thermal stability is determined by the energy barrier ΔE separating the stable states, and within harmonic rate theories ΔE is quantified by the energy difference between a saddle point and the minimum energy state [82, 83]. In biaxial magnets, this energy barrier remains constant ($\Delta E = K$) regardless of the ξ value, see Eq. (4.24). However, Φ_m , particularly for short switching times, is heavily influenced by ξ , which is particularly clear from Fig. 4.14 (note that Φ_m converges to Φ_∞ for $\xi \rightarrow \infty$ irrespective of the switching time). Thus, biaxial magnets offer the unique advantage of independently optimizing writability and thermal stability, making them efficient memory elements and a solution to magnetic recording challenges.

Optimal switching time

We have found that the minimum energy cost for switching has two clear asymptotics: $\Phi_m = \pi^2(1 + \alpha^2)/(\gamma^2 T) - 4K\xi/(\gamma\mu)$ when $T \rightarrow 0$, and $\Phi_m = \Phi_\infty$ when $T \rightarrow \infty$. Their intersection point [47]

$$T^* = \frac{(1 + \alpha^2) \pi^2}{2(\alpha + \xi)} \tau_0, \quad (4.26)$$

can be interpreted as an optimal switching time in a sense that increase in T beyond T^* does not lead to a significant reduction in the energy cost. Therefore, T^* provides a tradeoff between the switching speed and energy efficiency [45, 84]. Note that T^* decreases with increasing strength of the hard-axis anisotropy.

Perturbation theory analysis

Both anisotropies in the biaxial system can be treated as independent perturbations to the free macrospin. This results in two dimensionless perturbation parameters $\epsilon_1 \equiv \xi T/\tau_0$ and $\epsilon_2 \equiv T/\tau_0$ defined by the hard- and the easy-axis anisotropy, respectively. The perturbation series for the OCP can be obtained by solving the Euler-Lagrange (EL) equation. The EL equation in spherical coordinates θ and φ reads

$$\begin{aligned} \ddot{\theta} &= A_0 \dot{\varphi}^2 + A_1 \dot{\varphi} + A_2, \\ \ddot{\varphi} &= C_0 \dot{\theta} \dot{\varphi} + C_1 \dot{\theta} + C_2. \end{aligned} \quad (4.27)$$

for a biaxial system whose energy is defined by Eq. (4.24), the coefficients become

$$\begin{aligned} A_0 &= \frac{\sin 2\theta}{2}, \quad A_1 = \frac{(2 + \xi)(\sin \theta - 3 \sin 3\theta)}{8(1 + \alpha^2)\tau_0} + \frac{3\xi \cos 2\varphi \sin^3 \theta}{2(1 + \alpha^2)\tau_0}, \\ C_0 &= -2 \cot \theta, \quad C_1 = \frac{(2 + \xi)(3 \cos 2\theta + 1) \csc \theta}{4(1 + \alpha^2)\tau_0} - \frac{3\xi \cos 2\varphi \sin \theta}{2(1 + \alpha^2)\tau_0}. \end{aligned} \quad (4.28)$$

$$\begin{aligned} A_2 &= \frac{\sin 4\theta(2 + \xi \cos 2\varphi + \xi)^2}{16(1 + \alpha^2)\tau_0^2} + \frac{\xi^2 \sin^2 2\varphi \sin 2\theta}{8(1 + \alpha^2)\tau_0^2}, \\ C_2 &= \frac{-\xi(2 + \xi) \sin 2\varphi \cos^2 \theta}{2(1 + \alpha^2)\tau_0^2} + \frac{\xi^2 \sin 4\varphi \sin^2 \theta}{4(1 + \alpha^2)\tau_0^2}. \end{aligned} \quad (4.29)$$

We seek for $\theta_m(t)$ and $\varphi_m(t)$ – the solution of Eq. (4.27) – in a form of a series in the two perturbation parameters ϵ_1 and ϵ_2 defined by the biaxial anisotropy. In particular, the second-order expansion for $\theta_m(t)$ and $\varphi_m(t)$ reads

$$\begin{aligned} \theta_m(t) &\approx \theta_f(t) + \sum_{i=1}^2 \epsilon_i \theta_i(t) + \sum_{i,j=1}^2 \epsilon_i \theta_{ij}(t) \epsilon_j, \\ \varphi_m(t) &\approx \varphi_f(t) + \sum_{i=1}^2 \epsilon_i \varphi_i(t) + \sum_{i,j=1}^2 \epsilon_i \varphi_{ij}(t) \epsilon_j. \end{aligned} \quad (4.30)$$

4 Applications

Here, $\theta_f(t) \equiv \pi t/T$ and $\varphi_f(t) \equiv \pi/4, 5\pi/4$ describe the reversal of a free macrospin, and the coefficients $\theta_i(t), \varphi_i(t), \theta_{ij}(t), \varphi_{ij}(t)$ are obtained upon substituting Eqs. (4.30) into Eq. (4.27) and collecting terms with equal powers of ϵ_1 and ϵ_2 , which gives the following result

$$\begin{aligned} \theta_1 = 0, \theta_2 = 0, \varphi_{22} = 0, \theta_{11} &= \frac{\sin(2\pi t/T) [4 + 4\alpha^2 + \alpha^2 \cos(2\pi t/T)]}{128\pi^2 (\alpha^2)^2}, \\ \theta_{12} = \theta_{21} &= -\frac{\alpha^2 \sin(4\pi t/T)}{128\pi^2 (\alpha^2 + 1)^2}, \theta_{22} = 2\theta_{12}, \varphi_1 = \frac{(\alpha^2 - 8)}{64(\alpha^2 + 1)} + \frac{\sin(\pi t/T)}{2\pi(\alpha^2 + 1)}, \\ \varphi_2 = 2\varphi_1, \varphi_{11} = \varphi_{12} = \varphi_{21} &= \frac{(\alpha^2 + 4) \cos(2\pi t/T)}{32\pi^2 (\alpha^2 + 1)^2} + \frac{3(\alpha^2 - 8)}{2048(\alpha^2 + 1)} + \frac{100 + 73\alpha^2}{480\pi^2 (\alpha^2 + 1)^2}. \end{aligned} \quad (4.31)$$

The approximation to the minimum energy cost is obtained by substituting the perturbation series for the OCP into Eq. (2.10). The result, up to the second-order terms, reads

$$\Phi_m \approx \Phi_f - \frac{4K}{\gamma\mu} \xi + \frac{K^2 T}{2(1 + \alpha^2)\mu^2} \left[\alpha^2 + \alpha^2 \xi + \frac{1}{4}(4 + 5\alpha^2)\xi^2 \right], \quad (4.32)$$

where the contributions from the hard-axis anisotropy are recognized by the ξ -factor. The smallness of the perturbation parameters, $\epsilon_1, \epsilon_2 \ll 1$, can be translated into the condition on T : $T \ll \tau_0$. Therefore, Eq. (4.32) can be interpreted as a short switching time approximation for Φ_m .

Equation (4.32) clearly shows that the switching cost reduction in biaxial magnets is captured within the linear response to the hard-axis anisotropy. Note that the easy axis does not contribute to the first-order correction; It can be shown in fact that all odd-order corrections vanish in the uniaxial case. The approximation for Φ_m within zero-, first-, and second-order perturbation theory is shown in Fig. 4.15 for $\alpha = 0.2$. The numerically exact solution for Φ_m is also shown for comparison. The short switching time approximation eventually breaks down as T increases, and Φ_m converges on Φ_∞ .

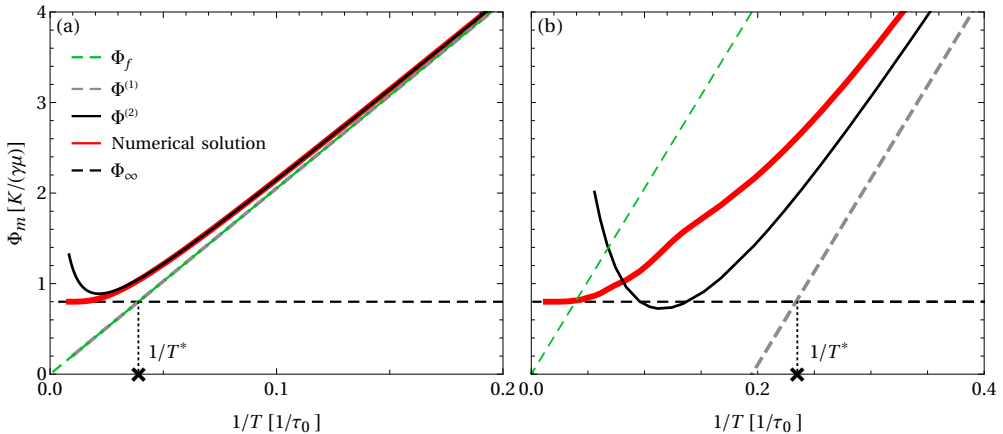


Figure 4.15: Approximation for the minimum energy cost of magnetization reversal for a macrospin within the zero- (Φ_f), first- ($\Phi^{(1)}$), and second-order ($\Phi^{(2)}$) perturbation theory [see Eq. (4.32)], as indicated in the legend, vs the inverse of the switching time. The strength of the hard-axis anisotropy ξ is (a) 0 and (b) 1. Red solid line shows the numerically exact solution. Black dashed line shows the infinite switching time asymptotic. The intersection of the short and the long switching time asymptotes provides the optimal switching time T^* [see Eq. (4.26)]. The magnitude of α is 0.2. Figure adapted from Ref. [47].

4.1.3 Optimal control of magnetization reversal in a bistable nanowire

Magnetic nanowires possess an elongated structure and nanoscale lateral size [85]. Their high length-to-width aspect ratio induces significant magnetic anisotropy, typically resulting in two stable magnetization orientations along the wire axis. This bistability renders magnetic nanowires highly promising as foundational elements for innovative devices dedicated to data transmission, storage, and processing. These devices can encode information within domains exhibiting opposite magnetization directions [2]. Nevertheless, the advancement of such technology critically relies on understanding the mechanisms governing magnetization reversal in bistable nanowires. Exploring how these reversal modes are influenced by factors like the applied switching stimulus, magnetic parameters, and geometry of the wire is intriguing from a fundamental perspective. Earlier theoretical [86–89] and experimental [90–94] studies have unveiled three principal mechanisms for switching magnetization in nanowires: homogeneous rotation of magnetization, propagation of transverse domain walls, and formation of vortex domain walls. The possibility of achieving magnetization switching through diverse transition mechanisms has prompted the idea of a unique, optimal mechanism that minimizes termination time and energy cost. Identifying such optimal reversal mechanisms is of particular importance for the development of energy-efficient information technologies founded on magnetic nanowires.

4 Applications

Here we apply, the optimal control theory to the problem of energy-efficient magnetization reversal in a one-dimensional nanowire. The theory makes it possible to identify mechanisms of energy-efficient magnetization reversal in the nanowire. We consider a nanowire consisting of N interacting magnetic moments and extended along the x axis. The energy of the wire is given by a classical Heisenberg-type Hamiltonian:

$$E = -J \sum_{i=1}^{N-1} \mathbf{m}_i \cdot \mathbf{m}_{i+1} - K \sum_{i=1}^N (\mathbf{m}_i \cdot \mathbf{e}^x)^2, \quad (4.33)$$

where \mathbf{m}_i is the unit vector defining the orientation of the magnetic moment at site i . The first term in Eq. (4.34) accounts for the exchange interaction between nearest neighbors with ferromagnetic coupling constant $J > 0$. The second term is due to magnetic uniaxial anisotropy characterized by the easy axis \mathbf{e}^x along the wire and effective parameter $K > 0$.

The system has two stable states due to anisotropy, aligned parallel or antiparallel to the x -axis, as depicted in Fig. 4.16. Magnetization switching between these states is achieved using an external magnetic field. Our goal is to identify an optimal pulse of the external magnetic field for achieving switching within a specified switching time T while minimizing energy cost Φ , see Eq. (2.12). The identification of the optimal mechanisms minimizing Φ as well as optimal pulses is done numerically.

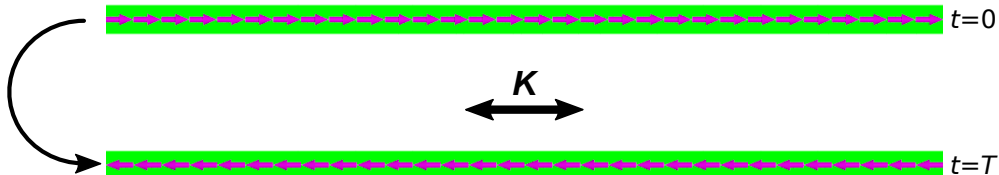


Figure 4.16: Stable orientations of the magnetization in a nanowire. The nanowire is represented by a chain of $N = 30$ magnetic moments. Arrows indicate orientation of the moments. Direction of the anisotropy axis is shown with the double-headed arrow. Transition between the states is schematically shown with the black arrow. In the OCP, the initial state is realized at $t = 0$, while the final state is realized at $t = T$. Figure adapted from Ref. [46].

Magnetization switching in a nanowire

Although the initial and final stable states are collinear, the transition between them can involve a non-uniform rotation of magnetization. In particular, the OCP calculations have revealed that the mechanisms of energy-efficient magnetization reversal in the nanowire might involve uniform rotation of magnetization [see Figure 4.17(a)] and the emergence of standing spin waves with variable wavelength [see Figures 4.17(b,c)]. We also compared the calculated OCPs with other distinguished paths lying lowest on the energy surface, i.e., the minimum energy path (MEP). The MEP for the

magnetization reversal in the nanowire considered here is calculated using the geodesic nudged elastic band method [50]. Since the length of the considered nanowire exceeds the domain wall width, the MEP corresponds to the domain wall movement, see the saddle-point configuration for the nanowire in Figure. 4.17(d). Interestingly, the MEP is very different from the calculated OCPs. In fact, the OCP calculations have never converged on the path corresponding to the single domain wall propagation, even if we start from an MEP with small random noise as an initial guess for the OCP calculations. It is noteworthy that in the case of the coherent rotation mechanism, each magnetic moment in the wire follows the same trajectory presented in Sec. 4.1.1.

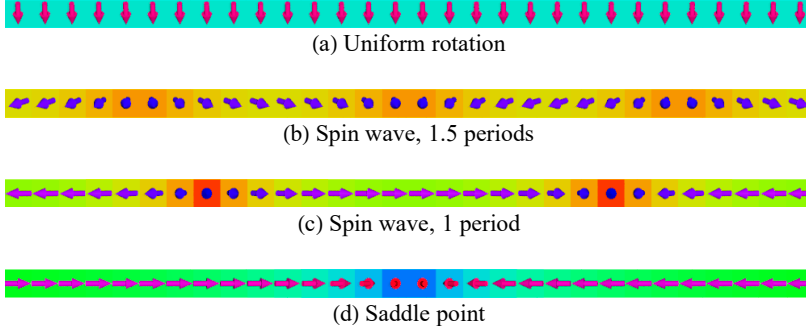


Figure 4.17: Magnetic configurations realized along OCPs (a)-(c) and MEP (d) for magnetization switching in the nanowire of length $N = 30$. For the OCPs, configurations at $t = T/2$ are shown where $T = 1$ ns. For the MEP, the saddle point configuration is presented. OCP corresponds to a coherent rotation of magnetic moments for $\alpha = 0.1$ (a) and to spin wave assisted switching with 1.5 wave periods for $\alpha = 0.5$ (b) and with 1 wave period for $\alpha = 0.6$ (c). MEP corresponds to a transient domain wall nucleation and propagation (d). Figure adapted from Ref. [46].

Minimum energy cost of magnetization switching

Figure 4.18(a) illustrates the minimum energy cost Φ of optimal switching as a function of the length N of the wire for the fixed values of the switching time and damping factor with $T = 1$ ns and $\alpha = 0.4$. Short nanowires reverse their magnetization via uniform rotation. However, when the length of the wire exceeds a certain critical length, the coherent rotation mechanism breaks down, and a crossover to spin-wave assisted switching occurs. Note that the number of the spin-wave periods can assume both half-integer and integer values [see Fig. 4.17(b,c)]. Interestingly, the energy-efficient magnetization switching mechanism varies with the damping parameter. In Fig. 4.18(b), Φ is plotted against α for $N = 50$ and $T = 1$ ns. For $\alpha \leq 0.4$, optimal switching involves uniform magnetization rotation, aligning with Ref. [45]. As damping α increases, the switching mechanism changes to the spin-wave mode.

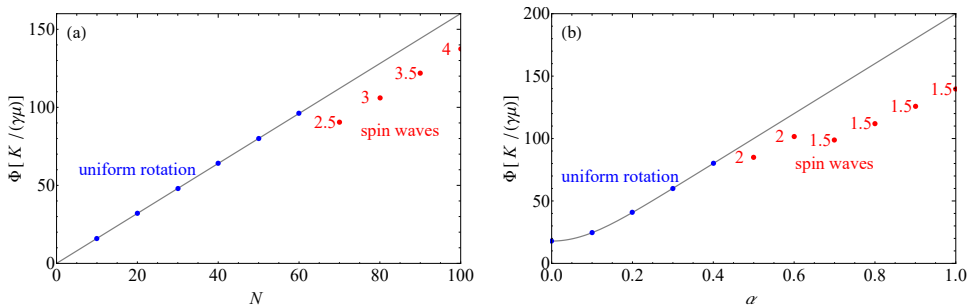


Figure 4.18: Minimum energy cost of magnetization switching as a function of the nanowire length N for $\alpha = 0.4$ and $T = 1$ ns (a) and damping parameter α for $N = 50$ and $T = 1$ ns (b). Uniform rotation and spin wave solutions are shown with blue and red circles, respectively. Red labels indicate the number of wavelengths in the spin-wave solutions. Solution for the macrospin approximation is shown with a gray line. Figure adapted from Ref. [46].

Energy variation along OCP

The energy variations along the calculated minimum energy path MEP and OCPs are compared in Figure. 4.19 for the nanowire with $N = 50$. Interestingly, the energy barrier derived from the MEP is much smaller than the highest energy point along the OCPs. This result suggests that optimal control of magnetization switching minimizing the energy cost does not necessarily translate into minimizing the energy barrier between the target states.

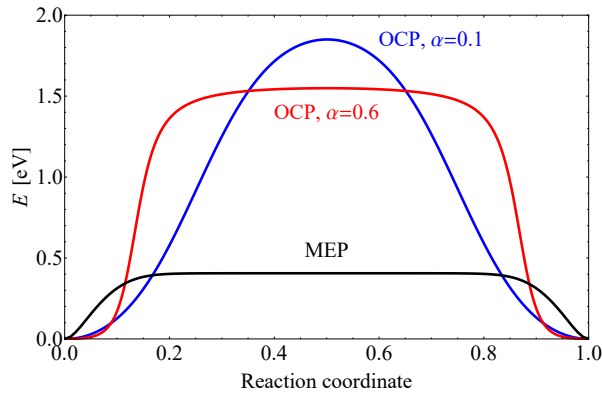


Figure 4.19: Variation of the energy of the nanowire with $N = 50$ along the MEP (black line) and the OCP for $T = 1$ ns, $\alpha = 0.1$ (blue line) and $\alpha = 0.6$ (red line). Reaction coordinate is defined as a normalized displacement along the path. Figure adapted from Ref. [46].

4.2 Constrained optimization

In this section, we apply the constrained optimal control theory proposed in section 2.3 to the problem of energy-efficient 2π domain wall movement using an optimized uniform time-dependent magnetic field. Here, our goal is to identify a uniform time-dependent pulse of the external magnetic field needed for achieving the required magnetization transition within a specified switching time T while minimizing energy cost Φ (see Eq. 2.28). The identification of the optimal mechanisms minimizing Φ as well as optimal pulses is done numerically.

4.2.1 Domain wall movement using an optimized uniform time-dependent magnetic field

Thin ferromagnetic stripes can unveil intriguing magnetization configurations, where the magnetization undergoes a complete 2π turn within a localized region of the stripe, while the remainder of the stripe maintains magnetization parallel to its edges. The ability to reliably control these domain wall structures is paramount for the effective design and implementation of magnetic nanodevices, underscoring the importance of understanding and manipulating these intriguing magnetic configurations.

Here, we apply constrained optimal control theory to address the problem of energy-efficient 2π domain wall movement in a one-dimensional nanowire. The theory enables identifying an optimal mechanism for the energy-efficient domain wall movement from which an optimal uniform time-dependent magnetic field is reconstructed.

We consider a nanowire composed of N interacting magnetic moments, extending along the x axis. The energy of the wire is described by a classical Heisenberg-type Hamiltonian:

$$E = -J \sum_{\langle i,j \rangle} \mathbf{m}_i \cdot \mathbf{m}_{i+1} - \sum_{\langle i,j \rangle} \mathbf{D}_{i,j} \cdot (\mathbf{m}_i \times \mathbf{m}_j) - K \sum_{i=1}^N (\mathbf{m}_i \cdot \mathbf{e}^x)^2, \quad (4.34)$$

where \mathbf{m}_i is the unit vector defining the orientation of the magnetic moment at lattice site i . $J > 0$ and $\mathbf{D}_{i,j} = D\mathbf{d}_{i,j}$ are the Heisenberg exchange constant and the Dzyaloshinskii-Moriya (DM) vector, respectively, $\mathbf{d}_{i,j}$ is the unit vector between sites i and j . The symbol $\langle i,j \rangle$ signifies summation over unique nearest neighbor pairs. The last term is due to magnetic uniaxial anisotropy characterized by the easy axis \mathbf{e}^x along the wire and effective parameter $K > 0$. Here, the ratio between J and D defines the equilibrium period of helical spin spirals, i.e., $L_D = 2\pi Ja/D$ with a being the lattice constant. In the following, we have chosen $J = 1$ meV and the length of the nanowire $L_x = 16L_D$. Thus, the DM constant $D = 0.392699082$ meV, while $K = 0.20047634$ meV. For such system parameters, the nanowire has a stable 2π domain wall with opposite charges, as depicted in Fig.4.20.



Figure 4.20: Stable 2π domain wall in a nanowire. The nanowire is represented by a chain of $N = 32$ magnetic moments. Arrows indicate orientation of the moments. Periodic boundary conditions are applied along x direction.

Constrained optimal control path calculations

In the constrained OCP simulations, magnetization transition between two stable states at $t = 0$ and $t = T$ (see Figure. 4.21) is achieved using an external magnetic field. For a given number of images involved in the local minimization of the energy cost functional Φ , the calculation is considered converged when the magnitude of the force as well as the penalty term have dropped below the set tolerance. Up to $Q = 200$ movable images was used, with the lowest force tolerance corresponding to the drop of the force by ten orders of magnitude with respect to the initial force calculated from the initial path. Here, the magnitude of the switching time $T = 1$ ns and the damping parameter $\alpha = 0.1$.

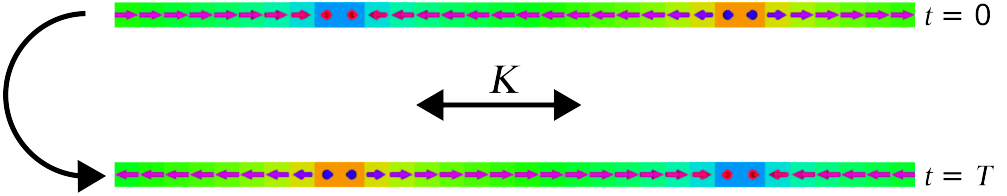


Figure 4.21: Stable 2π domain wall in a nanowire. The nanowire is represented by a chain of $N = 32$ magnetic moments. Arrows indicate orientation of the moments. Direction of the anisotropy axis is shown with the double-headed arrow. Transition between the states is schematically shown with the black arrow. In the constrained OCP calculations, the initial stable state is realized at $t = 0$, while the final stable state is realized at $t = T$.

After convergence, the penalty term, see Figure 4.22, has dropped below the set tolerance. Also, in Figure 2.31 we show the initial guess of the uniform time-dependent magnetic field and the converged one. Note that the initial guess of \mathbf{B}^* is set to zero, while the optimal \mathbf{B}^* overly has a component in the y direction.

In Figure 4.24 we show the converged space- time-dependent magnetic field \mathbf{B} and the corresponding fast variables, see Eq. 2.32. The optimal mechanism realized along the OCP at $t = T/2$ is shown in Figure 4.25(b).

Additional spin dynamics simulations were performed in order to test that the uniform time-dependent field \mathbf{B}^* induces the same net of magnetization change of the 2π domain wall movement. The simulations were carried out by integrating the Landau-Lifshitz-Gilbert (LLG) equation equipped with the optimal uniform time-dependent

switching pulse as an external field shown in Figure 4.23. The LLG equation was integrated numerically using the semi-implicit scheme B as described in Ref. [97]. The average magnetization change during the magnetic transition is shown in Figure 4.26, confirming that our results are reproducible by direct LLG simulations.

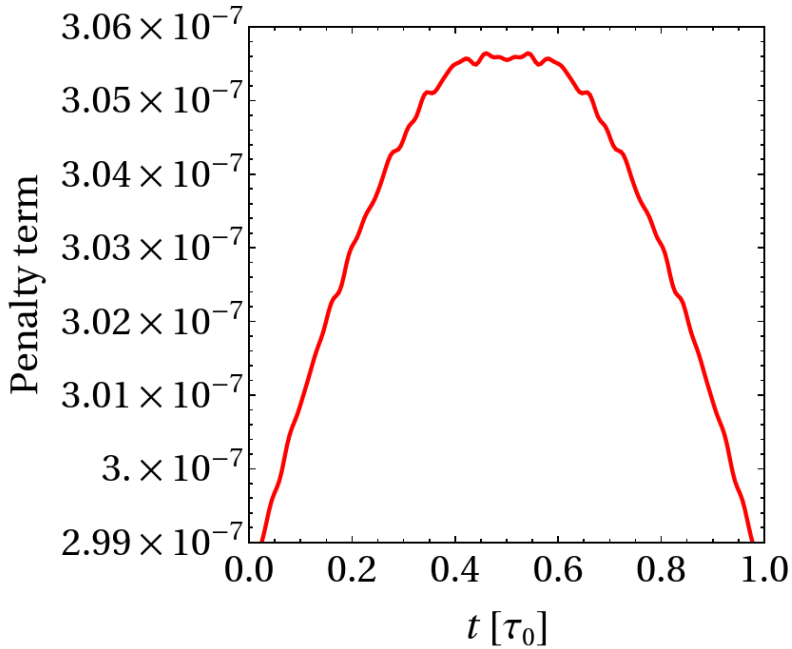


Figure 4.22: Penalty term, see Eq. 2.28, as a function of time.

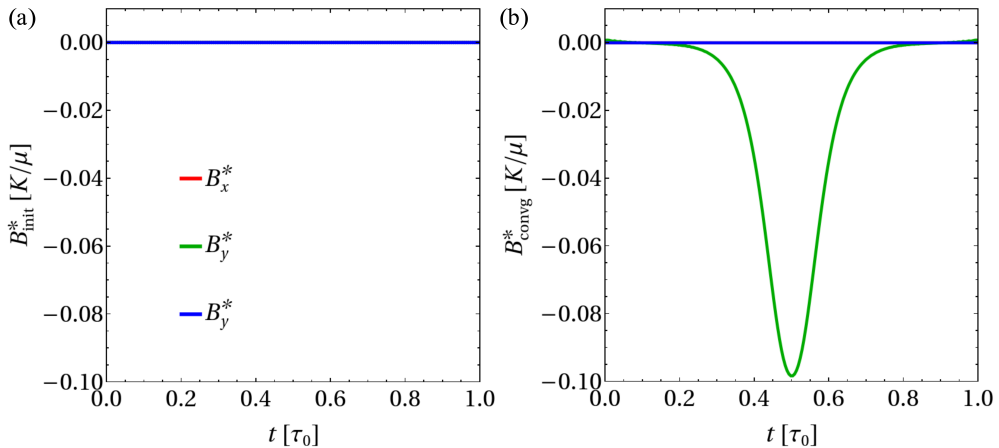


Figure 4.23: Initial guess of \mathbf{B}^* (a) and after convergence (b) as a function of time.

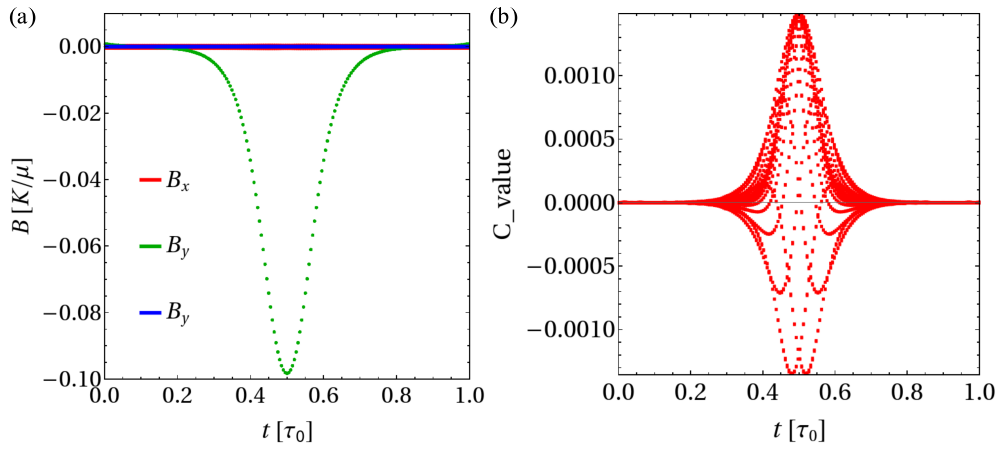


Figure 4.24: space- time-dependent magnetic field \mathbf{B} (a) and the site-dependent parameter (b) as a function of time.

4 Applications

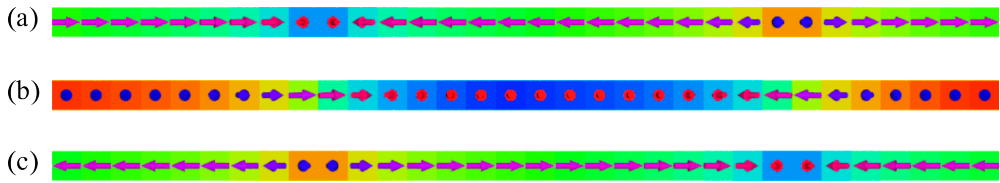


Figure 4.25: (a) and (c) Stable 2π domain wall, while (b) magnetic configurations realized along OCP at $t = T/2$. The switching time $T = 1$ ns and damping $\alpha = 0.1$.

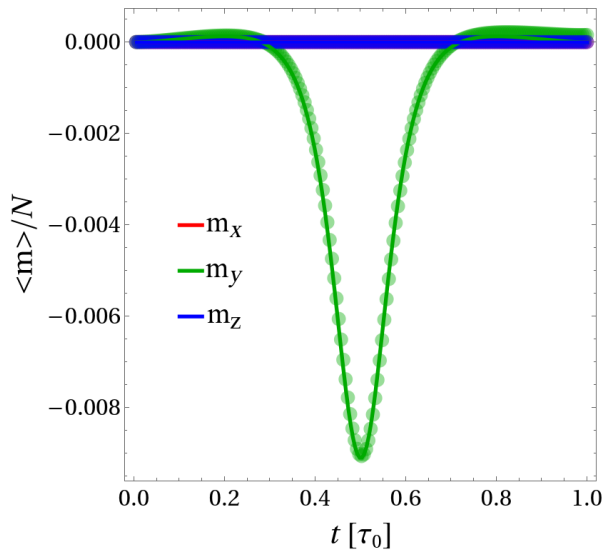


Figure 4.26: Average magnetization realized along OCP (solid line) and obtained by direct LLG simulations (points) as a function of time. The switching time $T = 1$ ns and damping $\alpha = 0.1$.

4.3 Enhancing thermal stability of optimal magnetization switching in a uniaxial nanoparticle

Energy-efficient switching of a uniaxial nanoparticle requires the application of a time-varying magnetic field characterized by microwave frequency (see Subsection. 4.1.1). However, at finite temperatures, even weak thermal fluctuations create perturbations in the magnetization that can accumulate in time, break the phase locking between the magnetization and the applied field, and eventually compromise magnetization switching. In this section, we apply the theory developed in Chapter 3 to the problem of enhancing thermal stability of optimal magnetization switching in a uniaxial nanoparticle. The theory demonstrated that the magnetization reversal is mostly disturbed by unstable perturbations arising in a certain domain of the configuration space of a nanomagnet. The instabilities can be suppressed by applying an additional stimulus, such as a weak longitudinal magnetic field, guaranteeing bounded dynamics of perturbations. Application of the stabilizing longitudinal field to a uniaxial nanomagnet makes it possible to reach a desired probability of magnetization switching even at elevated temperatures. It is noteworthy that at zero temperature, the longitudinal magnetic field does not affect the dynamics, but it plays a crucial role in stabilizing magnetization switching at finite temperatures, as demonstrated below.

Formalism and procedures

In this section, we will examine the effects of weak time-independent and time-dependent longitudinal magnetic fields, guaranteeing bounded dynamics of perturbations, on the likelihood of successful magnetization switching in a uniaxial nanoparticle at elevated temperatures. Concerning the external stimulus, we have selected two categories of an external magnetic field pulse that ensures inducing magnetization switching at absolute zero temperature:

- An optimal time-dependent pulse, akin to the one presented in our previous study [45].
- A non-optimal time-dependent Gaussian pulse, which finds common usage in experimental settings [95]. We label this pulse as 'non-optimal' because, upon our observation, the energy required to generate the Gaussian pulse is approximately 60 times greater than that needed for our derived optimal pulse, considering a specific switching time, damping level, and pulse characteristics [45].

The rationale behind employing these distinct switching pulse types is to confirm that the increase in the probability of magnetization switching is connected to the radial magnetic field itself, rather than being influenced by the choice of the driving pulse.

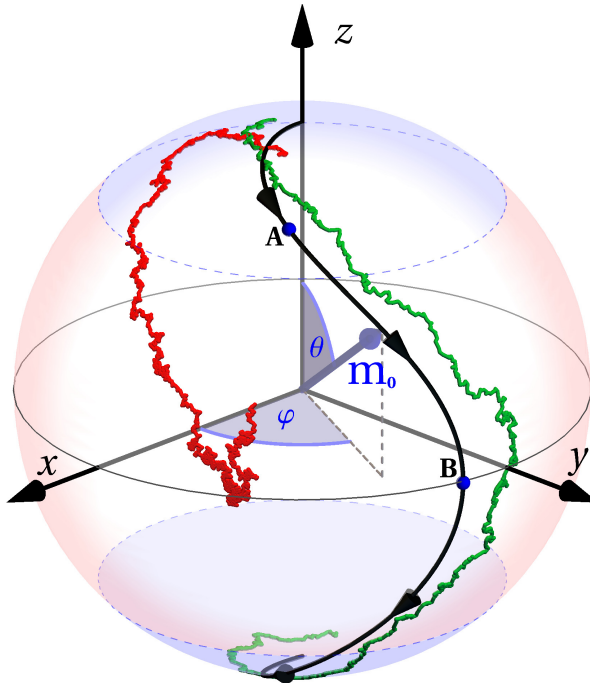


Figure 4.27: Calculated dynamics of the magnetic moment for a uniaxial nanoparticle induced by the optimal switching magnetic field. The black line shows the zero-temperature trajectory of the magnetic moment which corresponds to the optimal control path $\mathbf{m}_0(t)$ for the magnetization switching. The green (red) line shows the trajectory for successful (unsuccessful) switching at finite temperature corresponding to the thermal stability factor $\Delta = 20$. Labels A and B show positions of the magnetic moment for which the dynamics of local perturbations in the magnetization is illustrated in the corresponding insets of Fig. 4.28. The light red (blue) shaded area marks the domain for $\pi/4 \leq \theta \leq 3\pi/4$ ($\theta < \pi/4$ and $\theta > 3\pi/4$) where the perturbation dynamics is unstable (stable). The damping factor α is 0.2, and the switching time T is $5\tau_0$.

Model and spin dynamics simulations

We consider energy-efficient magnetization switching of a uniaxial monodomain nanoparticle, see Figure. 4.27, characterized by normalized magnetic moment \mathbf{m} and internal energy $E = -K(\mathbf{m} \cdot \mathbf{m}_z)^2/2$, with unit vector \mathbf{e}_z being the direction and $K > 0$ being the strength of the magnetic anisotropy. The switching is induced by an optimal pulse of a rotating magnetic field $\mathbf{B}(t)$ that, for a given switching time, minimizes the energy cost of switching [see Subsection. 4.1.1 for the exact time dependence of $\mathbf{B}(t)$ as a function of parameters of the nanoparticle]. The switching dynamics is simulated by the time integration of the the Landau-Lifshitz-Gilbert (LLG) equation [96] equipped with the optimal switching pulse as an external field. The LLG equation was integrated numerically using the semi-implicit scheme B [97] (see Appendix C). Each

simulation had three stages [45, 47]: 1) Initial equilibration at zero applied magnetic field to establish Boltzmann distribution; 2) Switching where the optimal magnetic field is applied (note that thermal fluctuations were also included during the switching stage); 3) Final equilibration at zero applied magnetic field.

At the end of the simulation, we inspected the value of m_z (z -component of the unit vector \mathbf{m} in the direction of the magnetic moment). We considered the value $m_z = -0.5$ as the threshold for the successful switching. For each value of temperature and damping constant, we repeated simulations $N = 10000$ times to accumulate the proper statistics. The switching success rate is defined as $f = N_s/N$ where N_s is the number of successful reversals. Fig. 4.27 illustrates an example of a successful (green trajectory) and unsuccessful (red trajectory) reversal. Hereafter, the period of Larmor precession $\tau_0 = \mu/(\gamma K)$ defines the timescale, while the thermal stability factor $\Delta = 20$ is defined as the ratio between the energy barrier separating the stable states and the thermal energy [98].

4.3.1 Effects of time-independent longitudinal magnetic field on the magnetization switching probability

The diagram in Fig. 4.28 shows evolution of w_1 and w_2 during magnetization switching. The eigenvalues w_1, w_2 are given by the following equations

$$w_1 = B_r + \frac{K}{\mu} \cos(2\theta), \quad (4.35)$$

$$w_2 = B_r + \frac{K}{\mu} \cos^2 \theta, \quad (4.36)$$

where θ is the polar angle of \mathbf{m}_0 and B_r is the component of the external magnetic field parallel to \mathbf{m}_0 . For zero B_r , a significant part of the switching trajectory lies in the region of unstable perturbations corresponding to the second quadrant of the diagram where the eigenvalues w_1 and w_2 have different signs. However, the values of w_1 and w_2 can be controlled by application of the longitudinal field B_r . In particular, the hyperbolic instabilities can be removed by shifting w_1 and w_2 either to the first ($B_r > K/\mu$) or to the third ($B_r < -K/\mu$) quadrant of the diagram in Fig. 4.28. Therefore, the longitudinal external magnetic field can be used as a control parameter to improve thermal stability of magnetization switching. This conclusion is confirmed in the following by direct simulations of magnetization dynamics at elevated temperature ($\Delta = 20$), here the switching is induced by a modified pulse $\mathcal{B}(t)$:

$$\mathcal{B}(t) = \mathbf{B}(t) + B_r \mathbf{m}_0(t). \quad (4.37)$$

Figure 4.29 shows calculated success rate of switching as a function of B_r for various values of the switching time and damping parameter. As predicted, the switching success rate reaches unity for $B_r > K/\mu$ regardless of the damping factor α and switching time T . Longer switching times require stronger longitudinal field to reach a certain value of the success rate, as expected, but the threshold value of B_r is not very sensitive to the damping parameter. Interestingly, the success rate as a function of the longitudinal field exhibits a minimum at $B_r \approx 0.5$ that becomes more pronounced for longer switching times. At $B_r = 0.5$, the ratio between the eigenvalues becomes $w_1/w_2 = -1$ at the top of the energy barrier. This corresponds to particularly unstable perturbations in the magnetization dynamics, therefore explaining the drop in the success rate of switching. The longer the switching time, the more time the system spends in the vicinity of the energy barrier [45]. This increases the chances of decoherence between the magnetization and the switching pulse, and lowers the switching probability. Application of the longitudinal field opposite to \mathbf{m}_0 ($B_r < 0$) renders both of the eigenvalues w_1, w_2 negative near the energy barrier, thus altering the hyperbolic character of the perturbation dynamics. As a result, the success rate of switching initially increases with rising B_r . However, further increases in B_r lead to the success rate reaching a maximum value before eventually declining (see Fig. 4.28). The drop in the success rate is a consequence of divergent dynamics due to relaxation, which becomes more prominent for larger damping parameters and longer switching

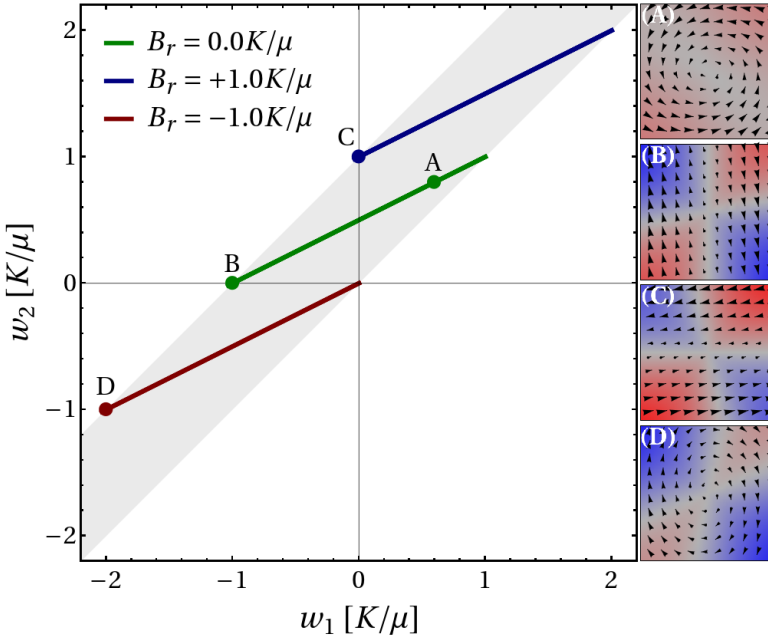


Figure 4.28: Diagram classifying dynamics of perturbations in the magnetization. The green, blue, and red lines show how the Hessian's eigenvalues w_1 and w_2 change along the zero temperature reversal trajectory (see the black line in Fig. 4.27) for three values of the longitudinal magnetic field as indicated in the legend. The right end of the lines correspond to the initial and the final states at the energy minima, while the left end of the lines corresponds to the top of the energy barrier. The gray shaded area marks the domain of possible w_1 , w_2 . Labels A-D indicate pairs of the eigenvalues for which the velocity diagrams illustrating the perturbation dynamics are shown in the insets. The background color in the insets signify whether the amplitude of the perturbation is increasing (blue), decreasing (red), or constant (gray). The damping factor α is 0.2.

times, as expected. The switching dynamics is further illustrated by Fig. 4.30 showing the calculated distribution of the copies of the system in the statistical ensemble at $t = T/2$ for $\alpha = 0.1$, $T = 10\tau_0$, and various values of B_r . For the unperturbed OCP, the system is at the top of the energy barrier. Thermal fluctuations make the system deviate from the OCP. For zero longitudinal field, the system copies spread quite far, with those corresponding to unsuccessful switching trajectories grouped closer to the initial state.

For $B_r = 0.5K/\mu$, the distribution of the copies becomes more elongated – the result of the hyperbolic of the perturbation dynamics at the energy barrier – and the number of the unsuccessful trajectories increases. As B_r increases beyond K/μ , a progressively tighter grouping of the copies around the OCP is observed due to the convergent dynamics of the perturbations, resulting in the switching probability approaching unity (see Fig. 4.29). For negative B_r , the copies of the system are grouped in an ellipse

4 Applications

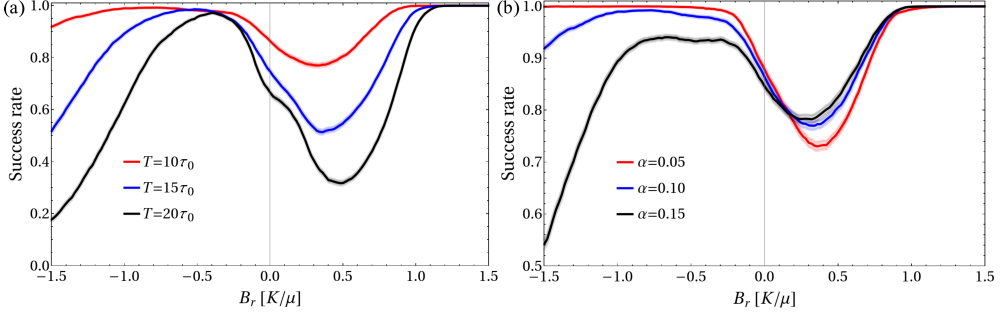


Figure 4.29: Calculated success rate of magnetization reversal as a function of the longitudinal magnetic field B_r for various values of the switching time T (a) and the damping parameter α (b). In (a), $\alpha = 0.1$; In (b), $T = 10\tau_0$. The thermal stability factor $\Delta = 20$. The shaded areas around the curves indicate the statistical error.

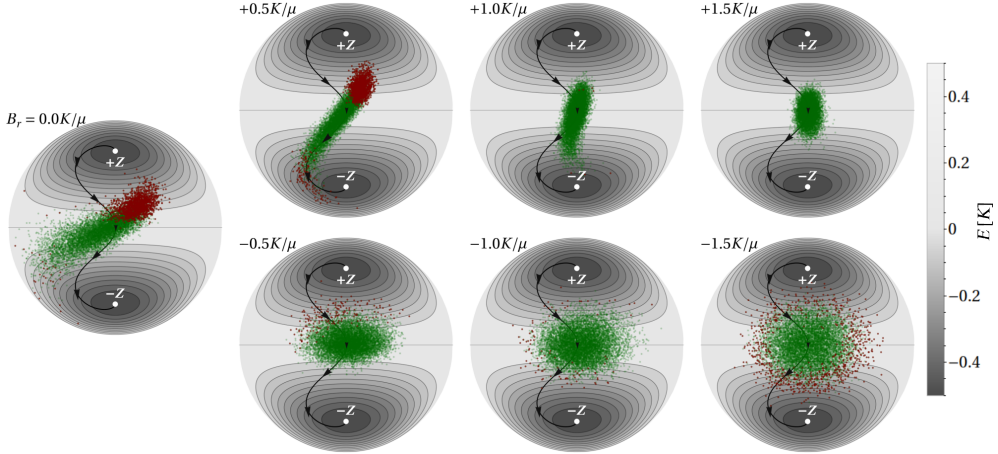


Figure 4.30: Calculated distribution of the copies of the system in the statistical ensemble at $t = T/2$ and various values of the longitudinal magnetic field, superimposed on the Lambert azimuthal projection [99] of the energy surface of the system. The green dots correspond to the copies that will eventually reach the final state at $-Z$ (successful switching), while the red dots mark the copies that will end up at the initial state at $+Z$ (unsuccessful switching). The black line shows the calculated OCP for the reversal. The damping factor α is 0.1, the thermal stability factor Δ is 20, and the switching time T is $10\tau_0$.

around the OCP even for $B_r = -0.5K/\mu$. For stronger anti-parallel fields, the spread of the distribution increases due to relaxation, resulting in a decrease in the success rate of switching. Figure 4.31 shows the calculated dependencies of the success rate on the damping constant α and switching time T for $B_r = 0$ and $B_r = \pm K/\mu$. Both cases with finite longitudinal field ensure $w_1 w_2 \geq 0$ for the whole switching trajectory. Positive (negative) B_r correspond to convergent (divergent) relaxation of the perturbation

4.3 Enhancing thermal stability of optimal magnetization switching in a uniaxial nanoparticle

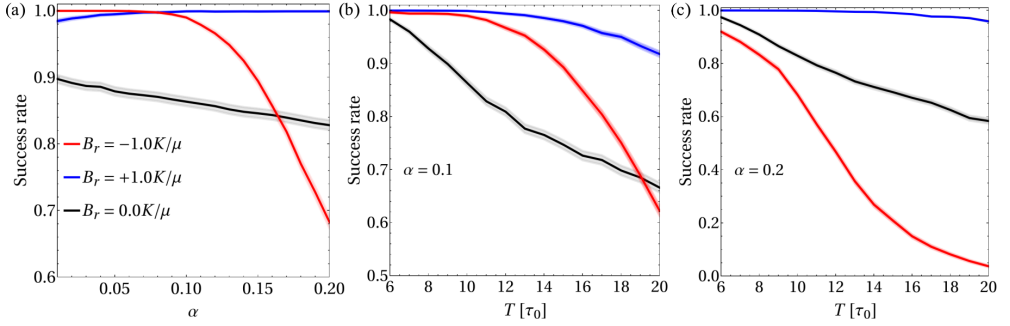


Figure 4.31: (a) Calculated success rate of magnetization reversal as a function of damping parameter α for switching time $T = 10\tau_0$. (b)-(c) Calculated success rate as a function of T for $\alpha = 0.1$ and $\alpha = 0.2$. The red, blue, and black lines correspond to the three values of the longitudinal magnetic field B_r as indicated in the legend. The thermal stability factor $\Delta = 20$. The shaded areas around the curves indicate the statistical error.

dynamics, which explains monotonic increase (decrease) of the switching probability with increasing α . However, for low damping and short switching times, applying the longitudinal field opposite to the magnetic moment ($B_r < 0$) is more efficient than applying the longitudinal field along the magnetic moment ($B_r > 0$), as it requires lower fields to achieve high success rates (see also Fig. 4.29). Longer switching times result in lower success rate in all considered cases, as expected. The decrease in the success rate with T becomes more (less) pronounced for negative (positive) B_r , as damping increases, which is a result of destabilizing (stabilizing) effect of relaxation.

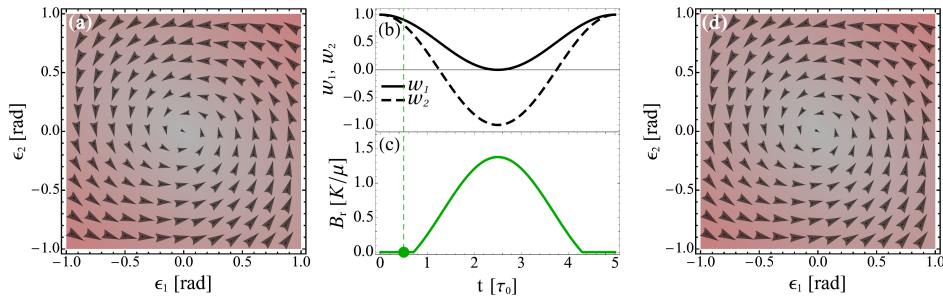


Figure 4.32: (a) Velocity diagram showing the dynamics of the perturbation in the tangent space obtained for $w_1 > 0$ and $w_2 > 0$ and zero B_r . Values of w_1 and w_2 are taken from (b) at which the dashed vertical green line intersects the solid and dashed black lines. Figure (b) shows the calculated eigenvalues of the projected Hessian along the zero-temperature reversal trajectory, see the black line in Figure. 4.27, as a function of the switching time. (c) The calculated radial field obtained using the scheme I defined in Chapter 3, see Eq. 3.10, as a function of the switching time. The green point shows the value of B_r used for shifting the eigenvalues. (d) Velocity diagram showing the effect of B_r on the dynamics of the perturbation in the tangent space after shifting the eigenvalues, compared to (a). The magnitude of the switching time T is $5\tau_0$, while the damping factor $\alpha = 0.2$ and $\lambda = 0.5$. The black arrows in Figures (a) and (d) show the distribution of the dynamics with the size of the arrows being proportional to the magnitude of the perturbation, and the colors in the background indicate that the amplitude of the perturbation is decreasing (red), or constant (gray).

4.3.2 Effects of time-dependent longitudinal magnetic field on the magnetization switching probability

Before investigating the influence of the longitudinal field $B_r(t)$ on magnetization switching probabilities, several essential preliminary steps are required. These steps involve examining its effects on perturbation dynamics within the tangent space, as well as its effects on the distribution of the ensemble copies.

Effect of longitudinal field on perturbation trajectories

Here we present a series of Figures (Figures 4.32-4.34) that depict the velocity diagram dynamics, specifically detailing perturbation behavior within the tangent space. This investigation encompasses scenarios with both zero and non-zero values of $B_r(t)$. Additionally, we incorporate the eigenvalues of the projected Hessian matrix, denoted as w_1 and w_2 , and track the temporal evolution of $B_r(t)$ relative to the switching time. Here, we only show the effect of $B_r(t)$ whose derivation follows scheme I, see chapter 3, for switching time $T = 5\tau_0$, alongside $\alpha = 0.2$ and $\lambda = 0.5$. The trajectories shown in Figures 4.32(a)-4.34(a) for a zero value of $B_r(t)$ exhibit varying shapes such as elliptical, straight, or hyperbolic, depending on the sign of w_1 and w_2 .

4.3 Enhancing thermal stability of optimal magnetization switching in a uniaxial nanoparticle

However, by introducing an influence of $B_r(t)$ through adjusting the eigenvalues, the trajectories transform into elliptical patterns, as depicted in Figure 4.32(d)-4.34(d), resulting in stable dynamics. It is worth noting that whenever the system's stability is ensured—when both w_1 and w_2 are positive—the value of $B_r(t)$ diminishes to zero. In contrast, the presence of non-zero $B_r(t)$ corresponds to an unstable system dynamics, see Figures 4.32(c)-4.34(c).

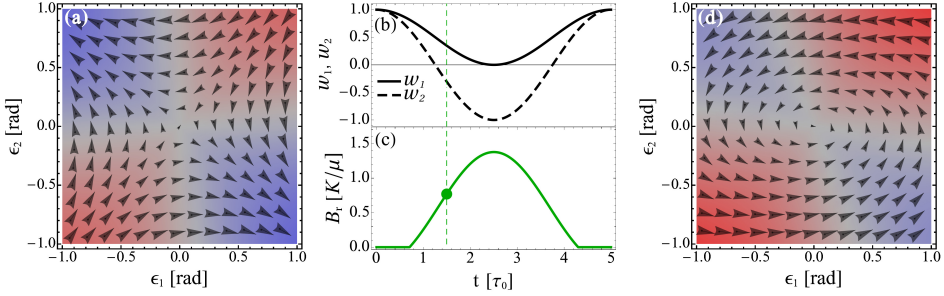


Figure 4.33: Similar to Figure 4.32, but for $w_1 > 0$ and $w_2 < 0$ and different value of B_r as shown in (c). The black arrows in Figures (a) and (d) show the distribution of the dynamics with the size of the arrows being proportional to the magnitude of the perturbation, and the colors in the background indicate if the amplitude of the perturbation is increasing (blue), decreasing (red), or constant (gray).

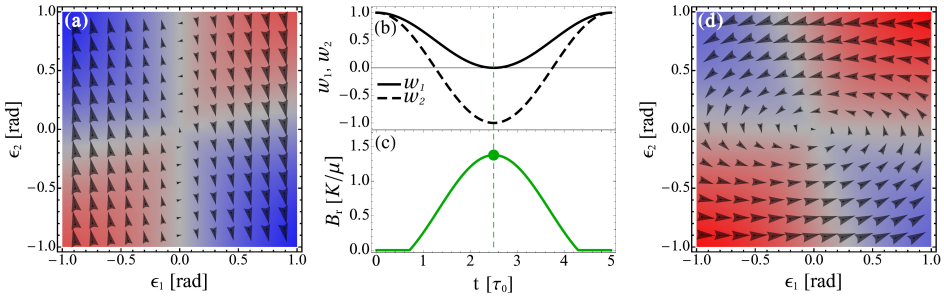


Figure 4.34: Similar to Figure 4.32, but for $w_1 = 0$ and $w_2 < 0$ and different value of B_r as shown in (c). The black arrows in Figures (a) and (d) show the distribution of the dynamics with the size of the arrows being proportional to the magnitude of the perturbation, and the colors in the background indicate if the amplitude of the perturbation is increasing (blue), decreasing (red), or constant (gray).

4 Applications

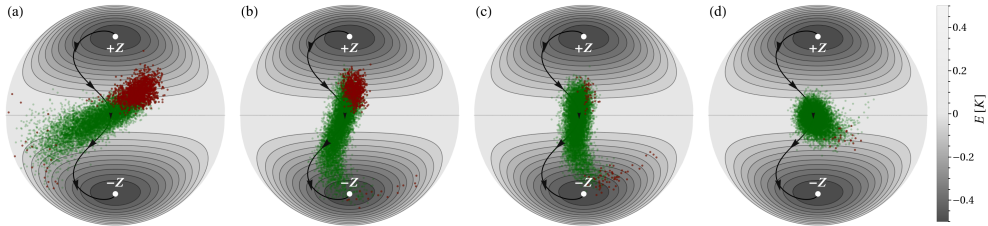


Figure 4.35: Calculated distribution of the copies of the system in the statistical ensemble at $t = T/2$ and various values of the longitudinal magnetic field, superimposed on the Lambert azimuthal projection [99] of the energy surface of the system. White points signify the energy minima at $\pm Z$. The black line shows the calculated reversal trajectory at zero temperature. The arrows along the black line demonstrate the velocity at different partitions of T , while the size of the arrows code the magnitude of the velocity. The copies of the ensemble that will eventually succeed and not succeed in the magnetization switching are marked with green and red points, respectively, and shown at $t = T/2$ without applying B_r (a) and with B_r for $\lambda = 1/\sqrt{2}$ (b), $\lambda = 0.85$ (c), and $\lambda = 0.95$ (d). The damping factor α is 0.2, the thermal stability factor Δ is 20, while the switching time T is $10\tau_0$.

Effect of the longitudinal field on the distribution of the copies of the system in the statistical ensemble

To gain insight into how B_r affects the distribution of ensemble copies, we present in Figures (4.35)(a)-(d) the distributions of successful and unsuccessful copies at $t = T/2$ for $\alpha = 0.2$, $T = 10\tau_0$, and $\Delta = 20$. These copies are superimposed on the Lambert projection of the energy surface of the macrospin, and their distributions are obtained both with and without applying B_r . In Fig.(4.35)(a), the results are obtained for $B_r = 0$, clearly showing that the copies are scattered around $\mathbf{m}_0(T/2)$. Overall, the cloud of successful and unsuccessful copies is separated, with the latter lagging behind $\mathbf{m}_0(T/2)$ and remaining close to the initial stable state. Interestingly, the addition of B_r for $\lambda = 1/\sqrt{2}$ and $\lambda = 0.85$, as shown in Figs.(4.35)(b)-(c), results in fewer scattered copies compared to the case with zero B_r . In contrast, for $\lambda = 0.95$, as depicted in Fig. (4.35)(d), the cloud of copies clusters around $\mathbf{m}_0(T/2)$. This occurs because, for such a high value of λ , the trajectories of the perturbations become elliptical with a high amplitude.

4.3 Enhancing thermal stability of optimal magnetization switching in a uniaxial nanoparticle

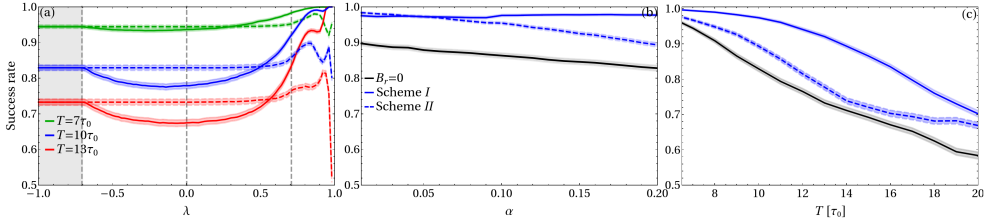


Figure 4.36: (a) Magnetization reversal success rate as a function of λ for damping $\alpha = 0.2$ and different values of the switching time T , as depicted in the legend. The solid and dashed lines are obtained with the corresponding B_r defined in scheme I and II, respectively. The gray shading area signifies the range of λ values at which B_r is zero for scheme I, while $B_r = 0$ for $\lambda \in (-1, 0]$ in scheme II. The vertical gray dashed lines mark the critical values of λ at $\lambda = 0$ and $\lambda = \pm 1/\sqrt{2}$. (b) Success rate as a function of damping α for $T = 10\tau_0$, where the black solid line shows the results for zero B_r , and the blue solid (dashed) line is obtained by applying B_r defined in scheme I (II) for $\lambda = 0.8$. (c) Success rate as a function of T for $\alpha = 0.2$ where the black, solid and dashed blue lines are the same as in (b). The thermal stability factor Δ is 20.

Effects of time-dependent radial pulse on the magnetization switching success rate

Here, the magnetization switching is induced by means of an optimal pulse. Then, we have considered a time-dependent radial field B_r based on scheme I and scheme II as detailed in Chapter 3. Figure 4.36 illustrates the outcome of applying a time-dependent radial field.

Figure (4.36)(a) shows the success rate as a function of λ for various values of the switching time T , while damping α is 0.2 and thermal stability factor Δ is 20. For the considered parameters, the success rate obtained using scheme I remains fixed for $\lambda \in [-1/\sqrt{2}, -1)$, as $B_r = 0$ within this range of λ values, see Eq. (3.12). However, B_r reduces to B_r^* for $\lambda \in (-1/\sqrt{2}, 0]$, resulting in a reduction of the success rate as B_r^* shifts the unstable eigenvalues towards the middle of the unstable region located in the quarter Q_2 shown in Fig. (3.4), where the trajectories of the perturbation are hyperbolic. As λ increases from 0 to $1/\sqrt{2}$, B_r^* transforms the saddle trajectories into straight ones, resulting in an increase in the success rate values. Further increasing the λ value beyond the critical one at $1/\sqrt{2}$ results in an increased success rate very close to 100%. In contrast, the results obtained using scheme II are qualitatively different than those for scheme I. In particular, B_r is always zero for $\lambda \in (-1, 0]$, see Eq. (3.12), thereby resulting in a fixed success rate. Also, the success rate can be enhanced for certain positive values of λ close to $1/\sqrt{2}$. Indeed, the success rate decreases significantly below its value at zero B_r as $\lambda \rightarrow 1$ since we have considered a large value of α . It is noteworthy that for relatively short switching time T and low values of damping α , scheme II can guarantee a success rate $\approx 100\%$ for high values of λ .

4 Applications

How the success rate depends on damping α for $T = 10\tau_0$ and $\Delta = 20$ is illustrated in Fig. (4.36)(b). Here the success rate is calculated for zero and nonzero B_r , obtained using scheme *I* and *II*, where the value of λ is 0.8. For zero B_r , the reduction in the success rate becomes more pronounced as α increases. This is because for high α values, the amplitude of the perturbation increases thereby resulting in instability against thermal fluctuations. However, the success rate can be significantly enhanced by applying B_r equipped with the proper value of λ , see the solid and dashed blue lines. The success rate shown with the blue solid line is slightly changed as α increases. This is because B_r shifts the eigenvalues equally and arranges them along a straight line defined by the angle η , hence, all shifted eigenvalues will have the same trajectory of the perturbation in the tangent space but with different perturbation amplitude depending on the value of both w_1/w_2 and α . In contrast, the success rate shown with the blue dashed line decreases as α increases since scheme *II* is unstable with respect to relaxation, as expected.

Fig. (4.36)(c) illustrates the success rate as a function of the switching time T for $\alpha = 0.2$ and $\Delta = 20$, calculated with and without B_r similar to Fig. (4.30)(b). The success rate is a monotonically decreasing function of T because for longer T values the thermal fluctuations can accumulate arbitrarily high thus giving rise to instability and reduction in the success rate.

Distribution of the successful and unsuccessful copies

The sudden decrease in the success rate shown in the main text, see Figure (4.36)(a), can be explained by the distribution of the copies of the ensemble during the magnetization switching. Figure (4.37) shows how the successful and unsuccessful copies of the ensemble evolve in time. Interestingly, the copies are precessing counter-clockwise about the black solid line due to the effect of the radial pulse B_r .

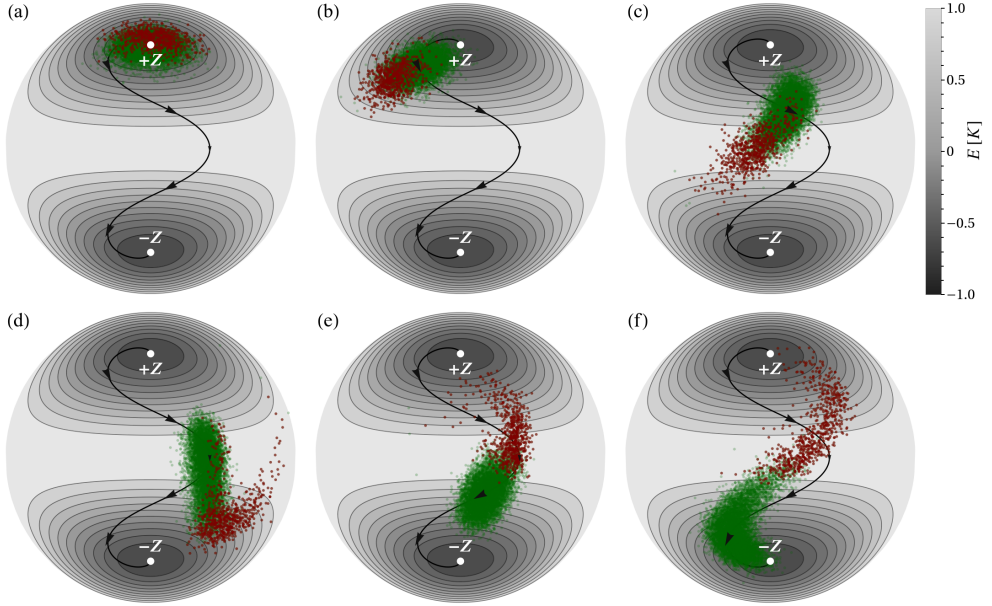


Figure 4.37: Lambert azimuthal equal-area projection of the energy surface of a macrospin with uniaxial anisotropy. The energy minima at $\pm Z$ are marked with the white points. Black line shows the calculated zero temperature reversal trajectory. The arrows along the black line show the velocity at $t = T/6$, $t = T/3$, $t = T/2$, $t = 2T/3$, and $t = 5T/6$, where the arrow size codes the magnitude of the velocity. The green cloud and red points show the distribution of the copies of the ensemble realized at a partition of the switching time T along OCP. The green cloud and red points signify the successful and unsuccessful copies, respectively. The radial component of the pulse B_r is included in the calculations with $\lambda = 0.88$. The damping factor α is 0.2, the thermal stability factor Δ is 20, while the switching time T is $13\tau_0$.

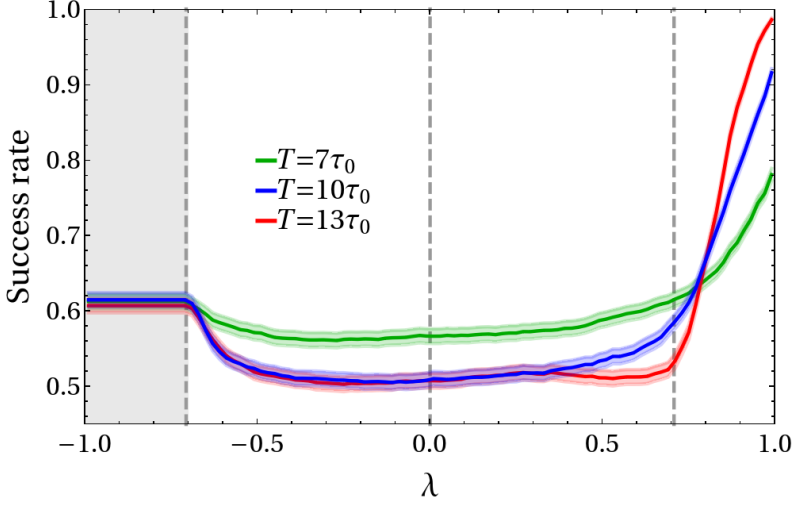


Figure 4.38: Magnetization reversal success rate as a function of λ for damping factor $\alpha = 0.2$ and different values of the switching time T , as depicted in the legend. The vertical gray dashed lines mark the critical values of λ at $\lambda = 0$ and $\lambda = \pm 1/\sqrt{2}$. The gray shading area signifies the range of λ values at which B_r is zero. The thermal stability factor Δ is 20.

Gaussian pulse of the external magnetic field

To confirm that the improvement in the success rate is associated with B_r rather than the choice of the external stimulus, we examine a non-optimal temporal pulse of the external magnetic field for inducing magnetization switching. The pulse can be described using a Gaussian function as follows:

$$\mathbf{B}(t) = B_0 \exp\left(-\frac{(t - t_p)^2}{2\sigma^2}\right) \hat{e}, \quad (4.38)$$

where B_0 is the amplitude of the pulse, t_p is the position of the maximum of the pulse, and σ is the Gaussian pulse width. The pulse is applied into a direction $\hat{e} = (\sin \theta \cos \varphi, \sin \theta \sin \varphi, \cos \theta)$ inclined by a polar angle θ with respect to the z direction and an azimuthal angle φ with respect to the x axis. Here, the results are obtained for $B_0 \approx 7.1[K/\mu]$, $t_p = 1.5\tau_0$, $\sigma = 0.7\tau_0$, $\theta = \pi/2$ and $\varphi = 0.027\pi$, where for such parameters and for $T = 10\tau_0$ and $\alpha = 0.2$ the ratio between the energy expended for generating the Gaussian pulse and the minimum switching cost Φ_m , see Eq. (12) in the main text, is ≈ 57.8 . Figure (4.38) shows that the success rate can be enhanced by applying B_r for $\lambda > 1/\sqrt{2}$ even though the driving pulse is non-optimal.

4.3 Enhancing thermal stability of optimal magnetization switching in a uniaxial nanoparticle

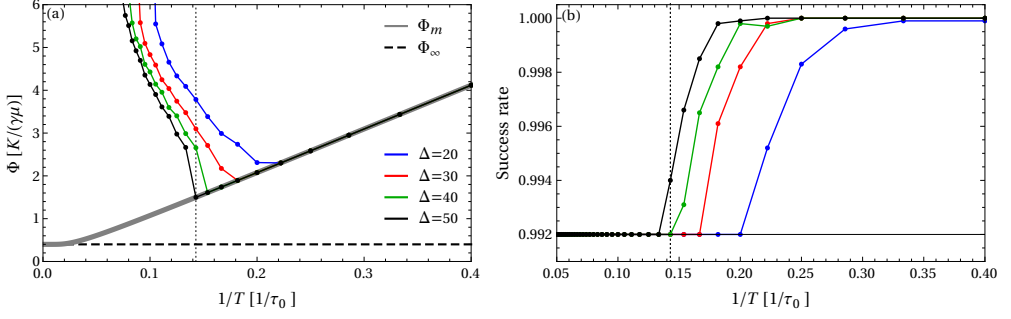


Figure 4.39: (a) Energy cost of magnetization switching as a function of the inverse of the switching time T for various values of the thermal stability factor Δ , as depicted in the legend. The gray solid line shows the minimum switching cost Φ_m [Eq. (4.22)], while the black dashed line is the infinite switching time asymptotic, $\Phi_\infty \equiv 2\alpha K/(\gamma\mu)$. The solid points deviating from Φ_m at specific T show the switching cost Φ at fixed success rate, 99.2%, as shown in (b). For instance, $\Phi|_{\Delta=50}$ coincides with (deviates from) Φ_m for $T \ll (\alpha + 1/\alpha)\tau_0$ ($T \gg (\alpha + 1/\alpha)\tau_0$) located to the right (left) of the black dotted line, where the success rate in this timescale is larger than 99.2% (fixed at 99.2%) without (with) applying B_r . The magnitude of the damping factor α is 0.2

Energy cost of magnetization switching We define the cost of the magnetization switching as follows (see Chapter 2):

$$\Phi = \int_0^T |\mathbf{B}(t)|^2 dt, \quad (4.39)$$

where T is the prescribed switching time and $\mathbf{B}(t) = \mathbf{B}^\perp(t) + B_r(t)\hat{e}_r$ is the external magnetic field at time t . Here $\mathbf{B}^\perp(t)$ and the corresponding minimum energy cost Φ_m are given by Eqs. 4.20 and Eq. 4.22, respectively, in the Supplemental material. The radial field $B_r(t)$ is defined through scheme *I* and *II*. In order to investigate how Φ depends on the inverse of the switching time T for a fixed success rate, we set a success rate goal \mathcal{P} below which B_r equipped with a proper amplitude is needed for fixing the success rate at \mathcal{P} . Hereafter, we set $\mathcal{P} = 99.2\%$.

Fig. (4.39)(a) shows the switching cost Φ as a function of the inverse of the switching time T for $\alpha = 0.2$ and various values of the thermal stability factor Δ . The gray solid line signifies Φ_m obtained for zero B_r , and approaching the infinite switching time asymptotic Φ_∞ for $T \gg (\alpha + 1/\alpha)\tau_0$. Indeed, for short switching time $T \ll (\alpha + 1/\alpha)\tau_0$, the switching cost Φ for the considered Δ values is equal to Φ_m thereby signifying that the optimal pulse $\mathbf{B}^\perp(t)$ is robust against thermal fluctuations and achieves success rate values higher than \mathcal{P} , as shown in Fig. (4.39)(b). However, as T increases beyond the short timescale, then B_r equipped with the proper amplitude is needed to guarantee a fixed success rate at \mathcal{P} . Thus, explaining the sudden deviation of Φ from Φ_m , i.e., $\Phi > \Phi_m$ for $B_r \neq 0$. Note that for high values of Δ , the condition $\Phi > \Phi_m$ is fulfilled for longer T , as expected.

5 Conclusions and outlook

This thesis presents the development of a theory aimed at energy-efficient manipulation of magnetic states using an external magnetic field. The foundation of this theory rests upon the postulate that the energy cost of a given magnetization change is a functional of the transition trajectory in the configuration space. Once the optimal trajectory for a given transition is determined, the desired control pulse can be systematically reconstructed. This reconstruction procedure is based on the requirement that the superposition of the sought-after pulse and the internal magnetic field defined by the system's Hamiltonian leads the system to advance precisely along the optimal switching path. This advancement also satisfies the equations of motion and terminates at a predefined switching time. Our approach consists of the following steps: first, selecting a magnetic Hamiltonian and identifying target magnetic states. We define the target magnetic states by locating minima on the energy surface of the system as a function of the orientation of the moments. Then, the optimal control paths minimizing the energy cost functional are calculated, followed by calculating the optimal control pulses.

An alternative approach worth considering involves utilizing a spin-polarized electric current \mathbf{J} as an external stimulus [26] rather than relying on an external magnetic field \mathbf{B} . Identifying an optimal mechanism to minimize $|\mathbf{J}|^2$ rather than $|\mathbf{B}|^2$ will closely parallel the one outlined in this thesis. However, it will necessitate the utilization of equations such as the Landau-Lifshitz-Gilbert-Slonchevsky equation and equations accounting for spin-orbit torque effects to compute electric current pulses. Moreover, the principle of Ohmic loss minimization can be applied to predict the optimal pulse of electric current for efficient control of the domain wall motion described by two collective coordinates in the spirit of the Thiele's equation [27]. To achieve a deeper understanding of the thermal reservoir's role in optimal control, temperature should be incorporated into the theory at a more fundamental level by modeling thermal effects by introducing stochastic forces into the equations of motion. Consequently, the position of the magnetic system within a specific region of configuration space will become a stochastic variable described by a particular probability distribution. As a result, the framework of optimal control can be applied to the probability density, and the objective will be to predict an external stimulus that guides the system to the desired target state with an acceptable probability and minimal energy expenditure. Reconstructing the control stimuli can be done such that the probability density evolves according to the Fokker-Planck equation.

Although the primary focus of this thesis is on the application of optimal control theory (OCT) to magnetic systems described by classical Hamiltonians, it is essential to highlight the potential extension of these concepts into the domain of quantum mechanics. This extension entails the utilization of the Schrödinger equation for describing quantum dynamics. For example, considering the laser electric field as the external stimulus for manipulating the isolated quantum system, the objective becomes to compute the optimal laser pulse. Here, optimality can be defined by the minimization of the fluence of the laser field required to excite a quantum system from its initial state to a predetermined quantum state within a specified target time frame. Thus, we can define a cost function to be proportional to the amplitude of the laser pulse squared, similar to the one defined in Chapter 2, where its minimization should be subject to a constraint imposed by the equation of motion defined by the Schrödinger equation. Such constrained optimization problem can be formulated as an unconstrained optimization through the introduction of a Lagrange multiplier or by means of the quadratic penalty function approach presented in Chapter 2. It is noteworthy that the OCT has been applied to quantum systems [100], especially in the field of Chemistry. An illustrative example of this is determining the optimal laser pulse necessary to selectively break a particular bond in a molecule [101]. Extending the OCT to open quantum systems presents significant challenges, primarily due to the necessity of incorporating the dynamics dictated by the stochastic Schrödinger equation for system evolution, and the need to treat the heat bath's influence in a quantum-mechanical framework. This requires careful consideration of the system's interaction with its environment using quantum bath approximations, e.g., Markovian or non-Markovian master equations.

As a final note, the OCT developed in Chapter 2 offers a versatile approach for energy-efficient control of magnetic states using pulses of an external magnetic field. This theory is applicable across various dimensions, including one-, two-, and three-dimensional magnetic systems. Examples could include 2D magnetic sheets [102], van der Waals interfaces [102], and magnetic twisted layers [103]. It is important to mention, however, that the complexity of computations increases significantly with the increase in system size and the number of images used in simulations. Thus, effective implementation and parallelization of the code are essential for broader applications of this theory. These applications could include exploring (i) *switching processes in magnetic nanostrips and nanowires, both with and without impurities*. Magnetic nanowires and nanostrips serve as convenient subjects for investigating the energy-efficient manipulation of domain walls. Their nanoscale dimensions introduce an interplay between short-range interactions, such as magnetic exchange, and long-range magnetostatic forces, resulting in a complex internal structure of the domain walls. The methodology developed in Chapter 2 provides a robust framework for exploring optimal mechanisms governing domain wall nucleation and propagation. This approach allows for an in-depth analysis of how these mechanisms and associated energy costs depend on the material parameters of the system. Furthermore, it enables the examination of the extent to which the velocity of the domain wall can be maximized for a given energy cost. An intriguing question is whether it is possible to surpass Walker's limit on the velocity [104]

by proper shaping of the pulse of the external magnetic field.; (ii) *energy-efficient nucleation, annihilation, and displacement of spin textures*. For example, optimal trajectories for skyrmion—localized, noncollinear spin textures arising in magnets of a certain class [105]—nucleation and annihilation and corresponding energy-efficient controls can be investigated as a function of magnetic interactions including exchange, Dzyaloshinskii-Moriya interaction and magnetic anisotropy. Moreover, for a given skyrmion speed, the control pulse of magnetic field can be optimized with respect to the expended energy. One known problem with the skyrmion motion by means of electric current is associated with gyrotropic force which deviates the skyrmion from the current direction. It will be interesting to see whether this effect can be bypassed by proper control pulse shaping; (iii) *vortex core reversal in magnetic nanodots*. A typical vortex displays four distinct stable states, characterized by its core polarity and vorticity. While previous studies have explored vortex core reversal processes [106], identifying the optimal mechanisms for transitioning between these states remains a compelling challenge. The methodology developed in Chapter 2 provides a tool to investigate how these transitions are influenced by factors such as switching time, damping, and the magnetic properties of the system; and (iv) *switching mechanisms in magnetic heterostructures*, among others.

6 Appendices

Appendix A: Velocity and force calculations

I. Velocity calculations

The configuration space of a magnetic system consisting of N interacting magnetic moments is a $2N$ -dimensional Riemannian manifold, \mathcal{R} . Such manifold is defined as a direct product of N two-dimensional unit spheres S_i^2 , i.e.,

$$\mathcal{R} = \prod_{i=1}^N S_i^2, \quad (6.1)$$

where S_i^2 signifies a two dimensional spherical surface associated with the i th magnetic moment vector \mathbf{m}_i . Calculating the velocity on such curved manifold requires taking into account its curvature. Therefore, the geodesic distance between $\mathbf{m}_{p+1} - \mathbf{m}_p$ images has been taken into account, see Eq. (2.30) in the main text. In particular, the velocity $\dot{\mathbf{m}}_{p+1/2,i}$ is approached via the finite difference approximation of the angular velocity, which is defined as the angle between $\mathbf{m}_{p+1} - \mathbf{m}_p$ (arc length), as shown in Figure. 2.2(b) in the main text, divided by $\Delta t = t_{p+1} - t_p$. In particular,

$$\dot{\mathbf{m}}_{p+\frac{1}{2},i} = \frac{\delta_p}{\Delta t} \frac{\mathbf{m}_{p+1,i} - \mathbf{m}_{p,i} - \mathbf{m}_{p+\frac{1}{2},i} \left[(\mathbf{m}_{p+1,i} - \mathbf{m}_{p,i}) \cdot \mathbf{m}_{p+\frac{1}{2},i} \right]}{\left| \mathbf{m}_{p+1,i} - \mathbf{m}_{p,i} - \mathbf{m}_{p+\frac{1}{2},i} \left[(\mathbf{m}_{p+1,i} - \mathbf{m}_{p,i}) \cdot \mathbf{m}_{p+\frac{1}{2},i} \right] \right|}, \quad (6.2)$$

where the midpoint $\mathbf{m}_{p+\frac{1}{2},i}$ as well as the angle δ_p between \mathbf{m}_p and \mathbf{m}_{p+1} are defined as

$$\mathbf{m}_{p+\frac{1}{2},i} = \frac{\mathbf{m}_{p+1,i} + \mathbf{m}_{p,i}}{|\mathbf{m}_{p+1,i} + \mathbf{m}_{p,i}|} \quad (6.3)$$

$$\delta_p = \arccos(\mathbf{m}_{p,i} \cdot \mathbf{m}_{p+1,i}). \quad (6.4)$$

However, one can simplify Eq. (6.2) as follows:

$$(\mathbf{m}_{p+1,i} - \mathbf{m}_{p,i}) \cdot \mathbf{m}_{p+\frac{1}{2}} = (\mathbf{m}_{p+1,i} - \mathbf{m}_{p,i}) \cdot \frac{\mathbf{m}_{p+1,i} + \mathbf{m}_{p,i}}{|\mathbf{m}_{p+1,i} + \mathbf{m}_{p,i}|} \quad (6.5)$$

$$(\mathbf{m}_{p+1,i} - \mathbf{m}_{p,i}) \cdot \frac{\mathbf{m}_{p+1,i} + \mathbf{m}_{p,i}}{|\mathbf{m}_{p+1,i} + \mathbf{m}_{p,i}|} = \frac{\mathbf{m}_{p+1,i}^2 - \mathbf{m}_{p,i}^2}{|\mathbf{m}_{p+1,i} + \mathbf{m}_{p,i}|} \quad (6.6)$$

$$\frac{\mathbf{m}_{p+1,i}^2 - \mathbf{m}_{p,i}^2}{|\mathbf{m}_{p+1,i} + \mathbf{m}_{p,i}|} = 0 \quad (6.7)$$

Therefore, the velocity at the midpoint defined by Eq. (6.2) reduces to

$$\dot{\mathbf{m}}_{p+\frac{1}{2},i} = \frac{\delta_p}{\Delta t} \frac{\mathbf{m}_{p+1,i} - \mathbf{m}_{p,i}}{|\mathbf{m}_{p+1,i} - \mathbf{m}_{p,i}|} \quad (6.8)$$

which is similar to Eq. (2.30) in the main text. It is noteworthy that if the angle between spins in two adjacent images approaches zero, then the denominator in Eq. (6.8) approaches zero as well which, in turn, results in singularity in the velocity calculations. Hence, a special treatment should be considered based on Taylor expansion.

It is worth mentioning that one could calculate the velocity using the Euclidean distance between images, however, we observe that our Eq. 6.8 requires fewer images to reach convergence in the optimal control path calculations because it takes into account the curvature of the configuration space of the system.

II. Force calculations

The sought-for the optimal control path minimizing the energy cost functional Φ is achieved by zeroing the force acting on the movable images. The force is defined as follows

$$\begin{aligned}\mathbf{F}_{q,j} &= -\frac{\partial\Phi[\mathcal{M}]}{\partial\mathbf{m}_{q,j}} \\ &= -\frac{\partial}{\partial\mathbf{m}_{q,j}} \left(\sum_{p=1}^Q \sum_{i=1}^N |\mathbf{B}_{p+\frac{1}{2},i}|^2 \Delta t \right)\end{aligned}\quad (6.9)$$

where $\Delta t = t_{p+1} - t_p$, and \mathbf{B}_i is given by Eq. (2.9) in the main text. The negative sign is introduced in order to follow the negative of the gradient of the functional during the optimization process. Note that the force here is not projected on the tangent of the configuration space. According to Eq. (2.9), $|\mathbf{B}_{p+\frac{1}{2},i}|^2$ is defined as

$$\begin{aligned}|\mathbf{B}_{p+\frac{1}{2},i}|^2 &= \frac{\alpha^2 + 1}{\gamma^2} |\dot{\mathbf{m}}_{p+\frac{1}{2},i}|^2 - \frac{2\alpha}{\gamma} \left(\dot{\mathbf{m}}_{p+\frac{1}{2},i} \cdot \mathbf{b}_{p+\frac{1}{2},i}^{\perp,eff} \right) \\ &\quad - \frac{2}{\gamma} \left(\mathbf{m}_{p+\frac{1}{2},i} \times \dot{\mathbf{m}}_{p+\frac{1}{2},i} \right) \cdot \mathbf{b}_{p+\frac{1}{2},i}^{\perp,eff} + |\mathbf{b}_{p+\frac{1}{2},i}^{\perp,eff}|^2,\end{aligned}\quad (6.10)$$

however, since $\mathbf{b}_{p+\frac{1}{2},i}^{\perp,eff} = \mathbf{b}_{p+\frac{1}{2},i}^{eff} - \mathbf{m}_{p+\frac{1}{2},i} \left(\mathbf{b}_{p+\frac{1}{2},i}^{eff} \cdot \mathbf{m}_{p+\frac{1}{2},i} \right)$, the following equations hold

$$\begin{aligned}\dot{\mathbf{m}}_{p+\frac{1}{2},i} \cdot \mathbf{b}_{p+\frac{1}{2},i}^{\perp,eff} &= \dot{\mathbf{m}}_{p+\frac{1}{2},i} \cdot \mathbf{b}_{p+\frac{1}{2},i}^{eff} \\ \left(\mathbf{m}_{p+\frac{1}{2},i} \times \dot{\mathbf{m}}_{p+\frac{1}{2},i} \right) \cdot \mathbf{b}_{p+\frac{1}{2},i}^{\perp,eff} &= \left(\mathbf{m}_{p+\frac{1}{2},i} \times \dot{\mathbf{m}}_{p+\frac{1}{2},i} \right) \cdot \mathbf{b}_{p+\frac{1}{2},i}^{eff} \\ |\mathbf{b}_{p+\frac{1}{2},i}^{\perp,eff}|^2 &= |\mathbf{b}_{p+\frac{1}{2},i}^{eff}|^2 - \left(\mathbf{b}_{p+\frac{1}{2},i}^{eff} \cdot \mathbf{m}_{p+\frac{1}{2},i} \right)^2.\end{aligned}\quad (6.11)$$

Thus, Eq. (6.10) can be written as follows

$$\begin{aligned}|\mathbf{B}_{p+\frac{1}{2},i}|^2 &= \frac{\alpha^2 + 1}{\gamma^2} |\dot{\mathbf{m}}_{p+\frac{1}{2},i}|^2 - \frac{2\alpha}{\gamma} \left(\dot{\mathbf{m}}_{p+\frac{1}{2},i} \cdot \mathbf{b}_{p+\frac{1}{2},i}^{eff} \right) \\ &\quad - \frac{2}{\gamma} \left(\mathbf{m}_{p+\frac{1}{2},i} \times \dot{\mathbf{m}}_{p+\frac{1}{2},i} \right) \cdot \mathbf{b}_{p+\frac{1}{2},i}^{eff} \\ &\quad + |\mathbf{b}_{p+\frac{1}{2},i}^{eff}|^2 - \left(\mathbf{b}_{p+\frac{1}{2},i}^{eff} \cdot \mathbf{m}_{p+\frac{1}{2},i} \right)^2.\end{aligned}\quad (6.12)$$

Now, our task is to calculate the variation of Φ with respect to the spin orientation, however, to make the derivation easier to read, we will divide the force into five parts

as follows

$$\begin{aligned}
\mathbf{F}_{q,j}^{(1)} &= -\frac{\alpha^2 + 1}{\gamma^2} \frac{\partial}{\partial \mathbf{m}_{q,j}} \sum_{p=1}^Q \sum_{i=1}^N |\dot{\mathbf{m}}_{p+\frac{1}{2},i}|^2 \Delta t, \\
\mathbf{F}_{q,j}^{(2)} &= \frac{2\alpha}{\gamma} \frac{\partial}{\partial \mathbf{m}_{q,j}} \sum_{p=1}^Q \sum_{i=1}^N \left(\dot{\mathbf{m}}_{p+\frac{1}{2},i} \cdot \mathbf{b}_{p+\frac{1}{2},i}^{eff} \right) \Delta t, \\
\mathbf{F}_{q,j}^{(3)} &= \frac{2}{\gamma} \frac{\partial}{\partial \mathbf{m}_{q,j}} \sum_{p=1}^Q \sum_{i=1}^N \left(\mathbf{m}_{p+\frac{1}{2},i} \times \dot{\mathbf{m}}_{p+\frac{1}{2},i} \right) \cdot \mathbf{b}_{p+\frac{1}{2},i}^{eff} \Delta t, \\
\mathbf{F}_{q,j}^{(4)} &= -\frac{\partial}{\partial \mathbf{m}_{q,j}} \sum_{p=1}^Q \sum_{i=1}^N |\mathbf{b}_{p+\frac{1}{2},i}^{eff}|^2 \Delta t, \\
\mathbf{F}_{q,j}^{(5)} &= \frac{\partial}{\partial \mathbf{m}_{q,j}} \sum_{p=1}^Q \sum_{i=1}^N \left(\mathbf{b}_{p+\frac{1}{2},i}^{eff} \cdot \mathbf{m}_{p+\frac{1}{2},i} \right)^2 \Delta t.
\end{aligned} \tag{6.13}$$

where $\mathbf{F}_{q,j} = \mathbf{F}_{q,j}^{(1)} + \mathbf{F}_{q,j}^{(2)} + \mathbf{F}_{q,j}^{(3)} + \mathbf{F}_{q,j}^{(4)} + \mathbf{F}_{q,j}^{(5)}$, and the upper scripts (1) ... (5) signify the term number.

Derivation of the first term: $\mathbf{F}_{q,j}^{(1)}$

The first term of the total force $\mathbf{F}_{q,j}$ is given by

$$\mathbf{F}_{q,j}^{(1)} = -\frac{\alpha^2 + 1}{\gamma^2} \frac{\partial}{\partial \mathbf{m}_{q,j}} \sum_{p=1}^Q \sum_{i=1}^N |\dot{\mathbf{m}}_{p+\frac{1}{2},i}|^2 \Delta t, \tag{6.14}$$

where

$$|\dot{\mathbf{m}}_{p+\frac{1}{2},i}|^2 = \frac{\arccos^2(\mathbf{m}_{p,i} \cdot \mathbf{m}_{p+1,i})}{\Delta t^2} \left(\frac{\mathbf{m}_{p+1,i} - \mathbf{m}_{p,i}}{|\mathbf{m}_{p+1,i} - \mathbf{m}_{p,i}|} \right)^2, \tag{6.15}$$

however, one can easily show that

$$\left(\frac{\mathbf{m}_{p+1,i} - \mathbf{m}_{p,i}}{|\mathbf{m}_{p+1,i} - \mathbf{m}_{p,i}|} \right)^2 = 1. \tag{6.16}$$

Therefore, Eq. (6.14) simplifies to

$$F_{q,j,\eta}^{(1)} = -\frac{\alpha^2 + 1}{\gamma^2} \frac{\partial}{\partial m_{q,j,\eta}} \sum_{p=1}^Q \sum_{i=1}^N \left[\frac{\arccos^2(m_{p,i,\xi} m_{p+1,i,\xi})}{\Delta t} \right], \tag{6.17}$$

where the Einstein summation convention over repeated indices is used, and the symbols $\eta, \xi = (x, y, z)$. After performing the derivative with respect to spin orientation,

one obtains the following formula for $F_{q,j,\eta}^{(1)}$:

$$F_{q,j,\eta}^{(1)} = \frac{\alpha^2 + 1}{\gamma^2} \sum_{p=1}^Q \sum_{i=1}^N \left(\frac{2 \arccos(m_{p,i,\lambda} m_{p+1,i,\lambda})}{\Delta t} \frac{m_{p,i,\xi} \delta_{qp+1} \delta_{ij} \delta_{\eta\xi} + m_{p+1,i,\xi} \delta_{qp} \delta_{ij} \delta_{\eta\xi}}{\sqrt{1 - (m_{p,i,\lambda} m_{p+1,i,\lambda})^2}} \right) \quad (6.18)$$

Derivation of the second term: $\mathbf{F}_{q,j}^{(2)}$

The second term of the total force $\mathbf{F}_{q,j}$ is given by

$$\mathbf{F}_{q,j}^{(2)} = \frac{2\alpha}{\gamma} \frac{\partial}{\partial \mathbf{m}_{q,j}} \sum_{p=1}^Q \sum_{i=1}^N \left(\dot{\mathbf{m}}_{p+\frac{1}{2},i} \cdot \mathbf{b}_{p+\frac{1}{2},i}^{eff} \right) \Delta t, \quad (6.19)$$

$$\begin{aligned} F_{q,j,\eta}^{(2)} &= \frac{2\alpha}{\gamma} \frac{\partial}{\partial m_{q,j,\eta}} \sum_{p=1}^Q \sum_{i=1}^N \left(\dot{m}_{p+\frac{1}{2},i,\beta} b_{p+\frac{1}{2},i,\beta}^{eff} \right) \Delta t, \\ &= \frac{2\alpha}{\gamma} \sum_{p=1}^Q \sum_{i=1}^N \left(\underbrace{\frac{\partial \dot{m}_{p+\frac{1}{2},i,\beta} b_{p+\frac{1}{2},i,\beta}^{eff}}{\partial m_{q,j,\eta}}}_{(F_{q,j,\eta}^{(2)})_{1st}} + \underbrace{\dot{m}_{p+\frac{1}{2},i,\beta} \frac{\partial b_{p+\frac{1}{2},i,\beta}^{eff}}{\partial m_{q,j,\eta}}}_{(F_{q,j,\eta}^{(2)})_{2nd}} \right) \Delta t \quad (6.20) \end{aligned}$$

where $\beta = (x, y, z)$. To simplify the following derivation, we will proceed by separately deriving both terms appearing in Eq. (6.20).

$$(F_{q,j,\eta}^{(2)})_{1st} = \frac{\partial \dot{m}_{p+\frac{1}{2},i,\beta} b_{p+\frac{1}{2},i,\beta}^{eff}}{\partial m_{q,j,\eta}} \quad (6.21)$$

then, after deriving the velocity we obtain

$$\begin{aligned} (F_{q,j,\eta}^{(2)})_{1st} &= \mathcal{A} \left[\frac{m_{p+1,i,\beta} - m_{p,i,\beta}}{\sqrt{(m_{p+1,i,\psi} - m_{p,i,\psi})(m_{p+1,i,\psi} - m_{p,i,\psi})}} \frac{-(\delta_{qp+1} \delta_{ij} m_{p,i,\eta} + \delta_{qp} \delta_{ij} m_{p+1,i,\eta})}{\sqrt{1 - (m_{p+1,i,\xi} m_{p,i,\xi})^2}} \right. \\ &\quad + \arccos(m_{p+1,i,\xi} m_{p,i,\xi}) \left(\frac{\delta_{qp+1} \delta_{ij} \delta_{\eta\beta} - \delta_{qp} \delta_{ij} \delta_{\eta\beta}}{\sqrt{(m_{p+1,i,\psi} - m_{p,i,\psi})(m_{p+1,i,\psi} - m_{p,i,\psi})}} \right. \\ &\quad \left. \left. - \frac{(m_{p+1,i,\beta} - m_{p,i,\beta})(m_{p+1,i,\eta} - m_{p,i,\eta})(\delta_{qp+1} \delta_{ij} - \delta_{qp} \delta_{ij})}{\left(\sqrt{(m_{p+1,i,\psi} - m_{p,i,\psi})(m_{p+1,i,\psi} - m_{p,i,\psi})} \right)^3} \right) \right] \quad (6.22) \end{aligned}$$

where $\psi = (x, y, z)$, and $\mathcal{A} = b_{p+\frac{1}{2},i,\beta}^{eff}/\Delta t$. The second part of Eq. (6.20) is given by

$$\begin{aligned} (F_{q,j,\eta}^{(2)})_{2^{nd}} &= \dot{m}_{p+\frac{1}{2},i,\beta} \frac{\partial b_{p+\frac{1}{2},i,\beta}^{eff}}{\partial m_{q,j,\eta}} \\ &= \dot{m}_{p+\frac{1}{2},i,\beta} \left(\frac{\partial b_{p+\frac{1}{2},i,\beta}^{eff}}{\partial m_{p+\frac{1}{2},r,\xi}} \frac{m_{p+\frac{1}{2},r,\xi}}{\partial m_{q,j,\eta}} \right) \end{aligned} \quad (6.23)$$

where $\frac{\partial b_{p+\frac{1}{2},i,\beta}^{eff}}{\partial m_{p+\frac{1}{2},r,\xi}}$ is the negative Hessian, i.e., the second derivative of the energy with respect to the spin orientation. Here, the matrix $\frac{\partial m_{p+\frac{1}{2},r,\xi}}{\partial m_{q,j,\eta}}$ is given by

$$\begin{aligned} \frac{\partial m_{p+\frac{1}{2},r,\xi}}{\partial m_{q,j,\eta}} &= \frac{\delta_{qp+1}\delta_{jr}\delta_{\eta\xi} + \delta_{qp}\delta_{jr}\delta_{\eta\xi}}{\sqrt{(m_{p+1,r,\xi} + m_{p,r,\xi})(m_{p+1,r,\xi} + m_{p,r,\xi})}} \\ &\quad - \frac{(m_{p+1,r,\xi} + m_{p,r,\xi})(m_{p+1,r,\eta} + m_{p,r,\eta})(\delta_{qp+1}\delta_{jr} + \delta_{qp}\delta_{jr})}{(\sqrt{(m_{p+1,r,\xi} + m_{p,r,\xi})(m_{p+1,r,\xi} + m_{p,r,\xi})})^3} \end{aligned} \quad (6.24)$$

Derivation of the third term: $\mathbf{F}_{q,j}^{(3)}$

The third term of the total force $\mathbf{F}_{q,j}$ is given by

$$\mathbf{F}_{q,j}^{(3)} = \frac{2}{\gamma} \frac{\partial}{\partial \mathbf{m}_{q,j}} \sum_{p=1}^Q \sum_{i=1}^N \left(\mathbf{m}_{p+\frac{1}{2},i} \times \dot{\mathbf{m}}_{p+\frac{1}{2},i} \right) \cdot \mathbf{b}_{p+\frac{1}{2},i}^{eff} \Delta t \quad (6.25)$$

the derivation of the above term can result in a large and complicated terms, therefore, in order to keep the terms in a more compact form a matrix notation will be used, as follows

$$\begin{aligned} \mathbf{F}_{q,j}^{(3)} &= \frac{2}{\gamma} \sum_{p=1}^Q \sum_{i=1}^N \left(\left[\nabla_{\mathbf{m}_{q,j}} \otimes \left(\mathbf{m}_{p+\frac{1}{2},i} \times \dot{\mathbf{m}}_{p+\frac{1}{2},i} \right) \right] \cdot \mathbf{b}_{p+\frac{1}{2},i}^{eff} \right. \\ &\quad \left. + \left(\mathbf{m}_{p+\frac{1}{2},i} \times \dot{\mathbf{m}}_{p+\frac{1}{2},i} \right) \cdot \nabla_{\mathbf{m}_{q,j}} \otimes \mathbf{b}_{p+\frac{1}{2},i}^{eff} \right) \Delta t \end{aligned} \quad (6.26)$$

where the dot notation appears in Eq. (6.26) represents a dot product over $\{x, y, z\}$ components, whereas the \otimes notation represents the outer product. The outer product can be defined by index notation as follows: $(\mathbf{U} \otimes \mathbf{V})_{\alpha\beta} = u_\alpha v_\beta$, where \mathbf{U} and \mathbf{V} are arbitrary vectors. Thus,

$$\begin{aligned} \nabla_{\mathbf{m}_{q,j}} &= \left[\frac{\partial}{\partial m_{q,j,x}}, \frac{\partial}{\partial m_{q,j,y}}, \frac{\partial}{\partial m_{q,j,z}} \right], \\ \nabla_{\mathbf{m}_{q,j}} \otimes \left(\mathbf{m}_{p+\frac{1}{2},i} \times \dot{\mathbf{m}}_{p+\frac{1}{2},i} \right) &= \left(\nabla_{\mathbf{m}_{q,j}} \otimes \mathbf{m}_{p+\frac{1}{2},i} \right) \times \dot{\mathbf{m}}_{p+\frac{1}{2},i} + \mathbf{m}_{p+\frac{1}{2},i} \times \left(\nabla_{\mathbf{m}_{q,j}} \otimes \dot{\mathbf{m}}_{p+\frac{1}{2},i} \right), \end{aligned} \quad (6.27)$$

$$\nabla_{\mathbf{m}_{q,j}} \otimes \mathbf{m}_{p+\frac{1}{2},i} = \begin{bmatrix} \frac{\partial m_{p+\frac{1}{2},i,x}}{\partial m_{q,j,x}} & \frac{\partial m_{p+\frac{1}{2},i,y}}{\partial m_{q,j,x}} & \frac{\partial m_{p+\frac{1}{2},i,x}}{\partial m_{q,j,x}} \\ \frac{\partial m_{p+\frac{1}{2},i,x}}{\partial m_{q,j,y}} & \frac{\partial m_{p+\frac{1}{2},i,y}}{\partial m_{q,j,y}} & \frac{\partial m_{p+\frac{1}{2},i,z}}{\partial m_{q,j,y}} \\ \frac{\partial m_{p+\frac{1}{2},i,x}}{\partial m_{q,j,z}} & \frac{\partial m_{p+\frac{1}{2},i,y}}{\partial m_{q,j,z}} & \frac{\partial m_{p+\frac{1}{2},i,z}}{\partial m_{q,j,z}} \end{bmatrix}, \quad (6.28)$$

$$\nabla_{\mathbf{m}_{q,j}} \otimes \dot{\mathbf{m}}_{p+\frac{1}{2},i} = \begin{bmatrix} \frac{\partial \dot{m}_{p+\frac{1}{2},i,x}}{\partial m_{q,j,x}} & \frac{\partial \dot{m}_{p+\frac{1}{2},i,y}}{\partial m_{q,j,x}} & \frac{\partial \dot{m}_{p+\frac{1}{2},i,x}}{\partial m_{q,j,x}} \\ \frac{\partial \dot{m}_{p+\frac{1}{2},i,x}}{\partial m_{q,j,y}} & \frac{\partial \dot{m}_{p+\frac{1}{2},i,y}}{\partial m_{q,j,y}} & \frac{\partial \dot{m}_{p+\frac{1}{2},i,z}}{\partial m_{q,j,y}} \\ \frac{\partial \dot{m}_{p+\frac{1}{2},i,x}}{\partial m_{q,j,z}} & \frac{\partial \dot{m}_{p+\frac{1}{2},i,y}}{\partial m_{q,j,z}} & \frac{\partial \dot{m}_{p+\frac{1}{2},i,z}}{\partial m_{q,j,z}} \end{bmatrix}. \quad (6.29)$$

Derivation of the fourth term: $\mathbf{F}_{q,j}^{(4)}$

The fourth term of the total force $\mathbf{F}_{q,j}$ is given by

$$\begin{aligned} \mathbf{F}_{q,j}^{(4)} &= -\frac{\partial}{\partial \mathbf{m}_{q,j}} \sum_{p=1}^Q \sum_{i=1}^N |\mathbf{b}_{p+\frac{1}{2},i}^{eff}|^2 \Delta t, \\ &= -2 \sum_{p=1}^Q \sum_{i=1}^N \mathbf{b}_{p+\frac{1}{2},i}^{eff} \cdot \nabla_{\mathbf{m}_{q,j}} \otimes \mathbf{b}_{p+\frac{1}{2},i}^{eff} \Delta t \end{aligned} \quad (6.30)$$

where

$$\nabla_{\mathbf{m}_{q,j}} \otimes \mathbf{b}_{p+\frac{1}{2},i}^{eff} = \frac{\partial b_{p+\frac{1}{2},i,\beta}^{eff}}{\partial m_{p+\frac{1}{2},r,\xi}} \frac{m_{p+\frac{1}{2},r,\xi}}{\partial m_{q,j,\eta}} \quad (6.31)$$

and the spin variation $\frac{m_{p+\frac{1}{2},r,\xi}}{\partial m_{q,j,\eta}}$ is given by Eq. (6.24).

Derivation of the fifth term: $\mathbf{F}_{q,j}^{(5)}$

The fifth term of the total force $\mathbf{F}_{q,j}$ is given by

$$\begin{aligned} \mathbf{F}_{q,j}^{(5)} &= \frac{\partial}{\partial \mathbf{m}_{q,j}} \sum_{p=1}^Q \sum_{i=1}^N \left(\mathbf{b}_{p+\frac{1}{2},i}^{eff} \cdot \mathbf{m}_{p+\frac{1}{2},i} \right)^2 \Delta t \\ &= 2 \sum_{p=1}^Q \sum_{i=1}^N \left(\mathbf{b}_{p+\frac{1}{2},i}^{eff} \cdot \mathbf{m}_{p+\frac{1}{2},i} \right) \nabla_{\mathbf{m}_{q,j}} \otimes \left(\mathbf{b}_{p+\frac{1}{2},i}^{eff} \cdot \mathbf{m}_{p+\frac{1}{2},i} \right) \Delta t, \end{aligned} \quad (6.32)$$

6 Appendices

where

$$\nabla_{\mathbf{m}_{q,j}} \otimes \left(\mathbf{b}_{p+\frac{1}{2},i}^{eff} \cdot \mathbf{m}_{p+\frac{1}{2},i} \right) = \left(\nabla_{\mathbf{m}_{q,j}} \otimes \mathbf{b}_{p+\frac{1}{2},i}^{eff} \right) \cdot \mathbf{m}_{p+\frac{1}{2},i} + \mathbf{b}_{p+\frac{1}{2},i}^{eff} \cdot \left(\nabla_{\mathbf{m}_{q,j}} \otimes \mathbf{m}_{p+\frac{1}{2},i} \right). \quad (6.33)$$

Appendix B: Testing FORTRAN implementation and the reproducibility of the calculated OCPs by directly solving LLG equation

I. Testing FORTRAN implementation

The numerical method described in Chapter 2 is illustrated with calculations of the OCP for the reversal of a single magnetic moment whose internal energy is defined by the anisotropy along z axis, see Sec. 4.1.1. The OCP between the energy minima at $m_z = \pm 1$ for such a magnetic system is obtained analytically in terms of elliptic functions, as shown in see Sec. 4.1.1, providing a benchmark for numerical calculations.

Analytical vs numerical forces

Finding the minimum of the cost functional Φ requires zeroing the force acting on the movable images, see Appendix A. However, to check if the implementation of the analytical forces defined in see Appendix A is correct, we compare their values with the numerical forces defined via the equation:

$$\nabla\Phi(\mathbf{S}) = \frac{\Phi(\mathbf{S} - 2\epsilon) - 8\Phi(\mathbf{S} - \epsilon) + 8\Phi(\mathbf{S} + \epsilon) - \Phi(\mathbf{S} + 2\epsilon)}{12\epsilon}, \quad (6.34)$$

where $\epsilon > 0$ signifies a small change in \mathbf{S} . Note that choosing ϵ to be too small can cause problems. In particular, Eq. (6.34) is composed of two errors: the first is the theoretical error due to the discretization scheme, and the second is caused by the roundoff error connected with floating point numbers. Thus, one has to be careful when choosing the value of ϵ .

We have found that the absolute error between the analytical and numerical forces for a 3D magnetic system consisting of N interacting magnetic moments, whose energy is given by Eq. 1.1, with complete random orientations is within the order of 10^{-12} . Thus, guaranteeing that my implementation is correct.

Once we have ensured the accurate implementation of the analytical forces, evaluating the minimizer's implementation becomes a matter of straightforwardly contrasting the

analytical and numerical OCPs for the uniaxial nanoparticle. This is discussed in the following.

Analytical vs numerical OCPs and optimal field pulses

The numerical OCP calculations were considered converged when the magnitude of the gradient of Φ had dropped by twelve orders of magnitude. We compare the analytical and numerical OCPs and optimal pulses for the cases (i) $\alpha = 0$, $T \ll \tau_0$ and $T \gg \tau_0$; (ii) $\alpha \neq 0$, $T \ll \tau_0$ and $T \gg \tau_0$, as shown in Figures 6.1-6.4. Agreement between the analytical and numerical results is better for larger number of images, as expected.

Order of accuracy

The order of accuracy is a measure of how quickly the error between the numerical and the exact (analytical) values of the minimum energy cost functional Φ_m decreases as the step size is reduced. Since we have used the midpoint discretization scheme in Chapter 2, the order of accuracy is expected to be quadratic. To confirm this, we calculate the error in Φ_m for the uniaxial nanoparticle case. In particular, we calculate the absolute value of the error $\Phi_m^{Anl} - \Phi_m^{Num}$ as a function of the step size $\Delta t = T/Q$ with T and Q being the switching time and number of movable images, respectively. The results are plotted on a log-log scale, where the slope of the line fitting the data defines the order of accuracy. Such results are shown in Figure 6.5.

II. Testing reproducibility of the calculated OCPs

In this thesis, the dynamical equations defined by the LLG are solved inversely with respect to the external magnetic field, given the total time of the switching and the Hamiltonian of the magnetic system. Thus, the problem of determining the optimal path for magnetization reversal becomes an Euler-Lagrange problem with constraints. After obtaining the optimal trajectory, one can directly obtain the optimal pulse.

Nevertheless, we show that the derived optimal pulses can indeed induce the same net of magnetization change by directly solving the LLG equation. In other words, the LLG equations equipped with the optimal pulse will be solved numerically, and the resultant trajectory will be compared with the OCPs. An illustrative example of such a test is presented in Figures 6.6-6.8 describing the OCPs and optimal pulse for the magnetization reversal of a biaxial nanoparticle.

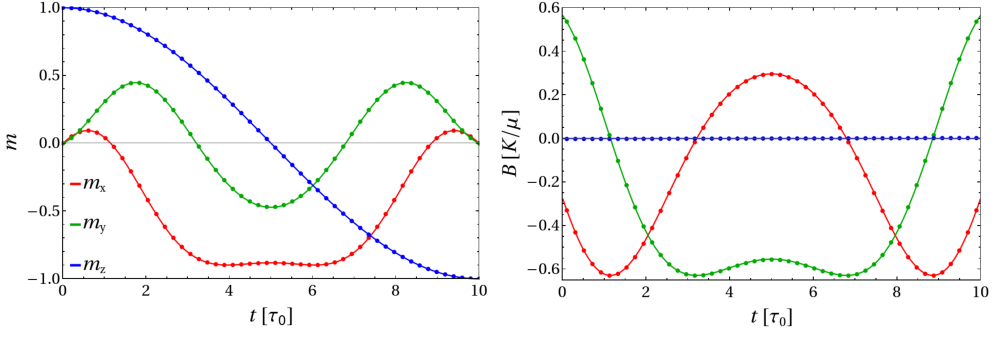


Figure 6.1: Evolution of the magnetic moment \mathbf{m} along the OCP for switching time $T = 10\tau_0$ and damping parameter $\alpha = 0$, and the corresponding optimal pulse \mathbf{B} derived from the calculated OCP. Analytical solution is given by solid lines, position of images included in the numerical calculations is shown with points. $Q = 50$ number of movable images were used in the numerical OCP calculations.

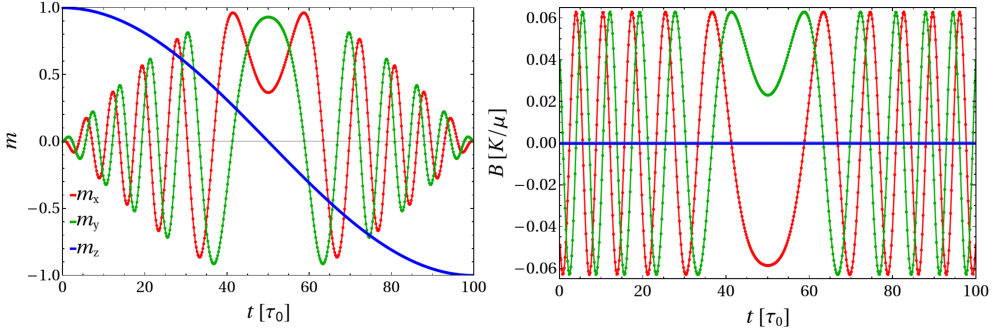


Figure 6.2: Similar to Figure 6.1 but for switching time $T = 100\tau_0$ and $Q = 500$ movable images.

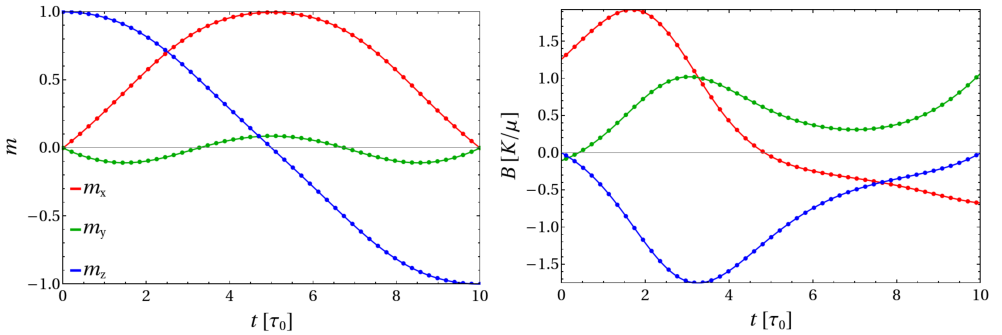


Figure 6.3: Similar to Figure 6.1 but for switching time $T = 10\tau_0$, damping parameter $\alpha = 2.0$ and $Q = 50$ movable images.

6 Appendices

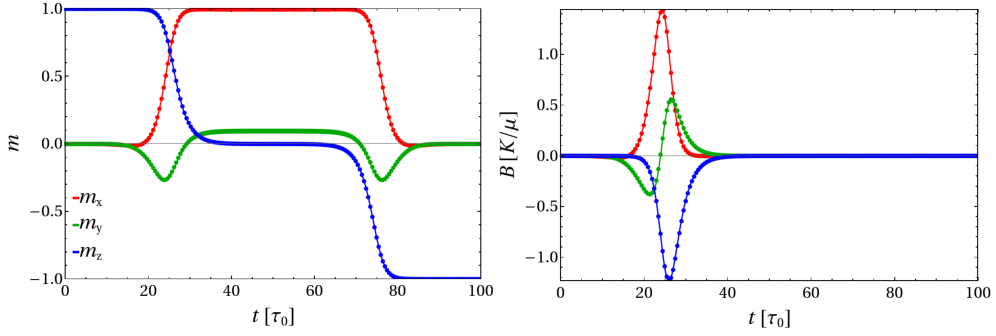


Figure 6.4: Similar to Figure 6.1 but for switching time $T = 100\tau_0$, damping parameter $\alpha = 2.0$ and $Q = 100$ movable images.

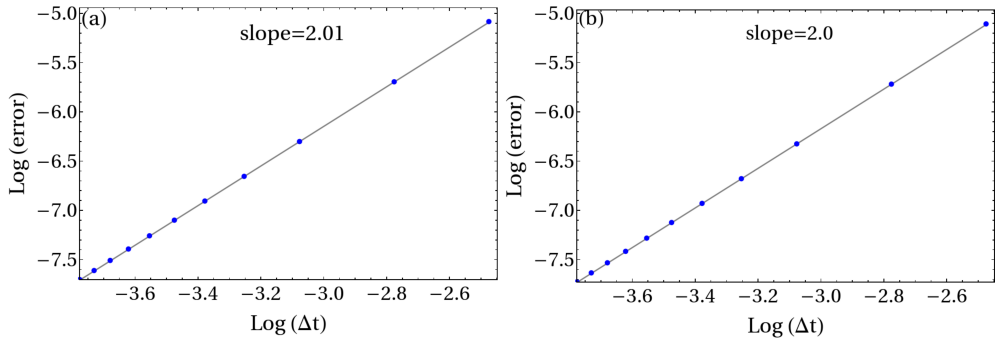


Figure 6.5: Log-log plot of the error as a function of the step size Δt . The magnitude of the damping parameter $\alpha = 0$ (a) $\alpha = 0.2$ (b). The switching time T is $10\tau_0$. The gray line on the graph represents a fitted line with a slope as shown in the legend.

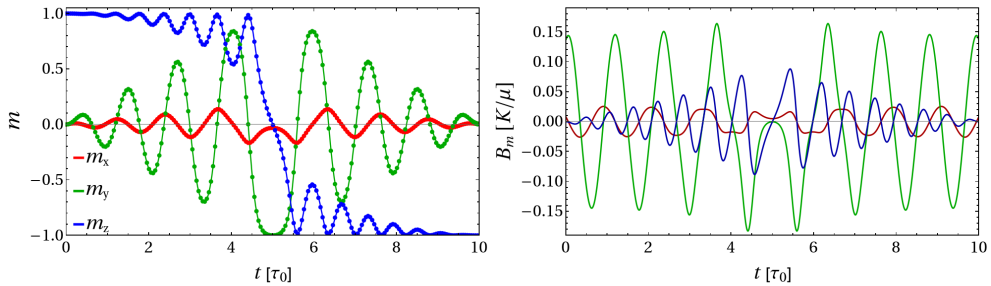


Figure 6.6: Evolution of the magnetic moment \mathbf{m} along the OCP (trajectory obtained by directly solving LLG) is shown with data points (solid lines). The optimal pulse \mathbf{B} is derived from the calculated OCP. The switching time $T = 10\tau_0$ and damping parameter $\alpha = 0.0$. The dimensionless parameter ξ determining the magnitude of the hard axis anisotropy is 30.

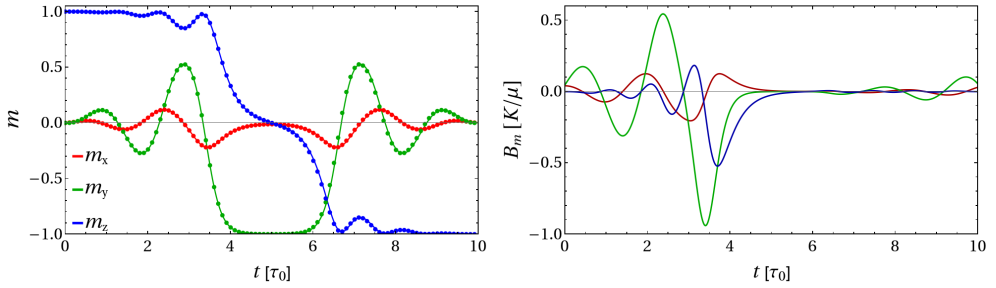


Figure 6.7: Similar to Figure 6.6 but for damping $\alpha = 0.01$ and $\xi = 10$.

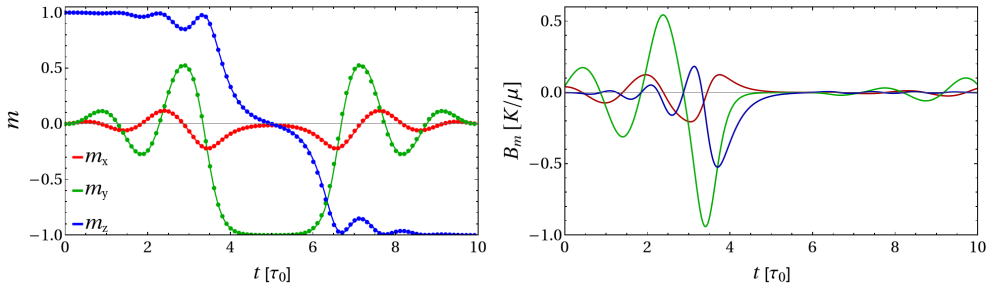


Figure 6.8: Similar to Figure 6.6 but for damping $\alpha = 0.1$ and $\xi = 10$.

Appendix C: The stochastic Landau-Lifshitz-Gilbert equation

Thermal fluctuation can be taken into account by adding a random field to the deterministic effective field in the zero-temperature LLG equation, see Eq. (1.7). This leads to the stochastic LLG (sLLG) equation for the magnetic moments motion [65, 96, 107]

$$(1 + \alpha^2) \frac{d\mathbf{m}_i}{dt} = -\gamma \mathbf{m}_i \times (\mathbf{B}_i^{\text{eff}} + \mathbf{B}_i^{rd}) - \alpha \gamma \mathbf{m}_i \times [\mathbf{m}_i \times (\mathbf{B}_i^{\text{eff}} + \mathbf{B}_i^{rd})], \quad (6.35)$$

which can be classified as a Langevin equation because of the stochastic field. The fluctuating fields \mathbf{B}_i^{rd} appearing in Eq. (6.35) couples multiplicatively to the time-dependent magnetization. Moreover, the fluctuating fields can be described using the Gaussian distribution thanks to the central limit theorem. We assume that the fluctuating fields have the following properties: (i) \mathbf{B}_i^{rd} are rotationally invariant and do not favor any direction, i.e., the mean value of the distribution must vanish; (ii) the Cartesian components of \mathbf{B}_i^{rd} are δ correlated in space and time. This can mathematically be formulated as follows:

$$\begin{aligned} \langle \mathbf{B}_i^{rd}(t) \rangle &= 0, \\ \langle \mathbf{B}_{\xi,i}^{rd}(t) \mathbf{B}_{\psi,j}^{rd}(t+\tau) \rangle &= 2D \delta(\tau) \delta_{ij} \delta_{\xi\psi}, \end{aligned} \quad (6.36)$$

with $\langle . \rangle$ being the ensemble averages, i, j are the magnetic moment indices, and $\xi, \psi = x, y, z$. The fluctuating field $\mathbf{B}_{\xi,i}^{rd}(t)$ and $\mathbf{B}_{\psi,j}^{rd}(t+\tau)$ are correlated only for time interval τ shorter than the time required for an appreciable change in the magnetic moment. The strength of the fluctuation D calculated using the fluctuation-dissipation theorem is proportional to the system temperature \mathcal{T} , and depends on the gyromagnetic ratio and damping parameter α [96]:

$$D = \frac{\alpha}{(1 + \alpha^2)} \frac{k_B \mathcal{T}}{\gamma}, \quad (6.37)$$

with k_B being the Boltzman factor.

Note that the fluctuating field \mathbf{B}_i^{rd} is called white-noise since field has a power spectrum completely independent of frequency. In particular, the power spectrum $S(w)$ of the random process with w being the frequency, can be calculated by means of the Fourier

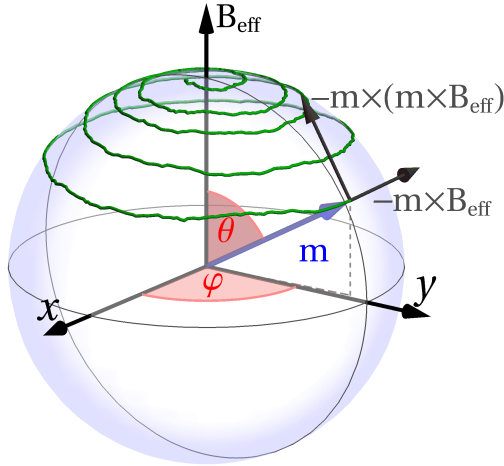


Figure 6.9: Dynamics of a magnetic moment \mathbf{m} induced by an effective magnetic field \mathbf{B}^{eff} under the effects of thermal fluctuations. The green line shows the calculated trajectory described by the stochastic Landau-Lifshitz-Gilbert equation, see Eq. (6.35). The black arrows in the tangent space show the precessional torque $-\mathbf{m} \times \mathbf{B}^{\text{eff}}$ and the damping torque $-\mathbf{m} \times (\mathbf{m} \times \mathbf{B}^{\text{eff}})$. The orientation of the magnetic moment is described by the polar angle θ and an azimuthal angle φ . The effective field \mathbf{B}^{eff} is pointing along z direction.

transform of the autocorrelation function $f(t') = \langle \mathbf{B}_{\xi,i}^{rd}(t) \mathbf{B}_{\psi,j}^{rd}(t + \tau) \rangle$:

$$S(w) = \int_{-\infty}^{\infty} f(t') \exp(iwt') dt' = 2D. \quad (6.38)$$

Figure. (6.9) shows the effect of thermal fluctuation on the damped precessional motion of a single-domain particle. The particle is exerted to deterministic precessional and damping torques as well as stochastic one causing the non-smooth behavior of the reversal trajectory compared to that in Fig. (1.1).

The dimensionless form of stochastic Landau-Lifshitz-Gilbert equation

The terms on the left- and right-hand side of the sLLG equation, see Eq. (6.35), are in units of joules per Tesla — when using the **SI** system. However, it is more convenient to work with dimensionless sLLG equation. This can be done, for example, by introducing a magnetic reference field strength B_0 to define the dimensionless magnetic fields \mathbf{B}_i and \mathbf{b}_i through $\mathbf{B}_i = \mathbf{B}_i^{\text{eff}}/B_0$ and $\mathbf{b}_i = \mathbf{B}_i^{rd}/B_0$. Note that the magnitude of the reference magnetic field B_0 is arbitrary. Also, a dimensionless time $t' = \gamma B_0 t / (1 + \alpha^2)$ needs to be introduced. In the following, we drop the prime on t' so that t denotes dimensionless time, and by dividing the dimensional sLLG equation by γB_0 we obtain

a dimensionless sLLG equation [97]

$$\frac{d\mathbf{m}_i}{dt} = -\mathbf{m}_i \times (\mathbf{B}_i(\mathcal{M}) + \mathbf{b}) - \alpha \mathbf{m}_i \times [\mathbf{m}_i \times (\mathbf{B}_i(\mathcal{M}) + \mathbf{b}_i)], i = 1, \dots, N \quad (6.39)$$

where N is the number of magnetic moments, $\mathbf{m}_i = (m_i^x, m_i^y, m_i^z)^T$ are unitary three-dimensional vectors, and $\mathcal{M} = (\mathbf{m}_1^T, \dots, \mathbf{m}_N^T)^T$ are $3N$ -dimensional column vector formed by the \mathbf{m}_i , also $\mathbf{B}_i = (B_i^x, B_i^y, B_i^z)^T$ and $\mathbf{b}_i = (b_i^x, b_i^y, b_i^z)$ are the effective and stochastic magnetic fields.

Since our motivation is to formulate the integrator for the sLLG equation, it is convenient to rewrite Eq. (6.39) in its differential form [108]

$$d\mathbf{m}_i = -\mathbf{m}_i \times (\mathbf{B}_i(\mathcal{M}) + \mathbf{b}) dt - \alpha \mathbf{m}_i \times [\mathbf{m}_i \times (\mathbf{B}_i(\mathcal{M}) + \mathbf{b}_i)] dt, \quad (6.40)$$

which can be written in a more compact form as follows

$$d\mathbf{m}_i = \mathbf{m}_i \times a_i(\mathcal{M})dt + \mathbf{m}_i \times \sigma(\mathbf{m}_i) \circ d\mathcal{W}^i(t), \quad (6.41)$$

where $d\mathcal{W}^i = \mathbf{b}_i dt$ is the differential of the Wiener process, the symbol " \circ " signifies that the corresponding stochastic integral is interpreted in the Stratonovich sense [108], and $a_i(\mathcal{M})$, $\mathcal{M} \in \mathbb{R}^{3N}$ signifies the drift deterministic three-dimensional column-vectors and defined by

$$a_i(\mathcal{M}) = -\mathbf{B}_i(\mathcal{M}) - \alpha \mathbf{m}_i \times \mathbf{B}_i(\mathcal{M}), \quad (6.42)$$

and $\sigma(\mathbf{m}_i)$, $\mathbf{m}_i \in \mathbb{R}^3$ is a 3×3 diffusion matrix such that

$$\sigma(\mathbf{m}_i)\xi = -\sqrt{2D'}\xi - \alpha\sqrt{2D'}\mathbf{m}_i \times \xi, \quad (6.43)$$

where $\xi \in \mathbb{R}^3$ are Gaussian random numbers with zero mean and unity variance, and D' is the dimensionless form the strength of the stochastic field D , see Eq. (6.37), which can be defined by [97]

$$D' = \frac{\alpha}{(1 + \alpha^2)} \frac{k_B \mathcal{T}}{B_0} \quad (6.44)$$

Numerical integration of the sLLG

Here, the stochastic LLG equation in its dimensionless form, see Eq. (6.39), is integrated using the semi-implicit scheme B (SIB) proposed by Mentink [97]. The approximate solution to the sLLG equation at discrete partition t_p of the simulated time interval $[0, T]$ such that $0 = t_0 < t_1 < \dots < t_Q = T$ is denoted as \mathbf{m}_p^i with $\mathbf{m}_p^i = \mathbf{m}^i(t_p)$. For simplicity, the partition has a regular spacing, i.e., $t_{p+1} - t_p = \Delta t = T/Q$, $p = 1, \dots, Q$, with Q being number of steps.

The SIB method uses a predictor-corrector scheme. The predictor step \mathcal{X}_p^i with $\mathcal{X}_p^i = \mathcal{X}^i(t_p)$ employs the implicit midpoint scheme to preserve the magnetic moments length, which is defined as

$$\mathcal{X}_p^i = \mathbf{m}_p^i + \Delta t \frac{\mathbf{m}_p^i + \mathcal{X}_p^i}{2} \times a_i(\mathcal{M}_p) + \sqrt{\Delta t} \frac{\mathbf{m}_p^i + \mathcal{X}_p^i}{2} \times \sigma(\mathbf{m}_p^i) \xi_{p+1}^{i,j}, \quad (6.45)$$

where $\xi_{p+1}^{i,j}$ are independent identically random variables with $i = 1, \dots, N, j = 1, 2, 3$. Note that SIB can diverge for the case that $\xi_{p+1}^{i,j} \sim \mathcal{N}(0, 1)$ is used as a random variable [97], where $\mathcal{N}(0, 1)$ signifies a Gaussian random variable with zero mean and unit variance. A possible way to solve this issue is to cut off the tail of the Gaussian distributed random variable by letting $\xi_{p+1}^{i,j}$ be distributed as an auxiliary variable ξ_h defined by

$$\xi_h = \begin{cases} \eta, & |\eta| \leq \mathcal{A}_h \\ \mathcal{A}_h, & \eta > \mathcal{A}_h \\ -\mathcal{A}_h, & \eta < -\mathcal{A}_h \end{cases} \quad (6.46)$$

where $\mathcal{A}_h = \sqrt{2|\ln \Delta t|}$ and $\eta \sim \mathcal{N}(0, 1)$ [97, 109].

One can notice that \mathcal{X}_p^i in Eq. (6.45) appears on both sides of the equation. A possible way to solve such an implicit equation is as follows:

$$\mathcal{X}_p^i = \mathbf{m}_p^i + (\mathbf{m}_p^i + \mathcal{X}_p^i) \times \mathcal{G}_p(\mathcal{M}_p), \quad (6.47)$$

where

$$\mathcal{G}(\mathcal{M}_p) = \frac{\Delta t}{2} a_i(\mathcal{M}_p) + \frac{\sqrt{\Delta t}}{2} \times \sigma(\mathbf{m}_p^i) \xi_{p+1}^{i,j}, \quad (6.48)$$

by taking dot product and cross product of both sides of Eq. (6.47) with respect to $\mathcal{G}(\mathcal{M}_p)$ results in

$$\begin{aligned} \mathcal{X}_p^i \cdot \mathcal{G}(\mathcal{M}_p) &= \mathbf{m}_p^i \cdot \mathcal{G}(\mathcal{M}_p), \\ \mathcal{G}(\mathcal{M}_p) \times \mathcal{X}_p^i &= \mathcal{G}(\mathcal{M}_p) \times \mathbf{m}_p^i + \mathbf{m}_p^i [\mathcal{G}(\mathcal{M}_p) \cdot \mathcal{G}(\mathcal{M}_p)] \\ &\quad - 2\mathcal{G}(\mathcal{M}_p) [\mathcal{G}(\mathcal{M}_p) \cdot \mathbf{m}_p^i] + \mathcal{X}_p^i [\mathcal{G}(\mathcal{M}_p) \cdot \mathcal{G}(\mathcal{M}_p)]. \end{aligned} \quad (6.49)$$

Thus, upon substituting Eq. (6.49) into Eq. (6.47), one can easily obtain the explicit formula for \mathcal{X}_p^i

$$\mathcal{X}_p^i = \frac{\mathbf{m}_p^i [1 - \mathcal{G}(\mathcal{M}_p) \cdot \mathcal{G}(\mathcal{M}_p)] + 2\mathbf{m}_p^i \times \mathcal{G}(\mathcal{M}_p) + 2\mathcal{G}(\mathcal{M}_p) [\mathcal{G}(\mathcal{M}_p) \cdot \mathbf{m}_p^i]}{1 + [\mathcal{G}(\mathcal{M}_p) \cdot \mathcal{G}(\mathcal{M}_p)]}. \quad (6.50)$$

The corrector step in the SIB solver is defined as

$$\mathbf{m}_{p+1}^i = \mathbf{m}_p^i + \Delta t \frac{\mathbf{m}_p^i + \mathbf{m}_{p+1}^i}{2} \times a_i\left(\frac{\mathcal{M}_p + \bar{\mathcal{X}}_p}{2}\right) + \sqrt{\Delta t} \frac{\mathbf{m}_p^i + \mathbf{m}_{p+1}^i}{2} \times \sigma\left(\frac{\mathbf{m}_p^i + \mathcal{X}_p^i}{2}\right) \xi_{p+1}^{i,j}, \quad (6.51)$$

where $\overline{\mathcal{X}}_p = \{\mathcal{X}_p^1, \dots, \mathcal{X}_p^N\}$. It is noteworthy that the predictor \mathcal{X}_p^i has to be calculated first for all magnetic moments before the corrected step \mathbf{m}_{p+1}^i is computed. Moreover, the magnetic effective field should be simultaneously updated after calculating \mathcal{X}_p^i before calculating \mathbf{m}_{p+1}^i .

For completeness, one can easily prove that the SIB method preserves the length of individual magnetic moments irrespective of the Δt when evolving the magnetic system over time $t_p \rightarrow t_{p+1}$. This property can be proven simply by showing that the difference $\mathbf{m}_{p+1}^i - \mathbf{m}_p^i$ is always perpendicular to $\mathbf{m}_{p+1}^i + \mathbf{m}_p^i$ (for simplicity, we will consider the zero-temperature case): from Eq. (6.51) it follows that

$$\mathbf{m}_{p+1}^i - \mathbf{m}_p^i = \frac{\Delta t}{2} \left[(\mathbf{m}_p^i + \mathbf{m}_{p+1}^i) \times a_i \left(\frac{\mathcal{M}_p + \overline{\mathcal{X}}_p}{2} \right) \right], \quad (6.52)$$

by multiplying both sides of the above equation with $\mathbf{m}_{p+1}^i + \mathbf{m}_p^i$ and cycling the factors in the scalar triple product, one obtains

$$|\mathbf{m}_{p+1}^i|^2 - |\mathbf{m}_p^i|^2 = \frac{\Delta t}{2} a_i \left(\frac{\mathcal{M}_p + \overline{\mathcal{X}}_p}{2} \right) \cdot [(\mathbf{m}_p^i + \mathbf{m}_{p+1}^i) \times (\mathbf{m}_{p+1}^i + \mathbf{m}_p^i)] = 0, \quad (6.53)$$

which shows that $|\mathbf{m}_{p+1}^i|^2 = |\mathbf{m}_p^i|^2$ when evolving the system over time $t_p \rightarrow t_{p+1}$.

Appendix D: Magnetization dynamics under constant magnetic field vs time-dependent magnetic field

Here we show that the magnetization dynamics at zero temperature and non-zero damping α under the effects of time-dependent external magnetic field is qualitatively different from that in a constant field. Let $w(\mathbf{m}, \mathbf{B}_{\text{ext}})$ be the magnetic energy density function, then the energy change rate $dw(\mathbf{m}, \mathbf{B}_{\text{ext}})/dt$ can be calculated as follows

$$\begin{aligned} \frac{dw}{dt} &= \frac{\partial w}{\partial \mathbf{m}} \cdot \frac{d\mathbf{m}}{dt} + \frac{\partial w}{\partial \mathbf{B}_{\text{ext}}} \cdot \frac{d\mathbf{B}_{\text{ext}}}{dt}, \\ &= -\mu_0 \mathbf{B}^{\text{eff}} \cdot \frac{d\mathbf{m}}{dt} - \mu_0 \mathbf{m} \cdot \frac{d\mathbf{B}_{\text{ext}}}{dt}, \end{aligned} \quad (6.54)$$

where $\frac{\partial w}{\partial \mathbf{m}} = -\mu_0 \mathbf{B}^{\text{eff}}$ and $\frac{\partial w}{\partial \mathbf{B}_{\text{ext}}} = -\mu_0 \mathbf{m}$. Taking into account that $\frac{d\mathbf{m}}{dt}$ is defined by the LLG equation, see Eq. (1.7), resulting in

$$\mathbf{B}^{\text{eff}} \cdot \frac{d\mathbf{m}}{dt} = -\frac{\alpha\gamma}{1+\alpha^2} \left[(\mathbf{m} \cdot \mathbf{B}^{\text{eff}})^2 - |\mathbf{B}^{\text{eff}}|^2 \right]. \quad (6.55)$$

Upon substituting Eq. (6.55) into Eq. (6.54) and using the relationship $(\mathbf{A} \times \mathbf{B})^2 = |\mathbf{A}|^2 |\mathbf{B}|^2 - (\mathbf{A} \cdot \mathbf{B})^2$, one can obtain the following expression for the energy change rate

$$\frac{dw}{dt} = -\mu_0 \left(\frac{\alpha\gamma}{1+\alpha^2} (\mathbf{m} \times \mathbf{B}^{\text{eff}})^2 + \mathbf{m} \cdot \frac{d\mathbf{B}_{\text{ext}}}{dt} \right), \quad (6.56)$$

where for the case of constant applied external magnetic field and the fact that $\gamma (\mathbf{m} \times \mathbf{B}^{\text{eff}})^2 / (1+\alpha^2) = \frac{1}{\gamma} |d\mathbf{m}/dt|^2$, the energy change rate simplifies to [110, 111]

$$\frac{dw}{dt} = -\frac{\alpha\mu_0}{\gamma} \left| \frac{d\mathbf{m}}{dt} \right|^2 < 0, \quad (6.57)$$

which signifies that in the case of the constant magnetic field the LLG equation has the Lyapunov structure [112], i.e., the internal energy of the system is a decreasing function of time along the trajectories of the LLG equation. This property is fundamental as it guarantees that under the effects of constant magnetic field, the system tends toward stable minima. Moreover, Eq. (6.57) demonstrates the nature of the Gilbert damping, i.e., the dissipation is given by a quadratic form of the vector field $d\mathbf{m}/dt$ which is due to the fact that Gilbert damping term can be introduced via a Rayleigh dissipation function [113]. It is noteworthy that the constant magnetic field is not an energy source [111].

Nevertheless, a time-dependent magnetic field can be an energy sink or source depending on the relative direction of \mathbf{m} and \mathbf{B}_{ext} , which can be immediately seen from Eq. (6.56). In particular, the second term on the right-hand-side (rhs) of Eq. (6.56) can be either positive or negative thereby resulting in the following cases: (i) if the second term on the rhs is negative and larger than the first term then $\frac{dw}{dt} > 0$, thus \mathbf{B}_{ext} is an energy source; (ii) if the second term on the rhs is positive then $\frac{dw}{dt} < 0$, thus \mathbf{B}_{ext} is an energy sink.

Appendix E: Testing robustness of the derived optimal protocols against thermal fluctuations and material parameters perturbation

The optimal pulses derived in this thesis demonstrate dependence on the material parameters, and this result provides valuable insight into the physics of optimal control. Identifying the link between optimal control protocol and material properties is one of the merits of this thesis. However, it is fundamentally and technologically important to test the robustness of the optimal pulses with respect to perturbations in the magnitude of material parameters and thermal fluctuations.

Here, the robustness of the optimal switching protocol for the uniaxial and biaxial nanoparticle [see Sec. 4.1.1 and Sec. 4.1.2] against thermal fluctuations and perturbations in the material parameters was tested by carrying out additional spin dynamics simulations. The simulations involved time integration of the Landau-Lifshitz-Gilbert (LLG) equation equipped with the optimal switching pulse as an external field. The LLG equation was integrated numerically using the semi-implicit scheme B [97]. The procedures for studying effects of temperature and material parameter perturbations are described in what follows.

(1) *Effect of thermal fluctuations.* Interaction of the magnetic systems with the heat bath was simulated by including a stochastic term in the LLG equation, see Appendix C. Each simulation had three stages: (i) Initial equilibration at zero applied magnetic field to establish Boltzmann distribution; (ii) Switching where the optimal magnetic field is applied (note that thermal fluctuations were also included during the switching stage); (iii) Final equilibration at zero applied magnetic field. At the end of the third stage, we inspected the value of s_z ; we have taken the value $s_z = -0.5$ as the threshold for successful switching. For each value of temperature and damping constant, we repeated simulations $L = 1000$ times to accumulate the proper statistics. The switching success rate is defined as $f = L_s/L$ where L_s is the number of successful reversals.

(2) *Effect of perturbations in the material parameter values.* Parameters determining the magnetization dynamics of the monodomain particle include the damping factor

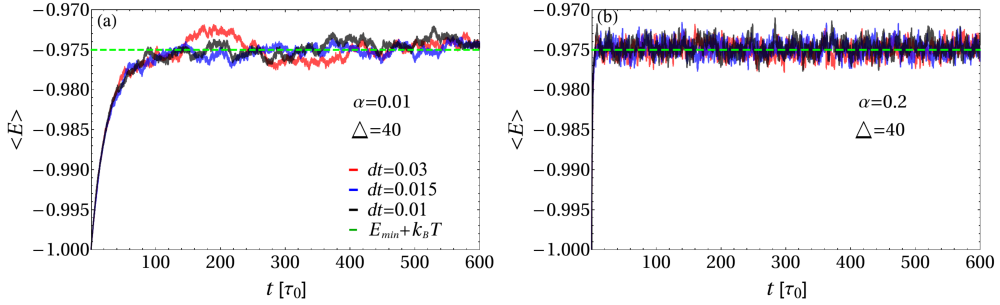


Figure 6.10: Average energy of a uniaxial nanoparticle, see Eq. 4.1, as a function of the equilibration time for damping $\alpha = 0.01$ (a) $\alpha = 0.2$ (b) for different timesteps dt as depicted in the legend. The magnitude of the thermal stability factor $\Delta = K/(k_B T)$ is 40. Dashed green line shows the thermal energy level due to the equipartition theorem.

α , anisotropy parameter K , magnetic moment μ , and in the case of biaxial nanoparticle the relative strength of the hard-axis anisotropy ξ . We applied an optimal field pulse derived for certain values of parameters to a particle characterized by perturbed parameter values.

Uniaxial nanoparticle case

Before assessing the robustness of the optimal pulses against thermal fluctuations, it is necessary to adequately stabilize the system at zero external magnetic fields through proper equilibration. As demonstrated in Figure. (6.10), the average energy is presented as a function of equilibration time for a thermal stability factor denoted as $\Delta = K/(k_B T) = 40$. The figure demonstrates the requirement for an equilibration time exceeding $300\tau_0$ in the case of $\alpha = 0.01$ to achieve thermal stability. As anticipated, a system with higher damping values for α reaches equilibrium at a faster rate. It is also noteworthy from the figure that the average energy remains unaffected by the value of α .

A typical outcome of the finite-temperature spin dynamics simulations is shown in Figure. 6.11. Table. 6.1 summarizes the results of the finite-temperature spin dynamics simulations for switching time $T = 10\tau_0$ and damping $\alpha = 0.1$. As expected, the reversal success rate decreases as Δ becomes smaller. However, when $\Delta > 70$, which is a standard requirement to ensure sufficient stability of the magnetic element with respect to thermal fluctuations to prevent data loss in magnetic memories [114, 115], the success rate is close to unity. This result demonstrates that the optimal switching protocol is robust with respect to thermal fluctuations in the technologically relevant regime.

Parameters determining the magnetization dynamics of the uniaxial nanoparticle include the damping factor α as well as the parameter $\tau_0 = \mu/(2\gamma K)$ with γ being the gyromagnetic ratio. Here, we consider perturbations in α and τ_0 only. In particular,

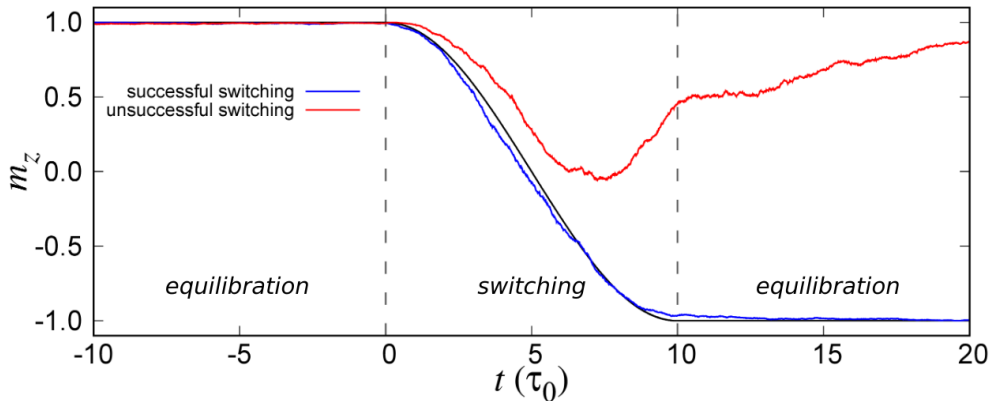


Figure 6.11: Effect of thermal fluctuations on the magnetization reversal induced by the optimal switching pulse. Dashed lines mark the beginning and the end of the applied pulse. Blue (red) line shows evolution of the z-component of the normalized magnetic moment during successful (unsuccessful) reversal at finite temperature. Black line corresponds to the zero-temperature reversal. The magnitude of the damping factor is

Table 6.1: Magnetization reversal success rate, f , for several values of the damping factor α , and the ratio $\Delta E/\Theta$, with ΔE being the energy barrier between the stable states and Θ being thermal energy.

$\Delta E/\Theta$	α	f (%)
80	0.01	99.0
80	0.1	97.0
70	0.01	98.0
70	0.1	97.0
10	0.01	81.0
10	0.1	77.0

we applied an optimal field pulse derived for a certain value of the intrinsic precession time τ_0 and damping factor α to a particle characterized by perturbed parameter values, $\tau_0 + \Delta\tau_0$, $\alpha + \Delta\alpha$. The switching time was chosen to be $10\tau_0$. Figure. 6.12 illustrates the results of these calculations. For a particular value of the damping factor, $\alpha = 0.1$, the switching pulse brings the system over the energy barrier if the strength of the parameter perturbations is not too large.

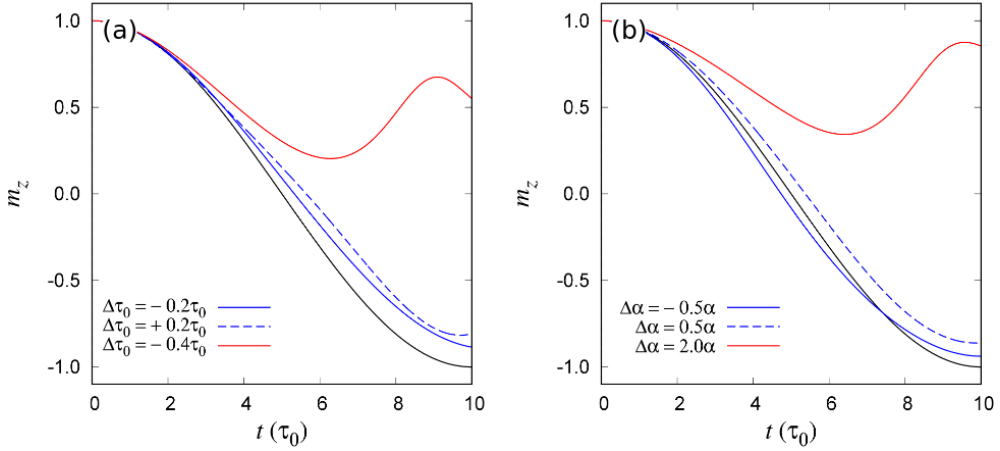


Figure 6.12: Effect of perturbations in the material parameters τ_0 (a) and α (b) on the magnetization reversal induced by the optimal switching pulse. Magnitude of the perturbations $\Delta\tau_0$ and $\Delta\alpha$ is shown in the legend. Blue (red) lines show evolution of the z-component of the normalized magnetic moment during successful (unsuccessful) reversal. Black line corresponds to the reversal in a particle characterized by unperturbed material parameters.

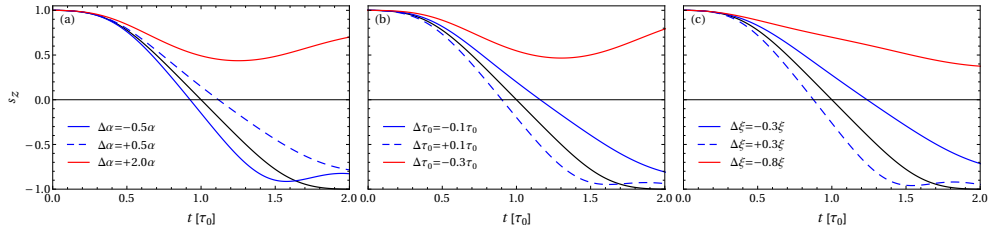


Figure 6.13: Effect of perturbations in the material parameters α (a), τ_0 (b), and ξ (c) on the magnetization reversal induced by the optimal switching pulse. Magnitude of the perturbations $\Delta\tau_0$, $\Delta\alpha$, and $\Delta\xi$ is shown in the legend. Blue (red) lines show evolution of the z-component of the normalized magnetic moment during successful (unsuccessful) reversal. Black line corresponds to the reversal in a particle characterized by unperturbed material parameters: $\alpha = 0.1$, $\xi = 5$. The switching time $T = 2\tau_0$.

Biaxial nanoparticle case

Similar to the uniaxial nanoparticle, the optimal pulses derived for the biaxial nanoparticle are also robust against thermal fluctuations as well as the perturbation in the material parameters values as shown in Table. 6.2 and Figure. 6.13.

Table 6.2: Magnetization reversal success rate, f , for several values of the damping factor α , and the ratio $\Delta E/\Theta$, with ΔE being the energy barrier between the stable states, see Eq. 4.24, and Θ being thermal energy. The switching time $T = 2\tau_0$

$\Delta E/\Theta$	α	f (%)
80	0.01	99.9
80	0.1	99.8
70	0.01	99.6
70	0.1	99.6
50	0.01	98.4
50	0.1	98.9
30	0.01	95.3
30	0.1	96.8

7 Original articles

Article I

Optimal Control of Magnetization Reversal in a Monodomain Particle by Means of Applied Magnetic Field

Kwiatkowski, G. J., Badarneh, M. H., Berkov, D. V., & Bessarab, P. F.

Physical Review Letters, **126**, 177206 (2021).

Optimal Control of Magnetization Reversal in a Monodomain Particle by Means of Applied Magnetic Field

Grzegorz J. Kwiatkowski,¹ Mohammad H. A. Badarneh,¹ Dmitry V. Berkov², and Pavel F. Bessarab^{1,3,4,*}

¹*Science Institute of the University of Iceland, 107 Reykjavík, Iceland*

²*General Numerics Research Lab, Moritz-von-Rohr-Straße 1A, 07745 Jena, Germany*

³*ITMO University, 197101 St. Petersburg, Russia*

⁴*Peter Grünberg Institute and Institute for Advanced Simulation, Forschungszentrum Jülich, 52425 Jülich, Germany*



(Received 20 April 2020; accepted 5 April 2021; published 29 April 2021)

A complete analytical solution to the optimal reversal of a macrospin with easy-axis anisotropy is presented. An optimal control path minimizing the energy cost of the reversal is identified and used to derive the time-dependent direction and amplitude of the optimal switching field. The minimum energy cost of the reversal scales inversely with the switching time for fast switching, follows exponential asymptotics for slow switching, and reaches the lower limit proportional to the energy barrier between the target states and to the damping parameter at infinitely long switching time. For a given switching time, the energy cost is never smaller than that for a free macrospin. This limitation can be bypassed by adding a hard anisotropy axis that activates the internal torque in the desired switching direction, thereby significantly reducing the energy cost. A comparison between the calculated optimal control path and minimum energy path reveals that optimal control does not translate to the minimization of the energy barrier but signifies effective use of the system's internal dynamics to aid the desired magnetic transition.

DOI: 10.1103/PhysRevLett.126.177206

Exact results concerning energy-efficient manipulation of magnetic structure are highly important for fundamental science and also for technological applications, as they could help improve the performance of computing and memory devices based on magnetic elements. Optimization of magnetization switching in bistable nanomagnets by tuning the external magnetic field has come under special focus. It has been shown that a switching field can be significantly reduced by application of a weak radio frequency field pulse [1–11]. Magnetization reversal can be achieved exclusively by a microwave field [2], whose amplitude can be reduced provided that the frequency is properly modulated [12–16]. Sun and Wang [17] obtained a theoretical limit of the minimal switching field and derived an optimal constant-amplitude pulse yielding the shortest switching time. Assuming a fixed magnitude but variable direction of the switching field, Wang *et al.* [18] derived the Euler-Lagrange equations for the fastest reversal of an arbitrary Stoner particle. Barros *et al.* [19] developed a general theoretical framework for the design of control field pulses that minimize the energy cost of switching, calculated numerically the optimal switching field for a macrospin with easy-axis anisotropy, and derived analytically the asymptotic properties of the reversal for infinitely long switching time [20]. So far, theoretical studies of optimal magnetization switching have imposed constraints on the switching field or involved numerical simulations, but a general analytical solution providing a transparent physical picture is still missing.

Here we present a complete analytical solution to the problem of energy-efficient switching of a nanomagnet with easy-axis anisotropy. In contrast to previous studies, our solution does not involve any assumptions about the shape of the optimal switching pulse, therefore providing a true theoretical limit to the energy cost of the switching as a function of the switching time and establishing a link between the optimal pulse and material properties. Our results reveal new fundamental properties of the reversal, including two asymptotic regimes of the energy cost and the optimal switching time. The easy-axis anisotropy cannot reduce the energy cost of switching compared with the free-macrospin case, but this limitation can be lifted by introducing a hard anisotropy axis in the system. Energy-efficient magnetization switching in the system with the hard axis illustrates the concept of using the system's internal dynamics to aid the desired change in the magnetic structure, thereby offering a new perspective on the design of magnetic memory elements.

The efficiency of the magnetization reversal is enhanced by minimizing the energy losses associated with the generation of the switching field. Assuming an electric circuit to be the source of the field and neglecting the losses on radiation, the energy cost is defined by Joule heating due to the resistance of the circuit. This is proportional to the electric current square integrated over the switching time. Taking into account the linear relationship between the current magnitude and the strength of the

generated field, we arrive at the cost functional proposed by Barros *et al.* [19]:

$$\Phi = \int_0^T |\vec{b}|^2 dt, \quad (1)$$

where T is the switching time and \vec{b} is the generated time-dependent magnetic field. The functional Φ needs to be minimized subject to boundary conditions and a constraint imposed by the equation of motion for the magnetic moment, chosen here to be the zero-temperature Landau-Lifshitz-Gilbert equation [21]

$$(1 + \alpha^2)\dot{\vec{s}} = -\gamma\vec{s} \times (\vec{b}_i + \vec{b}) - \alpha\gamma\vec{s} \times [\vec{s} \times (\vec{b}_i + \vec{b})], \quad (2)$$

where α is the Gilbert damping, γ is the gyromagnetic ratio, and \vec{s} is the unit vector along the magnetic moment $\vec{\mu}$. The internal field is defined as $\vec{b}_i = -\mu^{-1}\partial E/\partial\vec{s}$, with E being the energy of the system excluding the Zeeman term.

The constrained minimization of Φ can be formulated as an unconstrained optimization by expressing \vec{b} in terms of the dynamical trajectory of the system as well as the internal magnetic field,

$$\vec{b} = \frac{\alpha}{\gamma}\dot{\vec{s}} + \frac{1}{\gamma}[\vec{s} \times \dot{\vec{s}}] - \vec{b}_i^\perp. \quad (3)$$

Here $\vec{b}_i^\perp \equiv \vec{b}_i - (\vec{s} \cdot \vec{b}_i)\vec{s}$, which is the transverse component of \vec{b}_i (the longitudinal component is not included, as it does not affect the dynamics). On substituting (3) into (1), the energy cost of the reversal becomes a functional of the switching trajectory. By solving the Euler-Lagrange equation, the trajectory minimizing the cost functional Φ can be found. We denote this trajectory as the optimal control path (OCP) so as to distinguish it from other switching trajectories and to highlight its physical meaning. The optimal switching pulse can be obtained from the OCP using Eq. (3), thereby derived from the system's intrinsic magnetic properties, which are available via well-established techniques [22]. A similar paradigm was used to optimize electric current driving domain walls in nanowires [23].

We apply the concept outlined above to a uniaxial single-domain particle whose magnetic moment is reversed from one stable orientation to the other (see Fig. 1). The energy barrier between the stable states is assumed to be much larger than the thermal energy. This model mimics, e.g., a bit operation in a nanoscale magnetic memory element, where strong magnetic anisotropy ensures stability of the element against thermal fluctuations [24]. The internal energy E of the system is defined by the anisotropy along the z axis,

$$E = -Ks_z^2, \quad (4)$$

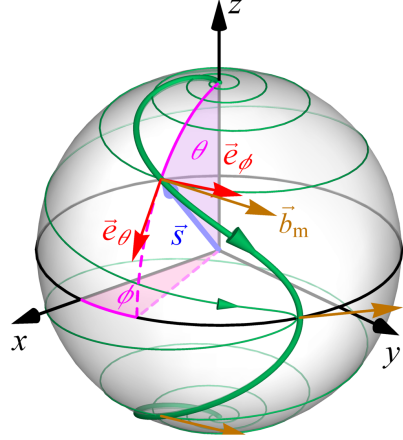


FIG. 1. Calculated optimal control paths (OCPs) for the reversal of a macrospin pointing along the unit vector \vec{s} . The initial and the final states are at the north and the south poles of the unit sphere, respectively. The damping factor α is 0.1. The switching time T is $10\tau_0$ and $100\tau_0$ for the paths shown with thick and thin green lines, respectively. The external magnetic field \vec{b}_m at $t = T/4$, $t = T/2$, and $t = 3T/4$ is shown for the shorter path with the brown arrows.

where $K > 0$ is the anisotropy constant. Euler-Lagrange equations in spherical coordinates θ and ϕ (Fig. 1) read

$$\tau_0^2 \ddot{\theta} = \frac{\alpha^2}{4(1 + \alpha^2)^2} \sin 4\theta, \quad \tau_0 \dot{\phi} = \frac{\cos \theta}{1 + \alpha^2}, \quad (5)$$

where the period of Larmor precession $\tau_0 = \mu(2\gamma K)^{-1}$ defines the timescale. The boundary conditions $\theta(0) = 0$, $\theta(T) = \pi$ correspond to the transition between the energy minima within the switching time T . Equation (5) for θ is the well-known Sine-Gordon equation [25,26], whose solutions are expressed by Jacobi elliptic functions [27,31]. The OCP described by Eq. (5) reveals the mechanism for the reversal: The moment moves steadily from the initial state upward the energy surface while precessing counterclockwise around the anisotropy axis until it reaches the top of the energy barrier at $t = T/2$. At this point, the precession reverses its direction and the system slides down to the target state minimum. This scenario was obtained numerically by Barros *et al.* [19,20], but the exact analytical solution makes it possible to derive general properties of the OCP [27].

Substitution of the solution for θ and ϕ into Eq. (3) results in the following expressions for the optimal switching field:

$$\vec{b}_m = \frac{b_m}{\sqrt{1 + \alpha^2}} (\alpha \vec{e}_\theta + \vec{e}_\phi), \quad (6)$$

$$b_m = \frac{K}{\mu p \sqrt{1 + \alpha^2}} \left[\operatorname{dn} \left(\frac{t}{p \tau_0 (1 + \alpha^2)} \middle| -\alpha^2 p^2 \right) + \alpha p \operatorname{sn} \left(\frac{t}{p \tau_0 (1 + \alpha^2)} \middle| -\alpha^2 p^2 \right) \right], \quad (7)$$

where $\vec{e}_\theta, \vec{e}_\phi$ are local time-dependent orthonormal vectors in the directions of increasing θ , and ϕ , respectively (see Fig. 1), while $\operatorname{dn}(\cdot)$ and $\operatorname{sn}(\cdot)$ are Jacobi elliptic functions [27,31] and p is a parameter implicitly defined through the following equation: $T = 4\tau_0(1 + \alpha^2)p\mathcal{K}(-\alpha^2 p^2)$, with $\mathcal{K}(\cdot)$ being the complete elliptic integral of the first kind [27,31]. Equation (6) signifies that the switching field points in a specific fixed direction in the time-varying frame of reference associated with the magnetic moment [17] evolving according to Eq. (5). The orientation of the field is such that its contribution to the precession around the anisotropy axis is exactly zero, and the external pulse contributes only to the part of motion that is relevant for switching, i.e., progressive increase in θ . The optimal orientation of the switching field can be obtained regardless of optimization of the pulse amplitude; e.g., Eq. (6) still holds for the constant field amplitude [17].

Equation (7) describes the optimal switching field amplitude b_m (see Fig. 2). When $\alpha = 0$, the amplitude is time independent: $b_m|_{\alpha=0} = \pi/(\gamma T)$. Note that for zero α there is no energy consumption by the magnetic moment itself, but energy is still expended on the creation of the switching field. We emphasize that the functional Φ characterizes the energy spent by the external field source and not the energy dissipated in the magnetic system.

For $\alpha > 0$, $b_m(t)$ has a more complex structure, but the symmetry $b_m(0) = b_m(T/2) = b_m(T)$ holds. Damping gives rise to the internal torque in the polar direction. This torque—produced by the anisotropy field—counteracts the switching motion before crossing the equator, and a

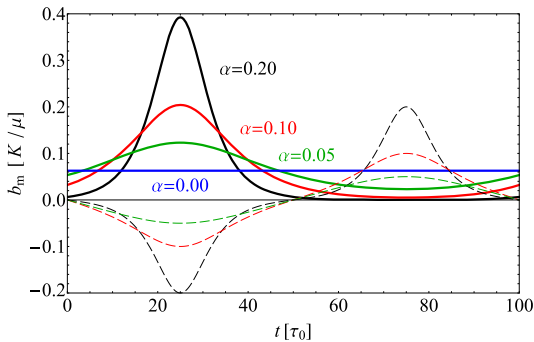


FIG. 2. Amplitude of the switching field as a function of time for $T = 100\tau_0$ and several values of α (solid lines). Dashed lines show ab_1^\pm , which is proportional to the polar component of the torque generated by the internal field.

maximum in the switching field forms at $t = T/4$ so as to neutralize this effect (see Fig. 2). After the trajectory has crossed the equator at $t = T/2$ [27], the internal torque aids the switching, and b_m reaches a minimum at $t = 3T/4$. The position of the maximum and the minimum of $b_m(t)$ coincides with that of the extrema of the polar component of the internal torque (see Fig. 2). Note that the external field, although reduced compared to that before barrier crossing, is still nonzero in general: Some field needs to be applied in order to terminate the reversal on time. However, for long enough switching time, $T \gg (\alpha + 1/\alpha)\tau_0$, damping alone is sufficient to complete the switching, and virtually no field needs to be applied after crossing the energy barrier (see black curve in Fig. 2). Although the magnitude of neither maximum b_{\max} nor minimum b_{\min} of the switching field amplitude can be described in terms of elementary functions in a general case, the difference between them is always

$$\Delta b = b_{\max} - b_{\min} = \frac{2\alpha K}{\mu \sqrt{1 + \alpha^2}}. \quad (8)$$

Moreover, the average amplitude b_{av} can be computed analytically, leading to an exact relation

$$b_{\text{av}} = \frac{1}{T} \int_0^T b_m(t) dt = \frac{\pi \sqrt{1 + \alpha^2}}{\gamma T}, \quad (9)$$

which demonstrates that overall larger fields are required to terminate the reversal in a shorter time, as expected. Interestingly, b_{av} does not depend on the magnetic potential. From Eqs. (8) and (9) it follows that $\Delta b/b_{\text{av}} \rightarrow 0$ for $T \rightarrow 0$; i.e., a decrease in the switching time progressively makes $b_m(t)$ resemble a time-independent function [27].

Equation (7) recovers the result of Barros *et al.* for $T \rightarrow \infty$ —see Eq. (13) in Ref. [20]—as well as that of Sun and Wang for $\alpha = 0$ —see Eqs. (7) and (9) in Ref. [17]. Additionally, for $T \ll (\alpha + 1/\alpha)\tau_0$ the pulse amplitude simplifies to $b_m \approx b_{\text{av}} + \Delta b \sin(2\pi t/T)/2$.

Substitution of Eq. (7) into Eq. (1) leads to the following formula for the minimum energy cost:

$$\Phi_m = \frac{2K[2\mathcal{E}(-\alpha^2 p^2) - \mathcal{K}(-\alpha^2 p^2)]}{\gamma \mu p}, \quad (10)$$

where $\mathcal{E}(\cdot)$ is the complete elliptic integral of the second kind [27,31]. According to (10), Φ_m is a monotonically decreasing (increasing) function of the switching time T (damping parameter α), as illustrated in Fig. 3. Energy cost as a function of the switching time has two asymptotic regimes corresponding to fast and slow switching. For the short switching time, the magnetic potential becomes irrelevant, and $\Phi_m(T)$ is described by a power law:

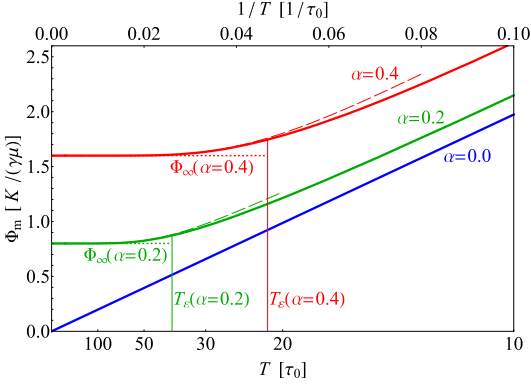


FIG. 3. Minimum energy cost of magnetization switching as a function of the inverse of the switching time. Dashed (dotted) lines show long (infinite) switching time asymptotics. Thin vertical lines indicate switching time T_ϵ , for which the minimum energy cost is $\epsilon = 10\%$ larger than the infinite switching time limit Φ_∞ .

$$\Phi_m \approx \frac{\pi^2(1 + \alpha^2)}{\gamma^2 T} + O(T), \quad T \ll (\alpha + 1/\alpha)\tau_0, \quad (11)$$

The leading term in Eq. (11) specifically recovers the potential-free case. The power-law regime changes to an exponential dependence on T for the long switching time:

$$\Phi_m \approx \Phi_\infty \left(1 + 4 \exp \left[-\frac{\alpha T}{2\tau_0(1 + \alpha^2)} \right] \right), \quad T \gg (\alpha + 1/\alpha)\tau_0, \quad (12)$$

which particularly demonstrates that, for a given anisotropy constant and damping parameter, the lower limit of the energy cost is $\Phi_\infty \equiv 4\alpha K/(\gamma\mu)^{-1}$, as predicted in [20]. Strictly speaking, this limit is reached at infinitely long switching time, but Eq. (12) makes it possible to analyze to what extent the limit can be approached within finite T . In particular, termination of the reversal within time $T_\epsilon = 2 \ln(4/\epsilon)[\alpha + 1/\alpha]\tau_0$ corresponds to the energy cost that is only by a fraction of $\epsilon < 1$ larger than Φ_∞ : $\Phi_m(T_\epsilon)/\Phi_\infty = 1 + \epsilon$. Therefore, T_ϵ has a meaning of optimal switching time in a sense that increase in T beyond T_ϵ does not lead to a significant gain in energy efficiency (see Fig. 3).

Analysis of Eq. (10) shows that for a given switching time T , the energy cost is never smaller than that in a zero-potential case: $\Phi_m(T) \geq \Phi_0(T) \equiv \pi^2(1 + \alpha^2)/(\gamma^2 T)$, where the equality is reached for $\alpha = 0$. In other words, the internal energy obstructs the reversal in a system with easy-axis anisotropy, and the purpose of the pulse optimization in this case is to minimize the unfavorable effect caused by the magnetic potential. To be able to use the internal energy

landscape to aid the switching process, additional terms in the magnetic potential are necessary. We have found that the energy cost can be reduced by adding a hard-axis anisotropy to the system. The internal energy \tilde{E} of such a biaxial anisotropy system can be written as

$$\tilde{E} = -Ks_y^2 + K_h s_z^2, \quad (13)$$

where the easy axis and the hard axis are along the y and z directions, respectively. The hard-axis anisotropy constant K_h is taken to be 10 times larger than K . This $K_h \gg K$ regime can be realized thanks to the large demagnetizing field [32] in thin flat elongated nanoelements. Such structures are used, e.g., as single bits in in-plane memory designs [24], or as elements of artificial spin ice systems [33,34]. The OCP between the energy minima at $s_y = \pm 1$ was obtained by a direct numerical minimization of the energy cost functional for the switching time $T = 0.32\tau_0$ and damping $\alpha = 0$. Surprisingly, the corresponding energy cost $\tilde{\Phi}_m$ turned out to be an order of magnitude smaller than that for the reversal with the same switching time and damping in the system with zero magnetic potential: $\tilde{\Phi}_m/\Phi_0 \approx 0.088$. This phenomenon can be explained by the distribution of the internal torque; see Fig. 4. Because of the hard axis, there is a region in the configuration space where the system's internal torque systematically points in the desired switching direction. By placing the switching path into this region, the optimal control efficiently exploits the internal torque to assist the switching. The external pulse has a minimal influence; its purpose is only to trigger the switching by directing the system toward the particular sector in the configuration space where the internal dynamics picks the system up and drags it to the desired target state. This effect was also noticed earlier for in-plane magnetized Co films [35] and Co nanoclusters characterized by complex magnetic anisotropy [36].

Finally, we compare our OCP with another distinguished path in the configuration space—the minimum energy path (MEP). An MEP connecting two stable states is a path lying lowermost on the energy surface, and the point of highest energy along the MEP defines the energy barrier within harmonic rate theories [37–39]. The MEP for the magnetization reversal in the biaxial system is the shortest path connecting the energy minima through the saddle point at $\theta = \pi/2$, $\phi = \pi$ (see Fig. 4). This path is very different from the calculated OCP, which demonstrates a more complex structure. To emphasize the difference between MEP and OCP, we note that the OCP is a dynamical trajectory defined by the parameters of the equation of motion, whereas the MEP is determined entirely by the energy surface of the system. Since the OCP does not even pass through the saddle point, the energy maximum along the OCP is higher than the energy barrier derived from the MEP (see the inset in Fig. 4). This result means that optimal

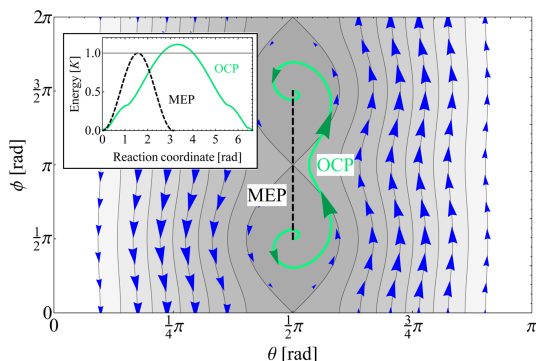


FIG. 4. Distribution of the torque (blue arrows) generated by the internal field of the macrospin system with both easy and hard anisotropy axes, superimposed on the contour plot showing the energy surface of the system defined by Eq. (13). The green line shows the calculated OCP for $T = 0.32\tau_0$ and $\alpha = 0$. Green arrows indicate the velocity of the system. The size of the blue (green) arrows code the magnitude of the torque (velocity). The black dashed line shows the minimum energy path (MEP). The inset shows the energy of the system as a function of displacement along the OCP (green solid line) and MEP (black dashed line).

control of a magnetic transition does not necessarily lead to a path that minimizes the energy barrier between the target states. Following an OCP involves rotation of magnetic moments in such a way that the influence of the external stimulus is minimized, but the system's internal dynamics is effectively used to aid the magnetic transition.

Experimental realization of optimal control pulses, such as the one given by Eqs. (6) and (7), is challenging but still feasible within current technology for pulse shaping [40–45]. Note also that the optimal switching protocol derived here is quite stable with respect to thermal fluctuations and material parameter perturbations, as confirmed by our spin dynamics simulations [27].

In conclusion, we have presented an exact analytical solution to the problem of optimal switching of a nano-magnet via the coherent magnetization rotation mode used in most modern magnetic memories. The easy-axis anisotropy alone can only increase the energy cost of the switching compared to the free-macrospin case, but this effect is minimized by following the OCP. The system's internal torque can be used to aid the switching by introducing a hard anisotropy axis. Our results deepen the understanding of the optimal control of magnetization switching in nanoparticles and provide guiding principles for the design of energy-efficient digital devices based on magnetic elements.

The authors would like to thank H. Jónsson, B. Hjörvarsson, V. Kapaklis, and T. Sigurjónsdóttir for helpful discussions. This work was funded by the Russian Science

Foundation (Grant No. 19-72-10138), the Icelandic Research Fund (Grant No. 184949-052), the Deutsche Forschungsgemeinschaft (DFG Grant No. BE2464/17-1), and the Alexander von Humboldt Foundation.

*bessarab@hi.is

- [1] C. Thirion, W. Wernsdorfer, and D. Mailly, Switching of magnetization by nonlinear resonance studied in single nanoparticles, *Nat. Mater.* **2**, 524 (2003).
- [2] Z. Z. Sun and X. R. Wang, Magnetization reversal through synchronization with a microwave, *Phys. Rev. B* **74**, 132401 (2006).
- [3] G. Woltersdorf and C. H. Back, Microwave assisted switching of single domain $\text{Ni}_{80}\text{Fe}_{20}$ elements, *Phys. Rev. Lett.* **99**, 227207 (2007).
- [4] J.-G. Zhu, X. Zhu, and Y. Tang, Microwave assisted magnetic recording, *IEEE Trans. Magn.* **44**, 125 (2008).
- [5] S. Okamoto, N. Kikuchi, and O. Kitakami, Magnetization switching behavior with microwave assistance, *Appl. Phys. Lett.* **93**, 102506 (2008).
- [6] S. Okamoto, N. Kikuchi, and O. Kitakami, Frequency modulation effect on microwave assisted magnetization switching, *Appl. Phys. Lett.* **93**, 142501 (2008).
- [7] G. Bertotti, I. D. Mayergoyz, C. Serpico, M. d'Aquino, and R. Bonin, Nonlinear-dynamical-system approach to microwave-assisted magnetization dynamics (invited), *J. Appl. Phys.* **105**, 07B712 (2009).
- [8] Z. Wang and M. Wu, Chirped-microwave assisted magnetization reversal, *J. Appl. Phys.* **105**, 093903 (2009).
- [9] R. Yanes, R. Rozada, F. García-Sánchez, O. Chubykalo-Fesenko, P. M. Pimentel, B. Leven, and B. Hillebrands, Modeling of microwave-assisted switching in micron-sized magnetic ellipsoids, *Phys. Rev. B* **79**, 224427 (2009).
- [10] S. Okamoto, N. Kikuchi, M. Furuta, O. Kitakami, and T. Shimatsu, Switching Behaviors and its Dynamics of a Co/Pt Nanodot under the Assistance of rf Fields, *Phys. Rev. Lett.* **109**, 237209 (2012).
- [11] S. Okamoto, M. Furuta, N. Kikuchi, O. Kitakami, and T. Shimatsu, Theory and experiment of microwave-assisted magnetization switching in perpendicular magnetic nanodots, *IEEE Trans. Magn.* **50**, 83 (2014).
- [12] K. Rivkin and J. B. Ketterson, Magnetization reversal in the anisotropy-dominated regime using time-dependent magnetic fields, *Appl. Phys. Lett.* **89**, 252507 (2006).
- [13] Z. Z. Sun and X. R. Wang, Strategy to reduce minimal magnetization switching field for Stoner particles, *Phys. Rev. B* **73**, 092416 (2006).
- [14] L. Cai, D. A. Garanin, and E. M. Chudnovsky, Reversal of magnetization of a single-domain magnetic particle by the ac field of time-dependent frequency, *Phys. Rev. B* **87**, 024418 (2013).
- [15] G. Klughertz, P.-A. Hervieux, and G. Manfredi, Autoresonant control of the magnetization switching in single-domain nanoparticles, *J. Phys. D* **47**, 345004 (2014).
- [16] M. T. Islam, X. S. Wang, Y. Zhang, and X. R. Wang, Subnanosecond magnetization reversal of a magnetic nanoparticle driven by a chirp microwave field pulse, *Phys. Rev. B* **97**, 224412 (2018).

- [17] Z. Z. Sun and X. R. Wang, Theoretical limit of the minimal magnetization switching field and the optimal field pulse for Stoner particles, *Phys. Rev. Lett.* **97**, 077205 (2006).
- [18] X. R. Wang, P. Yan, J. Lu, and C. He, Euler equation of the optimal trajectory for the fastest magnetization reversal of nano-magnetic structures, *Europhys. Lett.* **84**, 27008 (2008).
- [19] N. Barros, M. Rassam, H. Jirari, and H. Kachkachi, Optimal switching of a nanomagnet assisted by microwaves, *Phys. Rev. B* **83**, 144418 (2011).
- [20] N. Barros, H. Rassam, and H. Kachkachi, Microwave-assisted switching of a nanomagnet: Analytical determination of the optimal microwave field, *Phys. Rev. B* **88**, 014421 (2013).
- [21] D. V. Berkov, Magnetization dynamics including thermal fluctuations: Basic phenomenology, fast remagnetization processes and transitions over high-energy barriers, in *Handbook of Magnetism and Advanced Magnetic Materials*, edited by H. Kronmüller and S. Parkin (John Wiley & Sons, Chichester, UK, 2007), Vol. 2, pp. 795–823.
- [22] A. Barman and J. Sinha, *Spin Dynamics and Damping in Ferromagnetic Thin Films and Nanostructures* (Springer, Cham, Switzerland, 2018).
- [23] O. A. Tretiakov, Y. Liu, and A. Abanov, Minimization of Ohmic Losses for Domain Wall Motion in a Ferromagnetic Nanowire, *Phys. Rev. Lett.* **105**, 217203 (2010).
- [24] K. C. Chun, H. Zhao, J. D. Harms, T.-H. Kim, J.-P. Wang, and C. H. Kim, A scaling roadmap and performance evaluation of in-plane and perpendicular MTJ based STT-MRAMs for high-density cache memory, *IEEE J. Solid-State Circuits* **48**, 598 (2013).
- [25] H. Mikeska, Solitons in a one-dimensional magnet with an easy plane, *J. Phys. C* **11**, L29 (1978).
- [26] J. Cuevas-Maraver, P. G. Kevrekidis, and F. Williams, *The Sine-Gordon Model and its Applications* (Springer, Cham, Switzerland, 2014).
- [27] See Supplemental Material at <http://link.aps.org/supplemental/10.1103/PhysRevLett.126.177206> for the definitions of elliptic functions and integrals, discussion of the OCP and its symmetries, results of spin dynamics simulations showing stability of the optimal switching protocol against thermal fluctuations and material parameter perturbations, a figure showing the OCP as a function of time and α , a figure showing b_{\min} , b_{\max} , b_{av} as functions of α and T , and a figure illustrating how $b_m(t)$ profile changes with T , which includes Refs. [28–30].
- [28] J. H. Mentink, M. V. Tretiyakov, A. Fasolino, M. I. Katsnelson, and T. Rasing, Stable and fast semi-implicit integration of the stochastic Landau–Lifshitz equation, *J. Phys. Condens. Matter* **22**, 176001 (2010).
- [29] H. Richter, Density limits imposed by the microstructure of magnetic recording media, *J. Magn. Magn. Mater.* **321**, 467 (2009).
- [30] M. Krounbi, V. Nikitin, D. Apalkov, J. Lee, X. Tang, R. Beach, D. Erickson, and E. Chen, Status and challenges in spin-transfer torque MRAM technology, *ECS Trans.* **69**, 119 (2015).
- [31] *Handbook of Mathematical Functions with Formulas, Graphs, and Mathematical Tables*, edited by M. Abramowitz and I. A. Stegun (National Bureau of Standards, Washington, DC, 1964).
- [32] J. A. Osborn, Demagnetizing factors of the general ellipsoid, *Phys. Rev.* **67**, 351 (1945).
- [33] C. Nisoli, R. Moessner, and P. Schiffer, Colloquium: Artificial spin ice: Designing and imaging magnetic frustration, *Rev. Mod. Phys.* **85**, 1473 (2013).
- [34] G. M. Wysin, W. A. Moura-Melo, L. A. S. Mól, and A. R. Pereira, Magnetic anisotropy of elongated thin ferromagnetic nanoislands for artificial spin ice arrays, *J. Phys. Condens. Matter* **24**, 296001 (2012).
- [35] C. H. Back *et al.*, Minimum field strength in precessional magnetization reversal, *Science* **285**, 864 (1999).
- [36] C. Etz, M. Costa, O. Eriksson, and A. Bergman, Accelerating the switching of magnetic nanoclusters by anisotropy-driven magnetization dynamics, *Phys. Rev. B* **86**, 224401 (2012).
- [37] H. Kramers, Brownian motion in a field of force and the diffusion model of chemical reactions, *Physica (Amsterdam)* **7**, 284 (1940).
- [38] G. H. Vineyard, Frequency factors and isotope effects in solid state rate processes, *J. Phys. Chem. Solids* **3**, 121 (1957).
- [39] W. F. Brown, Thermal fluctuation of fine ferromagnetic particles, *IEEE Trans. Magn.* **15**, 1196 (1979).
- [40] T. Gerrits, H. A. M. van den Berg, J. Hohlfeld, L. Bär, and T. Rasing, Ultrafast precessional magnetization reversal by picosecond magnetic field pulse shaping, *Nature (London)* **418**, 509 (2002).
- [41] T. P. M. Alegre, A. C. Torrezan, and G. Medeiros-Ribeiro, Microstrip resonator for microwaves with controllable polarization, *Appl. Phys. Lett.* **91**, 204103 (2007).
- [42] M. Curcic *et al.*, Polarization Selective Magnetic Vortex Dynamics and Core Reversal in Rotating Magnetic Fields, *Phys. Rev. Lett.* **101**, 197204 (2008).
- [43] H. Gao, C. Lei, M. Chen, F. Xing, H. Chen, and S. Xie, A simple photonic generation of linearly chirped microwave pulse with large time-bandwidth product and high compression ratio, *Opt. Express* **21**, 23107 (2013).
- [44] A. Bisig *et al.*, Dynamic domain wall chirality rectification by rotating magnetic fields, *Appl. Phys. Lett.* **106**, 122401 (2015).
- [45] M. Rius, M. Bolea, J. Mora, and J. Capmany, Incoherent photonic processing for chirped microwave pulse generation, *IEEE Photonics Technol. Lett.* **29**, 7 (2017).

Supplemental Material: Optimal control of magnetization reversal in a monodomain particle by means of applied magnetic field

Grzegorz J. Kwiatkowski,¹ Mohammad H.A. Badarneh,¹

Dmitry V. Berkov,² and Pavel F. Bessarab^{1,3,4,*}

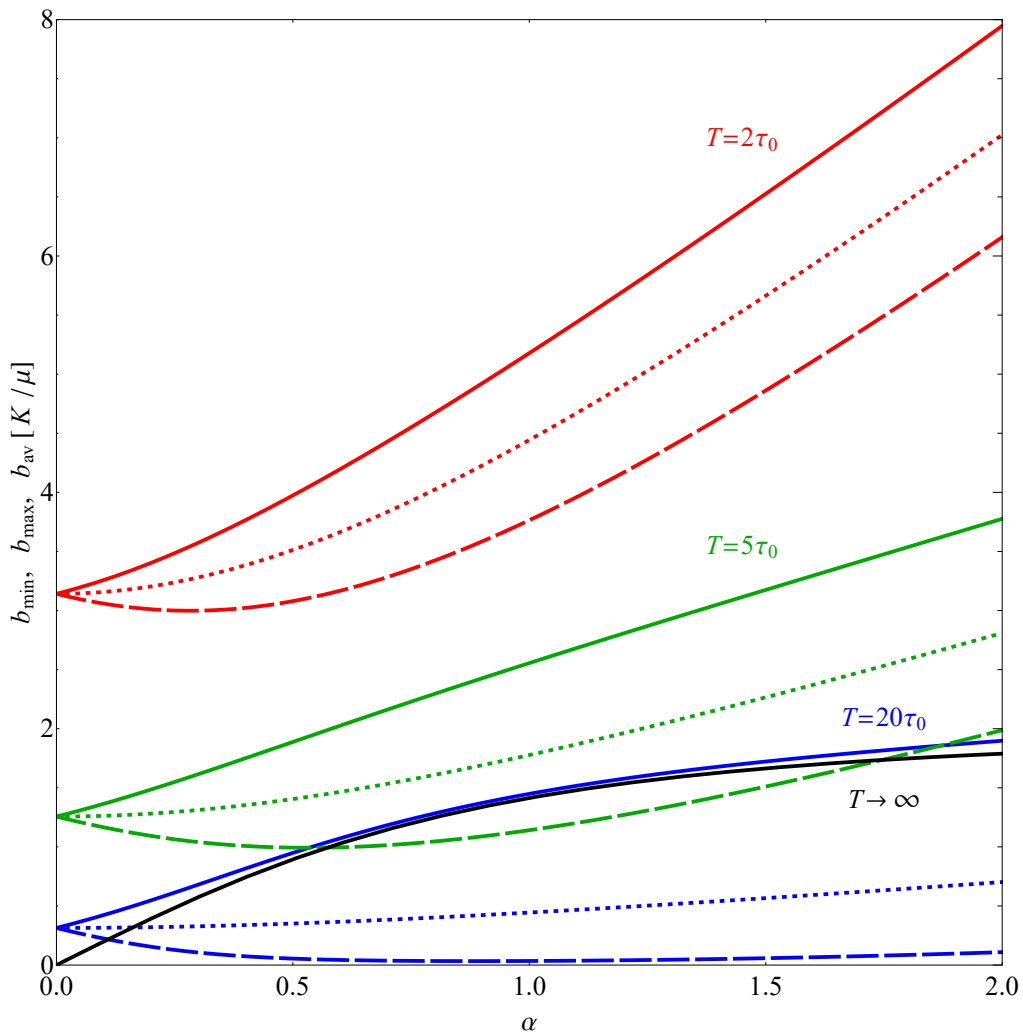
¹*Science Institute of the University of Iceland, 107 Reykjavík, Iceland*

²*General Numerics Research Lab, Moritz-von-Rohr-Straße 1A, 07745 Jena, Germany*

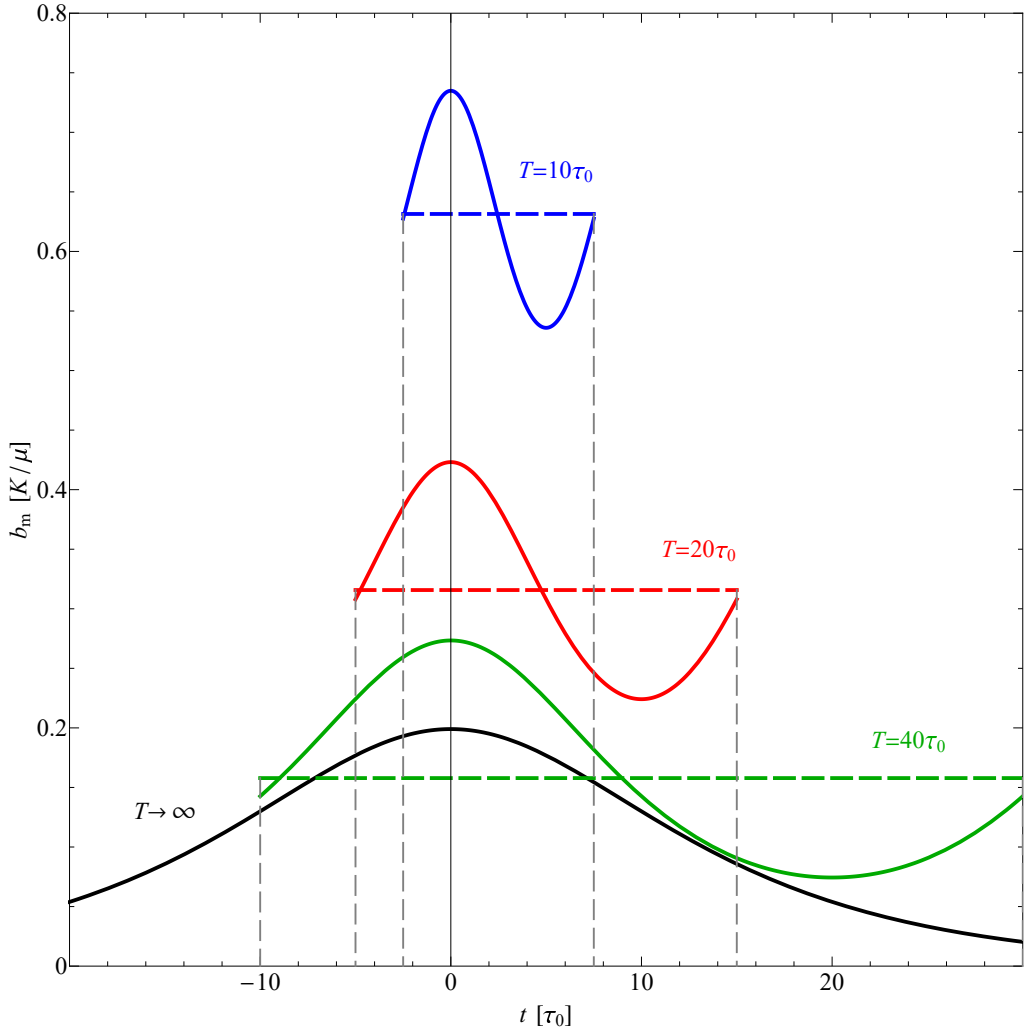
³*ITMO University, 197101 St. Petersburg, Russia*

⁴*Peter Grünberg Institute and Institute for Advanced Simulation,
Forschungszentrum Jülich, 52425 Jülich, Germany*

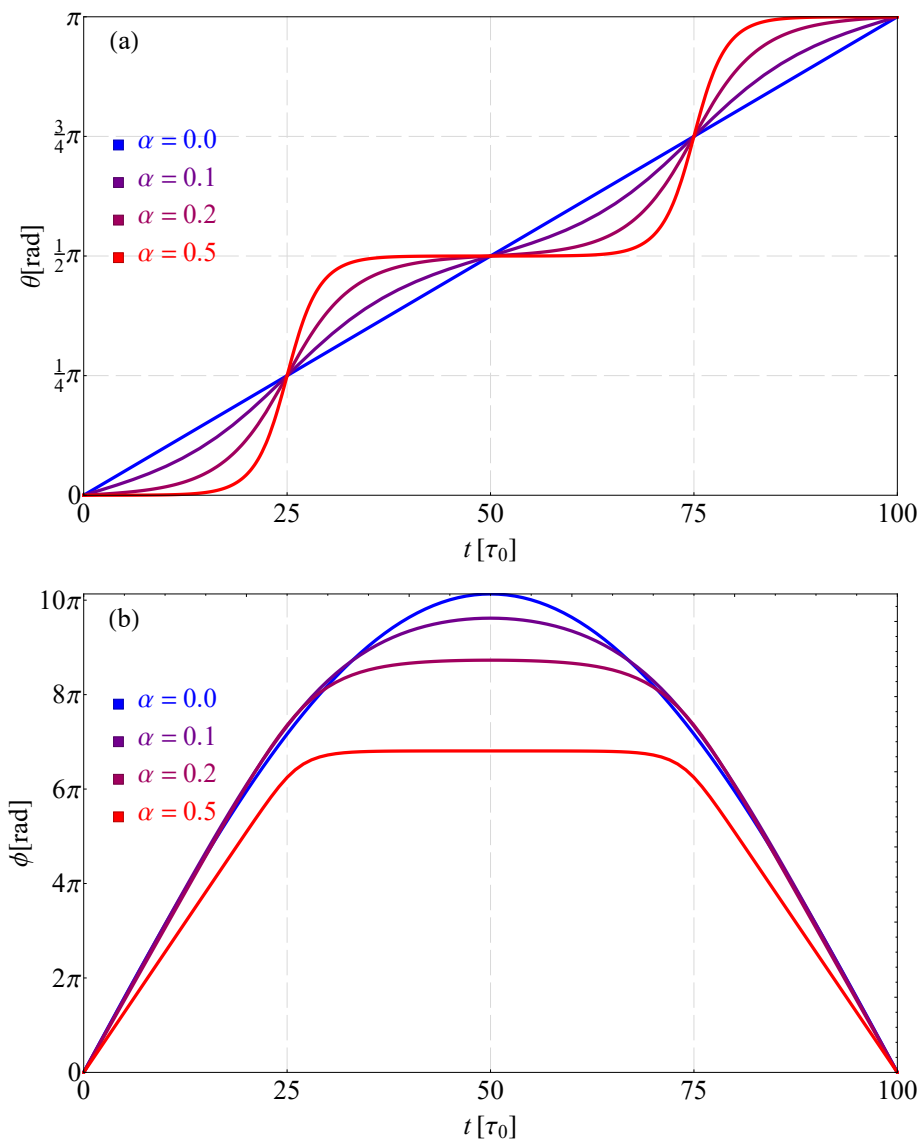
* Corresponding author: bessarab@hi.is



Supplementary Figure 1. Maximum (solid line), minimum (dashed line) and average (dotted line) value of the switching field amplitude as functions of the damping parameter α for several values of the switching time T .



Supplementary Figure 2. Amplitude of the switching field as a function of time for $\alpha = 0.1$ and several values of the switching time T . For all pulses, the zero of time coincides with the position of the maximum value of the amplitude, as indicated by a solid vertical line. Dashed vertical lines indicate starting and ending times of the pulses. Dashed horizontal lines show the average amplitude of the pulses.



Supplementary Figure 3. The optimal control path represented by the polar angle θ (a) and the azimuthal angle ϕ (b) as a function of time for $T = 100\tau_0$ and several values of the damping parameter α

Supplementary Note 1. Elliptic integrals and functions

Elliptic integral of the first kind is defined as

$$\mathcal{F}(\rho|k) = \int_0^\rho \frac{dr}{\sqrt{1 - k^2 \sin^2(r)}}, \quad (\text{S1})$$

where k is called the elliptic modulus. Complete elliptic integral of the first kind is given by

$$\mathcal{K}(k) = \mathcal{F}\left(\frac{\pi}{2} \middle| k\right). \quad (\text{S2})$$

Complete elliptic integral of the second kind is defined as

$$\mathcal{E}(k) = \int_0^{\frac{\pi}{2}} \sqrt{1 - k^2 \sin^2(r)} \, dr. \quad (\text{S3})$$

Jacobi amplitude am is defined as an inverse of the elliptic integral of the first kind:

$$u = \mathcal{F}(\rho|k), \quad (\text{S4})$$

$$\rho = \text{am}(u|k). \quad (\text{S5})$$

Jacobi sn function is defined as

$$\text{sn}(u|k) = \sin(\text{am}(u|k)). \quad (\text{S6})$$

Jacobi dn function is defined as

$$\text{dn}(u|k) = \sqrt{1 - k^2 \text{sn}^2(u|k)}. \quad (\text{S7})$$

See Ref. [S1] for further information about elliptic functions and integrals.

Supplementary Note 2. Properties of the optimal control path

The symmetries of the optimal control path described by Eqs. (5) of the main text are listed in the Supplementary Table 1. The symmetries particularly imply that the following

Supplementary Table 1. Symmetries of the optimal control path which is described by Eqs. (5) of the main text and represented by spherical coordinates $\theta(t)$ and $\phi(t)$.

symmetry point	$\theta(t)$	$\phi(t)$
$t = \frac{T}{4}$	$\theta\left(\frac{T}{4} + t\right) - \frac{\pi}{4} = \frac{\pi}{4} - \theta\left(\frac{T}{4} - t\right)$	-
$t = \frac{T}{2}$	$\theta\left(\frac{T}{2} + t\right) - \frac{\pi}{2} = \frac{\pi}{2} - \theta\left(\frac{T}{2} - t\right)$	$\phi\left(\frac{T}{2} + t\right) = \phi\left(\frac{T}{2} - t\right)$
$t = \frac{3T}{4}$	$\theta\left(\frac{3T}{4} + t\right) - \frac{3\pi}{4} = \frac{3\pi}{4} - \theta\left(\frac{3T}{4} - t\right)$	-

equations hold:

$$\theta\left(\frac{T}{4}\right) = \frac{\pi}{4}, \quad (\text{S8})$$

$$\theta\left(\frac{T}{2}\right) = \frac{\pi}{2}, \quad (\text{S9})$$

$$\theta\left(\frac{3T}{4}\right) = \frac{3\pi}{4}, \quad (\text{S10})$$

regardless of the value of the switching time T and damping parameter α .

$\theta(t)$ and $\phi(t)$ described by Eqs. (5) of the main text have two asymptotic regimes corresponding to fast and slow switching. For fast switching, $T \ll (\alpha + 1/\alpha)\tau_0$, the solution becomes

$$\theta(t) \approx \frac{\pi t}{T} - \frac{\alpha^2 T^2}{4\alpha^2 T^2 + 64(1 + \alpha^2)^2 \pi^2 \tau_0^2} \sin\left(\frac{4\pi t}{T}\right), \quad (\text{S11})$$

$$\begin{aligned} \phi(t) \approx & \frac{T}{\pi\tau_0(1 + \alpha^2)} \left\{ \sin\left(\frac{\pi t}{T}\right) \right. \\ & \left. + \frac{\alpha^2 T^2}{8\alpha^2 T^2 + 128(1 + \alpha^2)^2 \pi^2 \tau_0^2} \left[\frac{1}{3} \sin\left(\frac{3\pi t}{T}\right) - \frac{1}{5} \sin\left(\frac{5\pi t}{T}\right) \right] \right\}, \end{aligned} \quad (\text{S12})$$

which for $\alpha = 0$ simplifies to

$$\theta(t) = \frac{\pi t}{T}, \quad (\text{S13})$$

$$\phi(t) = \frac{T}{\pi\tau_0} \sin\left(\frac{\pi t}{T}\right). \quad (\text{S14})$$

For slow switching, $T \gg (\alpha + 1/\alpha)\tau_0$, the solution reduces to

$$\theta(t) \approx \arctan\left(e^{\frac{\alpha}{\tau_0(1+\alpha^2)}(t-T/4)}\right) + \arctan\left(e^{\frac{\alpha}{\tau_0(1+\alpha^2)}(t-3T/4)}\right), \quad (\text{S15})$$

$$\begin{aligned} \phi(t) \approx \frac{1}{\alpha} \left\{ \operatorname{arcsinh}\left(e^{\frac{\alpha T}{4\tau_0(1+\alpha^2)}}\right) - \operatorname{arcsinh}\left(e^{\frac{\alpha}{\tau_0(1+\alpha^2)}(T/4-t)}\right) \right. \\ \left. + \operatorname{arcsinh}\left(e^{-\frac{3\alpha T}{4\tau_0(1+\alpha^2)}}\right) - \operatorname{arcsinh}\left(e^{-\frac{\alpha}{\tau_0(1+\alpha^2)}(3T/4-t)}\right) \right\}. \end{aligned} \quad (\text{S16})$$

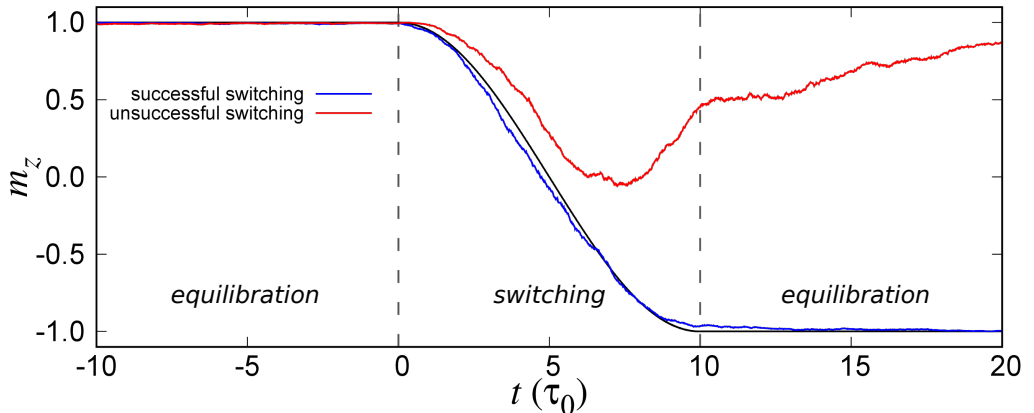
Supplementary Note 3. Spin dynamics simulations

Additional spin dynamics simulations were performed in order to test robustness of the optimal switching protocol for the uniaxial monodomain particle [whose internal energy is given by Eq. (4) in the main text] against thermal fluctuations and perturbations in the material parameters. The simulations were carried out by integrating the Landau-Lifshitz-Gilbert (LLG) equation equipped with the optimal switching pulse [see Eqs. (6)-(7) in the main text] as an external field. The LLG equation was integrated numerically using the semi-implicit scheme B as described in Ref. [S2]. Particular settings for studying effects of temperature and material parameter perturbations are described in the following subsections.

1. Effect of thermal fluctuations

Interaction of the magnetic systems with the heat bath was simulated by including a stochastic term in the LLG equation. Each simulation had three stages: 1) Initial equilibration at zero applied magnetic field to establish Boltzmann distribution; 2) Switching where the optimal magnetic field is applied (note that thermal fluctuations were also included during the switching stage); 3) Final equilibration at zero applied magnetic field. The duration of the switching stage, i.e. the switching time, was chosen to be $10\tau_0$, with τ_0 being the

period of Larmor precession, see the main text. At the end of the third stage, we inspected the value of m_z (z -component of the unit vector \vec{m} in the direction of the magnetic moment); we have taken the value $m_z = -0.5$ as the threshold for the successful switching. A typical outcome of the spin dynamics simulations is illustrated in Supplementary Fig. 4.



Supplementary Figure 4. Effect of thermal fluctuations on the magnetization reversal induced by the optimal switching pulse. Dashed lines mark the beginning and the end of the applied pulse. Blue (red) line shows evolution of the z -component of the normalized magnetic moment during successful (unsuccessful) reversal at finite temperature. Black line corresponds to the zero-temperature reversal. The magnitude of the damping factor is $\alpha = 0.1$.

For each value of temperature and damping constant, we repeated simulations $N = 1000$ times in order to accumulate the proper statistics. The switching success rate is defined as

$$f = N_s/N, \quad (\text{S17})$$

where N_s is the number of successful reversals.

Supplementary Table 2 summarizes results of the finite-temperature spin dynamics simulations. As expected, the reversal success rate decreases as the ratio $\Delta E/\Theta$, with $\Delta E = K$ [see Eq. (4) in the main text] being the energy barrier between the stable states and Θ being thermal energy, becomes smaller. However, when $\Delta E/\Theta \gtrsim 70$, which is a standard requirement to ensure sufficient stability of the magnetic element with respect to thermal fluctuations so as to prevent data loss in magnetic memories [S3, S4], the success rate is

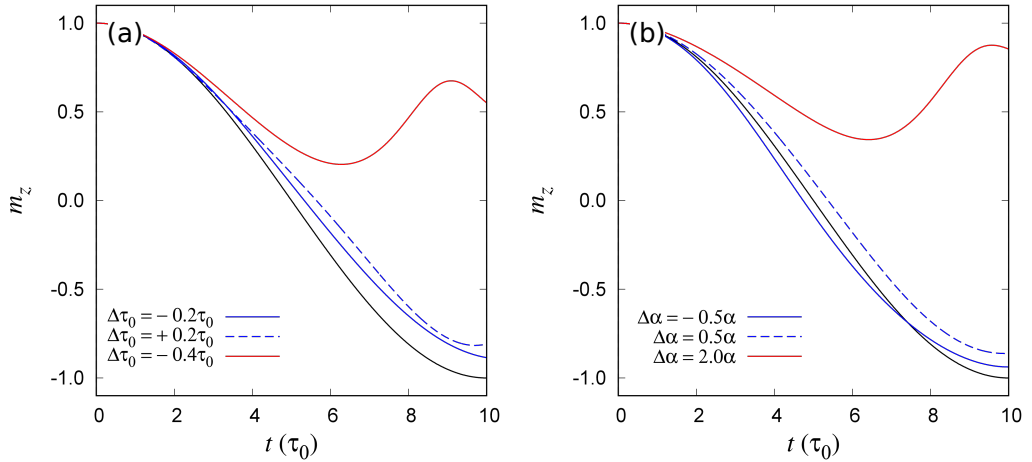
close to unity. This result demonstrates that the optimal switching protocol is robust with respect to thermal fluctuations in the technologically relevant regime.

Supplementary Table 2. Magnetization reversal success rate, f , for several values of the damping factor α , and the ratio $\Delta E/\Theta$, with ΔE being the energy barrier between the stable states and Θ being thermal energy.

$\Delta E/\Theta$	α	f
80	0.01	0.99
80	0.1	0.97
70	0.01	0.98
70	0.1	0.97
10	0.01	0.81
10	0.1	0.77

2. Effect of perturbations in the material parameter values

Parameters determining the magnetization dynamics of the monodomain particle include the damping factor α , anisotropy parameter K and magnetic moment μ . Since the latter two enter the equation of motion solely through the parameter $\tau_0 = \mu(2\gamma K)^{-1}$, with γ being the gyromagnetic ratio, we consider perturbations in α and τ_0 only. In particular, we applied an optimal field pulse derived for a certain value of the intrinsic precession time τ_0 and damping factor α to a particle characterized by perturbed parameter values, $\tau_0 + \Delta\tau_0$, $\alpha + \Delta\alpha$. The switching time was chosen to be $10\tau_0$. Figure 5 illustrates the results of these calculations.



Supplementary Figure 5. Effect of perturbations in the material parameters τ_0 (a) and α (b) on the magnetization reversal induced by the optimal switching pulse. Magnitude of the perturbations $\Delta\tau_0$ and $\Delta\alpha$ is shown in the legend. Blue (red) lines show evolution of the z -component of the normalized magnetic moment during successful (unsuccessful) reversal. Black line corresponds to the reversal in a particle characterized by unperturbed material parameters.

For a particular value of the damping factor, $\alpha = 0.1$, the switching pulse brings the system over the energy barrier if $-0.2\tau_0 < \Delta\tau_0 < 0.2\tau_0$ and $-0.5\alpha < \Delta\alpha < 0.5\alpha$.

-
- [S1] M. Abramowitz and I. A. Stegun, eds., *Handbook of mathematical functions with formulas, graphs, and mathematical tables* (National Bureau of Standards, Washington, DC, 1964).
- [S2] J. H. Mentink, M. V. Tretyakov, A. Fasolino, M. I. Katsnelson, and T. Rasing, *Journal of Physics: Condensed Matter* **22**, 176001 (2010).
- [S3] H. Richter, *Journal of Magnetism and Magnetic Materials* **321**, 467 (2009).
- [S4] M. Krounbi, V. Nikitin, D. Apalkov, J. Lee, X. Tang, R. Beach, D. Erickson, and E. Chen, *ECS Transactions* **69**, 119 (2015).




Article II

Reduction of energy cost of magnetization switching in a biaxial nanoparticle by use of internal dynamics

Badarneh, M. H., Kwiatkowski, G. J., & Bessarab, P. F.

Physical Review B, **107**, 214448. (2023)

Reduction of energy cost of magnetization switching in a biaxial nanoparticle by use of internal dynamics

Mohammad H. A. Badarneh ^{1,*}, Grzegorz J. Kwiatkowski ¹ and Pavel F. Bessarab ^{1,2}

¹Science Institute of the University of Iceland, 107 Reykjavík, Iceland

²Department of Physics and Electrical Engineering, Linnaeus University, SE-39231 Kalmar, Sweden



(Received 24 October 2022; revised 19 June 2023; accepted 22 June 2023; published 29 June 2023)

A solution to energy-efficient magnetization switching in a nanoparticle with biaxial anisotropy is presented. Optimal control paths minimizing the energy cost of magnetization reversal are calculated numerically as functions of the switching time and materials properties, and used to derive energy-efficient switching pulses of external magnetic field. Hard-axis anisotropy reduces the minimum energy cost of magnetization switching due to the internal torque in the desired switching direction. Analytical estimates quantifying this effect are obtained based on the perturbation theory. The optimal switching time providing a tradeoff between fast switching and energy efficiency is obtained. The energy cost of switching and the energy barrier between the stable states can be controlled independently in a biaxial nanomagnet. This provides a solution to the dilemma between energy-efficient writability and good thermal stability of magnetic memory elements.

DOI: [10.1103/PhysRevB.107.214448](https://doi.org/10.1103/PhysRevB.107.214448)

I. INTRODUCTION

Identification of energy limits for the control of magnetization is an important fundamental problem of condensed matter physics. It is also a prerequisite for the development of energy-efficient technologies based on magnetic materials. An important application is magnetic memory where writing of data is realized via selective magnetization reversals in nanoelements. Magnetization reversal can be achieved by various means, including optical pulses [1–3], spin-polarized electric current [4,5], external magnetic [6–9], and electric field [10], microwave-assisted reversal switching [11–13], stress [14], temperature gradient [15,16], etc. The challenge is to minimize the energy cost of the control stimulus generation.

In conventional bit recording, magnetization reversal in a memory element is achieved by applying a static external magnetic field in an opposite direction to the initial magnetization. This results in a relatively slow reversal process governed by damping as long as the magnitude of the external field exceeds the coercive field [17,18]. The coercive field and, thereby, the energy cost of switching can be reduced by decreasing the magnetic anisotropy, but this may lead to unwanted reversals induced by thermal fluctuations due to decrease in the energy barrier separating the stable states. One solution to this dilemma between good thermal stability and energy-efficient writability of magnetic elements for memory applications is use of exchange spring magnets [19], where the energy barrier and the coercive field can be tuned independently.

Decrease in the switching time and/or the switching field can also be achieved via realization of special reversal protocols such as precessional magnetization switching [20].

Precessional switching is typically induced by applying a magnetic field pulse transverse to the initial magnetization, but the pulse duration must be chosen accurately so as to avoid back switching [21]. Additionally, precessional switching is prone to instabilities due to the magnetization ringing effect [22] unless the switching pulse is properly shaped [22–24]. In microwave-assisted reversals, the switching field can also be reduced thanks to resonant energy pumping [11–13,25].

Clearly, the possibility to achieve the reversal by several different methods implies the existence of an optimal protocol, but its definite identification is a challenging problem. Barros *et al.* employed the optimal control theory (OCT) [26] to establish a formal approach to the magnetization switching optimization [27,28]. Within the approach, the optimal switching pulse is found as a result of a direct minimization of the switching cost functional under the constraint defined by a system-specific magnetization dynamics. In our previous article, we revisited the OCT due to Barros *et al.* using unconstrained minimization, which helped us find a complete analytical solution to the energy-efficient reversal of a nanomagnet with uniaxial anisotropy [29].

We also reported decrease in the switching cost for systems with biaxial anisotropy, the result of the internal torque produced by the hard axis [29]. That the internal torque can assist magnetization reversal was recognized earlier for several systems, for example for Co films [30] and Co nanoclusters [31]. The aim of the present study is to explore this effect quantitatively. We focus on nanomagnets with biaxial anisotropy, which can arise due to the demagnetizing field [32]. This scenario is realized in flat elongated nanoelements; see Fig. 1. Such systems are used, e.g., as single bits in in-plane memory [33], or as elements of artificial spin ice arrays [34,35].

We investigate by means of the OCT to what extent the energy cost of magnetization switching can be minimized by

*Corresponding author: mha5@hi.is

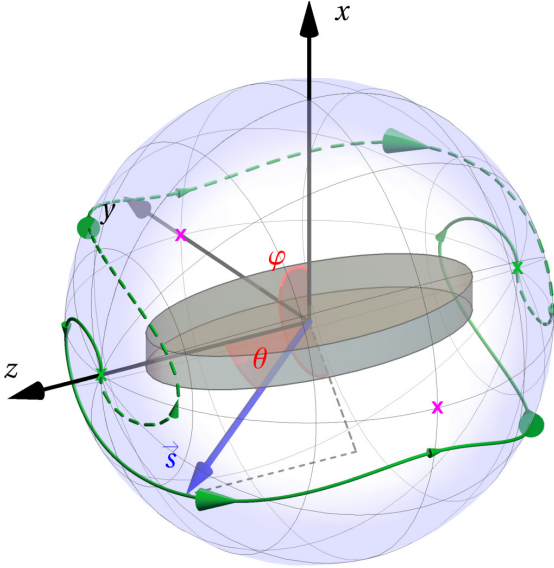


FIG. 1. Optimal switching of a flat elongated nanomagnet representing a biaxial anisotropy system. The direction of the normalized magnetic moment \vec{s} is shown with the blue arrow. Orientations of \vec{s} that correspond to the minima and the saddle points on the energy surface are shown with the green and magenta crosses, respectively. The calculated optimal control paths between the energy minima are shown with the solid and the dashed green lines. The damping factor α is 0.1, the switching time T is $8\tau_0$, and the hard-axis anisotropy constant is twice as large as the easy-axis anisotropy constant. The green arrows along the reversal paths show the velocity of the system at $t = T/6$, $t = T/3$, $t = T/2$, $t = 2T/3$, and $t = 5T/6$, with the size of the arrowheads being proportional to the magnitude of the velocity. The contours of constant azimuthal angle φ (meridians) and polar angle θ (parallels) are shown with thin black lines.

pulse shaping and how this depends on the parameters of the biaxial system and the switching time. Thanks to the internal torque generated by the hard-axis anisotropy, the energy cost can be reduced below the free-macrospin level. Based on the perturbation theory, we show some analytical estimates of the energy cost reduction. We show that in a biaxial system the energy barrier separating the stable states and energy cost of switching between them can be tuned independently, which provides a solution to the magnetic recording dilemma.

The article is organized as follows. Section II provides a theoretical framework for energy-efficient control of magnetization by means of external magnetic field: In Sec. II A, the OCT for magnetic systems is presented and the corresponding Euler-Lagrange equation for the optimal control path (OCP), a dynamical trajectory minimizing the energy cost of magnetization switching, is derived. In Sec. II B, the numerical method for finding OCPs and corresponding energy-efficient control pulses via direct minimization of the cost functional is presented. In Sec. II C, a method for finding an approximate solution for the minimum energy cost is worked out based on the perturbation theory. The application of the methodology

to a biaxial anisotropy system is presented in Sec. III. Conclusions and discussion are presented in Sec. IV.

II. METHODOLOGY

A. Optimal control theory

We define the cost of the magnetization switching as the amount of energy used to generate the control pulse that produces the desired change in the magnetic structure of the system. Assuming the control to be an external magnetic field generated by an electric circuit, the energy cost is mostly defined by Joule heating due to the resistance of the circuit. This is proportional to the square of the electric current integrated over the switching time. Taking into account the linear relationship between the current magnitude and the strength of the generated field, the cost functional can be written as [27,29,36]

$$\Phi = \int_0^T |\vec{B}(t)|^2 dt, \quad (1)$$

where T is the switching time and $\vec{B}(t)$ is the generated external magnetic field at time t . The aim of the OCT is to identify the optimal pulse $\vec{B}_m(t)$ that brings the system to the desired final state such that Φ is minimized. Whenever thermal fluctuations are negligible, the system dynamics can be described by the Landau-Lifshitz-Gilbert (LLG) equation [37],

$$(1 + \alpha^2)\dot{\vec{s}} = -\gamma\vec{s} \times (\vec{b} + \vec{B}) - \alpha\gamma\vec{s} \times [\vec{s} \times (\vec{b} + \vec{B})], \quad (2)$$

where \vec{s} is the normalized magnetic moment vector, γ is the gyromagnetic ratio, α is the damping factor, and \vec{b} is the internal magnetic field defined by the magnetic configuration through the following equation:

$$\vec{b} = \vec{b}(\vec{s}) = -\frac{1}{\mu} \frac{\partial E}{\partial \vec{s}} \quad (3)$$

with μ being the magnetic moment length and E the internal energy of the system.

Both $\vec{B}(t)$ and $\vec{s}(t)$ can be treated as independent variables, and Φ minimized subject to the constraint defined by Eq. (2) [27,28]. Alternatively, the optimal pulse $\vec{B}_m(t)$ can be calculated via unconstrained minimization of Φ . For this, Eq. (2) is used to express the external magnetic field in terms of the dynamical trajectory and the internal magnetic field [29],

$$\vec{B}(\vec{s}, \dot{\vec{s}}) = \frac{\alpha}{\gamma} \dot{\vec{s}} + \frac{1}{\gamma} [\vec{s} \times \dot{\vec{s}}] - \vec{b}^\perp, \quad (4)$$

with $\vec{b}^\perp = \vec{b} - \vec{s}(\vec{b} \cdot \vec{s})$ being the transverse component of the internal field, and the result substituted into Eq. (1). Subsequently, the energy cost Φ becomes a functional of the switching trajectory $\vec{s}(t)$,

$$\Phi = \Phi[\vec{s}(t)] = \int_0^T A(\vec{s}, \dot{\vec{s}}) dt, \quad (5)$$

where $A(\vec{s}, \dot{\vec{s}})$ is given by

$$A(\vec{s}, \dot{\vec{s}}) = \frac{\alpha^2 + 1}{\gamma^2} |\dot{\vec{s}}|^2 - \frac{2\alpha}{\gamma} \dot{\vec{s}} \cdot \vec{b}^\perp - \frac{2}{\gamma} (\vec{s} \times \dot{\vec{s}}) \cdot \vec{b}^\perp + |\vec{b}^\perp|^2. \quad (6)$$

The optimal reversal mechanism can be found by minimizing Φ with respect to path connecting the initial and the final state in the configuration space. Corresponding OCP $\vec{s}_m(t)$ can be identified by solving the Euler-Lagrange equation,

$$\begin{aligned} & \left[(\vec{s} \cdot \vec{b})\hat{I} - \frac{1}{\mu}\hat{H} \right] \left[\frac{1}{\gamma}\dot{\vec{s}} \times \dot{\vec{s}} - \vec{b}^\perp \right] \\ & + \frac{1}{\mu} \left[\vec{s} \cdot \hat{H} \left(\frac{1}{\gamma}\dot{\vec{s}} \times \dot{\vec{s}} - \vec{b}^\perp \right) \right] \vec{s} \\ & - \frac{1 + \alpha^2}{\gamma^2} [\ddot{\vec{s}} - (\vec{s} \cdot \ddot{\vec{s}})\vec{s}] + \frac{1}{\mu\gamma} \vec{s} \times \hat{H}\dot{\vec{s}} = 0 \end{aligned} \quad (7)$$

supplemented by the boundary conditions defined by the initial and the final orientation of the magnetic moment. Here, \hat{I} is a 3×3 identity matrix and \hat{H} is the matrix of second derivatives of the energy E with respect to components of the magnetic moment s_x, s_y, s_z . Note that Eq. (7) is derived under the constraint $|\vec{s}| = 1$. The optimal switching pulse is found upon substituting the OCP into Eq. (4).

It is not possible to find a general analytical solution to the Euler-Lagrange equation except for special cases where the symmetries of the system make it possible to simplify the problem. For example, for a free magnetic moment ($E = 0$) Eq. (7) simplifies to

$$\ddot{\vec{s}} - (\vec{s} \cdot \ddot{\vec{s}})\vec{s} = 0, \quad (8)$$

and the solution is a constant-speed rotation over the shortest distance between the initial and final states. The corresponding energy cost Φ_f for reversing of a free macrospin reads

$$\Phi_f = \pi^2(1 + \alpha^2)/(\gamma^2 T). \quad (9)$$

Another case with a fully analytical solution is the reversal of a macrospin with uniaxial anisotropy [29]. Because of the rotational symmetry of the problem, the separation of variables in the spherical coordinate system is possible if the z direction is chosen to be along the anisotropy axis. This leads to a well-known sine-Gordon equation for the polar angle θ of the magnetic moment and makes the azimuthal angle φ completely defined by θ (see Fig. 1 for the definition of θ and φ),

$$\tau_0^2 \ddot{\theta} = \frac{\alpha^2}{4(1 + \alpha^2)^2} \sin 4\theta, \quad \tau_0 \dot{\varphi} = \frac{\cos \theta}{1 + \alpha^2}, \quad (10)$$

where $\tau_0 = \mu/(2\gamma K)$ defines the timescale, and K is the anisotropy constant. Solution of Eq. (10) is explicitly expressed in terms of the Jacobi amplitude [29]; it describes a superposition of the steady rotation of the moment between the energy minima and its precession around the anisotropy axis, where the precession direction reverses when the system reaches the top of the energy barrier. The corresponding optimal switching field rotates synchronously with the magnetic moment in such a way that it generates the torque only in the direction of increasing θ [29]. The amplitude of the optimal switching field remains constant over time when $\alpha = 0$, but it exhibits a maximum (minimum) before (after) crossing the energy barrier for $\alpha > 0$ [29]. The optimal switching field is always perpendicular to the magnetic moment, see Eq. (4).

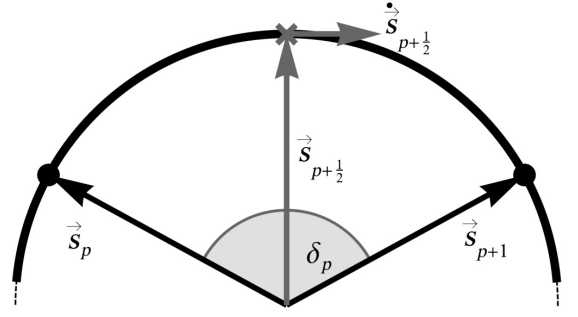


FIG. 2. Illustration of the midpoint scheme used in the numerical method for finding OCPs. Two images \vec{s}_p and \vec{s}_{p+1} are connected by a geodesic path in the configuration space. The position $\vec{s}_{p+1/2}$ and the velocity $\dot{\vec{s}}_{p+1/2}$ at the midpoint of the path are defined by \vec{s}_p and \vec{s}_{p+1} , and the angle δ_p between them.

Nevertheless, most cases are impossible to solve analytically, and numerical methods for finding OCPs are required. One such method is presented in the following.

B. Numerical calculation of optimal control paths

We find OCPs numerically via the direct minimization of the cost functional. For this, we discretize Φ using the midpoint rule [36],

$$\Phi[\vec{s}(t)] \approx \Phi[\mathbf{s}] = \sum_{p=0}^Q |\vec{B}_{p+1/2}|^2 (t_{p+1} - t_p), \quad (11)$$

where $\{t_p\}$ is a partition of the time interval $[0, T]$ such that $0 = t_0 < t_1 < \dots < t_{Q+1} = T$. Here, the partition has a regular spacing, i.e., $t_{p+1} - t_p = \Delta t = T/(Q + 1)$, $p = 0, \dots, Q$. A switching trajectory $\vec{s}(t)$ is represented by a polygeodesic line connecting $Q + 2$ points, referred to as “images”: $\vec{s}(t) \rightarrow \{\vec{s}_0, \vec{s}_1, c, \dots, \vec{s}_{Q+1}\}$, with $\vec{s}_p = \vec{s}(t_p)$. The first image \vec{s}_0 and the last image \vec{s}_{Q+1} correspond to the initial and the final orientation of the magnetic moment, respectively; They are fixed, but Q intermediate images can be moved. The external field $\vec{B}_{p+1/2} \equiv \vec{B}(\vec{s}_{p+1/2}, \dot{\vec{s}}_{p+1/2})$ is defined by the position and the velocity of the magnetic moment at the midpoint of discretization intervals, see Fig. 2, via Eq. (4). On the other hand, both $\vec{s}_{p+1/2}$ and $\dot{\vec{s}}_{p+1/2}$ can be expressed in terms of the position of the images,

$$\vec{s}_{p+1/2} = \frac{\vec{s}_{p+1} + \vec{s}_p}{|\vec{s}_{p+1} + \vec{s}_p|}, \quad (12)$$

$$\dot{\vec{s}}_{p+1/2} = \frac{\delta_p}{\Delta t} \frac{\vec{s}_{p+1} - \vec{s}_p}{|\vec{s}_{p+1} - \vec{s}_p|}, \quad (13)$$

where δ_p is the angle between \vec{s}_p and \vec{s}_{p+1} (see Fig. 2). Note that the magnitude of $\dot{\vec{s}}_{p+1/2}$ is defined by the finite-difference approximation for the angular velocity, and its direction is along the unit vector $(\vec{s}_{p+1} - \vec{s}_p)/|\vec{s}_{p+1} - \vec{s}_p|$ ensuring orthogonality to $\vec{s}_{p+1/2}$. Upon substituting Eqs. (12), (13), and (4) into Eq. (11), the functional Φ becomes a function of a $3Q$ -dimensional vector \mathbf{s} defining the position of the movable images, $\mathbf{s} = (\vec{s}_1, \dots, \vec{s}_Q)$.

Possible OCPs of the magnetization switching can be identified by locating minima of $\Phi(\mathbf{s})$. This is done using the velocity projection optimization (VPO) method [38] and/or the limited-memory Broyden-Fletcher-Goldfarb-Shanno (LBFGS) algorithm [39,40] equipped with the force acting on the movable images,

$$\mathbf{F} = -\nabla^\perp \Phi, \quad (14)$$

where ∇^\perp denotes the gradient projected on the tangent space of the configuration space, which is a curved manifold due to the constraint $|\vec{s}_p| = 1$, $p = 1, \dots, Q$. Explicitly,

$$\nabla^\perp = (\vec{\nabla}_1 - \vec{s}_1(\vec{s}_1 \cdot \vec{\nabla}_1), \dots, \vec{\nabla}_Q - \vec{s}_Q(\vec{s}_Q \cdot \vec{\nabla}_Q)), \quad (15)$$

where $\vec{\nabla}_p \equiv \partial/\partial \vec{s}_p$. For a given number of images involved in the local minimization of $\Phi(\mathbf{s})$, the calculation is considered converged when the magnitude of the force $|\mathbf{F}|$ has dropped below the set tolerance. However, even convergence with a tight force tolerance may be insufficient for a satisfactory resolution of the OCP if Q is not large enough. On the other hand, including too many images in the calculation would result in an unnecessarily high computational effort. Therefore, the following strategy is applied: The OCP search is started with a moderate number of images and the switching path is first converged only to a rather high tolerance so as to bring the images relatively close to the OCP with a reduced computational effort; after that, images are progressively added to the path and minimization of the energy cost is reiterated with a low force tolerance until $\Phi(\mathbf{s})$ stops changing. In this paper, up to $Q = 1500$ movable images was used depending on the parameters of the system and the switching time, with the lowest force tolerance corresponding to the drop of the force by ten orders of magnitude.

Some initial arrangement of the images is needed to start an OCP calculation. This can be generated, for example, by placing the images uniformly along the shortest-distance path between the initial and the final state of the transition, or by using some previously found OCP. It is also recommended to add small random noise to the initial path so as to avoid convergence on maxima or saddle points of $\Phi(\mathbf{s})$ due to possible symmetries in the system. A local minimization of $\Phi(\mathbf{s})$ will most likely converge to the OCP closest to the initially generated path. If multiple OCPs are present between the initial and the final state, several initial estimates need to be produced so as to enable convergence on the various solutions.

C. Perturbation theory

Although it is not possible to obtain a general analytical solution to the Euler-Lagrange equation [see Eq. (7)], some analytical estimates for the energy-efficient switching can still be derived using perturbation theory. For this, we expand Eq. (7) around the free-macrospin solution and obtain the OCP in terms of perturbation series with respect to the parameters defined by the Hamiltonian of the system (see Appendix A for details). The minimum energy cost of switching can be estimated based on the approximate solution for the

OCP. The second-order expansion for Φ_m is used in particular,

$$\Phi_m \approx \Phi_f + \sum_{i=1}^N \epsilon_i \Phi_i + \sum_{i,j=1}^N \epsilon_i \Phi_{ij} \epsilon_j, \quad (16)$$

where N is the number of independent perturbations, ϵ_i is the i th dimensionless perturbation parameter, and Φ_i , Φ_{ij} are the expansion coefficients describing the first- and the second-order corrections, respectively. The explicit expressions for ϵ_i , Φ_i , and Φ_{ij} for the biaxial system are presented in the following.

III. RESULTS

Here, we apply the methodology presented earlier to the magnetization reversal in a biaxial anisotropy system, e.g., to a flat elongated nanomagnet shown in Fig. 1. The internal energy of the system is given by the following equation:

$$E = \xi K s_x^2 - K s_z^2, \quad (17)$$

where the easy axis and the hard axis are along the z and x directions, respectively, $K > 0$ is the anisotropy constant, and ξ is a dimensionless parameter defining the relative strength of the hard-axis anisotropy. The energy surface of the system has two minima at $\vec{s} = (0, 0, 1)$ and $\vec{s} = (0, 0, -1)$, and two saddle points at $\vec{s} = (0, 1, 0)$ and $\vec{s} = (0, -1, 0)$ (see Fig. 1). This model is commonly used to describe in-plane memory bits [33] and elements of artificial spin ice systems [34,35]. Energy-efficient switching between the energy minima in time T is analysed in the following.

A. Optimal protocols for magnetization reversal

Figures 3(a)–3(c) show the calculated OCPs of the magnetization reversal for $\alpha = 0.1$ and various switching times and strengths of the hard-axis anisotropy, superimposed on the energy surface of the system. For short switching time, i.e., when $T \sim \tau_0$, the OCPs deviate weakly from geodesic paths between the energy minima. With increasing T , the OCPs acquire precessional motion around the easy axis, where the sense of precession changes upon reaching the top of the energy barrier at $s_z = 0$.

The $\xi = 0$ case describes a uniaxial-anisotropy system, for which OCPs can be found analytically [29]. Due to the axial symmetry, the OCPs for a fixed switching time are degenerate with respect to overall rotation around the easy axis. For example, the two OCPs shown by the solid and dashed pink lines in Fig. 3(a) are equivalent. In contrast, the axial symmetry is broken when $\xi \neq 0$, which results in the well-separated OCPs between the energy minima. In most cases, there are two equivalent, mirror-symmetric (with respect to the XY plane) OCPs in the biaxial system [28] for a given switching time, and the OCPs differ by a π -angle rotation around the easy axis, see Figs. 3(b) and 3(c) and also Fig. 1. However, more coexisting OCPs can be present for $\xi \gtrsim 4$, where the paths are different by the amount of precession around the initial and the final states (see Fig. 4). Note that the OCPs can break the XY -plane mirror symmetry. For certain parameter values, such asymmetric OCPs deliver the global minimum to the functional Φ , which is the case shown in Fig. 4, or even

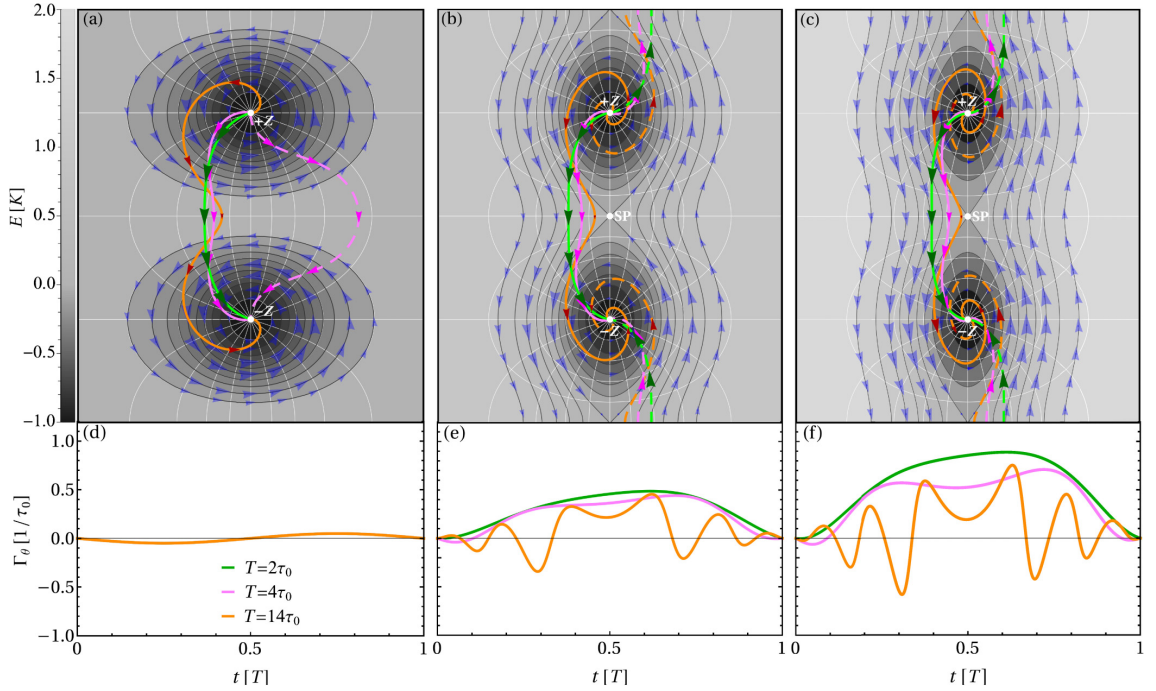


FIG. 3. Transverse Mercator projection [41] of the energy surface of a macrospin with (a) uniaxial anisotropy and biaxial anisotropy with (b) $\xi = 1$ and (c) $\xi = 2$. The meridians and the parallels (see Fig. 1) are shown with thin white lines. The blue arrows show the distribution of the internal torque, with the size of the arrows being proportional to the magnitude of the torque. The calculated OCPs between the energy minima at $+Z$ and $-Z$ are shown with the green, pink, and orange lines for $T = 2\tau_0$, $T = 4\tau_0$, and $T = 14\tau_0$, respectively. The arrows along each OCP show the velocity at $t = T/6$, $t = T/3$, $t = T/2$, $t = 2T/3$, and $t = 5T/6$, where the arrow size codes the magnitude of the velocity. The damping factor α is 0.1. The solid and the dashed lines of the same color show equivalent OCPs. They differ by an arbitrary rotation around the easy axis for the uniaxial case; For finite ξ , the degeneracy is lifted and there are two OCPs, symmetrical with respect to a π -angle rotation around the easy axis, for a given T . Note that the OCPs do not pass through saddle points (SP) on the energy surface. The θ projection of the internal torque along the OCPs from (a)–(c) are shown in (d)–(f), respectively.

represent the only type of solution. Nevertheless, the OCPs never pass through saddle points (SP) on the energy surface, therefore the system does not cross the lowest possible energy barrier within the energy efficient switching protocol.

The distribution of the internal torque $\vec{\Gamma}$ [see the blue arrows in Figs. 3(a)–3(c)] provides an insight into the mechanism of energy-efficient magnetization switching in biaxial systems and explains the position and shape of calculated OCPs. When $\xi = 0$, the torque only generates precession around the easy axis and, in case of nonzero damping, relaxation to the energy minima. In this case, the internal torque does not assist switching since it does not point in the direction of the final state anywhere in the region of the initial state ($s_z > 0$). This behavior is described quantitatively by the component of $\vec{\Gamma}$ in the direction of increasing θ , relevant for the reversal process,

$$\Gamma_\theta = \Gamma_0 \sin \theta [\xi \sin(2\varphi) - 2\alpha \cos \theta (1 + \xi \cos^2 \varphi)], \quad (18)$$

where $\Gamma_0 \equiv [2\tau_0(1 + \alpha^2)]^{-1}$. Γ_θ along the calculated OCPs is shown in Figs. 3(d)–3(f). Positive (negative) Γ_θ signifies positive (negative) contribution of the internal torque to the reversal. For $\xi = 0$, Eq. (18) reduces to $\Gamma_\theta|_{\xi=0} =$

$-\alpha\Gamma_0 \sin 2\theta$. Clearly, $\Gamma_\theta|_{\xi=0} < 0$ for $\theta < \pi/2$ and nonzero α [see Fig. 3(d)].

Adding a hard-axis anisotropy to the system for ($\xi > 0$) gives the contribution to the internal torque in the switching direction in a certain sector of the configuration space, see Figs. 3(b) and 3(c). The location of the calculated OCPs in this sector demonstrates the principle of energy-efficient control, which lies in the effective use of the system's internal dynamics. It is now clear why the OCPs do not pass through the SP, where the internal torque vanishes: It is beneficial to climb up the energy surface where the internal torque picks up and assists the switching process. In particular, Γ_θ is maximized at the equator ($\theta = \pi/2$) when $\varphi = \pi/4$ and $\varphi = 5\pi/4$ [see Eq. (18)]. In an optimal protocol, a balance is reached between the effort in climbing up the energy surface and the strength of the internal torque. As a result, the OCPs cross the equator at an optimal point $\pi/4 < \varphi_m < \pi/2$ or $5\pi/4 < \varphi_m < 3\pi/2$, see Figs. 3(b) and 3(c).

The favorable effect of the torque produced by the hard axis is also evident from the $\Gamma_\theta(t)$ dependencies calculated along the OCPs, see Figs. 3(e) and 3(f). Although there are regions where $\Gamma_\theta < 0$, the θ component of the torque is mostly positive, especially for shorter switching times, and

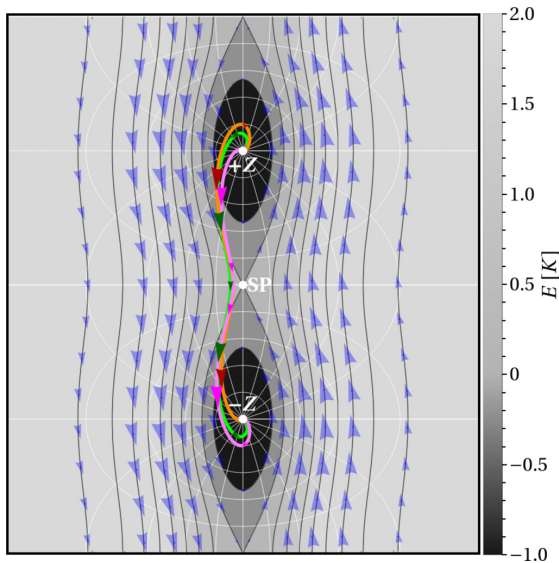


FIG. 4. Calculated OCPs for $\xi = 4$, $\alpha = 0.2$, and $T = 5.314\tau_0$. The notations are the same as in Figs. 3(a)–3(c). The OCP shown with the green line exhibits a mirror symmetry with respect to the XY plane, but the symmetry is broken for the OCPs shown with pink and orange lines. The asymmetric OCPs correspond to the global minimum of Φ for the given parameter values. Note that the asymmetric OCPs can be obtained from one another via reflection in the XY plane. More OCPs can be obtained by a π -angle rotation of the shown OCPs around the easy axis. There are in total six OCPs in the present case.

the magnitude of the torque increases with ξ . It is noteworthy that the asymmetric shape of Γ_θ about $T/2$ —the result of the damping contribution to the torque—does not contradict to the mirror symmetry of the OCPs. For symmetric OCPs, the total torque stays symmetric.

Figure 5 shows the calculated OCPs for $\xi = 1$ and $\alpha = 0.4$. The OCPs look similar to those calculated for weaker damping, but demonstrate less precession, which is particularly seen for longer switching time. Overall, increased damping makes the internal torque deviate stronger from the energy contours toward the energy minima, cf. Fig. 3(b), leading to an increase in the energy cost of switching. This effect is analysed quantitatively in the following section.

The optimal switching pulses of external magnetic field for $T = 14\tau_0$, $\alpha = 0.1$, and $\xi = 0, 1, 2$ are presented in Fig. 6. Note that the pulses are derived from the OCPs presented in Fig. 3 using Eq. (4). As expected, increasing strength of the hard-axis anisotropy leads to overall decrease in the field amplitude, although its peak values can exceed the maximum field value in the $\xi = 0$ case.

The experimental realization of optimal control pulses is a challenging task but still feasible within current pulse shaping technology [23,42–46]. It is worth noting that the optimal switching protocols remain quite stable with respect to thermal fluctuations and material parameter perturbations, as confirmed by our spin dynamics simulations (see Appendix B).

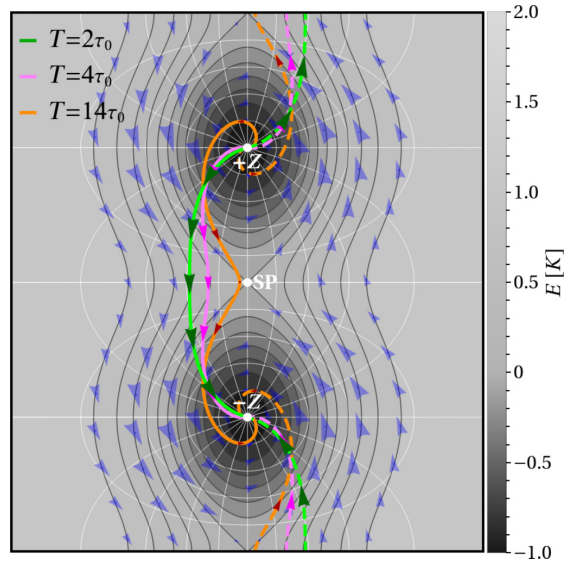


FIG. 5. Calculated OCPs for $\xi = 1$, $\alpha = 0.4$, and several values of the switching time, as indicated in the legend. The notations are the same as in Figs. 3(a)–3(c).

Similarly to the uniaxial case, the pulse is stronger in the first half of the reversal where relaxation works against the switching process, and weaker in the second half where relaxation pushes the system to the desired energy minimum. However, there is a distinct oscillation in the field amplitude associated with the broken axial symmetry of the system. This amplitude oscillation is present even at zero damping, which is in contrast to the uniaxial case where the field amplitude is time independent for $\alpha = 0$ [29]. The amplitude peaks when the magnetic moment deviates most from the easy plane where the energy gradient and, thereby, the internal torque are the largest. Furthermore, the external pulse amplitude is the lowest close to $t = T/2$, where the internal torque brings the system over the barrier. Irrespective of the ξ value, the switching field is always perpendicular to the magnetic moment [see Eq. (4)] and its amplitude B_m demonstrates the symmetry: $B_m(0) = B_m(T)$. Note that $B_m(0) = B_m(T/2) = B_m(T)$ in the $\xi = 0$ case [29].

B. Minimum energy cost of switching

The revealed optimal reversal protocols can now be used to calculate the minimum energy cost of switching Φ_m using Eq. (11) (see also Ref. [29] for the analytical solution for the $\xi = 0$ case). In the following, we always pick the lowest value of the energy cost whenever multiple OCPs are present for a given set of parameters. Figure 7(a) shows Φ_m as a function of the inverse of the switching time for $\alpha = 0.2$ and various strengths of the hard-axis anisotropy. For any ξ value, Φ_m decreases monotonically with T and approaches the universal lower limit

$$\Phi_\infty \equiv 4\alpha K/(\gamma\mu) \quad (19)$$

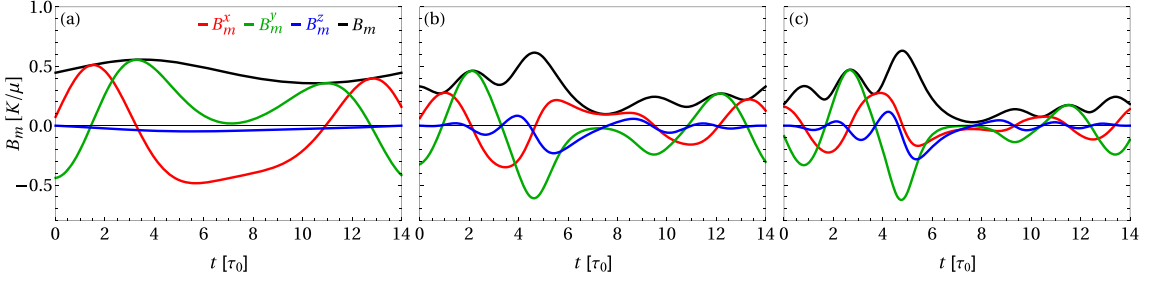


FIG. 6. Calculated optimal switching pulse of external magnetic field for a macrospin with (a) uniaxial anisotropy and biaxial anisotropy with (b) $\xi = 1$ and (c) $\xi = 2$. The switching time T is $14\tau_0$ and the damping parameter α is 0.1. The pulses are derived from the OCPs shown in Figs. 3(a)–3(c).

at infinitely long switching time [28]. Note that Φ_m reaches the limit faster for larger values of ξ . Overall, there is a decrease in Φ_m with ξ , as expected from the distribution of the torque in biaxial systems.

The switching cost for a free macrospin $\Phi_f(T)$ [see the green dashed line in Fig. 7(a)] provides a useful benchmark for evaluating the favorable effect of the torque produced by the hard axis. Notably, the switching cost can be significantly lower than $\Phi_f(T)$ in a certain range of T for finite strengths of the hard-axis anisotropy. For example, $\Phi_m(T)$ becomes almost an order of magnitude smaller than $\Phi_f(T)$ for $\xi = 10$ and $T \approx 2\tau_0$. This is in contrast to the uniaxial-anisotropy case ($\xi = 0$), where $\Phi_m(T) \geq \Phi_f(T)$ (the equality is reached for $\alpha = 0$) for any given T .

The α dependencies of the minimum switching cost for $T = 20\tau_0$ and several values of ξ are shown in Fig. 7(b). Irrespective of the strength of the hard-axis anisotropy, Φ_m is a monotonically increasing function of the damping parameter, approaching the Φ_∞ asymptote when $\alpha \rightarrow \infty$. It is noteworthy that the reduction in the switching cost with ξ becomes more pronounced as α decreases.

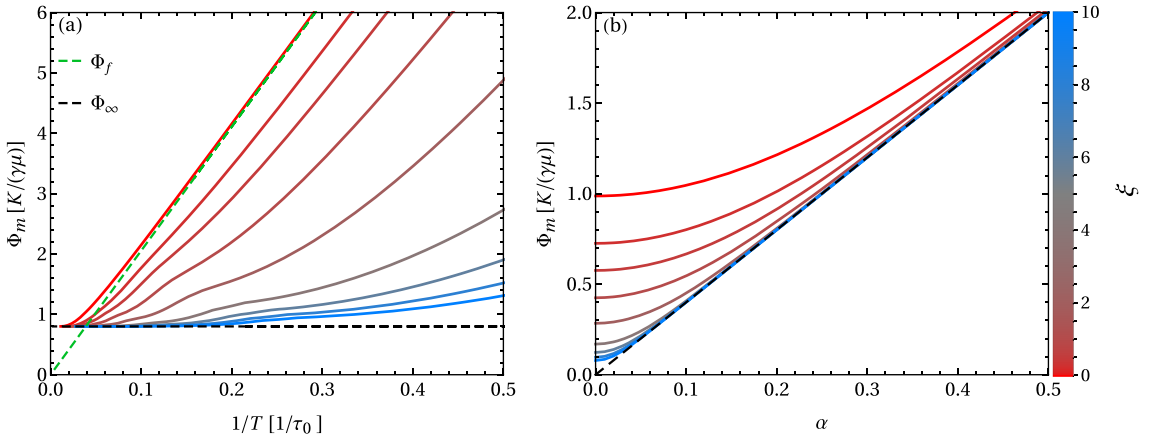


FIG. 7. Minimum energy cost of magnetization reversal as a function of (a) inverse of the switching time for $\alpha = 0.2$, (b) damping parameter for $T = 20\tau_0$, for various ξ values. Green dashed line corresponds to the solution of the reversal of a free macrospin, while the black dashed line shows the infinite switching time asymptotic.

C. Perturbation theory analysis

Both anisotropies in the biaxial system can be treated as independent perturbations to the free macrospin. This results in two dimensionless perturbation parameters $\epsilon_1 \equiv \xi T/\tau_0$ and $\epsilon_2 \equiv T/\tau_0$ defined by the hard- and the easy-axis anisotropy, respectively. The approximation to the minimum energy cost is obtained by substituting the perturbation series for the OCP (see Appendix A) into Eq. (5). The result, up to the second-order terms, reads

$$\Phi_m \approx \Phi_f - \frac{4K}{\gamma\mu}\xi + \frac{K^2T}{2(1+\alpha^2)\mu^2} \times \left[\alpha^2 + \alpha^2\xi + \frac{1}{4}(4+5\alpha^2)\xi^2 \right], \quad (20)$$

where the contributions from the hard-axis anisotropy are recognized by the ξ factor. The smallness of the perturbation parameters, $\epsilon_1, \epsilon_2 \ll 1$, can be translated into the condition on T : $T \ll \tau_0$. Therefore, Eq. (20) can be interpreted as a short switching time approximation for Φ_m .

In Eq. (20), the first and the second terms represent the free macrospin solution and the first-order correction, respectively;

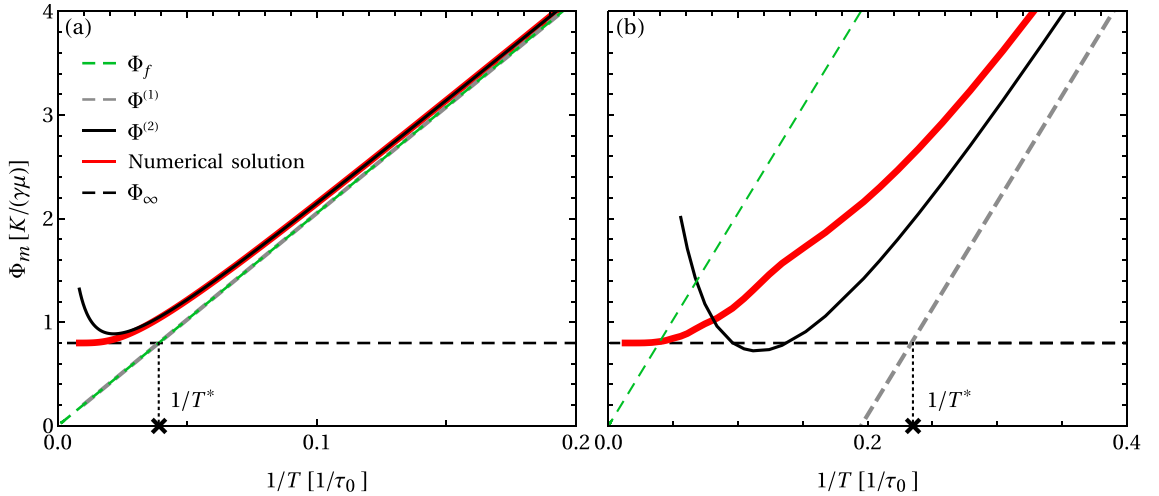


FIG. 8. Approximation for the minimum energy cost of magnetization reversal for a macrospin within the zero- (Φ_f), first- ($\Phi^{(1)}$), and second-order ($\Phi^{(2)}$) perturbation theory [see Eq. (20)], as indicated in the legend, vs the inverse of the switching time. The strength of the hard-axis anisotropy ξ is (a) 0 and (b) 1. Red solid line shows the numerically exact solution. Black dashed line shows the infinite switching time asymptotic. The intersection of the short and the long switching time asymptotes provides the optimal switching time T^* [see Eq. (21)]. The magnitude of α is 0.2.

the rest of the equation describes the second-order correction that includes the terms due to the easy- and the hard-axis anisotropies, as well as the cross term.

Equation (20) clearly shows that the switching cost reduction in biaxial magnets is captured within the linear response to the hard-axis anisotropy. Note that the easy axis does not contribute to the first-order correction; It can be shown in fact that all odd-order corrections vanish in the uniaxial case. The approximation for Φ_m within zero-, first-, and second-order perturbation theory is shown in Fig. 8 for $\alpha = 0.2$. The numerically exact solution for Φ_m is also shown for comparison. The short switching time approximation eventually breaks down as T increases, and Φ_m converges on Φ_∞ .

The minimum energy cost for switching has two clear asymptotics: $\Phi_m = \Phi_f - 4K\xi/(\gamma\mu)$ when $T \rightarrow 0$, and $\Phi_m = \Phi_\infty$ when $T \rightarrow \infty$. Their intersection point

$$T^* = \frac{(1 + \alpha^2)\pi^2}{2(\alpha + \xi)} \tau_0, \quad (21)$$

can be interpreted as an optimal switching time in a sense that increase in T beyond T^* does not lead to a significant reduction in the energy cost. Therefore, T^* provides a tradeoff between the switching speed and energy efficiency [29,47]. Note that T^* decreases with increasing strength of the hard-axis anisotropy.

IV. CONCLUSIONS AND DISCUSSION

In conclusion, we explored by means of the optimal control theory energy-efficient protocols for magnetization reversal in biaxial nanomagnets. We calculated OCPs of the reversal and used them to derive optimal switching pulses of external

magnetic field. We studied the energy cost of switching as a function of the system parameters and the switching time. The internal torque produced by the hard-axis anisotropy can significantly reduce the switching cost: For a given switching time, it can drop below what is needed to reverse a free macrospin, which is impossible in uniaxial-anisotropy systems. However, the energy cost can never be smaller than a universal lower limit defined by the energy barrier and damping [28].

We obtained some analytical estimates regarding the reduction of the energy cost using perturbation theory. In particular, we identified the optimal switching time providing a tradeoff between the switching speed and energy efficiency. The optimal switching time decreases with the strength of the hard-axis anisotropy.

It is important to realize that the decrease in the switching cost can be achieved in biaxial magnets without sacrificing their thermal stability. Indeed, the thermal stability is characterized by the energy barrier separating the stable states. Within harmonic rate theories, this is defined by the energy difference between the saddle point and the initial state minimum [48,49]. In a biaxial system, the energy barrier amounts to K irrespective of the ξ value, see Eq. (17) and the text around it. In contrast, Φ_m depends strongly on ξ , especially for short switching times, which is particularly clear from Fig. 9 (note that Φ_m converges to Φ_∞ for $\xi \rightarrow \infty$ irrespective of the switching time). The possibility to independently maximize both writability and thermal stability of biaxial magnets makes these systems efficient memory elements that provide a solution to the magnetic recording dilemma.

A macrospin approximation is used in the present study, but this is expected to break down with increasing system

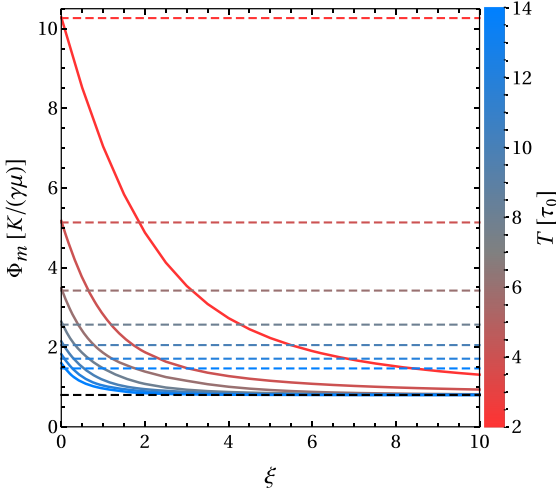


FIG. 9. Minimum energy cost of magnetization reversal as a function of ξ for various T values (solid lines). The dashed color lines show the switching cost for a free macrospin. The magnitude of the damping factor α is 0.2. Black dashed line shows the infinite switching time asymptotic.

size. Even if the initial and the final states are collinear, the transition between them may involve nonuniform rotation of

magnetization such as nucleation and propagation of domain walls [50–54] or excitation of spin waves [36,55–57]. It remains to be seen under what conditions these and possibly other, yet unknown switching mechanisms become optimal in terms of energy efficiency. This is a subject of future study.

ACKNOWLEDGMENTS

The authors would like to thank B. Hjörvarsson, V. Kapaklis, K. A. Thórarinsdóttir, T. Sigurjónsdóttir for helpful discussions and valuable comments. This work was supported by the Icelandic Research Fund (Grants No. 217813 and No. 184949), the University of Iceland Research Fund (Grant No. 15673), and the Swedish Research Council (Grant No. 2020-05110).

APPENDIX A: APPROXIMATE SOLUTION FOR OPTIMAL CONTROL PATH

The Euler-Lagrange equation [see Eq. (7)] in spherical coordinates θ and φ reads

$$\begin{aligned}\ddot{\theta} &= A_0\dot{\varphi}^2 + A_1\dot{\varphi} + A_2, \\ \ddot{\varphi} &= C_0\dot{\theta}\dot{\varphi} + C_1\dot{\theta} + C_2.\end{aligned}\quad (\text{A1})$$

For a biaxial system whose energy is defined by Eq. (17), the coefficients become

$$\begin{aligned}A_0 &= \frac{\sin 2\theta}{2}, & A_1 &= \frac{(2 + \xi)(\sin \theta - 3 \sin 3\theta)}{8(1 + \alpha^2)\tau_0} + \frac{3\xi \cos 2\varphi \sin^3 \theta}{2(1 + \alpha^2)\tau_0}, & A_2 &= \frac{\sin 4\theta(2 + \xi \cos 2\varphi + \xi)^2}{16(1 + \alpha^2)\tau_0^2} + \frac{\xi^2 \sin^2 2\varphi \sin 2\theta}{8(1 + \alpha^2)\tau_0^2}, \\ C_0 &= -2 \cot \theta, & C_1 &= \frac{(2 + \xi)(3 \cos 2\theta + 1) \csc \theta}{4(1 + \alpha^2)\tau_0} - \frac{3\xi \cos 2\varphi \sin \theta}{2(1 + \alpha^2)\tau_0}, & C_2 &= \frac{-\xi(2 + \xi) \sin 2\varphi \cos^2 \theta}{2(1 + \alpha^2)\tau_0^2} + \frac{\xi^2 \sin 4\varphi \sin^2 \theta}{4(1 + \alpha^2)\tau_0^2}.\end{aligned}\quad (\text{A2})$$

We seek for $\theta_m(t)$ and $\varphi_m(t)$ —the solution of Eq. (A1)—in a form of a series in the two perturbation parameters ϵ_1 and ϵ_2 defined by the biaxial anisotropy (see Sec. III C). In particular, the second-order expansion for $\theta_m(t)$ and $\varphi_m(t)$ reads

$$\begin{aligned}\theta_m(t) &\approx \theta_f(t) + \sum_{i=1}^2 \epsilon_i \theta_i(t) + \sum_{i,j=1}^2 \epsilon_i \theta_{ij}(t) \epsilon_j, \\ \varphi_m(t) &\approx \varphi_f(t) + \sum_{i=1}^2 \epsilon_i \varphi_i(t) + \sum_{i,j=1}^2 \epsilon_i \varphi_{ij}(t) \epsilon_j.\end{aligned}\quad (\text{A3})$$

Here, $\theta_f(t) \equiv \pi t/T$ and $\varphi_f(t) \equiv \pi/4, 5\pi/4$ describe the reversal of a free macrospin, and the coefficients $\theta_i(t)$, $\varphi_i(t)$, $\theta_{ij}(t)$, $\varphi_{ij}(t)$ are obtained upon substituting Eqs. (A3) into Eq. (A1) and collecting terms with equal powers of ϵ_1 and ϵ_2 , which gives the following result:

$$\begin{aligned}\theta_1 &= 0, & \theta_2 &= 0, & \varphi_{22} &= 0, & \theta_{11} &= \frac{\sin(2\pi t/T)[4 + 4\alpha^2 + \alpha^2 \cos(2\pi t/T)]}{128\pi^2(1 + \alpha^2)^2}, \\ \theta_{12} &= \theta_{21} = -\frac{\alpha^2 \sin(4\pi t/T)}{128\pi^2(1 + \alpha^2)^2}, & \theta_{22} &= 2\theta_{12}, & \varphi_1 &= -\frac{(8 - \alpha^2)}{64(1 + \alpha^2)} + \frac{\sin(\pi t/T)}{2\pi(1 + \alpha^2)}, \\ \varphi_2 &= 2\varphi_1, & \varphi_{11} &= \varphi_{12} = \varphi_{21} = \frac{(4 + \alpha^2) \cos(2\pi t/T)}{32\pi^2(1 + \alpha^2)^2} - \frac{3(8 - \alpha^2)}{2048(1 + \alpha^2)} + \frac{100 + 73\alpha^2}{480\pi^2(1 + \alpha^2)^2}.\end{aligned}\quad (\text{A4})$$

TABLE I. Magnetization reversal success rate f for several values of the damping factor α , and the ratio $\Delta E/\Theta$, with ΔE being the energy barrier between the stable states and Θ being thermal energy.

$\Delta E/\Theta$	α	f (%)
80	0.01	99.9
80	0.1	99.8
70	0.01	99.6
70	0.1	99.6
50	0.01	98.4
50	0.1	98.9
30	0.01	95.3
30	0.1	96.8

The approximation for the minimum energy cost of switching, Eq. (20), is obtained upon substituting Eq. (A3) into Eq. (5).

APPENDIX B: SPIN DYNAMICS SIMULATIONS

The robustness of the optimal switching protocol for the biaxial monodomain particle [see Eq. (17)] against thermal fluctuations and perturbations in the material parameters was tested by carrying out additional spin dynamics simulations. The simulations involved time integration of the Landau-Lifshitz-Gilbert (LLG) equation equipped with the optimal switching pulse as an external field. The LLG equation was integrated numerically using the semi-implicit scheme B as described in Ref. [58]. Particular settings for studying effects of temperature and material parameter perturbations are described in what follows.

Effect of thermal fluctuations. Interaction of the magnetic systems with the heat bath was simulated by including a stochastic term in the LLG equation. Each simulation had three stages: (1) Initial equilibration at zero applied mag-

netic field to establish Boltzmann distribution; (2) switching where the optimal magnetic field is applied (note that thermal fluctuations were also included during the switching stage); (3) final equilibration at zero applied magnetic field. The duration of the switching stage, i.e., the switching time, was chosen to be $T = 2\tau_0$, while the dimensionless parameter defining the relative strength of the hard-axis anisotropy was $\xi = 5$. At the end of the third stage, we inspected the value of s_z ; we have taken the value $s_z = -0.5$ as the threshold for the successful switching.

For each value of temperature and damping constant, we repeated simulations $L = 1000$ times in order to accumulate the proper statistics. The switching success rate is defined as $f = L_s/L$ where L_s is the number of successful reversals. We find that when the ratio $\Delta E/\Theta > 30$, with $\Delta E = K$ [see Eq. (17)] being the energy barrier between the stable states and Θ being thermal energy, the success rate is over 90%, see Table I. For $\Delta E/\Theta \gtrsim 60$, which is a standard requirement to ensure sufficient stability of the magnetic element with respect to thermal fluctuations so as to prevent data loss in magnetic memories [59,60], the success rate is close to unity. This result demonstrates that the optimal switching protocol is robust with respect to thermal fluctuations in the technologically relevant regime.

Effect of perturbations in the material parameter values. Parameters determining the magnetization dynamics of the monodomain particle include the damping factor α , anisotropy parameter K , the relative strength of the hard-axis anisotropy ξ , and magnetic moment μ . Since K and ξ enter the equation of motion through the parameter τ_0 , we only consider perturbations in α , ξ , and τ_0 . In particular, we applied an optimal field pulse derived for a certain value of τ_0 , ξ , and α to a particle characterized by perturbed parameter values $\tau_0 + \Delta\tau_0$, $\alpha + \Delta\alpha$, and $\xi + \Delta\xi$. The switching time and unperturbed material parameters were chosen to be $T = 2\tau_0$, $\alpha = 0.1$, $\xi = 5$. Figure 10 shows the results of these calculations. The switching pulse brings the system over the energy barrier if the strength of the parameter perturbations is not too large.

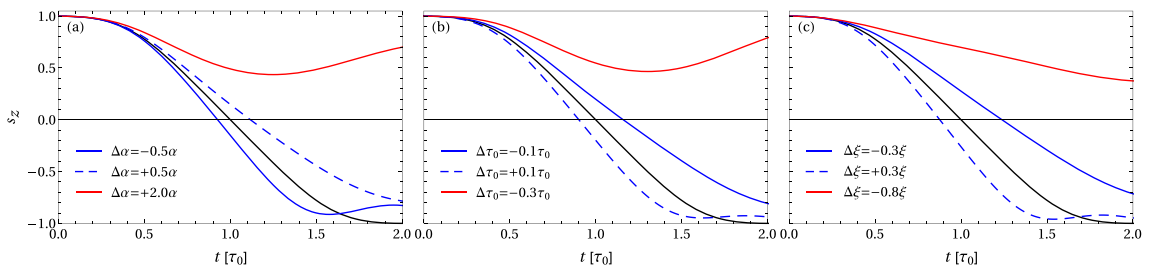


FIG. 10. Effect of perturbations in the material parameters α (a), τ_0 (b), and ξ (c) on the magnetization reversal induced by the optimal switching pulse. Magnitude of the perturbations $\Delta\tau_0$, $\Delta\alpha$, and $\Delta\xi$ is shown in the legend. Blue (red) lines show evolution of the z component of the normalized magnetic moment during successful (unsuccessful) reversal. Black line corresponds to the reversal in a particle characterized by unperturbed material parameters: $\alpha = 0.1$, $\xi = 5$.

- [1] M. Vomer, L. H. F. Andrade, L. Guidoni, E. Beaurepaire, and J.-Y. Bigot, *Phys. Rev. Lett.* **94**, 237601 (2005).
- [2] J. Hohlfield, T. Gerrits, M. Bilderbeek, T. Rasing, H. Awano, and N. Ohta, *Phys. Rev. B* **65**, 012413 (2001).
- [3] L. Le Guyader, S. El Moussaoui, M. Buzzi, R. V. Chopdekar, L. J. Heyderman, A. Tsukamoto, A. Itoh, A. Kirilyuk, T. Rasing, A. V. Kimel, and F. Nolting, *Appl. Phys. Lett.* **101**, 022410 (2012).
- [4] E. B. Myers, D. C. Ralph, J. A. Katine, R. N. Louie, and R. A. Buhrman, *Science* **285**, 867 (1999).
- [5] J. A. Katine, F. J. Albert, R. A. Buhrman, E. B. Myers, and D. C. Ralph, *Phys. Rev. Lett.* **84**, 3149 (2000).
- [6] Z. Z. Sun and X. R. Wang, *Phys. Rev. B* **71**, 174430 (2005).
- [7] Y. Acremann, C. H. Back, M. Buess, O. Portmann, A. Vaterlaus, D. Pescia, and H. Melchior, *Science* **290**, 492 (2000).
- [8] W. K. Hiebert, A. Stankiewicz, and M. R. Freeman, *Phys. Rev. Lett.* **79**, 1134 (1997).
- [9] D. Xiao, M. Tsoi, and Q. Niu, *J. Appl. Phys.* **99**, 013903 (2006).
- [10] Y. Yang, R. B. Wilson, J. Gorchon, C.-H. Lambert, S. Salahuddin, and J. Bokor, *Sci. Adv.* **3**, e1603117 (2017).
- [11] C. Thirion, W. Wernsdorfer, and D. Maily, *Nat. Mater.* **2**, 524 (2003).
- [12] Z. Z. Sun and X. R. Wang, *Phys. Rev. B* **74**, 132401 (2006).
- [13] L. Cai, D. A. Garanin, and E. M. Chudnovsky, *Phys. Rev. B* **87**, 024418 (2013).
- [14] S. Bandyopadhyay, J. Atulashimha, and A. Barman, *Appl. Phys. Rev.* **8**, 041323 (2021).
- [15] A. Pushp, T. Phung, C. Rettner, B. P. Hughes, S.-H. Yang, and S. S. P. Parkin, *Proc. Natl. Acad. Sci. U.S.A.* **112**, 6585 (2015).
- [16] A.-K. Michel, A. C. Niemann, T. Boehnert, S. Martens, J. M. M. Moreno, D. Goerlitz, R. Zierold, H. Reith, V. Vega, V. M. Prida *et al.*, *J. Phys. D* **50**, 494007 (2017).
- [17] G. Bertotti, I. Mayergoyz, C. Serpico, and M. Dimian, *J. Appl. Phys.* **93**, 6811 (2003).
- [18] J. Mallinson, *IEEE Trans. Magn.* **36**, 1976 (2000).
- [19] D. Suess, J. Lee, J. Fidler, and T. Schrefl, *J. Magn. Magn. Mater.* **321**, 545 (2009).
- [20] C. H. Back, D. Weller, J. Heidmann, D. Mauri, D. Guarisco, E. L. Garwin, and H. C. Siegmann, *Phys. Rev. Lett.* **81**, 3251 (1998).
- [21] G. Bertotti, I. Mayergoyz, and C. Serpico, *IEEE Trans. Magn.* **39**, 2504 (2003).
- [22] M. Bauer, R. Lopusnik, J. Fassbender, and B. Hillebrands, *Appl. Phys. Lett.* **76**, 2758 (2000).
- [23] T. Gerrits, H. A. M. van den Berg, J. Hohlfield, L. Bär, and T. Rasing, *Nature (London)* **418**, 509 (2002).
- [24] H. W. Schumacher, C. Chappert, P. Crozat, R. C. Sousa, P. P. Freitas, J. Miltat, J. Fassbender, and B. Hillebrands, *Phys. Rev. Lett.* **90**, 017201 (2003).
- [25] K. Rivkin and J. B. Ketterson, *Appl. Phys. Lett.* **89**, 252507 (2006).
- [26] L. S. Pontryagin, V. G. Boltyanskii, R. V. Gamkrelidze, and E. F. Mishchenko, *The Mathematical Theory of Optimal Processes* (Interscience, New York, 1962).
- [27] N. Barros, M. Rassam, H. Jirari, and H. Kachkachi, *Phys. Rev. B* **83**, 144418 (2011).
- [28] N. Barros, H. Rassam, and H. Kachkachi, *Phys. Rev. B* **88**, 014421 (2013).
- [29] G. J. Kwiatkowski, M. H. A. Badarneh, D. V. Berkov, and P. F. Bessarab, *Phys. Rev. Lett.* **126**, 177206 (2021).
- [30] C. H. Back, R. Allenspach, W. Weber, S. S. P. Parkin, D. Weller, E. L. Garwin, and H. C. Siegmann, *Science* **285**, 864 (1999).
- [31] C. Etz, M. Costa, O. Eriksson, and A. Bergman, *Phys. Rev. B* **86**, 224401 (2012).
- [32] J. A. Osborn, *Phys. Rev.* **67**, 351 (1945).
- [33] K. C. Chun, H. Zhao, J. D. Harms, T.-H. Kim, J.-P. Wang, and C. H. Kim, *IEEE J. Solid-State Circuits* **48**, 598 (2013).
- [34] C. Nisoli, R. Moessner, and P. Schiffer, *Rev. Mod. Phys.* **85**, 1473 (2013).
- [35] G. M. Wysin, W. A. Moura-Melo, L. A. S. Mól, and A. R. Pereira, *J. Phys.: Condens. Matter* **24**, 296001 (2012).
- [36] M. H. A. Badarneh, G. J. Kwiatkowski, and P. F. Bessarab, *Nanosys.: Phys. Chem. Math.* **11**, 294 (2020).
- [37] D. V. Berkov, *Handbook of Magnetism and Advanced Magnetic Materials*, edited by H. Kronmüller and S. Parkin, Vol. 2 (John Wiley, Chichester, UK, 2007), pp. 795–823.
- [38] P. F. Bessarab, V. M. Uzdin, and H. Jónsson, *Comput. Phys. Commun.* **196**, 335 (2015).
- [39] J. Nocedal and S. Wright, *Numerical Optimization* (Springer, New York, 2006).
- [40] A. Ivanov, V. Uzdin, and H. Jónsson, *Comput. Phys. Commun.* **260**, 107749 (2021).
- [41] C. H. Deetz and O. S. Adams, *Elements of Map Projection* (Citeseer, 1945).
- [42] T. Mayer Alegre, A. Torrezan, and G. Medeiros-Ribeiro, *Appl. Phys. Lett.* **91**, 204103 (2007).
- [43] M. Curcic, B. Van Waeyenberge, A. Vansteenkiste, M. Weigand, V. Sackmann, H. Stoll, M. Fähnle, T. Tylliszczak, G. Woltersdorf, C. H. Back, and G. Schutz, *Phys. Rev. Lett.* **101**, 197204 (2008).
- [44] H. Gao, C. Lei, M. Chen, F. Xing, H. Chen, and S. Xie, *Opt. Express* **21**, 23107 (2013).
- [45] A. Bisig, M.-A. Mawass, M. Stärk, C. Moutafis, J. Rhensius, J. Heidler, S. Gliga, M. Weigand, T. Tylliszczak, and B. Van Waeyenberge, *Appl. Phys. Lett.* **106**, 122401 (2015).
- [46] M. Rius, M. Bolea, J. Mora, and J. Capmany, *IEEE Photonics Technol. Lett.* **29**, 7 (2016).
- [47] S. M. Vlasov, G. J. Kwiatkowski, I. S. Lobanov, V. M. Uzdin, and P. F. Bessarab, *Phys. Rev. B* **105**, 134404 (2022).
- [48] P. F. Bessarab, V. M. Uzdin, and H. Jónsson, *Phys. Rev. B* **85**, 184409 (2012).
- [49] G. Fiedler, J. Fidler, J. Lee, T. Schrefl, R. L. Stamps, H. B. Braun, and D. Suess, *J. Appl. Phys.* **111**, 093917 (2012).
- [50] H.-B. Braun, *Phys. Rev. Lett.* **71**, 3557 (1993).
- [51] H.-B. Braun, *Phys. Rev. B* **50**, 16501 (1994).
- [52] M. Bode, O. Pietzsch, A. Kubetzka, and R. Wiesendanger, *Phys. Rev. Lett.* **92**, 067201 (2004).
- [53] S. Krause, G. Herzog, T. Stapelfeldt, L. Berbil-Bautista, M. Bode, E. Y. Vedmedenko, and R. Wiesendanger, *Phys. Rev. Lett.* **103**, 127202 (2009).
- [54] P. F. Bessarab, V. M. Uzdin, and H. Jónsson, *Phys. Rev. Lett.* **110**, 020604 (2013).
- [55] T. Seki, K. Utsumiya, Y. Nozaki, H. Imamura, and K. Takanashi, *Nat. Commun.* **4**, 1726 (2013).

- [56] A. Spinelli, B. Bryant, F. Delgado, J. Fernández-Rossier, and A. F. Otte, *Nat. Mater.* **13**, 782 (2014).
- [57] T. Yamaji and H. Imamura, *Appl. Phys. Lett.* **112**, 202406 (2018).
- [58] J. Mentink, M. Tretyakov, A. Fasolino, M. Katsnelson, and T. Rasing, *J. Phys.: Condens. Matter* **22**, 176001 (2010).
- [59] H. Richter, *J. Magn. Magn. Mater* **321**, 467 (2009).
- [60] M. Krounbi, V. Nikitin, D. Apalkov, J. Lee, X. Tang, R. Beach, D. Erickson, and E. Chen, *ECS Trans.* **69**, 119 (2015).

Article III

Enhancing thermal stability of optimal magnetization reversal in nanoparticles

Badarneh, M. H., Kwiatkowski, G. J., & Bessarab, P. F.

Submitted for publication

Enhancing thermal stability of optimal magnetization reversal in nanoparticles

Mohammad H. A. Badarneh,¹ Grzegorz J. Kwiatkowski,¹ and Pavel F. Bessarab^{1,2,*}

¹Science Institute of the University of Iceland, 107 Reykjavík, Iceland

²Department of Physics and Electrical Engineering, Linnaeus University, SE-39231 Kalmar, Sweden

(Dated: December 19, 2023)

Energy-efficient switching of nanoscale magnets requires the application of a time-varying magnetic field characterized by microwave frequency. At finite temperatures, even weak thermal fluctuations create perturbations in the magnetization that can accumulate in time, break the phase locking between the magnetization and the applied field, and eventually compromise magnetization switching. It is demonstrated here that the magnetization reversal is mostly disturbed by unstable perturbations arising in a certain domain of the configuration space of a nanomagnet. The instabilities can be suppressed and the probability of magnetization switching enhanced by applying an additional stimulus such as a weak longitudinal magnetic field that ensures bounded dynamics of the perturbations. Application of the stabilizing longitudinal field to a uniaxial nanomagnet makes it possible to reach a desired probability of magnetization switching even at elevated temperatures. The principle of suppressing instabilities provides a general approach to enhancing thermal stability of magnetization dynamics.

Introduction — Identification of energy-efficient methods for controlling magnetization is both fundamentally interesting and technologically relevant, e.g., in the development of magnetic memory devices. While magnetization switching in magnetic recording is conventionally achieved by applying a static external magnetic field opposite to the initial magnetization direction, previous studies have demonstrated that the energy cost of this process can be reduced by applying time-varying stimuli, such as a microwave magnetic field [1–5]. For a uniaxial monodomain particle, the optimal magnetization reversal is achieved by a rotating magnetic field synchronized with the precessional dynamics of the magnetic moment [6–9].

The assessment of the stability of energy-efficient switching protocols with respect to ever-present thermal fluctuations is an important problem. The thermal fluctuations perturb the phase locking between the magnetization and the external stimulus. As a result, the magnetization switching can be compromised unless the energy barrier between the initial and final states is much larger than the thermal energy, and the switching time does not exceed a few periods of Larmor precession [9]. This poses a challenge for the realization of energy-efficient switching protocols at elevated temperatures, such as a combination of a microwave and heat-assisted technique. Even at low temperatures, the perturbations in the dynamics can accumulate in time potentially leading to decoherence between the magnetization and the microwave pulse for relatively slow switching which is required for the autoresonance-based protocols [10]. In general, the assessment and control of dynamical stability of magnetic systems is a crucial problem [11, 12].

In this work, we demonstrate that thermal stability of magnetization switching in nanoparticles is mostly defined by unstable perturbations arising in a certain domain of the configuration space of the system. The instabilities can be suppressed by application of a longi-

tudinal magnetic field, which provides a mechanism for enhancing the thermal stability of optimal magnetization switching induced by rotating magnetic field. We show that the success rate of the switching for a given temperature and switching time can be tuned by adjusting the strength of the stabilizing field. Our results provide a perspective on the control of dynamical stability of magnetic systems subject to thermal fluctuations.

Model and spin dynamics simulations — We consider energy-efficient magnetization switching of a uniaxial monodomain nanoparticle characterized by normalized magnetic moment \vec{s} and internal energy $E = -K(\vec{s} \cdot \vec{e}_z)^2/2$, with unit vector \vec{e}_z being the direction and $K > 0$ being the strength of the magnetic anisotropy. The switching is induced by an optimal pulse of a rotating magnetic field $\vec{B}_0(t)$ that, for a given switching time, minimizes the energy cost of switching [see Ref. [9] for the exact time dependence of $\vec{B}_0(t)$ as a function of parameters of the nanoparticle]. The switching dynamics is simulated by the time integration of the the Landau-Lifshitz-Gilbert (LLG) equation:

$$(1 + \alpha^2)\dot{\vec{s}} = -\gamma\vec{s} \times \vec{B}_{\text{eff}} - \alpha\gamma\vec{s} \times (\vec{s} \times \vec{B}_{\text{eff}}), \quad (1)$$

where the dot denotes the time derivative, α is the Gilbert damping factor, γ is the gyromagnetic ratio, and $\vec{B}_{\text{eff}} \equiv \vec{B}_0 + \vec{b} + \vec{\xi}$ is the effective field that, in addition to the switching pulse, includes the internal field $\vec{b} = -\mu^{-1}\partial E/\partial\vec{s} = \mu^{-1}K(\vec{s} \cdot \vec{e}_z)\vec{e}_z$, with μ being the magnitude of the magnetic moment, and the stochastic term $\vec{\xi}$ mimicking interaction of the system with the heat bath [13]. Each simulation involves three stages [9, 14]: i) Initialization of the magnetic moment close to the energy minimum at $s_z = 1$ and equilibration of the system at zero applied magnetic field to establish local Boltzmann distribution at the initial state; ii) Switching where the optimal magnetic field is applied; iii) Final equilibration

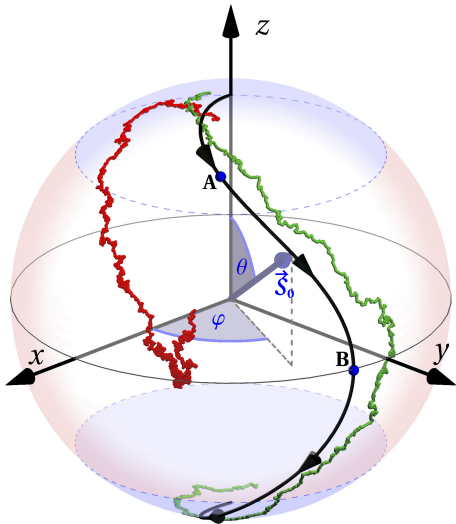


Figure 1. Calculated dynamics of the magnetic moment for a uniaxial nanoparticle induced by the optimal switching magnetic field. The black line shows the zero-temperature trajectory of the magnetic moment which corresponds to the optimal control path $\vec{s}_0(t)$ for the magnetization switching. The green (red) line shows the trajectory for successful (unsuccessful) switching at finite temperature corresponding to the thermal stability factor $\Delta = 20$. Labels A and B show positions of the magnetic moment for which the dynamics of local perturbations in the magnetization is illustrated in the corresponding insets of Fig. 2. The light red (blue) shaded area marks the domain where the perturbation dynamics is unstable (stable). The damping factor α is 0.2, the switching time T is $5\tau_0$.

at zero applied magnetic field. The switching is considered successful if the system is close to the reversed state at $s_z = -1$ at the end of the simulation. Proper statistics of switching is obtained by repeating simulations multiple times.

At zero temperature, the switching trajectory corresponds to optimal control path (OCP) $\vec{s}_0(t)$ between the energy minima of the system (see the black line in Fig. 1): magnetic moment rotates steadily from the initial state at $s_z = 1$ to the final state at $s_z = -1$ and simultaneously precesses around the anisotropy axis, where the sense of precession changes at the top of the energy barrier. Magnetization dynamics is synchronized with the switching field so that \vec{s}_0 is always perpendicular to \vec{B}_0 .

At nonzero temperature, thermal fluctuations perturb the magnetization dynamics making the switching trajectory deviate from the OCP (see the green line in Fig. 1). The deviation can become so large that the phase locking between the switching pulse and the magnetic moment is lost which may eventually prevent the magnetization

reversal (see the red line in Fig. 1).

The success rate of switching depends strongly on the switching time T and the strength of thermal fluctuations, which can be quantitatively described by the thermal stability factor Δ – the ratio between the energy barrier separating the stable states and the thermal energy. For $\Delta \gtrsim 70$, which is a standard case for magnetic memory elements [15, 16], and relatively fast switching with $T \lesssim 10\tau_0$, the switching success rate is close to unity [9]. However, the success rate becomes 0.85 for $\Delta = 20$ and $T = 10\tau_0$, and further decreases with decreasing Δ . Furthermore, an increase in the switching time leads to a higher chance for perturbations in the magnetization dynamics to accumulate, thereby increasing the likelihood of unsuccessful switching even for large thermal stability factors. For example, the switching success rate is 0.7 for $\Delta = 70$ and $T = 30\tau_0$. These effects make it problematic to realize energy-efficient protocols involving multiple precessions around the anisotropy axis, especially at elevated temperature [9]. In the following, we analyze the local dynamics of perturbations to gain insight into the mechanism of decoherence between the switching pulse and the magnetic moment. This analysis ultimately reveals a method to control the thermal stability of magnetization switching.

Local dynamics of perturbations — The interaction of the nanoparticle with the heat bath results in the perturbed trajectory: $\vec{s}(t) = \vec{s}_0(t) + \delta\vec{s}(t)$. If the perturbation becomes too large, the coherence between the switching pulse and the magnetic moment will be lost resulting in a failed switching attempt (see red trajectory in Fig. 1). Therefore, the dynamical stability of the system can be investigated by analyzing the time evolution of the perturbation $\delta\vec{s}(t)$. Linearization of Eq. (1) leads to the following equation of motion for the perturbation:

$$\frac{1 + \alpha^2}{\gamma} \dot{\vec{c}}(t) = \begin{bmatrix} -\alpha & -1 \\ 1 & -\alpha \end{bmatrix} \cdot \begin{bmatrix} w_1 & 0 \\ 0 & w_2 \end{bmatrix} \cdot \vec{c}(t). \quad (2)$$

Here, $\vec{c}(t) = (\epsilon_1, \epsilon_2)^T$ is the two-dimensional vector whose components are the coordinates of $\delta\vec{s}$ in the tangent space of $\vec{s}_0(t)$ defined by the eigenvectors of the Hessian of the energy of the system [17], and w_1, w_2 are the Hessian's eigenvalues given by the following equations:

$$w_1 = B_r + \frac{K}{\mu} \cos(2\theta), \quad (3)$$

$$w_2 = B_r + \frac{K}{\mu} \cos^2\theta, \quad (4)$$

where θ is the polar angle of \vec{s}_0 and B_r is the component of the external magnetic field parallel to \vec{s}_0 . Interestingly, local dynamics of the perturbations does not depend explicitly on the optimal switching pulse, for which $B_r = 0$.

For zero damping, Eq. (2) predicts two types of dynamical trajectories for the perturbation depending on

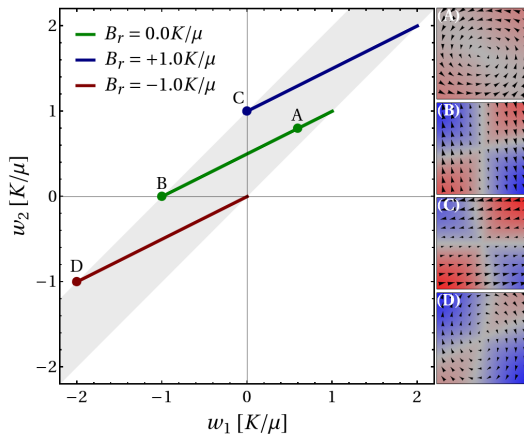


Figure 2. Diagram classifying dynamics of perturbations in the magnetization. The green, blue, and red lines show how the Hessian's eigenvalues w_1 and w_2 change along the zero temperature reversal trajectory (see the black line in Fig. (1)) for three values of the longitudinal magnetic field as indicated in the legend. The right end of the lines correspond to the initial and the final states at the energy minima, while the left end of the lines corresponds to the top of the energy barrier. The gray shaded area marks the domain of possible w_1 , w_2 . Labels A-D indicate pairs of the eigenvalues for which the velocity diagrams illustrating the perturbation dynamics are shown in the insets. The background color in the insets signify whether the amplitude of the perturbation is increasing (blue), decreasing (red), or constant (gray). The damping factor α is 0.2.

the sign of $w_1 w_2$. The trajectories are elliptic, bound for $w_1 w_2 > 0$. For the optimal switching pulse with $B_r = 0$, this regime is realized in the vicinity of the energy minima for $\theta < \pi/4$ and $\theta > 3\pi/4$ (see the blue regions in Fig. 1). However, the perturbation trajectories become hyperbolic, divergent for $\pi/4 \leq \theta \leq 3\pi/4$ where $w_1 w_2 \leq 0$ (see the red region in Fig. 1). It is important to realize that for $\alpha = 0$ the trajectories are equally stable regardless of whether both w_1 and w_2 are positive or negative. Situation changes with non-zero damping: for positive w_1, w_2 , the perturbations tend to relax toward $\vec{s}_0(t)$, while for negative w_1, w_2 , the relaxation amplifies the perturbations. In principle, the latter case is unstable. However, this instability is expected not to significantly affect the magnetization switching if the switching time is short on the time scale of relaxation dynamics which is defined by the damping parameter α . We conclude that the hyperbolic instabilities in the perturbation dynamics are the primary reason for the decoherence between the magnetization and the switching pulse. These instabilities ultimately define thermal stability of magnetization dynamics.

The diagram in Fig. 2 shows evolution of w_1 and w_2

during magnetization switching. For zero B_r , a significant part of the switching trajectory lies in the region of unstable perturbations corresponding to the second quadrant of the diagram where the eigenvalues w_1 and w_2 have different signs. However, the values of w_1 and w_2 can be controlled by application of the longitudinal field B_r . In particular, the hyperbolic instabilities can be removed by shifting w_1 and w_2 either to the first ($B_r > K/\mu$) or to the third ($B_r < -K/\mu$) quadrant of the diagram in Fig. 2. Therefore, the longitudinal external magnetic field can be used as a control parameter to improve thermal stability of magnetization switching. This conclusion is confirmed in the following by direct simulations of magnetization dynamics at elevated temperature ($\Delta = 20$), where the switching is induced by a modified pulse $\vec{B}(t)$:

$$\vec{B}(t) = \vec{B}_0(t) + B_r \vec{s}_0(t). \quad (5)$$

Effect of longitudinal magnetic field on the success rate of magnetization switching — Figure 3 shows calculated success rate of switching as a function of B_r for various values of the switching time and damping parameter. As predicted, the switching success rate reaches unity for $B_r > K/\mu$ regardless of the damping factor α and switching time T . Longer switching times require stronger longitudinal field to reach a certain value of the success rate, as expected, but the threshold value of B_r is not very sensitive to the damping parameter. Interestingly, the success rate as a function of the longitudinal field exhibits a minimum at $B_r \approx 0.5$ that becomes more pronounced for longer switching times. At $B_r = 0.5$, the ratio between the eigenvalues becomes $w_1/w_2 = -1$ at the top of the energy barrier. This corresponds to particularly unstable perturbations in the magnetization dynamics, therefore explaining the drop in the success rate of switching. The longer the switching time, the more time the system spends in the vicinity of the energy barrier [9]. This increases the chances of decoherence between the magnetization and the switching pulse, and lowers the switching probability.

Application of the longitudinal field opposite to \vec{s}_0 ($B_r < 0$) renders both of the eigenvalues w_1, w_2 negative near the energy barrier, thus altering the hyperbolic character of the perturbation dynamics. As a result, the success rate of switching initially increases with rising B_r . However, further increases in B_r lead to the success rate reaching a maximum value before eventually declining (see Fig. 3). The drop in the success rate is a consequence of divergent dynamics due to relaxation, which becomes more prominent for larger damping parameters and longer switching times, as expected.

The switching dynamics is further illustrated by Fig. 4 showing the calculated distribution of the copies of the system in the statistical ensemble at $t = T/2$ for $\alpha = 0.1$, $T = 10\tau_0$, and various values of B_r . For the unper-

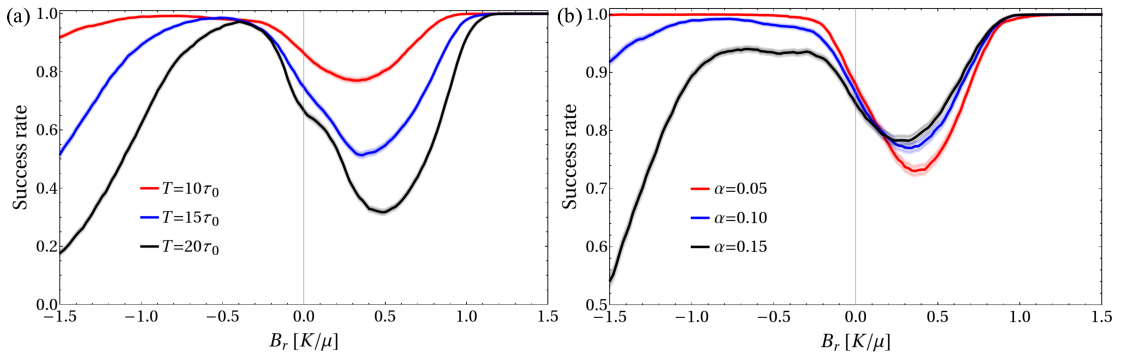


Figure 3. Calculated success rate of magnetization reversal as a function of the longitudinal magnetic field B_r for various values of the switching time T (a) and the damping parameter α (b). In (a), $\alpha = 0.1$; In (b), $T = 10\tau_0$. The thermal stability factor $\Delta = 20$. The shaded areas around the curves indicate the statistical error.

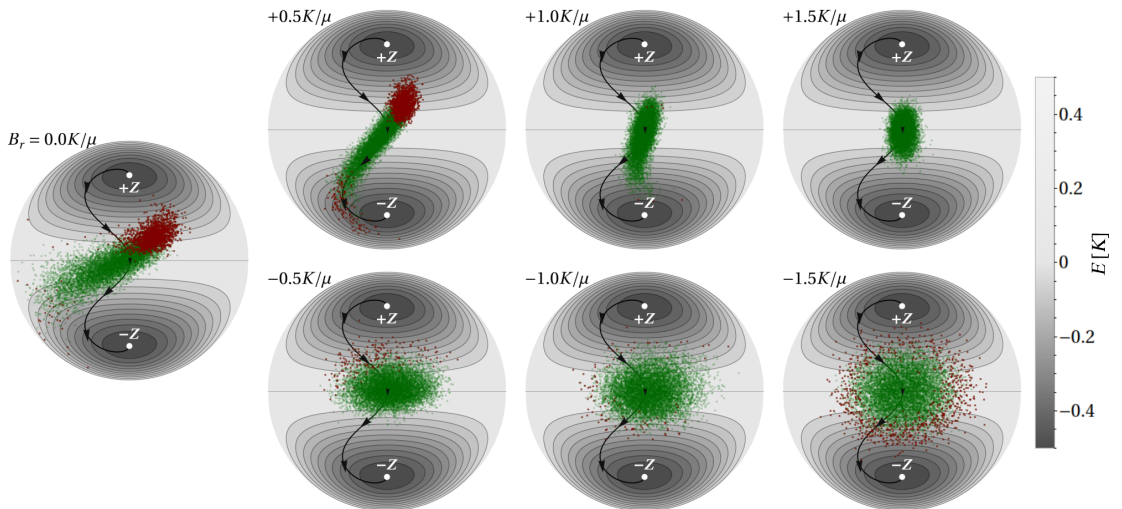


Figure 4. Calculated distribution of the copies of the system in the statistical ensemble at $t = T/2$ and various values of the longitudinal magnetic field, superimposed on the Lambert azimuthal projection [18] of the energy surface of the system. The green dots correspond to the copies that will eventually reach the final state at $-Z$ (successful switching), while the red dots mark the copies that will end up at the initial state at $+Z$ (unsuccessful switching). The black line shows the calculated OCP for the reversal. The damping factor α is 0.1, the thermal stability factor Δ is 20, and the switching time T is $10\tau_0$.

turbed OCP, the system is at the top of the energy barrier. Thermal fluctuations make the system deviate from the OCP. For zero longitudinal field, the system copies spread quite far, with those corresponding to unsuccessful switching trajectories grouped closer to the initial state. For $B_r = 0.5K/\mu$, the distribution of the copies becomes more elongated – the result of the hyperbolic character of the perturbation dynamics at the energy barrier – and the number of the unsuccessful trajectories increases. As B_r increases beyond K/μ , a progressively tighter grouping of the copies around the OCP is

observed due to the convergent dynamics of the perturbations, resulting in the switching probability approaching unity (see Fig. 3).

For negative B_r , the copies of the system are grouped in an ellipse around the OCP even for $B_r = -0.5K/\mu$. For stronger anti-parallel fields, the spread of the distribution increases due to relaxation, resulting in a decrease in the success rate of switching.

Figure 5 shows the calculated dependencies of the success rate on the damping constant α and switching time T for $B_r = 0$ and $B_r = \pm K/\mu$. Both cases with finite lon-

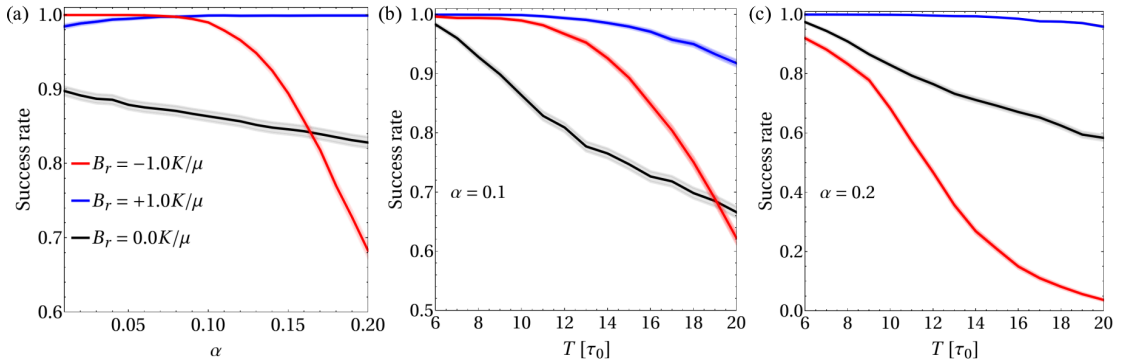


Figure 5. (a) Calculated success rate of magnetization reversal as a function of damping parameter α for switching time $T = 10\tau_0$. (b)-(c) Calculated success rate as a function of T for $\alpha = 0.1$ and $\alpha = 0.2$. The red, blue, and black lines correspond to the three values of the longitudinal magnetic field B_r as indicated in the legend. The thermal stability factor $\Delta = 20$. The shaded areas around the curves indicate the statistical error.

gitudinal field ensure $w_1 w_2 \geq 0$ for the whole switching trajectory. Positive (negative) B_r correspond to convergent (divergent) relaxation of the perturbation dynamics, which explains monotonic increase (decrease) of the switching probability with increasing α . However, for low damping and short switching times, applying the longitudinal field opposite to the magnetic moment ($B_r < 0$) is more efficient than applying the longitudinal field along the magnetic moment ($B_r > 0$), as it requires lower fields to achieve high success rates (see also Fig. 3). Longer switching times result in lower success rate in all considered cases, as expected. The decrease in the success rate with T becomes more (less) pronounced for negative (positive) B_r as damping increases, which is a result of destabilizing (stabilizing) effect of relaxation.

Conclusions — In this work, we uncovered that the instability of energy-efficient protocols for magnetization reversal in nanoparticles with respect to thermal fluctuations originates from the divergent magnetization dynamics arising around the top of the energy barrier of the system. We demonstrated that these instabilities can be eliminated by applying an additional magnetic field either aligned or opposed to the magnetic moment's direction, consequently enhancing the thermal stability of magnetization switching. We examined the success rate of switching at elevated temperatures as a function of various control parameters, such as the switching time, Gilbert damping, and the magnitude of the longitudinal field. The application of a longitudinal field along the magnetic moment consistently increases the success rate of switching, provided that the field magnitude surpasses the characteristic anisotropy field. However, for shorter switching times and weaker damping, employing a smaller field opposed to the magnetic moment can also augment the success rate. Our results warrant a general principle for improved control of magnetization dynamics

by suppressing divergent perturbations.

Acknowledgments — This work was supported by the Icelandic Research Fund (Grant Nos. 217750 and 217813), the University of Iceland Research Fund (Grant No. 15673), and the Swedish Research Council (Grant No. 2020-05110).

* Corresponding author: pavel.bessarab@lnu.se

- [1] C. Thirion, W. Wernsdorfer, and D. Mailly, *Nature Materials* **2**, 524 (2003).
- [2] Z. Z. Sun and X. R. Wang, *Phys. Rev. B* **74**, 132401 (2006).
- [3] K. Rivkin and J. B. Ketterson, *Appl. Phys. Lett.* **89**, 252507 (2006).
- [4] G. Woltersdorf and C. H. Back, *Phys. Rev. Lett.* **99**, 227207 (2007).
- [5] L. Cai, D. A. Garanin, and E. M. Chudnovsky, *Phys. Rev. B* **87**, 024418 (2013).
- [6] Z. Z. Sun and X. R. Wang, *Phys. Rev. Lett.* **97**, 077205 (2006).
- [7] N. Barros, M. Rassam, H. Jirari, and H. Kachkachi, *Phys. Rev. B* **83**, 144418 (2011).
- [8] N. Barros, H. Rassam, and H. Kachkachi, *Phys. Rev. B* **88**, 014421 (2013).
- [9] G. J. Kwiatkowski, M. H. A. Badarneh, D. V. Berkov, and P. F. Bessarab, *Phys. Rev. Lett.* **126**, 177206 (2021).
- [10] G. Klughertz, P.-A. Hervieux, and G. Manfredi, *Journal of Physics D: Applied Physics* **47**, 345004 (2014).
- [11] D. V. Berkov, *IEEE transactions on magnetics* **38**, 2489 (2002).
- [12] X. Wang, Y. Zheng, H. Xi, and D. Dimitrov, *Journal of Applied Physics* **103**, 034507 (2008).
- [13] D. V. Berkov, Magnetization dynamics including thermal fluctuations: Basic phenomenology, fast remagnetization processes and transitions over high-energy barriers, in *Handbook of Magnetism and Advanced Magnetic Materials*, Vol. 2 (John Wiley & Sons, Ltd, 2007) pp.

- 795–823.
- [14] M. H. Badarneh, G. J. Kwiatkowski, and P. F. Bessarab, *Physical Review B* **107**, 214448 (2023).
- [15] H. Richter, *Journal of Magnetism and Magnetic Materials* **321**, 467 (2009), current Perspectives: Perpendicular Recording.
- [16] M. Krounbi, V. Nikitin, D. Apalkov, J. Lee, X. Tang, R. Beach, D. Erickson, and E. Chen, *ECS Transactions* **69**, 119 (2015).
- [17] A. S. Varentcova, S. von Malottki, M. N. Potkina, G. Kwiatkowski, S. Heinze, and P. F. Bessarab, *npj Computational Materials* **6**, 193 (2020).
- [18] J. P. Snyder, *Map projections: A working manual*, Tech. Rep. (U.S. Geological Survey, Washington, D.C., 1987) report.

Article IV

Mechanisms of energy-efficient magnetization switching in a bistable nanowire

Badarneh, M. H., Kwiatkowski, G. J., & Bessarab, P. F.

Nanosystems: Physics, Chemistry, Mathematics **11**, 294 (2020).

Mechanisms of energy-efficient magnetization switching in a bistable nanowire

M. H. A. Badarneh¹, G. J. Kwiatkowski¹, P. F. Bessarab^{1,2,3}

¹Science Institute, University of Iceland, 107 Reykjavík, Iceland

²ITMO University, 197101 St. Petersburg, Russia

³Peter Grünberg Institute and Institute for Advanced Simulation,
Forschungszentrum Jülich, 52425 Jülich, Germany

bessarab@hi.is

PACS 62.23.Hj, 75.10.Dg, 75.30.Ds

DOI 10.17586/2220-8054-2020-11-3-294-300

Theoretical calculations of optimal control paths minimizing the energy cost of the magnetization reversal in 1D magnetic nanowires are presented. The energy-efficient reversal mechanism is studied as a function of the nanowire length and Gilbert damping parameter. For short nanowires, the optimal reversal mechanism corresponds to a uniform rotation of magnetization. If the length of the wire exceeds a certain critical length defined by the material parameters, switching time and damping, a standing spin wave emerges during magnetization switching. Comparison between the calculated optimal control paths and minimum energy paths reveals that realization of high energy efficiency of switching does not necessarily translate to the minimization of the energy barrier between the target magnetic states.

Keywords: magnetic nanowire, magnetization switching, optimal control.

Received: 8 May 2020

1. Introduction

Magnetic nanowires are characterized by an extended length and a nanoscale lateral size [1]. The high length-to-width aspect ratio gives rise to large magnetic anisotropy, which usually results in two stable orientations of magnetization along the wire's axis. Bistability makes magnetic nanowires particularly promising as a basis of novel devices for data transmission, storage and processing where information can be encoded by domains with opposite magnetization [2]. Development of this technology depends critically on the knowledge about mechanisms of the magnetization reversal – a physical implementation of a bit operation. How reversal modes depend on the switching stimulus, magnetic parameters and geometry of the wire is also interesting from a fundamental point of view. Previous theoretical [3–9] and experimental [10–14] studies revealed three main mechanisms of magnetization switching in nanowires, including homogeneous rotation of magnetization and propagation of transverse and vortex domain walls. The possibility to achieve magnetization switching by following different transition mechanisms leads to a notion about the existence of a special mechanism that is optimal in terms of the termination time and energy cost. Definite identification of such optimal reversal mechanisms is particularly important for the development of energy-efficient information technologies based on magnetic nanowires.

In this article, we describe the application of the optimal control theory [15, 16] to the problem of energy-efficient magnetization reversal in a 1D magnetic nanowire. The theory makes it possible to identify optimal control paths (OCPs), i.e. reversal trajectories minimizing the energy cost of magnetization switching. We present numerical calculations of OCPs for various values of the nanowire length and Gilbert damping parameter. We report a crossover between the coherent rotation of magnetization and spin wave assisted switching. Finally, we compare calculated OCPs with the other distinguished paths in the configuration space – the minimum energy paths (MEPs).

The article is organized as follows. In Section 2, theoretical background and details of numerical calculations are described. Results of applications of the optimal control method are given in Section 3. A single macrospin test system is considered first. Then, the application to the magnetization reversal in a nanowire is described. Comparison between calculated OCPs and MEPs is also given. Summary and outlook are presented in Section 4.

2. Methods

Magnetic nanowire is modeled as a 1D chain of N magnetic moments extending along the x axis, where each moment has the same magnitude μ . The energy of the wire is given by a classical Heisenberg-type Hamiltonian:

$$E = -J \sum_{i=1}^{N-1} \vec{s}_i \cdot \vec{s}_{i+1} - K \sum_{i=1}^N (\vec{s}_i \cdot \vec{e}^x)^2, \quad (1)$$

where \vec{s}_i is the unit vector defining the orientation of the magnetic moment at site i . The first term in Eq. (1) describes the exchange interaction between nearest neighbours with ferromagnetic coupling constant $J > 0$. The second term is due to magnetic uniaxial anisotropy characterized by the easy axis \vec{e}^x along the wire and effective parameter $K > 0$. Due to the anisotropy, there are two stable states in the system with moments aligned parallel or antiparallel to the x axis, as illustrated in Fig. 1. The following values of the material parameters are used:

$$J = 562 \text{ meV}, \quad (2)$$

$$K = 37 \text{ meV}, \quad (3)$$

$$\mu = 4076 \mu_B, \quad (4)$$

where μ_B is Bohr magneton.

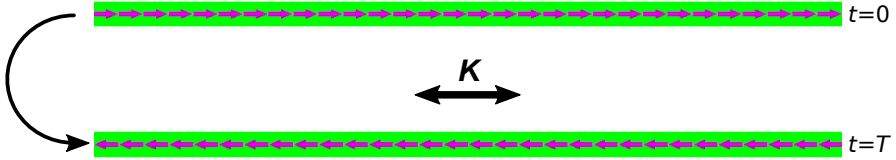


FIG. 1. Stable orientations of the magnetization in a nanowire. The nanowire is represented by a chain of $N = 30$ magnetic moments. Arrows indicate orientation of the moments. Direction of the anisotropy axis is shown with the double-headed arrow. Transition between the states is schematically shown with the black arrow. In the OCP, the initial state is realized at $t = 0$, while the final state is realized at $t = T$

We consider energy-efficient switching of magnetization in the wire from one stable orientation to the other. The switching process is induced by application of external magnetic field. The aim is to find the optimal field that realizes switching in a given time T while minimizing the energy cost. Following Refs. [15, 16], we define the energy cost to be proportional to the amplitude of the applied magnetic field squared:

$$\Phi = \int_0^T \sum_{j=1}^N |\vec{B}_j(t)|^2 dt, \quad (5)$$

where $\vec{B}_j(t)$ is the applied magnetic field at site j and time t . Summation over the sites where magnetic moments are localized is equivalent to spatial integration for a continuous system. The functional Φ needs to be minimized subject to the boundary conditions

$$s_j^x(t=0) = 1, \quad j = 1, \dots, N, \quad (6)$$

$$s_j^x(t=T) = -1, \quad j = 1, \dots, N, \quad (7)$$

and an equation of motion which is taken to be the Landau-Lifshitz-Gilbert equation:

$$(1 + \alpha^2) \dot{\vec{s}}_j = -\gamma \vec{s}_j \times (\vec{B}_{\text{int},j} + \vec{B}_j) - \alpha \gamma \vec{s}_j \times [\vec{s}_j \times (\vec{B}_{\text{int},j} + \vec{B}_j)], \quad (8)$$

where α is the Gilbert damping factor, γ is the gyromagnetic ratio, dot means time derivative and $\vec{B}_{\text{int},j}$ is the internal magnetic field defined through the following equation:

$$\vec{B}_{\text{int},j} = -\frac{1}{\mu} \frac{\partial E}{\partial \vec{s}_j}, \quad (9)$$

with internal energy E given by Eq. (1). Equation (8) can be used to express $\vec{B}_j(t)$ in terms of the dynamical trajectory of the system as well as the magnetic field [16]:

$$\vec{B}_j(t) = \frac{\alpha}{\gamma} \dot{\vec{s}}_j(t) + \frac{1}{\gamma} [\vec{s}_j(t) \times \dot{\vec{s}}_j(t)] - \vec{B}_{\text{int},j}^\perp(t). \quad (10)$$

Here, $\vec{B}_{\text{int},j}^\perp(t)$ is a transverse component of $\vec{B}_{\text{int},j}$:

$$\vec{B}_{\text{int},j}^\perp = \vec{B}_{\text{int},j} - (\vec{B}_{\text{int},j} \cdot \vec{s}_j) \vec{s}_j. \quad (11)$$

Upon substituting Eqs.(10)-(11) into Eq. (5), the energy cost Φ becomes a functional of $\vec{s}_1(t), \vec{s}_2(t), \dots, \vec{s}_N(t)$. Before applying the variational principle to the functional Φ , we discretize the time integral in Eq. (5) using the midpoint rule:

$$\Phi[\vec{s}_1(t), \dots, \vec{s}_N(t)] \approx \Phi(\mathbf{s}) = \sum_{p=0}^Q \sum_{j=1}^N B_{p+\frac{1}{2},j}^2 (t_{p+1} - t_p), \quad (12)$$

where $\{t_p\}$ is a partition of the time interval $[0, T]$ such that $0 = t_0 < t_1 < \dots < t_Q < t_{Q+1} = T$. In the current implementation, all time subintervals are the same, $t_{p+1} - t_p = \Delta t = T/(Q+1)$, $p = 0, \dots, Q$. Trajectory of each magnetic moment, $\vec{s}_j(t)$, is then represented by a polygeodesic line connecting $Q+2$ images, $\vec{s}_j(t): \{\vec{s}_{0,j}, \dots, \vec{s}_{Q+1,j}\}$, with $\vec{s}_{p,j} = \vec{s}_j(t_p)$, where the end points are fixed according to the boundary conditions [see Eqs. (6)-(7)], but Q intermediate images need to be adjusted to an optimal configuration representing the minimum of Φ . The functional Φ is turned into a $3QN$ -dimensional function of image positions, $\Phi = \Phi(\mathbf{s})$, with $\mathbf{s} = \{\vec{s}_{1,1}, \vec{s}_{1,2}, \dots, \vec{s}_{1,N}, \vec{s}_{2,1}, \dots, \vec{s}_{Q,N}\}$. The sought-for optimal control path (OCP) minimizing the energy cost of switching is found by choosing some initial guess for the position of the images and then bringing that to a local minimum of $\Phi(\mathbf{s})$ by means of the (limited-memory) Broyden-Fletcher-Goldfarb-Shanno algorithm [17] adapted to magnetic degrees of freedom [18, 19]. The final, relaxed configuration of the images gives a discrete representation of the OCP. The optimal external field pulse is then obtained from the OCP using Eq. (10).

3. Results and discussion

3.1. Test problem

The numerical method described earlier is first illustrated with calculations of the OCP for the reversal of a single magnetic moment whose internal energy is defined by the anisotropy along z axis,

$$E_1 = -K (\vec{s} \cdot \vec{e}^z)^2. \quad (13)$$

The value of the anisotropy constant K is defined in Eq. (3). The OCP between the energy minima at $s^z = \pm 1$ for this system can be obtained analytically in terms of elliptic functions [16], providing a benchmark for numerical calculations. Discrete representations of the OCP were obtained numerically by relaxing Q movable images to a local minimum of the energy cost Φ . The calculations were considered converged when the magnitude of the gradient of Φ had dropped by twelve orders of magnitude.

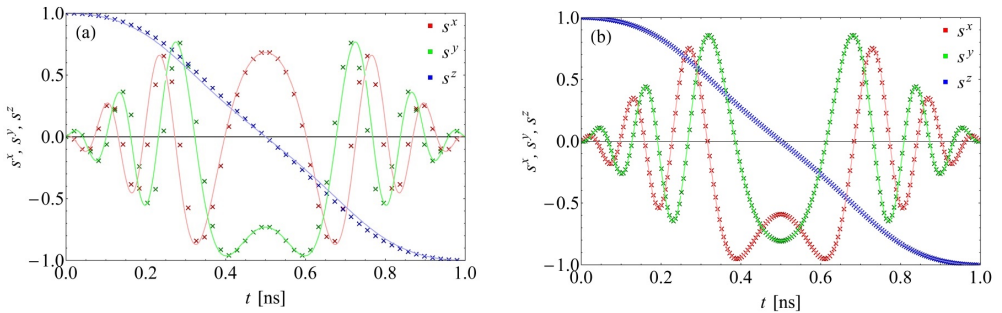


FIG. 2. Evolution of the magnetic moment along the OCP for switching time $T = 1$ ns and damping parameter $\alpha = 0.1$. Analytical solution is given by solid lines, position of images included in the numerical calculations is shown with crosses. $Q = 50$ (a) and $Q = 200$ (b) movable images were used in the numerical OCP calculations

Figure 2 shows comparison between the analytical solution and numerical results obtained for $Q = 50$ and $Q = 200$ images. Both analytical and numerical calculations were performed for $\alpha = 0.1$ and $T = 1$ ns. Agreement between the analytical and numerical results is better for larger number of images, as expected. We have found that using $Q \approx 200$ movable images in the OCP calculations was sufficient to ensure relative error to be below 1%.

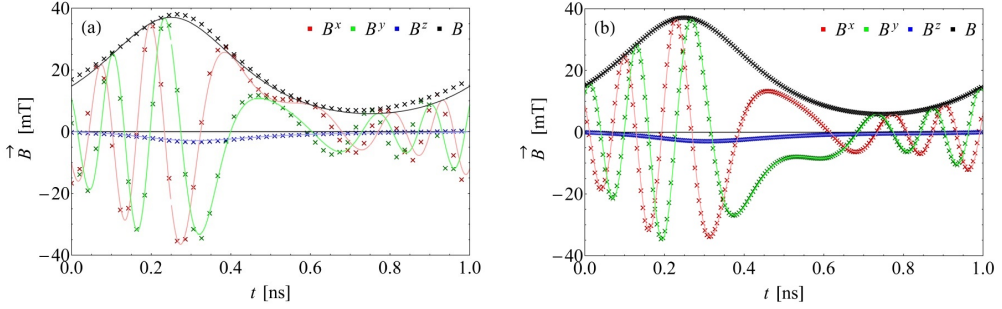


FIG. 3. Optimal switching field derived from the OCP shown in Fig. 2. Switching time $T = 1$ ns and damping parameter $\alpha = 0.1$. Analytical solution is given by solid lines, crosses correspond to position of images included in the numerical OCP calculations. $Q = 50$ (a) and $Q = 200$ (b) movable images were used in the OCP calculations

The calculated OCP describes a steady motion of the magnetic moment from the initial state at $s^z = 1$ to the final state at $s^z = -1$. The monotonic decrease in s^z is accompanied by a precessional motion around the anisotropy axis. Note that the precession reverses its direction upon reaching the top of the energy barrier at $t = T/2$. Fig. 3 shows how the optimal switching field derived from the OCP depends on time. Direction of the calculated optimal field is synchronized with the motion of the magnetic moment so that it is orthogonal to \vec{s} at any time. Moreover, $\vec{B}(t)$ is modulated in amplitude. The internal torque arising due to damping counteracts the switching motion before crossing the energy barrier. Therefore, overall larger field needs to be applied in the first half of the reversal process compared to that in the second half, where the damping torque aids switching. A careful analysis demonstrates that $B(t)$ reaches a maximum at $t = T/4$ and a minimum at $t = 3T/4$, which coincides with the position of the extrema of the polar component of the internal torque.

3.2. Magnetization switching in a nanowire

Fig. 4 illustrates mechanisms of energy efficient magnetization reversal in the nanowire revealed by the OCP calculations. Possible mechanisms include uniform rotation of magnetization [see Fig. 4(a)] and emergence of a standing spin wave with variable wavelength [see Fig. 4(b,c)]. In the case of the coherent rotation mechanism, each magnetic moment in the wire follows the same trajectory presented in the previous subsection.

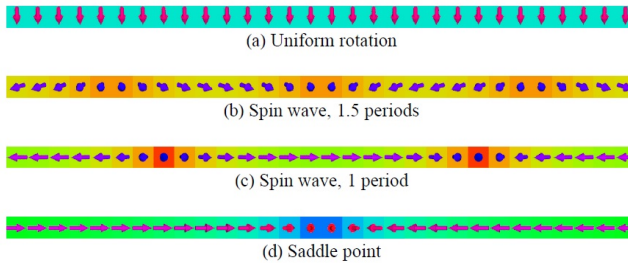


FIG. 4. Magnetic configurations realized along OCPs (a)-(c) and MEP (d) for magnetization switching in the nanowire of length $N = 30$. For the OCPs, configurations at $t = T/2$ are shown where $T = 1$ ns. For the MEP, the saddle point configuration is presented. OCP corresponds to a coherent rotation of magnetic moments for $\alpha = 0.1$ (a) and to spin wave assisted switching with 1.5 wave periods for $\alpha = 0.5$ (b) and with 1 wave period for $\alpha = 0.6$ (c). MEP corresponds to a transient domain wall nucleation and propagation (d)

How the result of the OCP calculations depend on the parameters of the nanowire is illustrated in Fig. 5. Specifically, Fig. 5(a) shows the calculated energy cost Φ of optimal switching as a function of the length N of the wire for the fixed values of the switching time and damping factor with $T = 1$ ns and $\alpha = 0.4$. For relatively short nanowires, Φ

scales linearly with the wire length which is a consequence of the uniform rotation of the magnetization. At $N \approx 60$, a salient point is evident in the $\Phi(N)$ dependence as a result of the crossover to spin-wave assisted switching. As the number of magnetic moments in the wire increases, progressively more periods of the spin wave is observed. Note that the number of the spin-wave periods can assume both half-integer and integer values [see Fig. 4(b,c)].

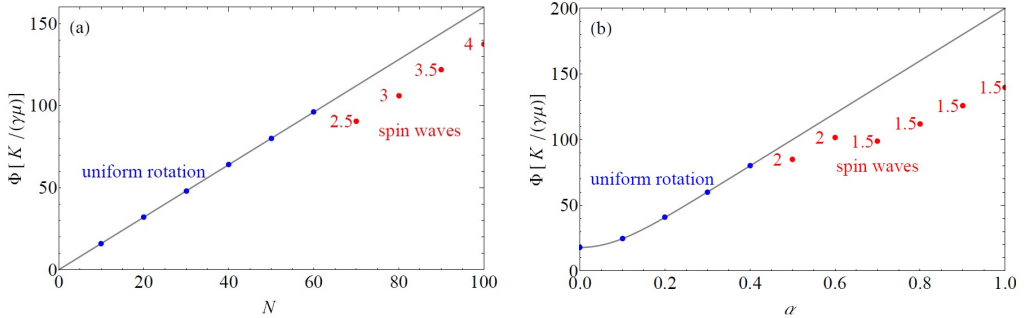


FIG. 5. Minimum energy cost of magnetization switching as a function of the nanowire length N for $\alpha = 0.4$ and $T = 1$ ns (a) and damping parameter α for $N = 50$ and $T = 1$ ns (b). Uniform rotation and spin wave solutions are shown with blue and red circles, respectively. Red labels indicate the number of wavelengths in the spin-wave solutions. Solution for the macrospin approximation is shown with a gray line

Interestingly, the mechanism of the energy-efficient magnetization switching depends on the damping parameter, as illustrated in Fig. 5(b) showing Φ as a function of α for $N = 50$ and $T = 1$ ns. When $\alpha \leq 0.4$, the optimal switching mechanism corresponds to the uniform rotation of magnetization and $\Phi(\alpha)$ follows the dependence predicted in Ref. [16]. As the damping factor increases, the switching mechanism changes to the spin-wave, first with 2 periods and then with 1.5 periods. Each crossover event is accompanied by a sharp change in the slope of the $\Phi(\alpha)$ function.

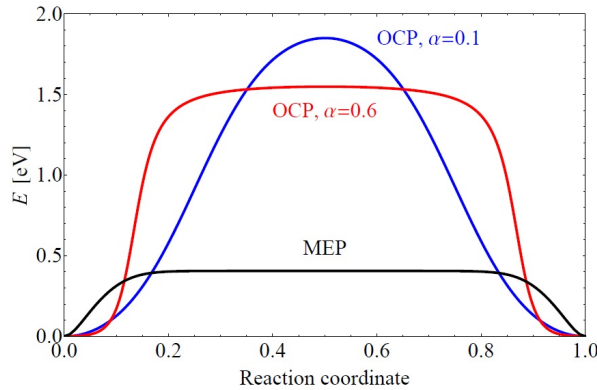


FIG. 6. Variation of the energy of the nanowire with $N = 50$ along the MEP (black line) and the OCP for $T = 1$ ns, $\alpha = 0.1$ (blue line) and $\alpha = 0.6$ (red line). Reaction coordinate is defined as a normalized displacement along the path

It is informative to compare the calculated OCPs with the other distinguished paths in the configuration space – minimum energy paths (MEPs). An MEP connecting two stable states is a path lying lowermost on the energy surface, and the point of the highest energy along the MEP – a saddle point on the energy surface – defines the energy barrier between the states, the primary quantity determining their thermal stability within harmonic rate theories [20–22]. The MEPs for the magnetization reversal in the nanowires considered here were calculated using the geodesic nudged elastic band method [23]. The MEP changes from the uniform rotation to the nucleation and propagation of a transient

domain wall when the length of the wire exceeds the domain wall width. The saddle-point configuration for the nanowire with $N = 30$ is shown in Fig. 4(d) as an example. These paths are very different from the calculated OCPs. In fact, the OCP calculations have never converged on the path corresponding to the single domain wall propagation, even if the initial guess was set to be the MEP. Note that an MEP is completely defined by the energy surface of the system, and, therefore, is independent of dynamical properties such as the switching time or damping parameter. In contrast, an OCP is a valid dynamical trajectory, which in particular results in that the mechanism of energy-efficient magnetization reversal depends on α , as demonstrated above.

Finally, the energy variations along the calculated MEP and OCPs are compared in Fig. 6 for the nanowire with $N = 50$. The energy profile along the MEP is flat, which is a typical feature for the domain wall propagation costing almost no energy. The energy barrier derived from the MEP is much smaller than the highest energy point along the OCPs. This result suggests a conclusion that optimal control of magnetization switching which minimizes the energy cost does not necessarily translate into the minimization of the energy barrier between the target states. Following an OCP involves rotation of magnetic moments in such a way that the influence of the external stimulus is minimized, but the system's internal dynamics is effectively used to aid magnetization switching.

4. Conclusion

In conclusion, we have studied energy-efficient magnetization reversal in bistable magnetic nanowires by means of OCP calculations. The calculations demonstrate that short nanowires reverse their magnetization via coherent rotation that combines a steady advancement toward the target state and precession around the anisotropy axis. If the length of the wire exceeds a certain critical length, a standing spin wave emerges during magnetization switching. In contrast to MEPs, OCPs demonstrate dependence on dynamical parameters such as switching time and damping. Our results deepen the understanding of the optimal control of magnetization switching in nanowires.

Acknowledgements

The authors would like to thank T. Sigurjónsdóttir for helpful discussions. This work was funded by the Russian Science Foundation (Grant No. 19-72-10138), the Icelandic Research Fund (Grant No. 184949-052), and the Alexander von Humboldt Foundation.

References

- [1] Staño M., Fruchart O. Magnetic nanowires and nanotubes. In *Handbook of Magnetic Materials*, vol. 27, ed. Brück E. Elsevier, Amsterdam, 2018, P. 155–267.
- [2] Parkin S. S. P., Hayashi M. Thomas L. Magnetic domain-wall racetrack memory. *Science*, 2008, **320**(5873), P. 190–194.
- [3] Hinze D., Nowak U. Magnetization switching in nanowires: Monte Carlo study with fast Fourier transformation for dipolar fields. *Journal of Magnetism and Magnetic Materials*, 2000, **221**, P. 365–372.
- [4] Hertel R., Kirschner J. Magnetization reversal dynamics in nickel nanowires. *Physica B*, 2004, **343**, P. 206–210.
- [5] Allende S., Altbir D., Salcedo E., Bahiana M., Sinnecker J. P. Propagation of transverse domain walls in homogeneous magnetic nanowires. *Journal of Applied Physics*, 2008, **104**, P. 013907.
- [6] Ivanov Yu. P., Vázquez M., Chubykalo-Fesenko O. Magnetic reversal modes in cylindrical nanowires. *Journal of Physics D: Applied Physics*, 2013, **46**, P. 485001.
- [7] Goussev A., Lund R. G., Robbins J. M., Slastikov V., Sonnenberg C. Domain wall motion in magnetic nanowires: an asymptotic approach. *Proceedings of the Royal Society A*, 2013, **469**, P. 20130308.
- [8] Sultan M. S., Atkinson D. Aspect-ratio dependence of magnetization reversal in cylindrical ferromagnetic nanowires. *Materials Research Express*, 2016, **3**, P. 056104.
- [9] Kuncser A., Antohe S., Kuncser, V. A general perspective on the magnetization reversal in cylindrical soft magnetic nanowires with dominant shape anisotropy. *Journal of Magnetism and Magnetic Materials*, 2017, **423**, P. 34–38.
- [10] Endo Y., Fujimoto H., Kumano S., Matsumura Y., Sasaki I., Kawamura Y., Yamamoto M., Nakatani R. Study on the magnetization reversal process in a magnetic nanowire and a magnetic dot observed by magnetic field sweeping magnetic force microscopy measurements. *Journal of Applied Physics*, 2008, **103**, P. 07D918.
- [11] Lavín R., Denardin J. C., Escrig J., Altbir D., Cortés A., Gómez H. Angular dependence of magnetic properties in Ni nanowire arrays. *Journal of Applied Physics*, 2009, **106**, P. 103903.
- [12] Vivas L. G., Vázquez M., Escrig J., Allende S., Altbir D., Leitao D. C., Araujo J. P. Magnetic anisotropy in CoNi nanowire arrays: Analytical calculations and experiments. *Physical Review B*, 2012, **85**, P. 035439.
- [13] García J., Prida V. M., Vivas L. G., Hernando B., Barriga-Castro E. D., Mendoza-Reséndez R., Luna C., Escrig J., Vázquez M. Magnetization reversal dependence on effective magnetic anisotropy in electroplated Co-Cu nanowire arrays. *Journal of Materials Chemistry C*, 2015, **3**, P. 4688.
- [14] Sultan M. S. Angular dependence of switching behaviour in template released isolated NiFe nanowires. *Physics Letters A*, 2017, **381**, P. 3896–3903.
- [15] Barros N., Rassam M., Jirari H., Kachkachi H. Optimal switching of a nanomagnet assisted by microwaves. *Physical Review B*, 2011, **83**, P. 144418.

- [16] Kwiatkowski G. J., Badarneh M. H. A., Berkov D. V., Bessarab P. F. Optimal control of magnetization reversal in a monodomain particle by means of applied magnetic field, 2020. arXiv: <https://arxiv.org/abs/2004.02146>.
- [17] Nocedal J., Wright S. J. *Numerical Optimization* (2nd ed.). Springer, New York, 2006.
- [18] Ivanov A. V., Uzdin V. M., Jónsson H. Fast and robust algorithm for the energy minimization of spin systems applied in an analysis of high temperature spin configurations in terms of skyrmion density, 2019. arXiv: <https://arxiv.org/abs/1904.02669>.
- [19] Ivanov A. V., Dagbjartsson D., Tranchida J., Uzdin V. M., Jónsson H. Efficient optimization method for finding minimum energy paths of magnetic transitions. *Journal of Physics: Condensed Matter*, 2020. *Accepted manuscript*. URL: <https://doi.org/10.1088/1361-648X/ab8b9c>.
- [20] Kramers H. Brownian motion in a field of force and the diffusion model of chemical reactions. *Physica*. 1940. **7**. P. 284–304.
- [21] Vineyard G. H. Frequency factors and isotope effects in solid state rate processes. *Journal of Physics and Chemistry of Solids*, 1957, **3**, P. 121–127.
- [22] W. F. Brown W. F. Thermal fluctuation of fine ferromagnetic particles. *IEEE Transactions on Magnetics*, 1979, **MAG-15**, P. 1196–1208.
- [23] Bessarab P. F., Uzdin V. M., Jónsson H. Method for finding mechanism and activation energy of magnetic transitions, applied to skyrmion and antivortex annihilation. *Computer Physics Communications*, 2015, **196**, P. 335–347.

Bibliography

- [1] Suess, Dieter, et al. *Exchange spring recording media for areal densities up to 10 Tbit/in²*, J. Magn. Magn. Mater. **290**, 551-554, (2005).
- [2] Parkin, Stuart SP, Masamitsu Hayashi, and Luc Thomas, *Magnetic domain-wall racetrack memory*, Science **320**, 190-194 (2008).
- [3] Kiselev, Nikolai S., et al. *Chiral skyrmions in thin magnetic films: new objects for magnetic storage technologies?*, J. Phys. D: Appl. Phys. **44**, 392001 (2011).
- [4] Bogdanov, Alexei N., and D. A. Yablonskii. *Thermodynamically stable “vortices” in magnetically ordered crystals. The mixed state of magnets*, Zh. Eksp. Teor. Fiz **95**, 178 (1989).
- [5] Hsu, Pin-Jui, et al. *Electric-field-driven switching of individual magnetic skyrmions*, Nat. Nanotechnol. **12**, 123-126 (2017).
- [6] Fert, Albert, Vincent Cros, and Joao Sampaio. *Skyrmions on the track*, Nat. Nanotechnol. **8**, 152-156 (2013).
- [7] Van Waeyenberge, Bartel, et al. *Magnetic vortex core reversal by excitation with short bursts of an alternating field*, Nature **444**, 461-464 (2006).
- [8] Mallinson, John C. *Damped gyromagnetic switching*, IEEE Trans. Magn. **36**, 1976-1981 (2000).
- [9] Bauer, Martin, et al. *Switching behavior of a Stoner particle beyond the relaxation time limit*, Phys. Rev. B **61**, 3410 (2000).
- [10] Bertotti, G., et al. *Comparison of analytical solutions of Landau–Lifshitz equation for “damping” and “precessional” switchings*, J. Appl. Phys. **93**, 6811-6813 (2003).
- [11] Bertotti, Giorgio, Isaak D. Mayergoyz, and Claudio Serpico. *Critical fields and pulse durations for precessional switching of thin magnetic films*, IEEE Trans. Magn. **39**, 2504-2506 (2003).
- [12] Choi, Byoung-Chul, et al. *Ultrafast magnetization reversal dynamics investigated by time domain imaging*, Phys. Rev. Lett. **86**, 728 (2001).
- [13] Schumacher, H. W., et al. *Precessional magnetization reversal in microscopic spin valve cells*, IEEE Trans. Magn. **38**, 2480-2483 (2002).

BIBLIOGRAPHY

- [14] Kaka, Shehzaad, and Stephen E. Russek. *Precessional switching of submicrometer spin valves*, Appl. Phys. Lett. **80**, 2958-2960 (2002).
- [15] Xiao, Q. F., et al. *Dynamics of vortex core switching in ferromagnetic nanodisks*, Appl. Phys. Lett. **89**, 262507 (2006).
- [16] Weigand, Markus, et al. *Vortex core switching by coherent excitation with single in-plane magnetic field pulses*, Phys. Rev. Lett. **102**, 077201 (2009).
- [17] Cowburn, Russell P. *Change of direction*, Nat. Mater. **6**, 255-256 (2007).
- [18] Kammerer, Matthias, et al. *Magnetic vortex core reversal by excitation of spin waves*, Nat. Commun. **2**, 279 (2011).
- [19] Chubykalo, O., et al. *Langevin dynamic simulation of spin waves in a micro-magnetic model*, Phys. Rev. B. **65**, 184428 (2002).
- [20] Dobin, A. Yu, and R. H. Victora. *Intrinsic nonlinear ferromagnetic relaxation in thin metallic films*, Phys. rev. lett. **90**, 167203 (2003).
- [21] Kashuba, A. *Domain instability during magnetization precession*, Phys. rev. lett. **96**, 047601 (2006).
- [22] Yanes, R., et al. "Modeling of microwave-assisted switching in micron-sized magnetic ellipsoids." Phys. Rev. B. **79**, 224427 (2009).
- [23] Pontryagin, Lev Semenovich. *Mathematical theory of optimal processes*, Routledge, 2018.
- [24] Barros, N., et al. *Optimal switching of a nanomagnet assisted by microwaves*, Phys. Rev. B. **83**, 144418 (2011).
- [25] Barros, N., H. Rassam, and H. Kachkachi. *Microwave-assisted switching of a nanomagnet: Analytical determination of the optimal microwave field*, Phys. Rev. B. **88**, 014421 (2013).
- [26] Vlasov, Sergei M., et al. *Optimal protocol for spin-orbit torque switching of a perpendicular nanomagnet*, Phys. Rev. B **105**, 134404 (2022).
- [27] Tretiakov, Oleg A., Y. Liu, and Ar Abanov. *Minimization of ohmic losses for domain wall motion in a ferromagnetic nanowire*, Phys. rev. lett. **105**, 217203 (2010).
- [28] Blügel, Stefan, et al. *Topological matter-topological insulators, skyrmions and majoranas*, No. FZJ-2017-02620. Halbleiter-Nanoelektronik, 2017.
- [29] Aharoni, Amikam. *Introduction to the Theory of Ferromagnetism*, **109**, 2000 Clarendon Press
- [30] Cullity, Bernard Dennis, and Chad D. Graham. *Introduction to magnetic materials*, John Wiley & Sons, 2011.

- [31] Dzyaloshinsky, Igor. *A thermodynamic theory of “weak” ferromagnetism of anti-ferromagnetics*, J. Phys. Chem. Solids **4**, 241-255 (1958).
- [32] Moriya, Tôru. *Anisotropic superexchange interaction and weak ferromagnetism*, Phys. Rev. **120**, 91 (1960).
- [33] Kuchkin, Vladyslav M., and Nikolai S. Kiselev. *Skyrmions and antiskyrmions in monoaxial chiral magnets*, arXiv preprint arXiv:2305.13003 (2023).
- [34] Kuchkin, Vladyslav M., et al. *Heliknoton in a film of cubic chiral magnet*, Front. Phys. **11**, 1201018 (2023).
- [35] Kuchkin, Vladyslav M., et al. *Tailed skyrmions—An obscure branch of magnetic solitons*, Front. Phys. **11**, 302 (2023).
- [36] Kuchkin, Vladyslav M., and Nikolai S. Kiselev. *Turning a chiral skyrmion inside out*, Phys. Rev. B **101**, 064408 (2020).
- [37] Kuchkin, Vladyslav M., Pavel F. Bessarab, and Nikolai S. Kiselev. *Thermal generation of droplet soliton in chiral magnet*, Phys. Rev. B **105**, 184403 (2022).
- [38] Hadjipanayis, George C., and Gary A. Prinz, eds. *Science and technology of nanostructured magnetic materials*, **259**. Springer Science & Business Media, 2013.
- [39] Gubin, Sergei P., et al. *Magnetic nanoparticles: preparation, structure and properties*, Russ. Chem. Rev. **74**, 489 (2005)
- [40] Stoner, Edmund Clifton, and E. P. Wohlfarth. *A mechanism of magnetic hysteresis in heterogeneous alloys*, Philos. Trans. Royal Soc. A **240**, 599-642 (1948)
- [41] Wernsdorfer, W., et al. *Nucleation of magnetization reversal in individual nano-sized nickel wires*, Phys. Rev. Lett. **77**, 1873 (1996)
- [42] Wernsdorfer, W., et al. *Mesoscopic effects in magnetism: Submicron to nanometer size single particle measurements*, J. Appl. Phys **81**, 5543-5545 (1997)
- [43] Wernsdorfer, W., et al. *Experimental evidence of the Néel-Brown model of magnetization reversal*, Phys. Rev. Lett **78**, 1791 (1997)
- [44] D. V. Berkov, *Handbook of Magnetism and Advanced Magnetic Materials*, edited by H. Kronmüller and S. Parkin, Vol. 2 (John Wiley, Chichester, UK, 2007), pp. 795–823.
- [45] Kwiatkowski, Grzegorz J., et al. *Optimal control of magnetization reversal in a monodomain particle by means of applied magnetic field*, Phys. rev. Lett. **126**, 177206 (2021).
- [46] Badarneh, Mohammad H., et al. *Mechanisms of energy-efficient magnetization switching in a bistable nanowire*, Nanosystems: Physics, Chemistry, Mathematics **11**, 294 (2020).

BIBLIOGRAPHY

- [47] Badarneh, Mohammad HA, Grzegorz J. Kwiatkowski, and Pavel F. Bessarab. *Reduction of energy cost of magnetization switching in a biaxial nanoparticle by use of internal dynamics*, Phys. Rev. B. **107**, 214448 (2023).
- [48] Griffiths, David J. *Introduction to electrodynamics* (2005).
- [49] Barman, Anjan, and Jaivardhan Sinha. *Spin dynamics and damping in ferromagnetic thin films and nanostructures*, Vol. 1. Cham: Springer International Publishing, 2018.
- [50] Bessarab, Pavel F., Valery M. Uzdin, and Hannes Jónsson. *Method for finding mechanism and activation energy of magnetic transitions, applied to skyrmion and antivortex annihilation*, Comput. Phys. Commun **196**, 335-347 (2015).
- [51] Nocedal, Jorge, and Stephen J. Wright, eds. *Numerical optimization*, New York, NY: Springer New York, 1999.
- [52] Ivanov, Aleksei V., Valery M. Uzdin, and Hannes Jónsson. *Fast and robust algorithm for energy minimization of spin systems applied in an analysis of high temperature spin configurations in terms of skyrmion density*, Comput. Phys. Commun **260**,107749 (2021).
- [53] Murray, Richard M., et al. *A mathematical introduction to robotic manipulation*, CRC press, 1994.
- [54] Nocedal, Jorge, and Stephen J. Wright, eds. *Numerical optimization*, New York, NY: Springer New York, 1999.
- [55] Fortin, Michel, and Roland Glowinski. *Augmented Lagrangian methods: applications to the numerical solution of boundary-value problems*, Elsevier, 2000.
- [56] Thirion, Christophe, Wolfgang Wernsdorfer, and Dominique Maily. *Switching of magnetization by nonlinear resonance studied in single nanoparticles*, Nat. Mater. **2**, 524-527 (2003)
- [57] Sun, Z. Z., and X. R. Wang. *Magnetization reversal through synchronization with a microwave*, Phys. Rev. B **74**, 132401 (2006)
- [58] Rivkin, K., and J. B. Ketterson. *Magnetization reversal in the anisotropy-dominated regime using time-dependent magnetic fields*, Appl. Phys. Lett **89**, 252507 (2006)
- [59] Woltersdorf, Georg, and Christian H. Back. *Microwave assisted switching of single domain $Ni_{80}Fe_{20}$ elements*, Phys. rev. lett. **99**, 227207 (2007)
- [60] Cai, Liufei, Dmitry A. Garanin, and Eugene M. Chudnovsky. *Reversal of magnetization of a single-domain magnetic particle by the ac field of time-dependent frequency*, Phys. Rev. B **87**, 024418 (2013)

- [61] Sun, Z. Z., and X. R. Wang. *Theoretical limit of the minimal magnetization switching field and the optimal field pulse for Stoner particles*, Phys. rev. lett. **97**, 077205 (2006).
- [62] Klughertz, Guillaume, Paul-Antoine Hervieux, and Giovanni Manfredi. *Autoresonant control of the magnetization switching in single-domain nanoparticles*, J. Phys. D: Appl. Phys **47** 345004 (2014)
- [63] Berkov, Dmitri V. *Fast switching of magnetic nanoparticles: Simulation of thermal noise effects using the Langevin dynamics*, IEEE trans. Magn. **38**, 2489-2495 (2002)
- [64] Wang, Xiaobin, et al. *Thermal fluctuation effects on spin torque induced switching: Mean and variations*, J. Appl. Phys **103** (2008).
- [65] Brown Jr, William Fuller. *Thermal fluctuations of a single-domain particle*, Phys. rev. **130**, 1677 (1963).
- [66] Varentcova, Anastasiia S., et al. *Toward room-temperature nanoscale skyrmions in ultrathin films*, NPJ Comput. Mater. **6**, 193 (2020).
- [67] Chun, Ki Chul, et al. *A scaling roadmap and performance evaluation of in-plane and perpendicular MTJ based STT-MRAMs for high-density cache memory*, IEEE J. Solid-State Circuits. **48**, 598-610 (2012).
- [68] Mikeska, H. J. *Solitons in a one-dimensional magnet with an easy plane*, Journal of Physics C: Solid State Physics **11**, L29 (1978).
- [69] Cuevas-Maraver, Jesús, Panayotis G. Kevrekidis, and Floyd Williams. *The sine-Gordon model and its applications*, Nonlinear systems and complexity **10** (2014).
- [70] Abramowitz, Milton, and Irene A. Stegun, eds. *Handbook of mathematical functions with formulas, graphs, and mathematical tables*. Vol. 55. US Government printing office, 1968.
- [71] Deetz, Charles Henry, and Oscar Sherman Adams. *Elements of map projection*. US Government Printing Office, 1945.
- [72] Gerrits, Th, et al. *Ultrafast precessional magnetization reversal by picosecond magnetic field pulse shaping*, Nature **418**, 509-512 (2002).
- [73] Mayer Alegre, T. P., A. C. Torrezan, and Gilberto Medeiros-Ribeiro. *Microstrip resonator for microwaves with controllable polarization*, Appl. Phys. Lett. **91**, (2007).
- [74] Curcic, Michael, et al. *Polarization selective magnetic vortex dynamics and core reversal in rotating magnetic fields*, Phys. rev. lett. **101**, 197204 (2008).
- [75] Gao, Hongbiao, et al. *A simple photonic generation of linearly chirped microwave pulse with large time-bandwidth product and high compression ratio*, Opt. Express **21**, 23107-23115 (2013).

BIBLIOGRAPHY

- [76] Bisig, Andre, et al. *Dynamic domain wall chirality rectification by rotating magnetic fields*, Appl. Phys. Lett. **106**, (2015).
- [77] Back, C. H., et al. *Minimum field strength in precessional magnetization reversal*, Science **285**, 864-867 (1999).
- [78] Etz, Corina, et al. *Accelerating the switching of magnetic nanoclusters by anisotropy-driven magnetization dynamics* Phys. Rev. B **86**, 224401 (2012).
- [79] Osborn, John A. *Demagnetizing factors of the general ellipsoid*, Phys. Rev. **67**, 351 (1945).
- [80] Nisoli, Cristiano, Roderich Moessner, and Peter Schiffer. *Colloquium: Artificial spin ice: Designing and imaging magnetic frustration*, Rev. Mod. Phys. **85**, 1473 (2013).
- [81] Wysin, Gary M., et al. *Magnetic anisotropy of elongated thin ferromagnetic nano-islands for artificial spin ice arrays*, J. Phys. Condens. Matter **24**, 296001 (2012).
- [82] Bessarab, Pavel F., Valery M. Uzdin, and Hannes Jónsson. *Harmonic transition-state theory of thermal spin transitions*, Phys. Rev. B **85**, 184409 (2012).
- [83] Fiedler, G., et al. *Direct calculation of the attempt frequency of magnetic structures using the finite element method*, J. Appl. Phys. **111** (2012).
- [84] Vlasov, Sergei M., et al. *Optimal protocol for spin-orbit torque switching of a perpendicular nanomagnet*, Phys. Rev. B **105**, 134404 (2022).
- [85] Staňo, Michal, and Olivier Fruchart. *Magnetic nanowires and nanotubes*, Handbook of magnetic materials. Vol. **27** Elsevier, 2018.
- [86] Hinzke, Denise, and Ulrich Nowak. *Magnetization switching in nanowires: Monte Carlo study with fast Fourier transformation for dipolar fields*, J. Magn. Magn. Mater. **221**, 365-372 (2000).
- [87] Hertel, Riccardo, and Jürgen Kirschner. *Magnetization reversal dynamics in nickel nanowires*, Phys. B: Condens. Matter **343**, 206-210 (2004).
- [88] Allende, S., et al. *Propagation of transverse domain walls in homogeneous magnetic nanowires*, J. Appl. Phys. **104**, 013907 (2008).
- [89] Ivanov, Yu P., M. Vázquez, and O. Chubykalo-Fesenko. *Magnetic reversal modes in cylindrical nanowires*, J. Phys. D: Appl. Phys **46**, 485001 (2013).
- [90] Endo, Yasushi, et al. *Study on the magnetization reversal process in a magnetic nanowire and a magnetic dot observed by magnetic field sweeping magnetic force microscopy measurements*, J. Appl. Phys. **103**, 07D918 (2008).
- [91] Lavin, R., et al. *Angular dependence of magnetic properties in Ni nanowire arrays*, J. Appl. Phys. **106**, 103903 (2009).

- [92] Vivas, L. G., et al. *Magnetic anisotropy in CoNi nanowire arrays: analytical calculations and experiments* Phys. Rev. B **85**, 035439 (2012).
- [93] García, J., et al. *Magnetization reversal dependence on effective magnetic anisotropy in electroplated Co–Cu nanowire arrays*, J. Mater. Chem. C **3**, 4688-4697 (2015).
- [94] Sultan, Musaab Salman. *Angular dependence of switching behaviour in template released isolated NiFe nanowires*, Phys. Lett. A **381**, 3896-3903 (2017).
- [95] Back, C. H., et al. *Magnetization reversal in ultrashort magnetic field pulses*, Phys. Rev. Lett. **81**, 3251 (1998).
- [96] Berkov, Dmitri V. *Magnetization Dynamics Including Thermal Fluctuations: Basic Phenomenology, Fast Remagnetization Processes and Transitions Over High-energy Barriers*, Handbook of Magnetism and Advanced Magnetic Materials (2007).
- [97] Mentink, J. H., et al. *Stable and fast semi-implicit integration of the stochastic Landau–Lifshitz equation*, J. Phys. Condens. Matter, **22**, 176001 (2010).
- [98] Bhatti, Sabpreet, et al. *Spintronics based random access memory: a review*, Mater. Today **20**, 530-548 (2017).
- [99] Snyder, John Parr. *Map projections—A working manual*, **1395**, US Government Printing Office, 1987.
- [100] Werschnik, J., and E. K. U. Gross. *Quantum optimal control theory*, J. Phys. B **40**, R175 (2007).
- [101] Rabitz, Herschel. *The role of theory in the laboratory control of quantum dynamics phenomena*, Theor. Chem. Acc. **109**, 64-70 (2003).
- [102] Tang, Chunli, et al. *Spin dynamics in van der Waals magnetic systems*, Phy. Rep. **1032**, 1-36 (2023).
- [103] Boix-Constant, Carla, et al. *Multistep magnetization switching in orthogonally twisted ferromagnetic monolayers*, Nat. Mater. 1-7 (2023).
- [104] Schryer, Norman L., and Laurence R. Walker. *The motion of 180 domain walls in uniform dc magnetic fields*, J. Appl. Phys **45**, 5406-5421 (1974).
- [105] Bogdanov, Alexei N., and D. A. Yablonskii. *Thermodynamically stable “vortices” in magnetically ordered crystals. The mixed state of magnets*, Zh. Eksp. Teor. Fiz **95**, 178 (1989).
- [106] Van Waeyenberge, Bartel, et al. *Magnetic vortex core reversal by excitation with short bursts of an alternating field*, Nature **444**, 461-464 (2006).

BIBLIOGRAPHY

- [107] Aron, Camille, et al. *Magnetization dynamics: path-integral formalism for the stochastic Landau–Lifshitz–Gilbert equation*, J. Stat. Mech.: Theory Exp **2014**, P09008 (2014).
- [108] Gardiner, Crispin, and Peter Zoller. *Quantum noise: a handbook of Markovian and non-Markovian quantum stochastic methods with applications to quantum optics*, Springer Science & Business Media, 2004.
- [109] Eriksson, Olle, et al. *Atomistic spin dynamics: foundations and applications*, Oxford university press, 2017.
- [110] d’Aquino, Massimiliano, Claudio Serpico, and Giovanni Miano. *Geometrical integration of Landau–Lifshitz–Gilbert equation based on the mid-point rule*, J. Comput. Phys **209**, 730-753 (2005).
- [111] Sun, Z. Z., and X. R. Wang. *Strategy to reduce minimal magnetization switching field for Stoner particles*, Phys. Rev. B. **73**, 092416 (2006).
- [112] Podio-Guidugli, P. *On dissipation mechanisms in micromagnetics*, Eur. Phys. J. B **19**, 417-424 (2001).
- [113] Gilbert, Thomas L. *A phenomenological theory of damping in ferromagnetic materials*, IEEE Trans. Magn. **40**, 3443-3449 (2004).
- [114] Richter, H. *Density limits imposed by the microstructure of magnetic recording media*, J. Magn. Magn. Mater. **321**, 467-476 (2009).
- [115] Krounbi, Mohamad, et al. *(Keynote) status and challenges in spin-transfer torque MRAM technology*, ECS Trans. **69**, 119 (2015).